



LUND UNIVERSITY

Femoral Strength Prediction using Finite Element Models

Validation of models based on CT and reconstructed DXA images against full-field strain measurements

Grassi, Lorenzo

DOI:

[10.13140/RG.2.2.26512.00000](https://doi.org/10.13140/RG.2.2.26512.00000)

2016

Document Version:

Publisher's PDF, also known as Version of record

[Link to publication](#)

Citation for published version (APA):

Grassi, L. (2016). *Femoral Strength Prediction using Finite Element Models: Validation of models based on CT and reconstructed DXA images against full-field strain measurements*. [Doctoral Thesis (compilation), Department of Biomedical Engineering]. LTH Tryckeriet E-huset. <https://doi.org/10.13140/RG.2.2.26512.00000>

Total number of authors:

1

Creative Commons License:

GNU GPL

General rights

Unless other specific re-use rights are stated the following general rights apply:

Copyright and moral rights for the publications made accessible in the public portal are retained by the authors and/or other copyright owners and it is a condition of accessing publications that users recognise and abide by the legal requirements associated with these rights.

- Users may download and print one copy of any publication from the public portal for the purpose of private study or research.
- You may not further distribute the material or use it for any profit-making activity or commercial gain
- You may freely distribute the URL identifying the publication in the public portal

Read more about Creative commons licenses: <https://creativecommons.org/licenses/>

Take down policy

If you believe that this document breaches copyright please contact us providing details, and we will remove access to the work immediately and investigate your claim.

LUND UNIVERSITY

PO Box 117
221 00 Lund
+46 46-222 00 00

Femoral strength prediction using finite element models

—

Validation of models based on CT and reconstructed DXA
images against full-field strain measurements

Lorenzo Grassi



LUND
UNIVERSITY

Doctoral Dissertation, November, 25th, 2016

Department of Biomedical Engineering
Lund University
P.O. Box 118, SE-221 00 Lund
Sweden

ISBN: 978-91-7753-030-5 (print)
ISBN: 978-91-7753-031-2 (pdf)
ISRN: LUTEDX/TEEM - 1106 – SE
Report No. 7/16

© 2016 Lorenzo Grassi
Printed in October 2016 by *Tryckeriet i E-huset*, Lund.

Public defence

November, 25th, 2016, 09.15 in Belfragesalen
BMC D15, Lund University
Klinikgatan 32, 222 42, Lund, Sweden

Supervisors

Assoc. Prof. Hanna Isaksson
Department of Biomedical Engineering, Lund University

Prof. Matti Ristinmaa
Division of Solid Mechanics, Lund University

Faculty opponent

Prof. Mark Taylor
*School of Computer Science, Engineering & Mathematics
Flinders University, Adelaide, Australia*

Board of examination

Prof. Kristofer Gamstedt
*Department of Engineering Sciences, Applied Mechanics
Uppsala University, Uppsala, Sweden*

Prof. Thomas Christian Gasser
*Department of Solid Mechanics
Royal Institute of Technology (KTH), Stockholm, Sweden*

Assoc. Prof. Cecilia Rogmark
*Department of Orthopaedics
Skåne University Hospital, Malmö, Sweden*

Deputy member: Assoc. Prof. Christina Bjerken
*Faculty of Technology and Society
Malmö Högskola, Malmö, Sweden*

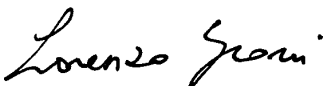
Cover illustration

Finite element model of a human femur, where mineral density is mapped from low (blue) to high (gold)

Organization: LUND UNIVERSITY	Document name: DOCTORAL DISSERTATION	
Department of Biomedical Engineering Box 118, 211 00 Lund, Sweden	Date of issue: November 25 th , 2016	
Author: Lorenzo Grassi	Sponsoring organization	
Title: Femoral strength prediction using finite element models - Validation of models based on CT and reconstructed DXA images against full-field strain measurements.		
<p>Osteoporosis is defined as low bone density, and results in a markedly increased risk of skeletal fractures. It has been estimated that about 40% of all women above 50 years old will suffer from an osteoporotic fracture leading to hospitalization. Current osteoporosis diagnostics is largely based on statistical tools, using epidemiological parameters and bone mineral density (BMD) measured with dual energy X-ray absorptiometry (DXA). However, DXA-based BMD proved to be only a moderate predictor of bone strength. Therefore, novel methods that take into account all mechanical characteristics of the bone and their influence on bone resistance to fracture are advocated. Finite element (FE) models may improve the bone strength prediction accuracy, since they can account for the structural determinants of bone strength, and the variety of external loads acting on the bones during daily life.</p> <p>Several studies have proved that FE models can perform better than BMD as a bone strength predictor. However, these FE models are built from Computed Tomography (CT) datasets, as the 3D bone geometry is required, and take several hours of work by an experienced engineer. Moreover, the radiation dose for the patient is higher for CT than for DXA scan. All these factors contributed to the low impact that FE-based methods have had on the current clinical practice so far.</p> <p>This thesis work aimed at developing accurate and thoroughly validated FE models to enable a more accurate prediction of femoral strength. An accurate estimation of femoral strength could be used as one of the main determinant of a patient's fracture risk during population screening.</p> <p>In the first part of the thesis, the ex vivo mechanical tests performed on cadaver human femurs are presented. Digital image correlation (DIC), an optical method that allows for a full-field measurement of the displacements over the femur surface, was used to retrieve strains during the test. Then, a subject-specific FE modelling technique able to predict the deformation state and the overall strength of human femurs is presented. The FE models were based on clinical images from 3D CT datasets, and were validated against the measurements collected during the ex vivo mechanical tests. Both the experimental setup with DIC and the FE modelling procedure have been initially tested using composite bones (only the FE part of the composite bone study is presented in this thesis). After that, the method was extended to human cadaver bones. Once validated against experimental strain measurements, the FE modelling procedure could be used to predict bone strength.</p> <p>In the last part of the thesis, the predictive ability of FE models based on the shape and BMD distribution reconstructed from a single DXA image using a statistical shape and appearance model (SSAM, developed outside this thesis) was assessed. The predictions were compared to the experimental measurements, and the obtained accuracy compared to that of CT-based FE models. The results obtained were encouraging. The CT-based FE models were able to predict the deformation state with very good accuracy when compared to thousands of full-field measurements from DIC (normalized root mean square error, NRMSE, below 11%), and, most importantly, could predict the femoral strength with an error below 2%. The performances of SSAM-based FE models were also promising, showing only a slight reduction of the performances when compared to the CT-based approach (NRMSE below 20% for the strain prediction, average strength prediction error of 12%), but with the significant advantage of the models being built from one single conventional DXA image.</p> <p>In conclusion, the concept of a new, accurate and semi-automatic FE modelling procedure aimed at predicting fracture risk on individuals was developed. The performances of CT-based and SSAM-based models were thoroughly compared, and the results support the future translation of SSAM-based FE model built from a single DXA image into the clinics. The developed tool could therefore allow to include a mechanistic information into the fracture risk screening, which may ultimately lead to an increased accuracy in the identification of the subjects at risk.</p>		
Keywords: bone strength, femur, osteoporosis, statistical appearance model, finite element, mechanical test		
Classification system and/or index terms (if any)		
Supplementary bibliographical information: ISRN: LUTEDX/TEEM - 1106 – SE Report-nr: 7/16	Language: English	
ISBN printed copy: 978-91-7753-030-5	ISBN digital copy: 978-91-7753-031-2	
Recipient's notes	Number of pages: 171	Price
	Security classification	

Distribution by (name and address)

I, the undersigned, being the copyright owner of the abstract of the above-mentioned dissertation, hereby grant to all reference sources permission to publish and disseminate the abstract of the above-mentioned dissertation.

Signature: 

Date: October 20th, 2016

Populärvetenskaplig sammanfattning

Benskörhet är en folksjukdom där de drabbade framförallt tappar stora mängder benmassa, vilket medför en ökad risk för benbrott. Omkring 40% av alla kvinnor över 50 år kommer drabbas av ett benbrott till följd av benskörhet. De flesta benbroten sker i lårbenshalsen, kotorna i ryggraden eller i handleden. Trots att behandlingar av benbrott har förbättrats betydligt under de senaste åren så leder ofta brott av lårbenshalsen till komplikationer som medför att 20-24% av de drabbade avlider inom ett år efter benbrottet. I dag diagnostiseras benskörhet genom att mäta bentätheten i lårbenshalsen eller ryggraden från en 2D röntgen-liknande bild. Metoden är inte tillräcklig, eftersom omkring 30% av patienterna som bryter ett ben på grund av benskörhet inte identifieras som individer med hög risk för benbrott. Nya metoder som tar hänsyn till fler faktorer för att beräkna risken för benbrott behövs.

Datorsimuleringar kan skapa tredimensionella modeller som beskriver formen och de mekaniska egenskaperna av lårbenet hos varje individ. Sådana datormodeller kan beräkna vilken kraft som behövs för att bryta ett ben. Den beräknade kraften kan korreleras till risken för benbrott. Datormodeller skapas vanligtvis utifrån 3D datortomografi-bilder, vilket kräver en högre stråldos för patienten och högre kostnader för hälso- och sjukvården jämfört med 2D-röntgenbilder. Tidigare har en metod som kan rekonstruera höftbenets geometri och bentäthetsfördelning i 3D baserat på endast en 2D-röntgenbild utvecklats. Metoden består av kliniska datortomografi bilder av lårbenet och innehåller information om form och bentäthet i befolkningen. Syftet med den nuvarande avhandlingen var därför att utveckla en metod som kan förbättra diagnostiseringen av benskörhet. Detta genom att kombinera den redan utvecklade 3D-rekonstruktionen av benets geometri och densitet från en 2D-röntgenbild med noggranna beräkningar av benstyrka och risk för benbrott. Målet med den nya metoden är att förutsäga vilken kraft som behövs för att

bryta ett ben för att slutligen kunna förutspå individens risk för att bryta lårbenshalsen.

De nya utvecklade beräkningsmodellerna i det här arbetet måste valideras noggrant innan de kan tillämpas i kliniken. Första steget i projektet blev därför att utföra experimentella mekaniska tester på lårben där förskjutningen av benet mättes med hjälp av två kameror och en teknik som kallas digital bildkorrelation. Tekniken gör det möjligt att följa förskjutningarna av olika punkter i bilden och därmed beräkna töjningarna över ett brett område. Det möjliggör en mer omfattande validering av beräkningsmodellerna än vad som tidigare gjorts, när endast data från ett fåtal mätpunkter använts för validering. Sedan byggdes beräkningsmodeller som med hjälp av finita element metoden förutsa det mekaniska beteendet av benen. Klassiska beräkningsmodeller byggdes från 3D datortomografibilder för att bestämma den högsta noggrannheten som kan uppnås med beräkningsmodeller. Därefter kombinerades den traditionella finita element metoden med en 3D-rekonstruktion från en 2D-röntgenbild, där syftet var att förutspå kraften vid brott utifrån en enda 2D-röntgenbild.

Beräkningsmodellerna är lovande och gav bra resultat. De klassiska modellerna baserat på datortomografibilder kunde förutse kraften vid brott med en felmarginal på 1-2%. Datormodellerna från en rekonstruerad 3D benstruktur kunde förutse kraften vid brott med en genomsnittlig felmarginal på 12%. Den lägre noggrannheten i de 3D-rekonstruerade modellerna kompenseras av att dessa modeller kan skapas utifrån endast bilder som används i dagens diagnostik av benskörhet.

Förhoppningen är att inom en snar framtid jämföra utfallen från beräkningsmodellerna med data från observationsstudier om benskörhet och benbrott på grupper av personer som följs över lång tid. Om resultatet från en sådan pre-klinisk studie uppfyller förväntningarna så har metoden potential att testas i kliniken inom några år. Att mer exakt kunna förutspå en individs risk för benbrott på detta sätt skulle möjliggöra mer riktade medicinska behandlingar av benskörhet utan att öka kostnaderna för hälso- och sjukvården.

Abstract

Osteoporosis is defined as low bone density, and results in a markedly increased risk of skeletal fractures. It has been estimated that about 40% of all women above 50 years old will suffer from an osteoporotic fracture leading to hospitalization. Current osteoporosis diagnostics is largely based on statistical tools, using epidemiological parameters and bone mineral density (BMD) measured with dual energy X-ray absorptiometry (DXA). However, DXA-based BMD proved to be only a moderate predictor of bone strength. Therefore, novel methods that take into account all mechanical characteristics of the bone and their influence on bone resistance to fracture are advocated. Finite element (FE) models may improve the bone strength prediction accuracy, since they can account for the structural determinants of bone strength, and the variety of external loads acting on the bones during daily life.

Several studies have proved that FE models can perform better than BMD as a bone strength predictor. However, these FE models are built from Computed Tomography (CT) datasets, as the 3D bone geometry is required, and take several hours of work by an experienced engineer. Moreover, the radiation dose for the patient is higher for CT than for DXA scan. All these factors contributed to the low impact that FE-based methods have had on the current clinical practice so far.

This thesis work aimed at developing accurate and thoroughly validated FE models to enable a more accurate prediction of femoral strength. An accurate estimation of femoral strength could be used as one of the main determinant of a patient's fracture risk during population screening.

In the first part of the thesis, the *ex vivo* mechanical tests performed on cadaver human femurs are presented. Digital image correlation (DIC), an optical method that allows for a full-field measurement of the displacements over the femur surface, was used to retrieve strains during the test. Then, a subject-specific FE modelling technique able to predict the deformation state and the overall strength of human femurs is presented. The FE models were based on clinical images from 3D CT datasets, and were validated against the measurements collected during the *ex vivo* mechanical tests. Both the experimental setup with DIC and the FE modelling

procedure have been initially tested using composite bones (only the FE part of the composite bone study is presented in this thesis). After that, the method was extended to human cadaver bones. Once validated against experimental strain measurements, the FE modelling procedure could be used to predict bone strength.

In the last part of the thesis, the predictive ability of FE models based on the shape and BMD distribution reconstructed from a single DXA image using a statistical shape and appearance model (SSAM, developed outside this thesis) was assessed. The predictions were compared to the experimental measurements, and the obtained accuracy compared to that of CT-based FE models. The results obtained were encouraging. The CT-based FE models were able to predict the deformation state with very good accuracy when compared to thousands of full-field measurements from DIC (normalised root mean square error, NRMSE, below 11%), and, most importantly, could predict the femoral strength with an error below 2%. The performances of SSAM-based FE models were also promising, showing only a slight reduction of the performances when compared to the CT-based approach (NRMSE below 20% for the strain prediction, average strength prediction error of 12%), but with the significant advantage of the models being built from one single conventional DXA image.

In conclusion, the concept of a new, accurate and semi-automatic FE modelling procedure aimed at predicting fracture risk on individuals was developed. The performances of CT-based and SSAM-based models were thoroughly compared, and the results support the future translation of SSAM-based FE model built from a single DXA image into the clinics. The developed tool could therefore allow to include a mechanistic information into the fracture risk screening, which may ultimately lead to an increased accuracy in the identification of the subjects at risk.

List of appended papers

This thesis consists of a review of the author's work in the field of biomedical engineering. The following selection of the author's publications is referred to in the text by their Roman numerals. Papers I-V are appended at the end of the thesis, and have been reproduced with the permission of the copyright holders.

- I. Lorenzo Grassi, Hanna Isaksson, "Extracting Accurate Strain Measurements in Bone Mechanics: a Critical Review of Current Methods," in *Journal of the Mechanical Behavior of Biomedical Materials*, vol. 50, pp. 43–54, 2015.
- II. Lorenzo Grassi, Sami P. Väänänen, Saber Amin Yavari, Harrie Weinans, Jukka S. Jurvelin, Amir A. Zadpoor, Hanna Isaksson, "Experimental Validation of Finite Element Model for Proximal Composite Femur Using Optical Measurements," in *Journal of the Mechanical Behavior of Biomedical Materials*, vol. 21, pp. 86–94, 2013.
- III. Lorenzo Grassi, Sami P. Väänänen, Saber Amin Yavari, Harrie Weinans, Jukka S. Jurvelin, Matti Ristinmaa, Amir A. Zadpoor, Hanna Isaksson, "Full-field Strain Measurement During Mechanical Testing of the Human Femur at Physiologically Relevant Strain Rates," in *Journal of Biomechanical Engineering*, vol. 136, no. 11, 2014.
- IV. Lorenzo Grassi, Sami P. Väänänen, Matti Ristinmaa, Jukka S. Jurvelin, Hanna Isaksson, "How Accurately Can Subject-specific Finite Element Models Predict Strains and Strength of Human Femora? Investigation Using Full-field Measurements," in *Journal of Biomechanics*, vol. 49, no. 5, pp. 802–806, 2016.
- V. Lorenzo Grassi, Sami P. Väänänen, Matti Ristinmaa, Jukka S. Jurvelin, Hanna Isaksson, "Prediction of Femoral Strength Using 3D Finite Element Models Reconstructed from DXA Images: Validation Against Experiments," submitted for publication.

In papers I-V, the author of this thesis contributed to the study design, and carried out the development of the experimental and numerical methods presented. The author of this thesis was the main writer of papers I-V.

Other related publications by the author (not appended at the end of this thesis):

- VI. Sami P. Väänänen, Lorenzo Grassi, Gunnar Flivik, Jukka S. Jurvelin, Hanna Isaksson, “Generation of 3D Shape, Density, Cortical Thickness and Finite Element Mesh of Proximal Femur from a DXA Image,” in *Medical Image Analysis*, vol. 24, no. 1, pp. 125–134, 2015.

In paper VI, the author of this thesis contributed to the development of the finite element models used for 3D reconstruction from DXA images.

Acknowledgements

There are many people I wish to thank for this five year long journey.

First of all, I would like to thank my two supervisors for their patient guidance. Hanna Isaksson, thank you for your great supervision, you allowed me to take many decisions, but at the same time you were always there to guide me and support me when I needed help. I am also grateful for all the help and support I received from you in the life outside academia; that was not a duty, and it therefore feels more special. Matti Ristinmaa, you have been an excellent co-supervisor, always present when I needed you, sharing your knowledge and complementing Hanna with your solid mechanics background. I do admire how you can combine the rigorousness of your work with the smiles and the light-heartedness. Every meeting with you helped me to keep things in the right perspective.

Professor Mark Taylor, thank you for having accepted to be my opponent and for having travelled from the other side of the World to be here. Professor Kristofer Gamstedt, Professor Thomas Christian Gasser, Associate Professor Cecilia Rogmark, and Associate Professor Christina Bjerken, thank you for having accepted to be my examiners.

I wish to thank all the co-authors of the studies included in this thesis: Sami P. Väänänen, Saber Amin Yavari, Harrie Weinans, Amir Abbas Zadpoor, Jukka S. Jurvelin. Saber, Harrie and Amir, thank you for your support during my stay in Delft and for sharing your knowledge about mechanical testing. Jukka, thanks for the time you have always managed to find for me, and for your priceless advice on life. Sami, thanks for being not only a very skilful and methodical colleague, but also a loyal friend. Thanks to you and to your dear Tiina, Onni, Helmi and Seppo for making me feel like home during my stays in Kuopio.

I want to thank all the colleagues I had during these five years. The guys of the research group in Biomechanics have been my daily company during the whole journey. It has been a pleasure to be a member of the group since the beginning, and to have seen it growing and evolving over these years, without ever losing its friendly

and positive atmosphere. The guys at the Division of Solid Mechanics have been my travel companions during the first half of my PhD journey. You guys are a very tight group, which is a pleasure to belong to. Thanks to the people at the Department of Biomedical Engineering and all those sitting in the BMC D13 corridor, who I have enjoyed my coffee breaks with during the second half of my PhD journey, in particular at the Monday fika that sweetened each start of the week. A well-deserved thanks for their patience should also go to the Master students I had the pleasure to supervise during these years.

Enrico Schileo and Fulvia Taddei, I thank you on behalf of the whole group at the Laboratory of Medical Technology of the Rizzoli Orthopaedic Institute, Bologna. You made me love the world of research, and gave me the best training one could ever desire when coming out of University. I will never be thankful enough for all the fantastic time spent together, from the bicycle rides over the Bologna hills to the time spent helping you fixing your lovely house.

I would like to thank all my friends, starting from my childhood friends in Italy, going to my neighbours in Billeberga, passing through all the fantastic people I met in Bologna first, and in Lund later. I feel lucky every time I have the pleasure of spending some time with you.

Babbo, Mamma, and Leonardo, thanks for your constant support and for letting me feel your presence, despite the distance.

Elisa, thank you for having decided to follow me to Sweden. You have been strong, learned a new language, and found your own way in a new country. I am proud of you.



Lorenzo Grassi

List of Acronyms and Abbreviations

BMD	Bone Mineral Density
BW	Body Weight
CBCT	Cone Beam Computed Tomography
CT	Computed Tomography
DAQ	Digital Acquisition
DIC	Digital Image Correlation
DRR	Digital Reconstructed Radiography
DVC	Digital Volume Correlation
DXA	Dual energy X-ray Absorptiometry
FBGS	Fibre Bragg Grating Sensors
FE	Finite Element
FRAX	Fracture Risk Assessment Tool
HU	Hounsfield Unit
NRMSE	Normalised Root Mean Square Error
NURBS	Non-Uniform Rational B-Splines
PCA	Principal Component Analysis

SAM Statistical Appearance Model

SD Standard Deviation

SEE Standard Error of Estimation

SG Strain Gauge

SSAM Statistical Shape and Appearance Model

SSM Statistical Shape Model

SVD Singular Value Decomposition

TRL Technology Readiness Level

WHO World Health Organization

Contents

Populärvetenskaplig sammanfattning	vii
Abstract	ix
List of appended papers	xi
Acknowledgements	xiii
List of Acronyms and Abbreviations	xv
1 Preamble	1
2 Aim and design of the study	3
2.1 Aim of the study	3
2.2 Design of the study	4
3 Background	5
3.1 Osteoporosis	5
3.2 Finite element models for prediction of bone strength	9
3.3 Strain measurements in bone	12
3.4 Statistical reconstruction of 3D shape and BMD distribution of bones	18
4 Material and Methods	21
4.1 Material	21
4.2 The DIC experiment	22
4.3 CT-based FE models	28
4.4 Combining SSAM and FE modelling	34

5 Results	39
5.1 The DIC experiment	39
5.2 CT-based FE models	47
5.3 Combining SSAM and FE modelling	52
6 Discussion	57
6.1 Collection of experimental measurements from ex vivo mechanical tests	57
6.2 Development of a CT-based FE modelling procedure to predict femoral strength	60
6.3 Development of SSAM-based FE models to predict femoral strength from DXA	62
6.4 Limitations	64
6.5 Future perspectives	66
7 Summary and Conclusions	71
References	73
Paper I – Extracting Accurate Strain Measurements in Bone Mechanics: a Critical Review of Current Methods	93
Paper II – Experimental Validation of Finite Element Model for Proximal Composite Femur Using Optical Measurements	107
Paper III – Full-field Strain Measurement During Mechanical Testing of the Human Femur at Physiologically Relevant Strain Rates	119
Paper IV – How Accurately Can Subject-specific Finite Element Models Predict Strains and Strength of Human Femora? Investigation Using Full-field Measurements	129
Paper V – Prediction of Femoral Strength Using 3D Finite Element Models Reconstructed from DXA Images: Validation Against Experiments	137

Chapter 1

Preamble

Osteoporosis is a metabolic bone disease which results in a reduction of bone density and in an alteration of bone quality. The main effect of osteoporosis is an increased fracture risk consequent to the loss of bone density. Osteoporotic fractures typically occur in the hip, spine and wrist [1]. Such fractures are associated with a dramatic increase of the patient morbidity and mortality as a consequence of the surgical operation and immobilization periods needed to treat them. It has been estimated that the lifetime risk of any fracture of the hip, spine or wrist is almost 40% in Caucasian women and 13% in Caucasian men from 50 years of age onwards [2]. These data, combined with the progressively increasing ageing of the population (median age increased by 0.3 years per year during the past decade, [3]) convey the idea of how crucial it is to timely identify the subjects at risk in order to treat them and prevent osteoporotic fractures.

Current diagnostics of osteoporosis is based on measurement of bone mineral density (BMD) at either the hip or the lumbar spine, using dual energy X-ray absorptiometry (DXA) [4]. The BMD value is compared with the average value for healthy young female subjects of the same population. According to the World Health Organization (WHO) criteria, osteoporosis is defined as a BMD that lies 2.5 standard deviations (SD) or more below this reference value. The risk of sustaining an osteoporotic fracture is in turn estimated based on the measured BMD values. A series of epidemiological parameters can be added to complement BMD in fracture risk prediction such as in, e.g., FRAX [5]. These methods present the advantage of being very easy to administer. However, there are evidences that BMD is only a moderate predictor of fracture risk [6, 7]. It has been reported that BMD alone can predict fractures with a detection rate of 30-50% with a false positive rate of 15% [6]. These numbers indicate that a more accurate method to predict fracture risk in elderly individuals should be developed [8].

It has been hypothesised that bone strength could be a better predictor of the fracture risk, since the ultimate strength of a bone is not only a function of the

mineral density, but also of the bone shape, material distribution, and the different loading conditions. Consistently with this hypothesis, BMD alone was reported to be only a moderate predictor of bone strength [9]. Subject-specific finite element (FE) models have the potential to accurately predict the strength of human bones. Since the first investigations by Lotz et al. [10, 11], many improvements have been achieved, and FE models have proved their ability to predict femoral strength better than what BMD does [12]. Despite the promising results, FE models have not yet been introduced in the clinical practice [13], with the first clinical experimentations only being proposed in the last years [14]. Among the reasons that prevented FE models to be adopted in clinical practice is the fact that FE models are typically built from computed tomography (CT) data, while DXA images are normally taken in clinics for fracture risk prediction. Besides, the generation of FE models is usually not fully automatic, and requires the intervention of a trained engineer. These factors would ultimately result in an increased cost of a screening, with the improvement in fracture risk prediction accuracy not justifying the increase in costs [15]. Developing an FE modelling procedure which is more automatic and relies on DXA images would overcome the above mentioned limitations, thus facilitating direct clinical experimentation of the new method.

Statistical shape and appearance models (SSAMs) have the potential to reconstruct the 3D shape and density distribution of an object given its 2D projection and a statistical atlas of the shape and density variability. The creation of the statistical atlas is typically based on principal component analysis (PCA), while the reconstruction of a particular sample is performed through solving an optimization problem. Statistical shape and appearance models could therefore be used to reconstruct the shape and BMD distribution of human femurs, and ultimately build three dimensional FE models from a two dimensional DXA image. The assessment of the accuracy of such a modelling framework represents the thread of this thesis.

Chapter 2

Aim and design of the study

The main objective of this thesis is to develop and validate a subject-specific FE modelling procedure that could predict femoral strength from a DXA image and a SSAM-based reconstruction.

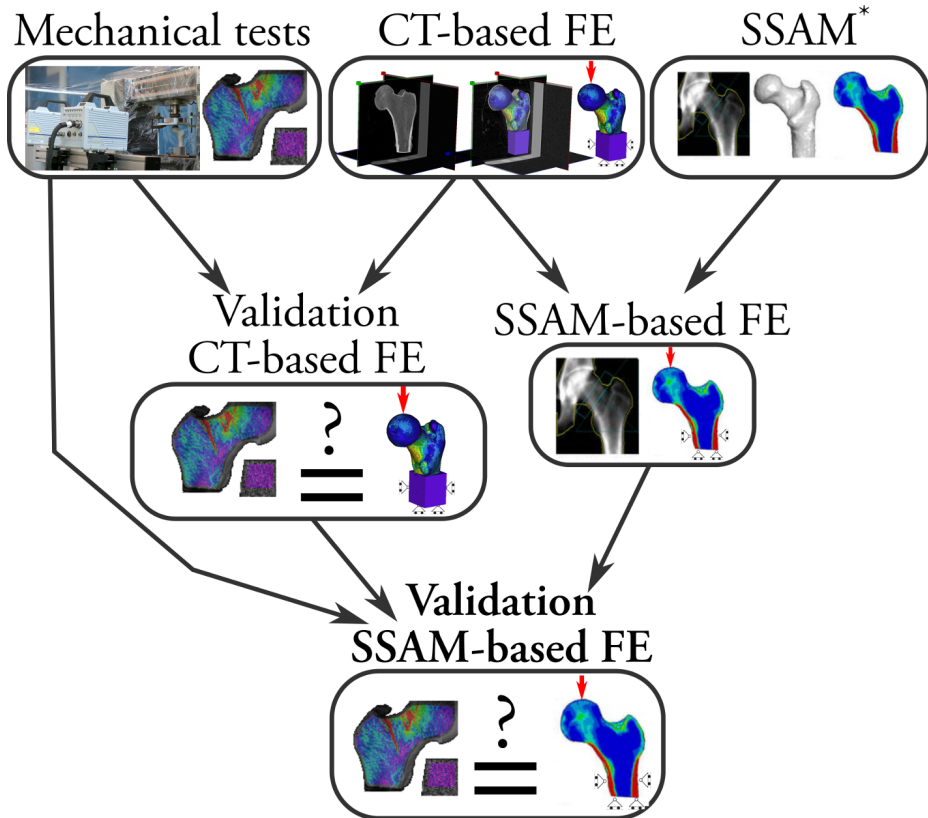
2.1 Aim of the study

The specific aims of this thesis are:

- To develop an experimental setup that collects reliable and spatially resolved strain measurements of human femurs subjected to a single leg stance loading scenario.
- To develop a subject-specific FE modelling procedure from CT data that can predict the mechanical behaviour and strength of a human femur, and validate the models against experimental measurements.
- To incorporate a SSAM algorithm in the subject-specific FE modelling procedure, and evaluate the performance of the SSAM-based models against the CT-based models and the experimental measurements.

2.2 Design of the study

In order to fulfil the declared aims, the study design depicted in figure 2.1 was followed.



* developed outside this thesis, details of SSAM technology are reported in paper VI

Figure 2.1: Design of the study.

Chapter 3

Background

This chapter is briefly reviewing the topics constituting the basis of this thesis work. First, osteoporosis is defined, and the impact of osteoporotic fractures on the society is delineated. The methodology used to assess fracture risk for individuals in the clinical practice is described. Then, the potential of FE models to provide an improved accuracy of fracture risk prediction is discussed. As FE models need to be thoroughly validated, the main techniques to measure deformation on bones during ex vivo mechanical tests are also introduced. Last, the methodologies that allow to reconstruct the three-dimensional shape and bone density distribution from a two-dimensional clinical image are treated.

3.1 Osteoporosis

Osteoporosis is a condition resulting in skeletal fragility, where bone strength is sufficiently low for fractures to occur with minimal trauma, often no more than what is applied by routine daily activities [16]. Osteoporosis has been operationally defined on the basis of BMD. The most widely validated technique to measure BMD is DXA. According to the WHO criteria, osteoporosis is defined as a BMD that lies 2.5 SD or more below the average value for young healthy women [4]. The difference in SD units from the given mean is called T-score. The four categories for diagnosis are:

- normal (T-score -1.0 and above)
- low bone mass, referred to as osteopenia (T-score between -1.0 and -2.5)
- osteoporosis (T-score -2.5 and below)
- severe osteoporosis (T-score -2.5 and below, with history of a fracture)

These definitions are widely accepted and have also served as a diagnostic and intervention threshold level for many years. However, advances in research demonstrated limitations of adopting the osteoporosis definition alone as a fracture risk predictor [6]. Defining fracture risk by BMD alone does not capture the majority of people at risk for breaking a bone. In 2004, a scientific group gathered to re-evaluate the assessment of osteoporosis and fracture risk. As an outcome, a revised description of osteopenia and assessment of osteoporosis was released in 2008. The revised assessment complemented BMD with selected risk factors for fracture. The developed methodology was called FRAX, and determines the 10-year probability of incurring in a major osteoporotic fracture (i.e., in the humerus, wrist, hip or spine). FRAX was developed by WHO and its estimates have been incorporated into clinical guidelines of several national osteoporosis societies [17, 18, 19, 20], which regards it as the current gold standard for osteoporosis and fracture risk diagnostics. FRAX will be covered in more detail in section 3.1.2.

3.1.1 Hip fractures: epidemiology

Osteoporotic hip fractures (hereafter referred to as hip fractures) are fractures occurring in the proximal end of the femur (the long bone running through the thigh, see figure 3.1) as a consequence of a minor trauma (or no trauma at all in some cases) in osteoporotic subjects. The impact of all osteoporotic fractures, and hip fractures in particular, is huge on our society. Osteoporosis ranks high among dis-

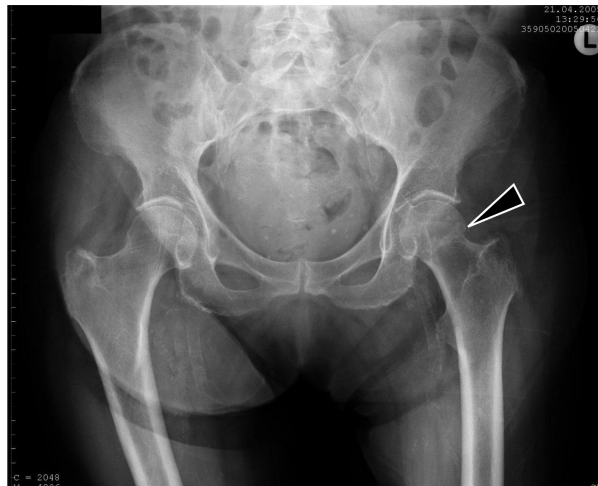


Figure 3.1: An X-ray image of the hip bones. The arrow points to the osteoporotic hip fracture. Retrieved from https://en.wikipedia.org/wiki/Hip_fracture.

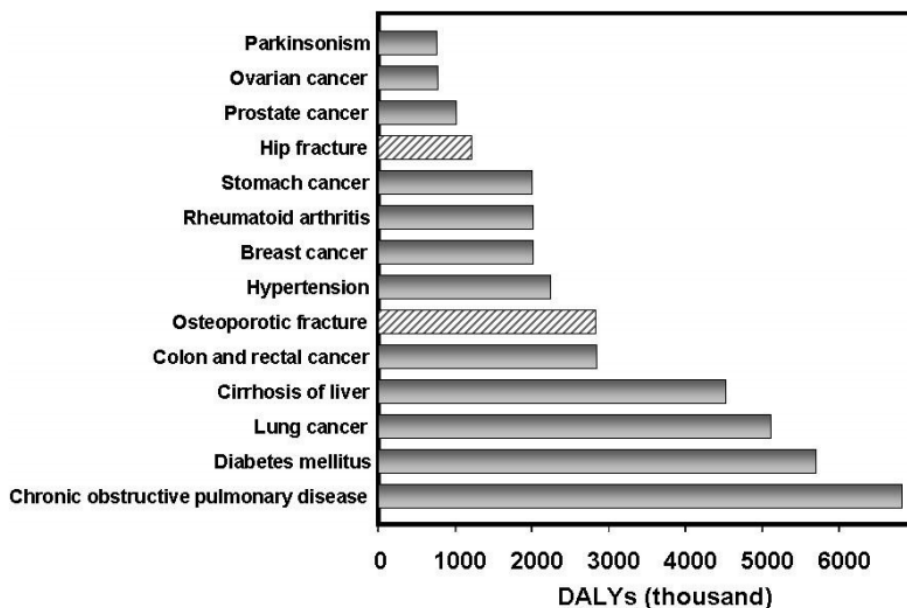


Figure 3.2: Burden of diseases estimated as disability-adjusted life years (DALYs) in 2002 in the Americas and Europe combined. Reprinted from the summary meeting report (Brussels, 5-7 May 2004) of the WHO Scientific Group on the Assessment of Osteoporosis at Primary Health Care Level [21], Copyright WHO (2007).

eases that cause people to become bedridden, which in turn exposes them to the risk of serious complications. The occurrence of complication can be a life-threatening event especially in elderly people. The WHO estimated that 2.8 million disability-adjusted life years were lost in 2002 in the Americas and Europe combined [21]. The comparison of this data with the burden of other diseases can help to realise the impact of osteoporosis on Western society (figure 3.2). Osteoporotic fractures are responsible of a greater burden than breast cancer and hypertension, with hip fractures themselves accounting for a burden superior to that of prostate cancer.

In epidemiological terms, the impact of osteoporosis and osteoporotic hip fractures can be analysed in terms of their prevalence, incidence, morbidity and mortality.

- *Prevalence:* the prevalence of osteoporosis increases with age for both sexes. A study conducted in Germany reported a prevalence of osteoporosis in patients with fractures of 36% for patients older than 60 years, and 50% for patients older than 70 years [22].
- *Incidence:* the incidence of hip fracture was found to increase exponentially

with age. Regional differences are also considerable, with Scandinavia having world highest reported incidence of hip fracture [23]. The incidence at 80 years in Sweden is 933 cases per 100000 person-years in men, and 1549 cases per 100000 person-years in women. These data can be compared with those from a region with relatively high risk such as Italy, 295/100000 in men, 871/100000 in women, and a region with low risk like Chile, whose incidence is 44/100000 in men, and 119/100000 in women [23].

Seventy percent of hip fractures occurs in women (and 61% of all osteoporotic fractures) [24]. This difference between men and women is likely to be associated with the decreased oestrogen levels following menopause. Bone cells contain functional oestrogen receptors and, although the molecular mechanisms of the oestrogen action have not been fully elucidated, there is convincing evidence that oestrogen loss is associated with bone loss and increased risk of fracture [25, 26].

- *Morbidity*: hip fractures are associated with high morbidity rates. Loss of function and independence among fractured individuals is profound, with 40% unable to walk independently and 60% requiring assistance a year later [27]. Less than half of those who survive the hip fracture regain their previous level of function [28]. Because of these losses, 33% are totally dependent or in a nursing home in the year following a hip fracture [29, 30, 31], and the health-related quality of life was found to be significantly lower in subjects with an osteoporotic fracture as compared with subjects without fractures [32].
- *Mortality*: up to 20% of patients die in the first year following hip fractures [33, 29], mostly due to pre-existing medical conditions, and increased risk of passing away persists for at least 5 years [34].

Although no significant variation in neither age-adjusted prevalence of osteoporosis nor age-adjusted hip fracture incidence was detected in the past 45 years [35], the demographic changes in the population will lead to an increase of the hip fracture cases. Assuming no further change in the age- and sex-specific incidence, the number of hip fractures is estimated to be 2.6 million per year by the year 2025, and 4.5 million per year by the year 2050, with a percentage increase of 310% and 240% for men and women, respectively [36].

3.1.2 Estimation of fracture risk

Although low BMD confers increased risk for fracture, most fractures occur in postmenopausal women at moderate risk [37, 38, 39, 40], and evidence suggests that

many women who sustained a fragility fracture have not been appropriately diagnosed and treated for probable osteoporosis [41, 42]. Therefore, attempts have been made to include other clinical factors in the computation of a patient's fracture risk.

The clinical gold standard for the assessment of fracture risk is FRAX. FRAX was released in 2008 by WHO, and is currently available as a free online tool (www.shef.ac.uk/FRAX/) [43, 44]. The aim of FRAX is to predict the 10-year probability of a major osteoporotic fracture in men and women by combining the areal BMD information with a series of clinical risk factors. FRAX can also provide an estimation based on the risk factors only, without any areal BMD data provided to the statistical algorithm. The risk factors include age, sex, race, height, weight, body mass index, a history of fragility fracture, a parental history of hip fracture, use of oral glucocorticoids, rheumatoid arthritis, current smoking, and alcohol intake of three or more units per day. According to the American National Osteoporosis Foundation, FRAX should be used to calculate fracture risk for patients with a T-score between -1.0 and -2.5 in the spine, femoral neck, or total hip region [44].

Although representing a step forward in terms of analysing fracture risk as a multi-factorial event, FRAX is not free from limitations. Criticisms have been arisen concerning the lack of a publicly available description of the equations implemented in FRAX [45]. While indulging on these aspects is not among the scope of this section, it is more interesting to observe that FRAX has been reported not to perform consistently better than simpler fracture risk assessment tools [46], or even BMD alone [47]. The inclusion of more clinical risk factors has been proposed to increase the FRAX predictive accuracy [48, 44, 49], most of them targeted at addressing the propensity to fall. A major improvement could also be provided by the ability to calculate the load that a patient's bone could withstand without fracturing [50]. This information could be predicted with greater accuracy using mechanistic approaches such as personalised FE models [12].

3.2 Finite element models for prediction of bone strength

The FE method is a numerical approach to obtain approximate solutions to arbitrary differential equations. In a nutshell, analysing a physical domain using the FE method consists in dividing the domain into smaller parts, so-called finite elements. For each finite element, an approximate solution to the partial differential equations describing its physical phenomena of interest can be found. Typically, the approximation consists in assuming that the variable of interest, which might vary in a highly non-linear manner over the entire domain, is varying in a simpler fashion (usually polynomially) over a finite element. The equations describing each finite element are assembled into a larger system of equations that covers the en-

tire finite element mesh. The solution of the system of equations can be found, and the discrete solution of the original continuous problem is retrieved. A more comprehensive treatment of the theory of FE analysis can be found in Ottosen and Petersson [51].

While the emergence of the FE method took place in the late 1950s and early 1960s, the method is reported to appear first in the orthopaedic literature in 1972 [52]. The stress or strain state in bones had earlier been postulated to play a relevant role in several biomechanics or orthopaedics related problems [53]. However, the classic mechanics approach could not fully answer many of the questions about the stress state in bones, due to the highly non-linear structural properties of bone. The ability of the FE method to evaluate stresses and strains in structures with complex shape, loading and material behaviour was therefore seen as a promising tool to answer these questions.

The first study using subject-specific FE models to predict the mechanical behaviour of human femurs was conducted by Lotz et al. in 1991 [10, 11]. The study, divided in two separate publications analysing the linear and non-linear behaviour, used two human cadaver femurs, whose FE models were built by retrieving shape and material properties from their CT scans. One femur was tested in a configuration resembling single leg stance, whereas the second femur was tested in a configuration resembling a fall to the side. The yield and fracture load were accurately predicted when compared to data from the in vitro tests performed on the two femurs. However, the predicted surface stresses correlated poorly with the measurements acquired in vitro using strain gauges.

In the following years, many other studies employing subject-specific FE models to predict bone mechanics have been proposed [54, 55, 56, 57, 58]. Although the level of complexity of the models has constantly been increasing with the increase in the available computational power, the approach to build a subject-specific FE model has remained almost the same. A schematic of the modelling framework is shown in figure 3.3. First, the specific femur is imaged using CT (or, less frequently, using magnetic resonance imaging). The femur geometry is then retrieved from the CT images, a procedure usually referred to as segmentation. Segmentation consists in labelling the region corresponding to bone in each CT slice, with a process that can be more or less automatic. Once the femur geometry is obtained and converted to a format that is suitable for meshing, a 3D mesh is created. For this step, an automatic mesh generation software is generally adopted to subdivide the domain into a set of small, as geometrically regular as possible, finite elements [59]. The subsequent step is to map the material properties of each finite element based on the bone density. For this purpose, the CT images are calibrated using a calibration phantom with known equivalent bone density, and different empirical relationships [60] can be used to convert bone density to bone mechanical properties (typically, the Young's modulus). More or less complex material behaviours (from simple lin-

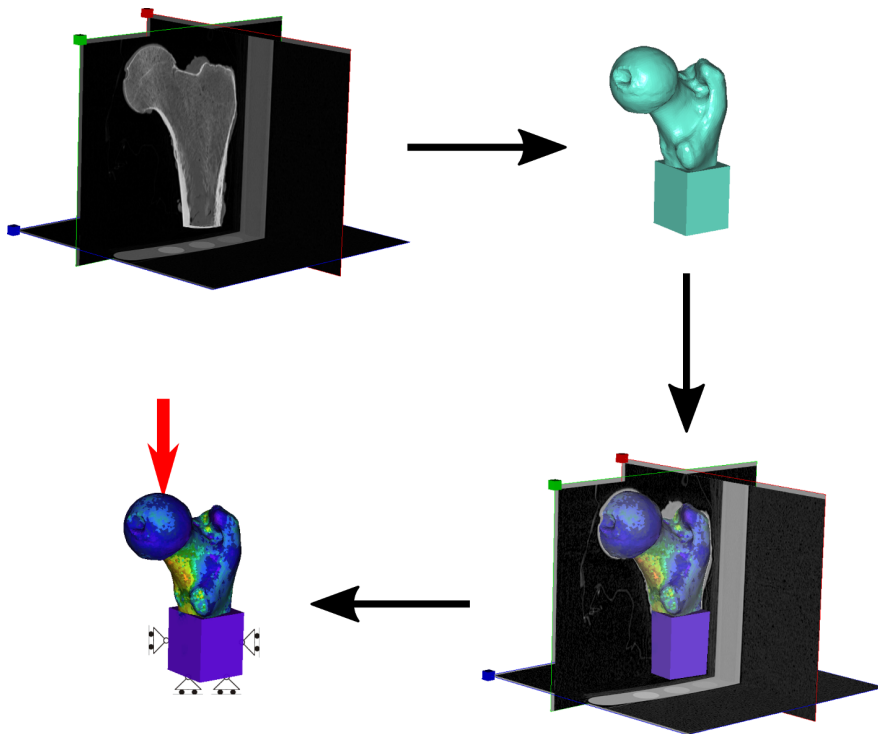


Figure 3.3: Typical modelling framework to build a subject-specific FE model. First, the CT images are acquired (top left). Then, the three-dimensional geometry of the bone is retrieved by segmentation of the CT images, and a three-dimensional finite element mesh is built (top right). The FE mesh is superimposed to the CT scan, and the calibrated grey values of the CT images are used to map the specific material properties for each element (bottom right). Last, the boundary conditions are prescribed to the FE mesh, and the FE problem is solved (bottom left).

ear elastic approach to including yield, strain rate dependency, anisotropy, etc.) can be defined for bone [61]. The desired boundary conditions can ultimately be prescribed for the FE model, and the solution obtained using an FE solver package.

Following the described modelling approach, FE models have reached a high degree of accuracy. The prediction accuracy is determined relatively to a set of observations, typically from *ex vivo* mechanical tests [62, 63, 64]. A short review of the most common measurement techniques used in *ex vivo* mechanical tests is provided in section 3.3. The ultimate aim of FE models is often to accurately predict bone strength, therefore the majority of the studies compares the predicted values versus the experimentally obtained fracture loads [65, 66]. However, since most of the bone strength criteria adopted in FE computations are based on either the strain or stress levels predicted on the specimen, a validation in terms of strain/stress

prediction accuracy is often advocated [62, 64]. For the case of human femurs in a configuration resembling single leg stance, studies reported a strain prediction accuracy with a coefficient of determination in the range of 0.95-0.97 [67, 55], whereas the femoral strength was predicted with an absolute error of a few hundred Newtons, and coefficient of determination between 0.75 and 0.96 [13].

3.3 Strain measurements in bone

Accurately measuring strains during *ex vivo* mechanical tests is crucial both to derive improved constitutive laws for bone, and to appropriately validate numerical predictions from, e.g., FE analyses. Different techniques can be used to experimentally measure strains. Here, a brief recap of the four most relevant techniques to measure strains on bone at the organ level is proposed.

3.3.1 Strain gauges

A strain gauge (SG) is a device that can measure the deformations of the material to which it is attached by reading the variation of the resistance of a conductor exposed to a force that elongates or contracts it. A backing material carries the deformation from the tested material to the electrical grid. Given the resistance of the conductor in the undeformed state, R , its variation as a function of the applied strain, ϵ , is given by:

$$\frac{\Delta R}{R} = K_s \epsilon, \quad (3.1)$$

where K_s is the so-called gauge factor, which expresses the sensitivity of the strain gauge. Strain gauges are usually either mono-axial, with one single gauge grid, or tri-axial. In the latter, three gauge grids are placed in a "rosette" configuration, which allows to determine the principal strains magnitudes and directions.

The first documented application of strain gauges to bone mechanics is from 1944 [68], and since then strain gauges represented the most commonly adopted mean to measure deformation on bones during *ex vivo* mechanical tests [69, 70, 71, 72]. One of the main challenges of using SGs onto bones is to obtain a proper bonding. Typically, the bone surface has to be cleaned from soft tissue and degreased using acetone. The SGs are then bonded using cyanoacrylate glue or epoxy resins. A waterproofing layer of silicon or Teflon is usually added [69] to preserve the electrical contacts of SGs while keeping the bones wet in order to maintain their original mechanical properties [73].

Strain gauges are still considered the gold standard, due to their high and well documented accuracy. They do, however, present some limitations, mainly due to the discreteness of the measurements (typically no more than 12-15 SGs per

proximal femur are applied, each covering an area of 1-5 mm²). Bonding SGs to regions with very thin cortex (such as, e.g., the femoral neck) has also been shown to provide a reinforcement effect that can in turn underestimate the measured strains by a factor up to 15 % [74, 75].

3.3.2 Fibre Bragg grating sensors

Although only sporadically used, fibre Bragg grating sensors (FBGSs) represent an interesting solution to measure strains. First commercialised in 1995, FBGSs consist of a fibre with different refraction indexes in the inner and outer cores. When the fibre gets stretched, its grating period changes, which ultimately results in a change in the wavelength of the reflected ultraviolet light. The latter is linked to the change in the spatial period of the refractive index modulation, according to [76]:

$$\lambda_B = 2\eta_{\text{eff}}\Lambda, \quad (3.2)$$

where λ_B is the Bragg wavelength of the FBGS, η_{eff} is the index of the fibre, and Λ is the periodicity of the grating. A longitudinal deformation of the fibre causes a change of both Λ and η_{eff} . The resulting change in λ_B can then be related to the applied longitudinal strain via:

$$\frac{\Delta\lambda_B}{\lambda_B} = (1 - \rho_e)\epsilon_z. \quad (3.3)$$

It follows that if the photoelastic coefficient ρ_e is known, the longitudinal strain ϵ_z in the fibre can be derived.

FBGSs are small (typical diameter around 100 μm), lightweight, and biocompatible. The absence of electrical circuits allows the positioning in very narrow environments such as, for example, the interface between a bone and an implant. Despite these very interesting features, the applications to bone mechanics are limited [77, 78], mostly because the accuracy of FBGSs did not prove to be comparable to that of strain gauges [76].

3.3.3 Digital image correlation

Digital image correlation (DIC) is a non-contact technique which consists in acquiring digital images of the tested specimen during different stages of the mechanical test. One digital image is then compared to another by taking a block of pixels (subset), and minimizing the grey value difference between a subset from the first image (template) and a displaced copy in the second image. DIC measurements can be classified based on the dimensionality: 2D (one camera used, 2 components of the position and displacement vector obtained as an output), 3D-surface (two

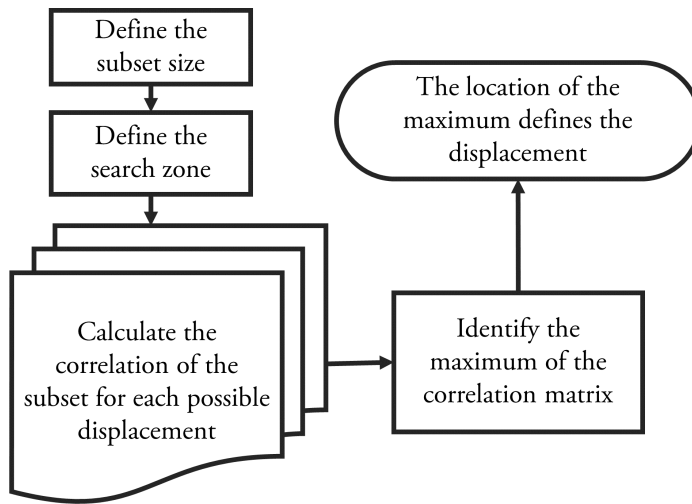


Figure 3.4: Schematic of a simple 2D DIC algorithm.

cameras in a stereo-vision system, 3 components of the position and displacement vector obtained for the surface of the specimen), 3D-volume (also known as digital volume correlation, a tomographic imaging device is used, and the full 3D volume deformation field is obtained).

The main principles of DIC are hereby described for a simple 2D case. The reader is referred to Sutton et al. [79] for a more comprehensive essay on the topic. A flowchart representation of a simple DIC algorithm is shown in figure 3.4. The process starts with taking two pictures, one of which is the template (usually, a picture taken in the undeformed state of the specimen). The two digital pictures can be seen as two matrices of grey level values, with each entry representing a physical point in the analysed grid (figure 3.5). The size of the subset (i.e., the window over which the correlation between the two pictures is evaluated) is then determined. There is not a univocal formula to calculate the optimal size of the subset, although some practical recommendations exist [79, 80]. Sutton et al. proposed, as a general guideline, to have image plane speckles sampled by at least a 3 by 3 pixel array, with each image plane subset containing at least 3 by 3 speckles [79]. Once the subset size is set, a search zone is usually defined. A search zone is a submatrix over which the correlation of the subset between the two pictures is calculated. The definition of a search zone is not strictly necessary, but it dramatically reduces the computational cost of the DIC algorithm.

The DIC algorithm works then as a loop for each point of the analysed grid: the correlation (typically, Zero-normalised squared differences are used) between the subset for the specific entry in the template and all the possible subset configurations within the search zone of the second image is calculated. The matrix of the

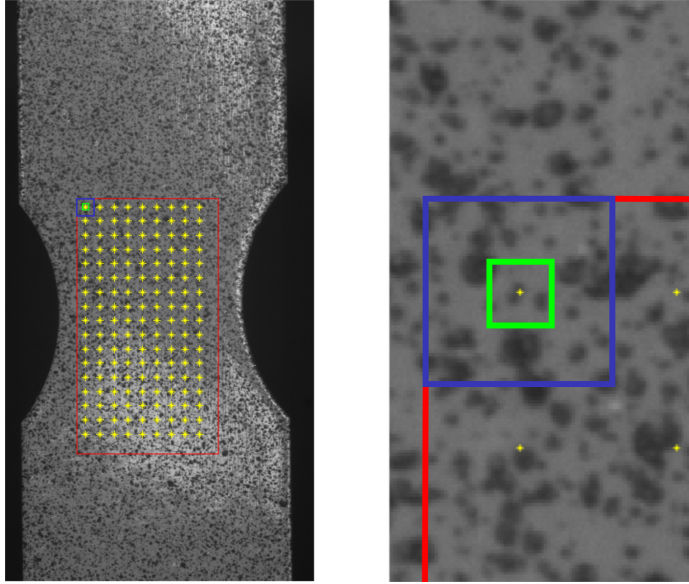


Figure 3.5: Region of interest of a simple 2D DIC analysis (red), analysed point grid (yellow), search zone (blue), and subset zone (green).

correlation coefficients is stored, and the entry giving its maximum value is taken as the new position of the analysed entry.

When the DIC algorithm is executed over all the entries, a matrix with the displacements over the horizontal and vertical directions is obtained for each entry. This allows to extrapolate a full-field displacement field by, e.g., direct linear interpolation. Strains can then be calculated using different techniques. One of them consists in triangulating the point grid, thus defining a set of constant strain triangles. These triangles are then treated following the FE theory, where the nodal coordinates and displacements can be used to derive the Green strain tensor:

$$\mathbf{E} = \frac{1}{2}(\mathbf{F}^T \mathbf{F} - \mathbf{I}), \quad (3.4)$$

where \mathbf{E} is the Green strain tensor, \mathbf{I} is the unit tensor, and \mathbf{F} is the deformation gradient tensor, which can be defined as:

$$\mathbf{F} = \mathbf{I} + \mathbf{D} = \mathbf{I} + \begin{bmatrix} \frac{\partial u}{\partial X} & \frac{\partial u}{\partial Y} \\ \frac{\partial v}{\partial X} & \frac{\partial v}{\partial Y} \end{bmatrix}, \quad (3.5)$$

where \mathbf{D} is the displacement gradient tensor, and u and v are the components of the displacement vector. The displacement gradient tensor \mathbf{D} can be derived for

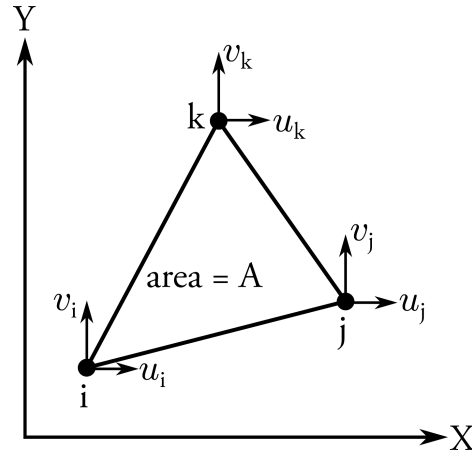


Figure 3.6: Representation of a constant strain triangular element in its undeformed state. The nodal coordinates are displaced by $u_{i,j,k}$ and $v_{i,j,k}$ along the X and Y direction.

constant strain triangular elements (figure 3.6) by considering that the displacement vector can be obtained from the element shape functions N_i, N_j, N_k , and the displacement components at each node, $u_{i,j,k}$ and $v_{i,j,k}$:

$$\mathbf{u} = \begin{bmatrix} u \\ v \end{bmatrix} = \begin{bmatrix} N_i & 0 & N_j & 0 & N_k & 0 \\ 0 & N_i & 0 & N_j & 0 & N_k \end{bmatrix} \begin{bmatrix} u_i \\ v_i \\ u_j \\ v_j \\ u_k \\ v_k \end{bmatrix}, \quad (3.6)$$

where:

$$N_i = \frac{1}{2A} [x_j y_k - x_k y_j + (y_j - y_k)X + (x_k - x_j)Y] \quad (3.7)$$

$$N_j = \frac{1}{2A} [x_k y_i - x_i y_k + (y_k - y_i)X + (x_i - x_k)Y] \quad (3.8)$$

$$N_k = \frac{1}{2A} [x_i y_j - x_j y_i + (y_i - y_j)X + (x_j - x_i)Y] \quad (3.9)$$

The components of the displacement vector as of equation 3.6 can thus be derived with respect to X and Y , which in turns allows the deformation gradient tensor \mathbf{F}

(equation 3.5) and the Green strain tensor \mathbf{E} (equation 3.4) to be calculated as a function of the nodal coordinates and displacements.

Initially adopted for measurement of large displacements and deformations, DIC started being applied to small strain tests with the emergence of high resolution digital cameras. A review about the use of DIC in the field of biomechanics has been recently presented by Palanca et al. [81].

The first application of DIC with femurs during *ex vivo* mechanical tests was reported in 2011 [82]. 2D DIC was used to measure displacements and strains over 22 cadaver femurs tested in a configuration resembling a fall to the side. The displacement rate was 100 mm/s, which required using high-speed cameras (6000 fps, 1024 x 512 pixels). However, the 2D DIC approach was only able to qualitatively describe the strain distribution over the femurs, as a 3D-surface approach would be more suitable for the curvilinear surfaces of human femurs.

Gilchrist et al. [83] compared the strains measured with 3D-surface DIC with the measurements from SGs. One rosette strain gauge was glued on the antero-superior aspect of the femoral neck of 20 cadaver femurs, and a speckle pattern air-brushed over the same area. Femurs were loaded to 50% of their estimated fracture load ([84], 0.5 mm/s, 100 fps at a resolution of 1280 x 800 pixels) in a configuration resembling a fall to the side. Minor principal strains at the peak force of the test were compared between DIC and SG, showing good correlation (root mean square average difference 127 $\mu\epsilon$, SD = 239 $\mu\epsilon$), as well as the presence of a random noise in the DIC data from one image to the other. After that, the femurs were tested in an impact simulator of a sideways fall (impact velocity 3 m/s, 9216 fps, 576 x 188 pixels), and the strains recorded using DIC only. However, quantitative strain data were not reported in the paper for the impact test.

Helgason et al. [85] also performed a drop tower test in a sideways fall configuration using DIC. One proximal human femur was used in this case (16.5 kg impactor, 3.5 m/s impact speed, 9009 fps, 384 x 384 pixels). However, also in this study the strains collected with DIC were presented only qualitatively.

3.3.4 Digital volume correlation

Digital volume correlation (DVC) is essentially the extension of the 2D-DIC algorithm to the third dimension. It can be applied to, e.g., tomographic datasets, as proposed first by Bay et al. in 1999 [86]. The different type of input images is indeed the main difference between DIC and DVC. While DIC is relying on digital images, in which an artificial speckle pattern can be used to improve the correlation, DVC works on tomographic, attenuation-based, datasets, and has therefore to rely on the naturally occurring patterns in the material. As a consequence, most of the studies applying DVC to bone were performed at the tissue level [87, 88, 89] in order to take advantage of the natural features of bone, such as the spongy trabec-

ular network. Only one study used DVC to investigate human bone at the organ level by scanning whole L1 vertebra samples [89]. However, the noise levels in the measured strain data were only 10 times lower than yield strain. DVC cannot therefore be considered a mature technique for the investigation of strains at the organ level for physiological load magnitudes. For a more comprehensive review of the literature of DVC studies on bone, we refer the reader to the review paper recently published by Roberts et al. [90].

3.4 Statistical reconstruction of 3D shape and BMD distribution of bones

Although FE models can accurately predict bone mechanics and strength, they have not yet been introduced into the clinical practice. One of the reasons is that subject-specific FE models, as illustrated in section 3.2, necessitate a tomographic scan to be built. CT scans are not usually taken for the purpose of osteoporosis diagnostics. Instead, DXA, which is less expensive while still providing the required densitometric information, is used for the diagnosis.

It would therefore be optimal to build subject-specific FE models from DXA images to predict bone strength and fracture risk. In this context, the easiest and most intuitive approach is to build two-dimensional FE models using the subject's DXA image of the hip. Although such modelling approach proved to accurately predict bone strength [91, 92, 93, 94, 95], it is not able to overcome some of the intrinsic limitations due to the 2D nature of the imaging, mainly related to the impossibility to test the bone in the out of plane directions.

Another approach to the issue consists in reconstructing the 3D shape and BMD distribution of a specific bone based on its 2D DXA image. While reconstructing the 3D femoral shape and density based on solely a DXA image is technically not possible, a solution can be accomplished by introducing some *a priori* information. A common method is to use a statistical model that includes information about how the shape and the density change between individuals of the same population [96, 97]. A statistical model describing the variability of the shape of an object inside a population is called statistical shape model (SSM). A statistical model describing the variability of the appearance (e.g., the mineral density in the case of bone) of an object inside a population is called statistical appearance model (SAM). A model that implements both shape and appearance in the same mathematical framework is referred to as statistical shape and appearance model (SSAM).

Statistical shape models have been proposed by Cootes and Taylor in the early 1990s [98, 99], while statistical appearance models were presented in 2001 [100]. The idea behind SSM and SAM is to describe the variability of a set of parameters in an elegant and compact fashion. Typically, PCA is calculated, and the obtained

statistical model consists of a mean shape/appearance and a set of principal modes of variation. Each specimen of the population used to build the SSM/SAM can then be reconstructed as a linear combination of a finite amount of principal modes. With respect to medical image analysis of bone, SSMs have mainly been used for achieving automatic image segmentation [101], but have also found successful application in the generation of realistic synthetic anatomies [102], object classification [97], and 3D reconstruction from 2D images [103, 104, 105].

To build a SSM, the shapes of the bones in the training set are typically described through a set of commonly defined landmark points. Once the landmarks are positioned, the different bones are aligned with each other. The average shape is defined as the shape having each landmark in the mean position, and the SSM can be built by performing a PCA of the covariance matrix. The latter is a matrix that measures the variation of the different shapes from the average shape.

Building a SAM follows the same principles of building a SSM, with the difference that the appearance of the model (typically BMD) has to be captured instead of the shape. When building a SSAM, shape and BMD are combined in one single covariance matrix (which implies that these two entities have to be normalised), and PCA is applied only once. Volumetric FE meshes are usually adopted as a tool that can contain both the shape and the BMD distribution for each sample [97], although image-based approaches can also be used [106].

The reconstruction of the 3D shape/density distribution from a single planar image can be obtained by solving an optimization problem, in which the statistical model template is registered over the planar image. SSM-based templates are generally registered using a set of anatomical landmarks, whereas SAM-based templates are registered based on the intensity levels in the image. For SSAM models, a radiographic image can be digitally reconstructed from the SSAM and be used to solve the optimization problem based on shape and density together.

The combination of the 3D reconstruction of a specific femur using SSAM with FE analysis has therefore the potential to produce accurate 3D FE models of human femurs starting from the single DXA image commonly used in the current clinical screening.

Chapter 4

Material and Methods

This chapter describes the methodologies adopted in the studies conducted during this thesis work. First, a list of the material used for the studies is provided. Then, the experimental mechanical tests performed with the aim to collect meaningful data for the validation of the numerical models are described. The methodologies used to build subject-specific FE models of human femurs from tomographic images are presented. Finally, the techniques to combine FE modelling with the statistical reconstruction of the 3D shape and density from a single 2D image are presented.

4.1 Material

Composite bones were used to perform feasibility studies of both the experimental and numerical methodologies used in this thesis. Six 4th generation, medium-sized, composite femur bones were obtained (model 3403, Sawbones, Pacific Research Laboratories, Inc., USA). These composite femurs mimic the shape and material properties of human bones, and consist of a cortical compartment made of short glass fibre reinforced epoxy and an internal trabecular compartment made of solid foam [107]. Composite bones were CT-scanned (SOMATOM Definition Flash, Siemens, Germany) in air (pixel size 0.24-0.29 mm, 0.4 mm slice thickness).

The actual experimental and numerical studies were conducted using cadaver bones. To this purpose, three proximal cadaver femurs have been harvested fresh at Kuopio University Hospital. Ethical approval for the collection of samples was granted by the Finnish National Authority for Medicolegal Affairs (permission number: 5783/04/044/07). All the donors have been inspected, and no conditions that could affect bone metabolism have been detected. The full list of the collected proximal femurs, together with the most relevant patient data is reported in table 4.1. For each of the specimens, imaging with both CT (Somatom Definition AS64, Siemens AG, 0.4 x 0.4 x 0.6 mm voxel size) and DXA with two different

Specimen [ID]	Side [L/R]	Age at death [yrs.]	Gender [M/F]	BMD [g/cm^3]	Height [cm]	Weight [kg]
1	L	22	M	1.16	186	106
2	R	58	M	0.60	183	85
3	L	58	M	0.89	183	112

Table 4.1: Material set adopted in this thesis. For each proximal femur the main patient information is provided, together with the BMD at the femoral neck measured with DXA.

devices (Lunar Prodigy and Lunar iDXA, GE Healthcare, pixel size 1.05 x 0.60 mm and 0.25 x 0.3 mm pixel size, respectively) were available. Besides, tomographic scans were performed on the specimens after the mechanical tests (section 4.2) using a cone beam CT (CBCT, Planmed Verity, 0.2 x 0.2 x 0.2 mm voxel size). When performing mechanical tests, the specimens were kept wet, immersed in phosphate buffered saline solution to preserve tissue hydration when not in use, and put back into the freezer as soon as possible.

4.2 The DIC experiment

Experimental strain measurements for the composite bones were available from a previous study [108]. Briefly, strains were collected with DIC in a configuration resembling single leg stance. The composite bones were tested up to fracture at a controlled displacement rate of 1.0 mm/min. Two cameras (4M pixels, 4 fps) recorded the anterior surface of the composite bones during the test, and DIC was calculated over the recorded images using Vic3D (v2007, Correlated Solutions, Inc.). This set of experimental measurements has been used to validate the predictions of the specimen-specific FE models of composite bones (section 4.3.1).

In the following of this section, the experimental mechanical tests performed on the three cadaver bones are described.

4.2.1 Specimen preparation and embedding

The three proximal cadaver femurs were allowed to thaw, and the soft tissue was carefully removed using a scalpel and fine sandpaper in order not to damage the periosteum. The specimens were distally resected 5.5 cm below the minor trochanter level and the most distal part was embedded in epoxy. The epoxy pot was eventually used to constrain the distal end by inserting it into a custom made steel holder.

In order to ensure a consistent alignment between the different specimens, an experimental reference system was defined based on the proximal femur anatomy.

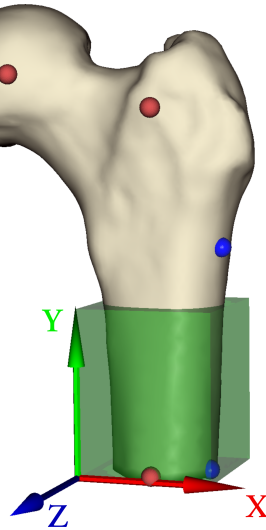


Figure 4.1: Schematic of the alignment procedure of the specimens, and definition of the experimental reference system: the red landmarks show the 3 contact points of a femur when lying on its anterior side. The plane passing through these 3 points defines the anterior plane XY. The blue landmarks show the two most lateral points of the specimen at the greater trochanter level, and at the level of the distal cut. The line passing through these two points defines the longitudinal direction (Y-axis, green). The Z-axis (in blue) is finally defined as the axis orthogonal to the XY plane.

First, the bone was leaned on a horizontal, flat surface with the anterior side down. The three contact points of the femur with the surface, located at the femoral head, at the greater trochanter and in the shaft (red points in figure 4.1) defined the anterior plane. The longitudinal shaft axis was defined as the line connecting the most lateral points (identified as the contact points of the femur with a pin placed perpendicularly to the defined anterior plane) at the minor trochanter level and at the most distal part of the shaft available (blue points in figure 4.1). The combination of the anterior plane and the longitudinal axis allowed to univocally define a Euclidean reference system, and the specimens were embedded in epoxy (Technovit 4071, Heraeus Kulzer, Germany) by aligning the anatomical longitudinal axis to the actuator direction of the loading device, and the anatomical anterior plane to one face of the steel holder. Specimen #3 was embedded in a 2.5 cm deep epoxy pot, whereas specimens #1 and #2 were embedded in a 5 cm deep epoxy pot. This was because the initially planned 2.5 cm deep embedding was later judged to be at risk for local failures of the epoxy. The latter event could potentially compromise the validity of the obtained measurements, and also hinder an accurate reproduction of the prescribed boundary conditions in the corresponding FE models (section 4.3).

The superior aspect of the femoral head was covered with a stainless steel spherical cap in order to prevent local crushing and evenly distribute the loading. The cap was applied by aligning its small circle plane to the XZ plane of the experimental reference system (figure 4.1). This solution proved to be effective in protecting the femoral head in previous experiments [109]. The three specimens were then prepared for the camera recordings and the following DIC analysis of the images by applying a random speckle pattern. First, a matt white background was applied over the anterior femoral surface using a solvent-based spray paint (Gamma, The Netherlands). The white background served to increase the contrast of the acquired images, thus reducing the noise and improving the correlation when performing DIC. After the paint had dried, a random speckle pattern was applied using a permanent marker. Although more time consuming than the more conventional airbrush, using a permanent marker allowed for a better control and repeatability of the speckle size, and an enhanced contrast. The desired size of the speckle was chosen based on the camera settings, with the aim of having each speckle sampled by at least a 3 by 3 pixel array [79]. This setting minimises the oversampling and provides a reasonable intensity pattern reconstruction via interpolation. Based on these considerations, speckles of an average size of 0.6 x 0.6 mm were applied over the anterior surface of the femur, which resulted in 6 by 6 pixel sampling for each speckle with the adopted camera settings (figure 4.2).

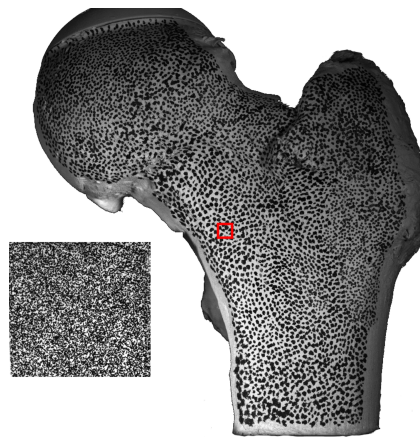


Figure 4.2: Picture acquired from one high-speed camera showing the speckle pattern applied over the anterior surface of the specimen, and over the control plate. A 25 x 25 pixel subset is shown in red to provide a reference for the image spatial resolution.

4.2.2 Mechanical testing

The three specimens were placed in the loading device (5500R, Instron, Inc.), with the distal pot rigidly constrained to the moving part of the loading device using 6 bolts (figure 4.3). The steel cap on the femoral head was greased in order to reduce friction, with the ultimate aim of avoiding the onset of undesired load components along the plane perpendicular to the prescribed loading direction. A 100 kN load cell (accuracy 0.5% of the reading down to 1/500th of the load cell capacity, Instron, Inc.) was placed on the upper part of the loading device at the contact point with the femoral head. The analogue signals of the load cell and of the rotary encoder (providing information about the applied displacement) of the loading device were sent to a digital acquisition (DAQ) module (Isi-DAQ-STD-8D, Isi-Sys, GmbH, Germany). The DAQ module sampled the analogue signals at the same frequency as the camera recordings, and synchronised them with the digital clock signal from the master camera. This allowed to have global force and displacement measurements associated with each of the acquired camera images. A control plate of approximately 35 x 35 mm size was placed on a side of the tested specimen (figure 4.2). The control plate translated jointly with the distal steel pot during the test, and an optimal speckle pattern was applied over its anterior surface using a sticker. The purpose of the control plate was to have an undeformed entity moving alongside the specimen during the test, which could be used to evaluate the noise level in the DIC data during the image processing phase (section 4.2.3). In fact, the control plate should theoretically record only a rigid translation with no deformation throughout the whole test. Whichever strain other than zero recorded onto the plate could be considered to be an artefact due to the noise in the measurements, and could therefore serve as an indicator of the noise levels in the DIC measurements.

The mechanical tests were performed by putting the femoral head in contact with the upper part of the loading device, and then applying a constant displacement rate of 15 mm/s until macroscopic failure of each specimen. Two high-speed cameras (Fastcam SA1.1, Photron, Inc.) with resolution of 1M pixels (giving approximately a 0.1 mm/pixel spatial resolution for the acquired images) recorded the experiment at a frame rate of 3000 fps. The two cameras were placed in front of the anterior aspect of the tested specimens, and had a baseline camera distance of 280 mm, with a pan angle of 29°. The two cameras were synchronised with each other, using a master-slave configuration, and with the analogue measurements from the loading device, using the DAQ module. Two high intensity cold light sources (DX15, Hedler GmbH, Germany) provided a diffuse light to the recorded scene, thus allowing for a short shutter time and high aperture of the cameras.

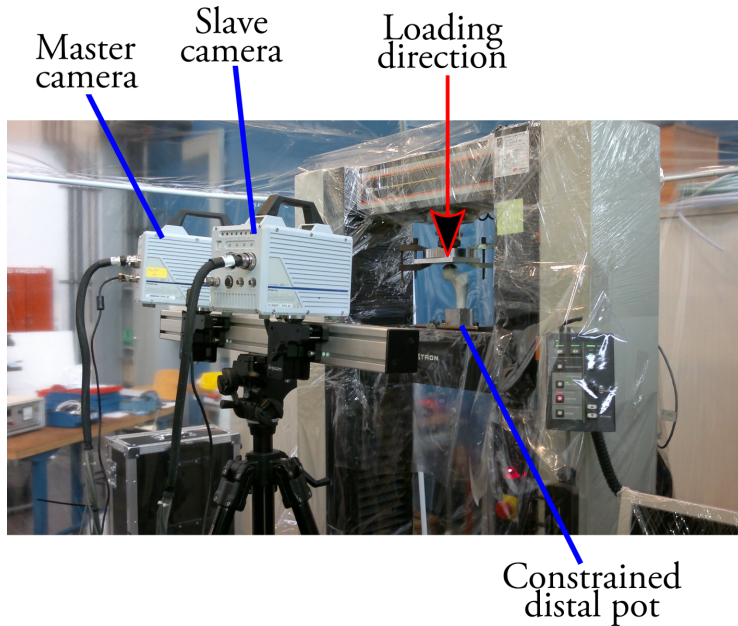


Figure 4.3: A picture of the experimental setup. A composite bone was used instead of the actual cadaver femurs to take this picture to avoid unnecessary dehydration of the cadaveric bones.

4.2.3 Image processing and data extraction

The images acquired during the experiments were processed using DIC to extract the displacement field, which could then be differentiated to obtain the strain field. The software Vic-3D (v7, Correlated Solutions, Inc.) was used to perform the calculations. As DIC is based on the assumption of the examined medium being a continuum, two different set of parameters were defined: the first, which will be referred to as the pre-fracture parameter set, was applied to all the acquired frames until a crack formation was noticeable with the naked eye. The second set, which will be referred to as the near-fracture parameter set, was applied to the 50 frames preceding and following the crack formation. The two DIC parameter sets were defined as reported in table 4.2.

The pre-fracture parameter set was meant to analyse the strain levels in the femur during the whole test, including the elastic phase of the test where the strain levels are moderate. A filter was therefore applied to the calculated DIC displacement in order to remove some noise in the measurements before taking the derivative to calculate the strains. Conversely, the near-fracture parameter set was meant to investigate the local strains before the crack generation: therefore, no filtering was implemented, and the step size was reduced in order to get a better coverage of the

	Subset size [px]	Step size [px]	Filtering	Strain calculation
Pre-fracture	25	5	Low-pass filter with 100 Hz cut-off on the obtained displacements	Green-Lagrangian, spatial decay filter of 5 px size
Near-fracture	25	1	No filter	Green-Lagrangian, spatial decay filter of 5 px size

Table 4.2: Parameter sets adopted to run DIC.

area close to the crack formation.

The noise levels in the strain measurements were determined using the control plate. The average and maximum values of the major principal strain measured over the plate were taken as indicators of the noise level of the DIC measurements. The noise levels were evaluated first when the loading device was turned on, but not operating (resting mode), and subsequently when the actual test was ongoing (operating mode).

Three virtual strain gauges were defined on the anterior surface of each specimen in order to enable a qualitative comparison with the strain gauge data available in literature for similar experiments. The position of the three SGs was identified on the anterior surface of the femoral head, femoral neck, and diaphysis, consistently with the procedure for strain gauge placement adopted by Cristofolini et al. [75]. In order to replicate the same placement procedure on a digital geometry, the 3D shape of each specimen was first obtained via semi-automatic segmentation of the CT images (Seg3D2, CIBC, University of Utah) and spatially registered to the DIC point cloud via a Matlab (v8.1, The Mathworks, Inc.) code based on the genetic optimization algorithm. The procedure described in [75] was finally replicated on the registered 3D model using a multimodal data framework software which allowed to pick landmarks on the surface [110]. The position of the virtual SGs is shown in figure 4.4. The strains at the three selected locations were evaluated by averaging the strain levels over a 3 mm^2 circular area around each point, as the strain gauges used in [75] covered the same area. The calculated principal strains were finally plotted as a function of the applied force.

The overall distribution of the principal strain magnitude and orientation over the time of the experiment was also obtained for two representative loads, namely: 100% of the subject's body weight (BW), and at the last frame before a crack could be detected on the images with the naked eye.

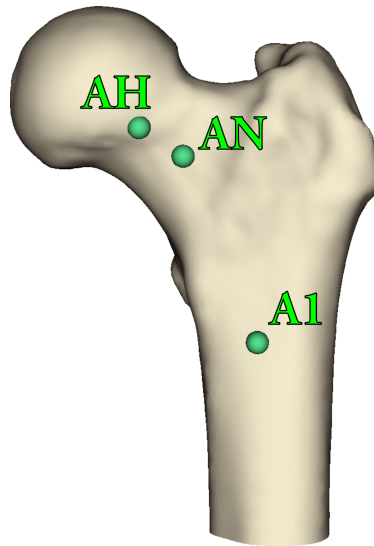


Figure 4.4: The location of the virtual strain gauges on the anterior head (AH), neck (AN), and diaphysis (A1). The nomenclature of the three virtual strain gauges was chosen in consistency with the work of Cristofolini et al. [75].

4.3 CT-based FE models

In this section, the methodology used to build subject-specific FE models based on CT images of the specimen is presented first, for both composite and cadaver bones. Then, the methods to validate the predictions against the experimental measurements are reported.

4.3.1 FE modelling of composite bones

The FE models for the composite bones were built based on their CT images. First, the triangulated geometry was extracted using a semi-automatic segmentation procedure based on active contours [111]. The geometry of the epoxy pot used to constrain the distal part of the composite bones during the mechanical tests was also retrieved from the CT images, and used to reconstruct the experimental reference system. The obtained geometry was converted to Non-uniform rational B-spline (NURBS) surfaces through a reverse engineering process (Rhinoceors 4.0, Robert McNeel & Associates, USA, with RhinoResurf plugin, Resurf3D, China). The NURBS geometry was then used to create a quadratic tetrahedral mesh (approximately 150000 nodes and 100000 elements, mean element volume 2.75 mm^3 , Hypermesh v11.0, Altair Engineering, Inc.). Material properties were assigned based on the material data provided by the manufacturer, with transversely isotropic prop-

erties implemented in the cortical compartment of the femoral neck and diaphysis, and isotropic properties elsewhere (figure 4.5). The boundary conditions reproduced the load and constraints imposed during the mechanical tests for which strain measurements were available [108].

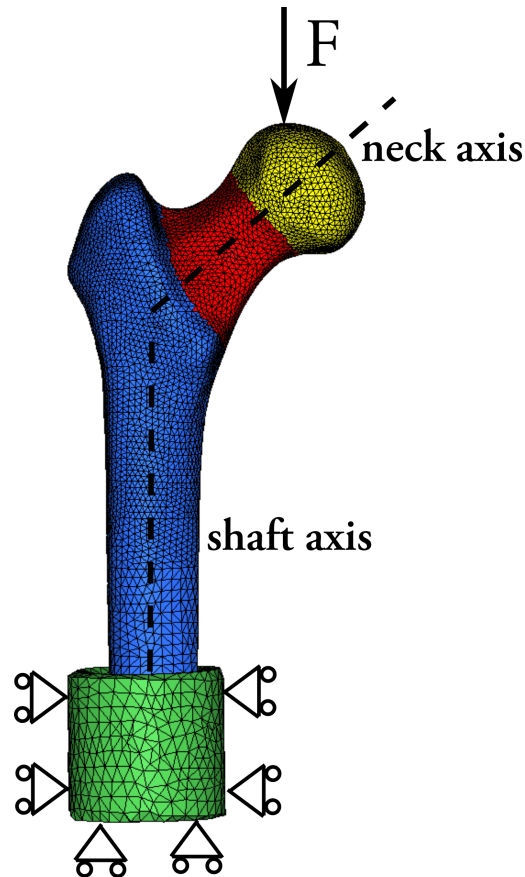


Figure 4.5: FE models of a composite bone. Transversely isotropic material properties (longitudinal Young's modulus 16 GPa, transverse Young's modulus 10 GPa, Poisson's ratio 0.26) were assigned to the cortical compartment at the femoral shaft (depicted in blue) and femoral neck (in red), with the longitudinal direction assumed to be parallel to their respective anatomical axes. Isotropic material properties were assigned to the epoxy pot (Young's modulus 2.5 GPa, Poisson's ratio 0.3, in green), the internal spongy compartment (Young's modulus 155 MPa, Poisson's ratio 0.3), the femoral head region (Young's modulus 16 GPa, Poisson's ratio 0.26, in yellow). Reprinted from paper II with permission from Elsevier.

4.3.2 FE modelling of cadaver bones

Subject-specific CT-based FE models were built for the three cadaver bones based on a consolidated procedure [112, 55]. The femur geometry was segmented from the CT images using a semi-automatic procedure. This procedure consisted of a first thresholding to coarsely obtain the femur shape, followed by a dilation/erosion step, and a hole filling filter. Finally, the obtained segmentation was inspected slice by slice, and manual corrections were applied wherever necessary. The whole segmentation procedure was performed using Seg3D (v2.1.5, CIBC, University of Utah). The same segmentation procedure was applied to the CBCT images acquired after the mechanical tests in order to extract the shape of the distal epoxy pot and of the distal fragment of the femur after fracture. The latter was registered to the femur shape obtained from the CT images. This procedure allowed to accurately identify the experimental reference system over the FE models by using the registered distal epoxy pot. Besides, the registered distal fragment of the femur was used during the validation stage to verify how close the predicted fracture onset was to the actual fracture rim obtained during the mechanical tests.

The segmented femoral geometry was converted to NURBS surfaces through a reverse engineering process (RhinoCeros 4.0, Robert McNeel & Associates, USA, with RhinoResurf plugin, Resurf3D, China). The NURBS geometry was then used to create a mesh of quadratic tetrahedral elements (approximately 140000 nodes and 100000 elements, Hypermesh v13.0, Altair Engineering, Inc.).

The elements belonging to the epoxy pot were assigned an isotropic Young's modulus of 2.5 GPa, in accordance with the mechanical properties reported for the product (Technovit 4071) by the manufacturer (Heraeus Kulzer, Germany). The elements belonging to the femur were instead assigned an isotropic Young's modulus based on the Hounsfield Unit (HU) values of the CT voxels that are within the element volume. The available CT images were reconstructed using a sharp convolution kernel (B60f, Siemens AG, Germany). This kernel aims at providing sharp images with high contrast between different objects. To achieve this, the kernel behaves as a high-pass filter, and overestimates the intensity gradients on the periosteal and endosteal bone surface. This would ultimately result in an overestimated Young's modulus in the FE models at the periosteal and endosteal surface. The optimal solution to this issue would have been to perform a new reconstruction of the CT images using a softer kernel. However, the raw images were no longer available at the time the FE models were built. Therefore, the effect of the sharp kernel was instead mildened by applying a 5 x 5 pixel size mean filter over the reconstructed images. Bonemat_V3 algorithm [113] was used to assign the Young's modulus to each element based on the filtered CT values. Bonemat_V3 uses a trilinear interpolation to calculate the HU field; the HU field is then transformed into a Young's modulus field, and finally the numerical integration over each element volume is performed to assign an element-specific Young's modulus [114, 113]. To

transform the HU field into a Young's modulus field, the calibrated HU values had to be converted to an equivalent radiological density of phosphate dipotassium using a phantom (Model 3 CT, Mindways, Inc.). The Young's modulus was derived from the equivalent radiological density using a set of relationships that was first proposed by Schileo et al. [55]: the equivalent radiological density was considered to be equivalent to the ash density, which was then converted to apparent density using the relation:

$$\rho_{\text{ash}}/\rho_{\text{app}} = 0.6. \quad (4.1)$$

Finally, the apparent density was converted to Young's modulus using the relation proposed by Morgan et al. [115]:

$$E = 6850 * \rho_{\text{app}}^{1.49}. \quad (4.2)$$

The Poisson's ratio was set to 0.4 [116] for all the elements. The load was equally distributed among the 10 most superior first order surface nodes of the femoral head.

A rate-dependent material model with different strain limit values for yield and failure was implemented to predict the femoral strength (figure 4.6). The rate dependence was given by changing the Young's modulus of each specific element at each increment as a function of the strain rate for that specific element at the previous increment:

$$E_{\text{elem}}^i = E_{\text{elem}}^{\text{ref}} * SRCF_{\text{elem}}. \quad (4.3)$$

In the above equation, $SRCF_{\text{elem}}$ is the strain rate correction factor for the specific element, defined as:

$$SRCF_{\text{elem}} = \begin{cases} 1, & \text{if } \left(\frac{\dot{\epsilon}_{\text{elem}}^{i-1}}{\dot{\epsilon}_{\text{ref}}} \right)^{0.06} \leq 1 \\ \left(\frac{\dot{\epsilon}_{\text{elem}}^{i-1}}{\dot{\epsilon}_{\text{ref}}} \right)^{0.06}, & \text{otherwise} \end{cases}, \quad (4.4)$$

where $\dot{\epsilon}_{\text{elem}}^{i-1}$ is the absolute major principal strain rate for the specific element at the previous calculated increment, and $\dot{\epsilon}_{\text{ref}}$ is the strain rate at which both the limit yield strain [117] and the density-elasticity relationships [115] were experimentally obtained (5000 $\mu\epsilon/s$).

The bi-linear behaviour was given by defining strain limit values for element yielding (figure 4.6). Different limit values for tension and compression were defined, where tension in the FE models was given by the major principal strain values, and compression by the minor principal strain values. When an element reached the yield strain limit (10 400 $\mu\epsilon$ in compression, 7300 $\mu\epsilon$ in tension, [117]), the modulus of the element was reduced to 5.5% of the tangent modulus [118], and the simulation proceeded to the subsequent increment. The femoral strength was

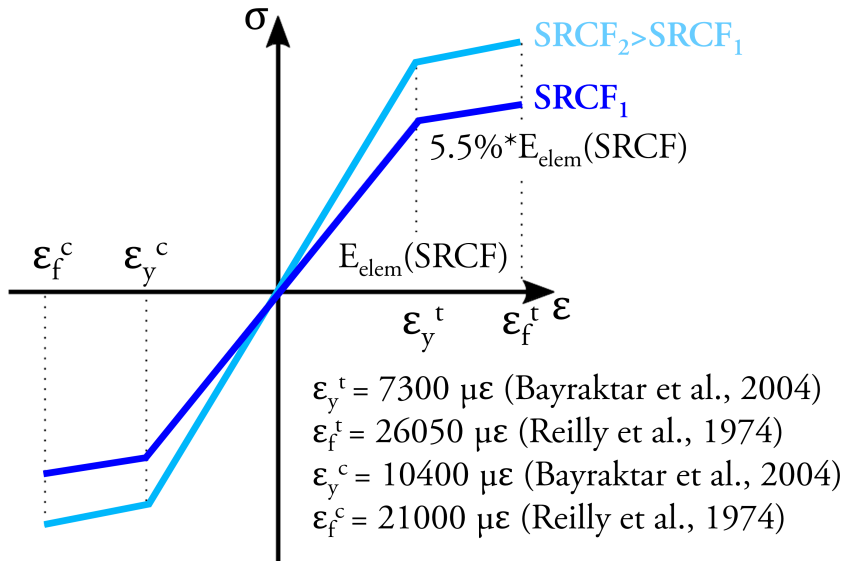


Figure 4.6: The material model used to predict bone strength in the FE models. The mechanical behaviour of an element changes for different SRCFs, according to equation 4.4. The femoral strength was predicted using threshold strain values for yield (ϵ_y) and failure (ϵ_f). The different thresholds for tension and compression are marked with "t" and "c" superscript, respectively. The tangent modulus is reduced to 5.5% of its value in the elastic phase, as extrapolated from the raw measurements from Reilly et al. [118]. Reprinted from paper IV with permission from Elsevier.

determined by defining strain limit values for element failure. Analogously to the yielding, different limit values for tension and compression were defined. According to the experimental findings of Reilly et al. [118], 21 000 $\mu\epsilon$ was taken as the ultimate strain in compression, and 26 050 $\mu\epsilon$ as the ultimate strain in tension.

All the FE simulations were solved using Abaqus (v6.12-4, Dassault Systèmes, France). When assessing the strain prediction accuracy of the FE models, a load corresponding to 4 times the body weight of the subject was imposed, and the simulation was solved as a linear elastic problem in one single increment. Geometrical non-linearities were accounted for by activating the NLGEOM option. Prediction of the femoral strength was performed by imposing consecutive 0.05 mm displacement increments to the FE model, with the simulation time increment opportunely tuned in order to obtain a displacement rate of 15 mm/s (i.e., the same displacement rate imposed during the experimental tests). The specimen was considered to be failed at the increment when the first element failed, and the sum of the reaction forces at the constraints during that increment taken as the predicted femoral strength.

4.3.3 Validation

Validation of composite bones

The FE predictions for the six composite bones were compared in terms of principal strains to the experimental data available [108]. The validation was performed for each composite bone at a load of 3500 N, and at the last available frame before fracture.

The strain prediction accuracy was assessed by comparing the principal strain pattern predicted by the FE models to the principal strains measured with DIC for the same load magnitude applied. Typically, FE and DIC data have different spatial resolution. Therefore, an automatic registration and data comparison method was developed in Matlab. The DIC point cloud was first registered to the corresponding FE mesh using a genetic optimization algorithm. Then, the experimental measurement points for which the tracking quality parameter was greater than two times the optimal value declared by the software developer (confidence interval for the point matching greater than 0.02 pixels, Correlated Solutions, Inc.) were removed from the analysis. The DIC point cloud was then shrunk by removing the 5 outermost layers of points. This was done in order to drop the strains calculated at the borders of the cloud from the analysis, since these were more prone to artefacts due to either higher surface curvatures or reduced search zone. Then, for each surface element of the FE mesh, the radius (R_{smallest}) of the smallest sphere circumscribing it was calculated. The principal strains of all the DIC points located inside a spherical volume of radius equal to $2 * R_{\text{smallest}}$ were averaged, and the obtained values compared to the element principal strains predicted by the FE simulation. The strain prediction accuracy was finally evaluated by performing a linear regression analysis of the major and minor principal strains magnitudes. Determination coefficient (R^2), slope and intercept of the regression, normalised root mean square error (NRMSE) and peak error of the FE predictions were calculated. Bland-Altman [119] plots were also presented to graphically show the overall agreement between experimentally measured principal strains and FE predicted principal strains.

Validation of cadaver bones

The validation of the FE predictions for the three cadaver bones was performed both in terms of strain prediction accuracy in the elastic sector of the force-displacement curve and in terms of the predicted femoral strength.

The assessment of the strain prediction accuracy was performed using a method similar to the one adopted for the composite bones. Two substantial modifications were introduced when validating cadaver bones, namely: (i) the principal strains of the DIC points were averaged over the volume of a sphere with radius equal to $1 * R_{\text{smallest}}$, and (ii) a robust regression analysis with bi-square weighting function was performed instead of the more conventional linear regression analysis. The latter

change was motivated by the fact that the robust regression analysis is less sensitive to non-normality in the distribution of the residuals and heteroscedasticity in the data.

When assessing the femoral strength prediction accuracy for the three cadaver femurs, the strength predicted by the FE models was compared to the maximum force recorded during the *ex vivo* mechanical tests. Relative error and standard error of the estimate (SEE) were reported, as well as a graphical representation of the distance between the predicted fracture onset and the experimentally obtained fracture rim.

4.4 Combining SSAM and FE modelling

In this section, the methodology to build subject-specific FE models based on the 3D shape and BMD distribution as reconstructed using a shape template and a SSAM is described. The methodology to build the statistical shape and appearance models is also reported. The performances of FE models based on SSAM reconstructions are compared to those of the CT-based FE models (as described in section 4.3) for the reconstructed femoral shape only, the reconstructed BMD distribution only, and the combination of the two.

4.4.1 SSAM generation and bone reconstruction

The generation of the SSAM and the algorithm for bone reconstruction were developed by Sami P. Väänänen during his PhD studies [120], and were presented in [121]. The SSAM was generated using 34 proximal femur anatomies, whose CT images were segmented. The average shape was calculated using a set of automatically detected landmarks, and a template mesh with fine tetrahedral elements (1.6 million elements, Hypermesh 11.0, Altair, Inc.) was built for this average shape. The template mesh was subsequently morphed over the geometry of each bone of the 34 bone anatomies available, and element-specific bone density was assigned based on the HU values using Bonemat_V2 algorithm [113]. The SSAM was finally created by performing a singular value decomposition (SVD) of the matrix containing the nodal coordinates of the meshes and the density values associated to each element. As nodal coordinates and element densities had different scales and unit of measure, their values were separately normalised before calculation of the SVD.

To reconstruct the 3D shape and density distribution starting from a single 2D image, a genetic algorithm was used to register the SSAM to the 2D reference image. A digital reconstructed radiography (DRR), consisting of a projection of the SSAM instance onto the coronal plane, was generated at each iteration round and used for the registration. The cost function was defined in order to take into account

mesh quality [122], anatomical positioning, and the sum of the absolute difference of the areal BMD between reference image and DRR of the SSAM instance. The reconstruction was performed for all the three specimens, each of them using three types of reference images:

- DXA image acquired with Lunar iDXA (hereafter referred to as simply "iDXA")
- DXA image acquired with Lunar Prodigy (hereafter referred to as simply "Prodigy")
- 2D image obtained by projecting the CT images along the anteroposterior plane (hereafter referred to as simply "CTproj")

All the analyses and comparisons described in the remaining of this chapter were performed for all specimens and all 2D reference images.

4.4.2 Comparison of SSAM-based and CT-based FE models

The SSAM-based FE models were compared to the CT-based FE models by dividing the comparison into the different components reconstructed by the SSAM: the femoral shape, the BMD distribution, and the combination of the two.

In order to allow a proper comparison of the results, the FE models obtained as an output of the SSAM-based reconstruction, consisting of 1.6 million elements, were all remeshed (Hypermesh v14.0, Altair Engineering, Inc.) with the same parameters used to generate the CT-based FE models described in section 4.3.2. The remeshed SSAM-based models had approximately 100000 elements each. The remeshed SSAM-based models were used in all the comparisons described in this subsection, and will be referred to as SSAM-based models for the sake of simplicity.

SSAM-based shape models

To evaluate the effect of the SSAM-based shape on the FE models accuracy, the SSAM-based models were superimposed to the CT datasets. Then, the material properties were assigned to each element of the SSAM-based models using Bone-mat_V3 and the same density-elasticity relationships used for the CT-based models.

When compared to the CT-based models described in section 4.3.2, the reconstructed SSAM-based models were shorter, and the epoxy pot used to constrain the distal part was also missing. Therefore, the SSAM-based models were merged to the CT-based models in order to apply the same boundary conditions as in the mechanical tests described in section 4.2. The SSAM-based models were first registered to the experimental reference system. Then, the lowest nodal coordinate along the

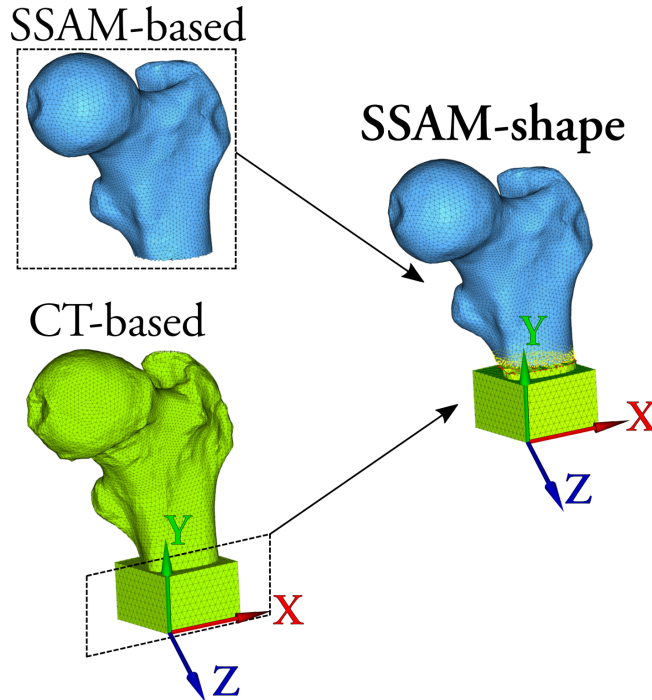


Figure 4.7: Generation of the FE models implementing the SSAM-based shape (*SSAM-based shape* and *SSAM-based shape and BMD* models): the model produced by the SSAM-based reconstruction (depicted in blue, left side) has a shorter shaft than the actual sample, as reconstructed by segmentation of its CT scan (CT-based model depicted in green, left side). In order to replicate the same boundary conditions as in the experiments (section 4.2), the most distal part of the CT-based FE model was added to the SSAM-based FE model, and connected to it using tie constraints (right side, the yellow nodes from the SSAM-based models are tied to the red nodes of from the CT-based model).

Y-direction was determined for the SSAM-based FE model, and the CT-based FE model cut along the XZ plane at that Y-coordinate (figure 4.7). The part of the CT-based model above the cutting point along the XZ plane was removed. The epoxy pot from the CT-based model was added, and the three components (SSAM-based model, distal CT-based femur model, CT-based epoxy model) were connected together using surface based tie elements (Abaqus v2016, Dassault Systèmes, France). The constraints at the epoxy pot were thus kept unaltered, while the vertical loading was again equally shared among the 10 uppermost single-order nodes on the femoral head. The whole cutting and merging operation, together with the definition of the boundary conditions, was automatically performed via a custom made Matlab code.

SSAM-based BMD models

To evaluate the effect of the SSAM-based BMD on the FE models accuracy, the CT-based FE models were taken, and the Young's modulus for each element assigned based on the SSAM-based reconstructed BMD values. To do that, a custom made Matlab code was developed. The code took both the CT-based and the SSAM-based FE models, and warped the latter onto the first. Then, a scan through all the elements of the CT-based FE models was performed to find the elements of the SSAM-based FE models that intersected each element. The intersection volume was calculated, and the element density was defined as the average of the densities in the intersecting SSAM-based elements, weighted by the intersection volumes:

$$\rho_{\text{CT-based}}^i = \sum_j \left(\frac{\rho_{\text{SSAM-based}}^j * V_{ij}}{\sum_j V_{ij}} \right), \quad (4.5)$$

where $\rho_{\text{CT-based}}^i$ was the density of the i^{th} element of the CT-based mesh, $\rho_{\text{SSAM-based}}^j$ was the density of the j^{th} element of the SSAM-based mesh, and V_{ij} was the volume of the intersection between the i^{th} element of the CT-based mesh and the j^{th} element of the SSAM-based mesh. The Young's modulus for each element was then obtained by converting the density into Young's modulus using equations 4.1 and 4.2.

Not all the elements of the CT-based mesh could be assigned a Young's modulus based on the intersection with the elements of the SSAM-based mesh, as the CT-based mesh was longer than the SSAM-based one. Therefore, all the elements of the CT-based mesh that did not intersect with any element of the SSAM-based mesh were allowed to keep the Young's modulus assigned using the CT-based material mapping described in section 4.3. An additional step was also added to compensate for potential artefacts in the BMD distribution due to inaccuracies in the SSAM-based reconstruction. This consisted in:

1. a compensation for the partial volume effect: for each surface element of the model, the Young's modulus was defined as the maximum between the value originally assigned through the mapping and the Young's moduli of the elements lying directly underneath it.
2. a compensation for potential over- and undershoot in the SSAM-based reconstructed material properties: the maximum Young's modulus allowed for all the elements was set to 22 GPa, and the minimum Young's modulus for the surface elements was set to 5 GPa.

SSAM-based shape and BMD models

The combined effect of SSAM-based shape and BMD distribution on the accuracy of the FE predictions was also assessed. This was done by combining the techniques

adopted for comparing SSAM-based shape alone and BMD distribution alone. This generated an FE model which had both the shape and the BMD distribution as they were reconstructed using the SSAM, but in a model which had approximately 100000 elements, and the distal part added to apply the desired boundary conditions.

4.4.3 Validation

The validation for all the SSAM-based models was performed analogously to what was done for the CT-based FE models of cadaver bones, and described in section 4.3.3. The strain prediction accuracy was assessed by robust regression analysis at a load corresponding to 4 times the subject's BW. The only difference was in the method to register the DIC point cloud over the FE models. Here, an additional step consisting in a point-to-surface projection was added after the registration itself, with the aim of correcting local inaccuracies due to possible reconstruction errors of the SSAM-based models. The ability to predict bone strength was assessed by implementing the rate-dependent material behaviour with different limit values for yield and fracture in tension and compression, as described in section 4.3.2, and comparing the obtained femoral strength values with the maximum force recorded during the ex vivo mechanical tests (section 4.2).

Chapter 5

Results

This chapter reports the results obtained during this thesis work using the methodologies described in chapter 4.

5.1 The DIC experiment

5.1.1 Mechanical testing

The three cadaver bones broke at an applied load of 13383 N (specimen #1), 7856 N (specimen #2), and 9080 N (specimen #3). The recorded force versus displacement curves are reported in figure 5.1. The coefficient of determination (R^2) for

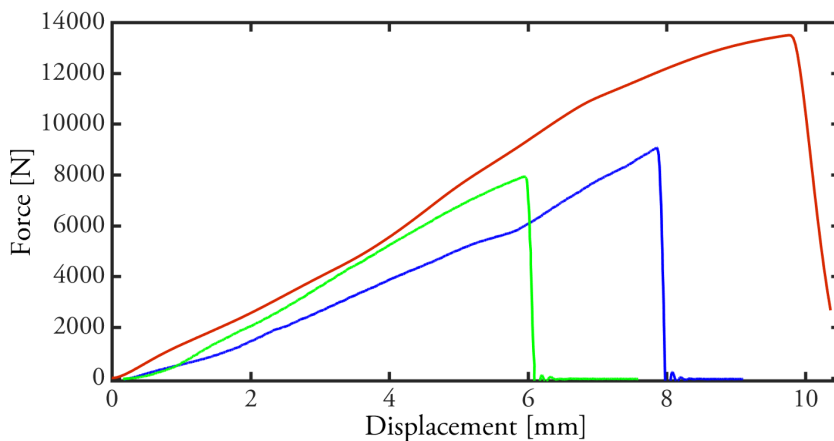


Figure 5.1: The force versus displacement curves for specimen #1 (red), specimen #2 (green), and specimen #3 (blue). Reprinted from paper III with permission from ASME.

the three force versus displacement curves up to the maximum recorded force was equal or greater than 0.99. A sudden drop in the measured force was present in all the curves after the maximum recorded force had been reached. The linearity of the displacement versus time curves was also assessed, to verify if the prescribed boundary conditions of 15 mm/s constant displacement rate had actually been achieved. The coefficient of determination was greater than 0.99 for all the three tests, with a NRMSE always below 11%.

5.1.2 Image processing and data extraction

The noise in the DIC measurements was estimated using the control plate. When using the pre-fracture parameter set, and with the loading device turned on but not operating, the average major principal strain detected on the control plate was $31 \pm 22 \mu\epsilon$, $49 \pm 30 \mu\epsilon$, and $16 \pm 12 \mu\epsilon$ for specimens #1, #2, and #3, respectively. The corresponding maximum values of the major principal strain were $142 \mu\epsilon$, $361 \mu\epsilon$, and $51 \mu\epsilon$. The noise levels increased when the loading device was turned on and operating. The average major principal strain on the control plate while the tests were ongoing rose to $164 \pm 27 \mu\epsilon$, $106 \pm 29 \mu\epsilon$, and $81 \pm 19 \mu\epsilon$, with maximum recorded values of $593 \mu\epsilon$, $659 \mu\epsilon$, and $532 \mu\epsilon$, respectively.

The principal strains collected from the three virtual SGs also showed a linear relationship with respect to the applied force (figure 5.2). The coefficient of determination was always greater than 0.96 (NRMSE always smaller than 19%), except for the major principal strains collected by the virtual SGs at the diaphysis level of specimens #1 and #2. The locations covered by these two virtual SGs seemed indeed to be subjected to pure compression, with the major principal strains being constantly around zero throughout the whole test. No good linear correlation could therefore be detected for these two measurements with respect to the applied force (figure 5.2).

The strain rate was also calculated for the virtual SGs. The von Mises strain rate at the three virtual strain gauges was reported for each specimen (figure 5.3). The strain rate varied between the different locations, with the highest strain rates always located at the femoral head or neck, while the diaphysis was subjected to a lower strain rate.

The linearity of the principal strains with respect to the applied force was also investigated for each single DIC point acquired. When considering all the data from the three specimens, 91% of the data points had a coefficient of determination greater than 0.9 (average NRMSE = $12\% \pm 7\%$, maximum NRMSE = 32%), with 81% of the data points having a coefficient of determination greater than 0.95 (average NRMSE = $11\% \pm 5\%$, maximum NRMSE = 22%).

The major and minor principal strain directions for a force corresponding to the subjects' body weight and at the frame right before fracture are reported in figures

5.4 and 5.5, respectively. The principal strain directions did not drastically change during the test as the applied force increased. Nevertheless, a more uniform alignment of the principal directions could be noticed for higher values of the applied force. The corresponding major and minor principal strain magnitudes at the same stages of the mechanical test were reported in figures 5.6 and 5.7.

The fracture limit plots are presented in figure 5.8. The video recording of specimen #1 was interrupted a few frames before the fracture, likely due to a human error in actioning the trigger. The fracture limit plots are therefore presented only for specimens #2 and #3. These plots show that tensile strains (major principal strains) were higher than compressive strains (minor principal strains) in the anterior surface of the specimens at the frame immediately before the crack was detected. The major principal strains in the specimens at crack formation are shown in figure 5.9. The strain magnitudes in the crack region after the crack formation have to be interpreted only in a qualitative manner, as DIC calculations imply the existence of a medium that can be described as a continuum. The points whose sum of the absolute value of the major and minor principal strains was highest were consistently located where the crack was going to be detected in the following frame (figure 5.8, red points).

The residual strains 0.08 s after the crack formation were in the order of a few hundred microstrains. Higher strain magnitudes (greater than $1000 \mu\epsilon$) could be found in the crack region. The mean and median values of the residual principal strains are reported in table 5.1.

Specimen ID	Principal strain	Median [$\mu\epsilon$]	Mean [$\mu\epsilon$]
2	major	153	339
2	minor	239	433
3	major	329	760
3	minor	319	560

Table 5.1: Mean and medial value for the major and minor principal strains detected in the specimens 0.08 s after the crack formation.

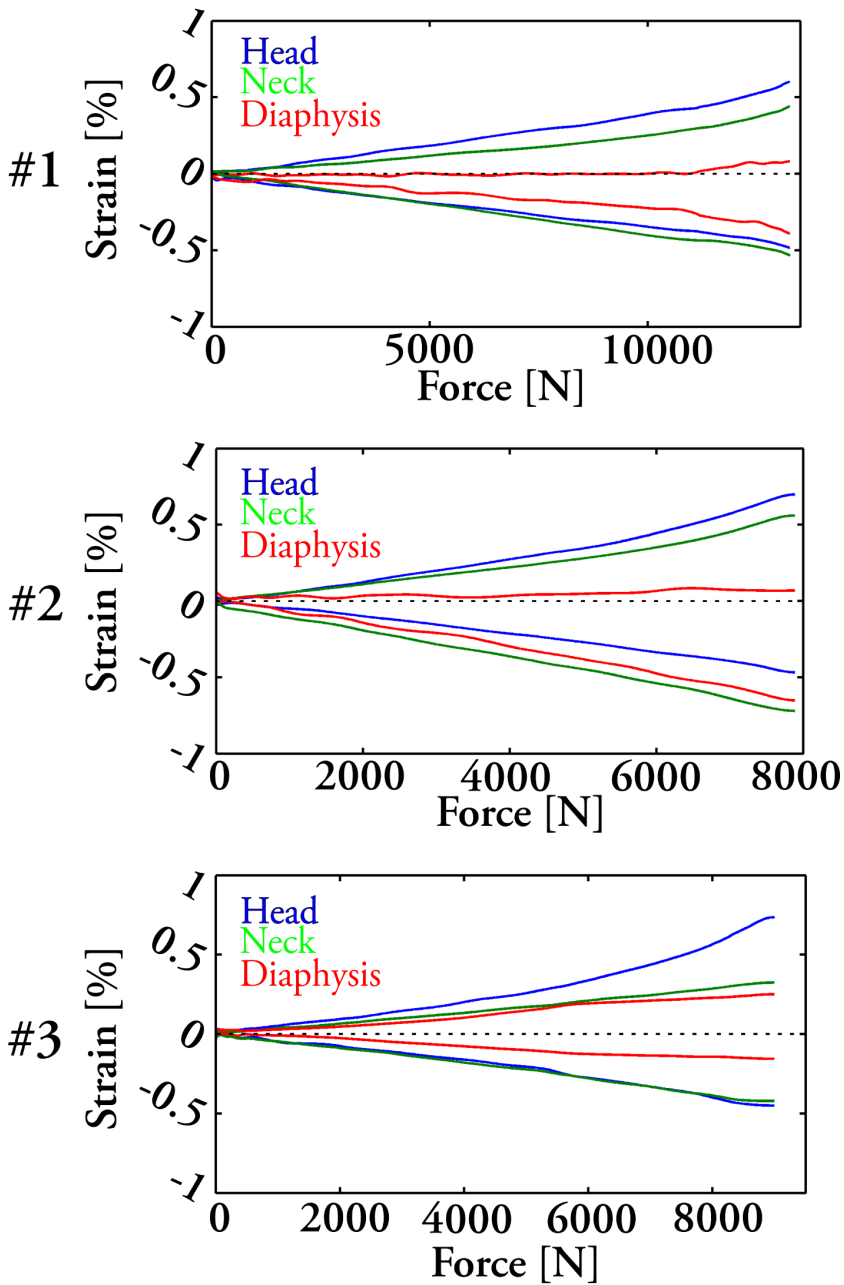


Figure 5.2: Major (positive sector) and minor (negative sector) principal strains as a function of the applied force in the virtual SGs for the three specimens tested. The SGs on the head are shown in blue, those on the femoral neck in green, and those at the diaphysis in red. Reprinted from paper III with permission from ASME.

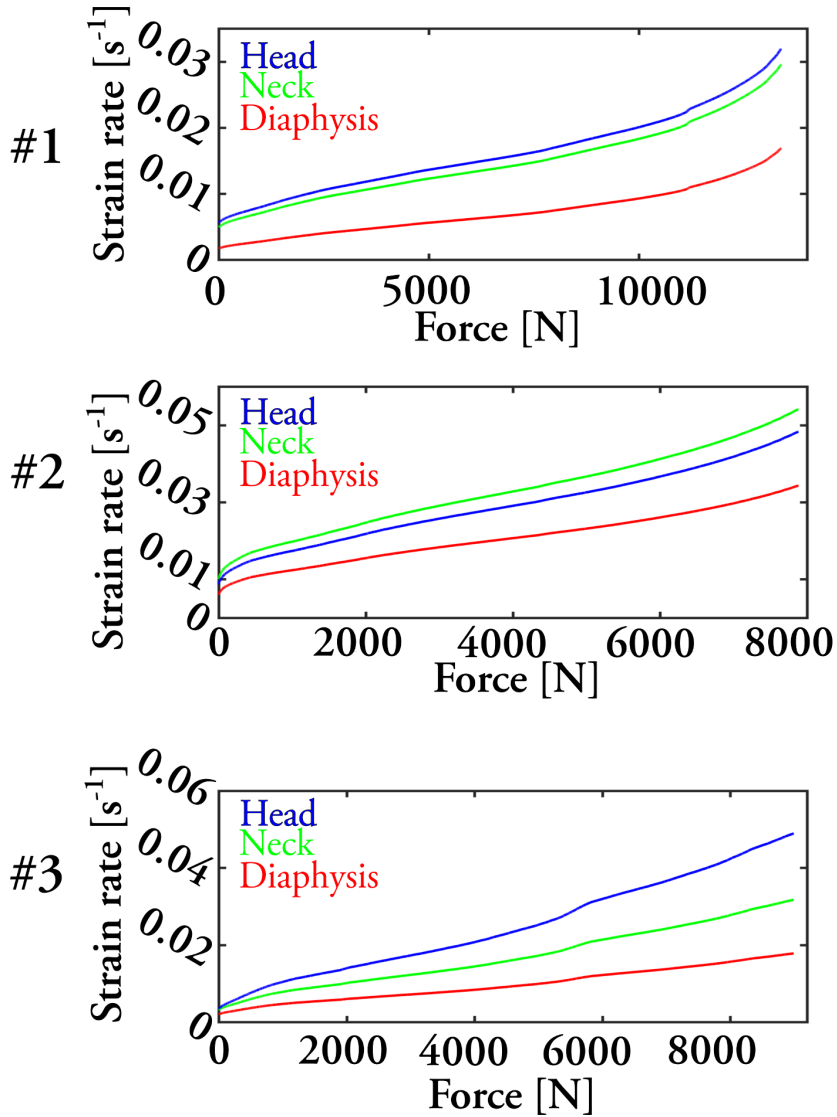


Figure 5.3: Von Mises strain rate versus the applied force for the three virtual strain gauges, for all the three specimens tested. The SGs on the head are shown in blue, those on the femoral neck in green, and those at the diaphysis in red.

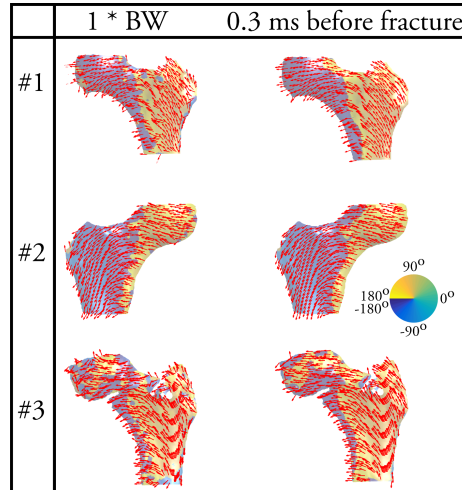


Figure 5.4: The major principal strain directions for the three specimens for a force corresponding to the subjects' body weight and at the frame right before the crack formation. Only a sub-sample of the DIC points was depicted with red arrows, while the direction of all the points is indicated by the background colour of the bone, according to the legend on the right of the figure.

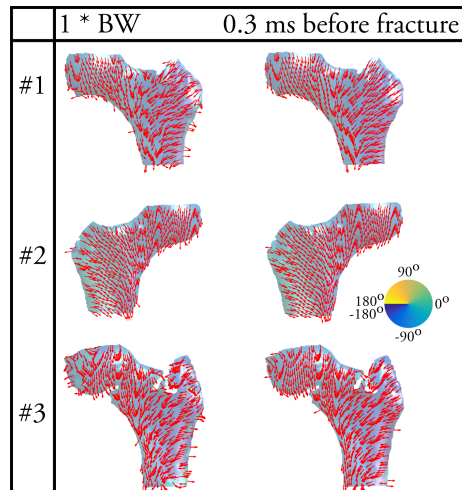


Figure 5.5: The minor principal strain directions for the three specimens for a force corresponding to the subjects' body weight and at the frame right before the crack formation. Only a sub-sample of the DIC points was depicted with red arrows, while the direction of all the points is indicated by the background colour of the bone, according to the legend on the right of the figure.

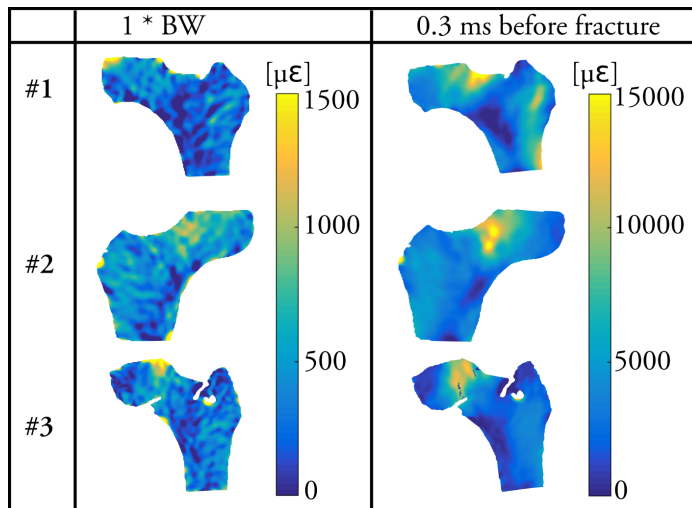


Figure 5.6: The major principal strain distribution for the three specimens for a force corresponding to the subjects' body weight and at the frame right before the crack formation.

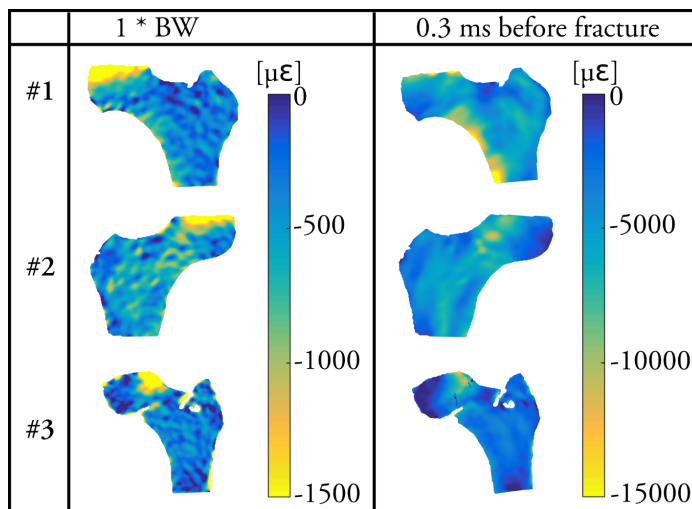


Figure 5.7: The minor principal strain distribution for the three specimens for a force corresponding to the subjects' body weight and at the frame right before the crack formation.

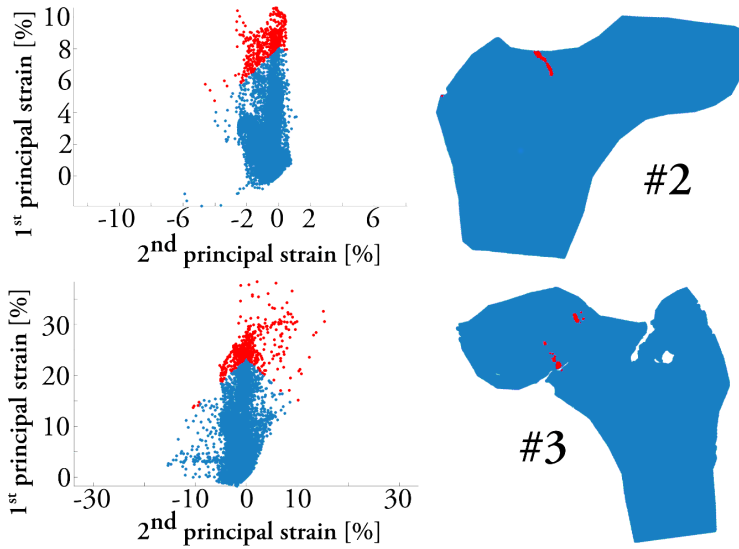


Figure 5.8: Fracture limit plot for specimens #2 (top) and #3 (bottom) at the last frame available before a crack could be detected. The 5% of the points whose sum of the absolute major and minor principal strain is highest are depicted in red (left), and their anatomical location is shown in the same colour (right). Reprinted from paper III with permission from ASME.

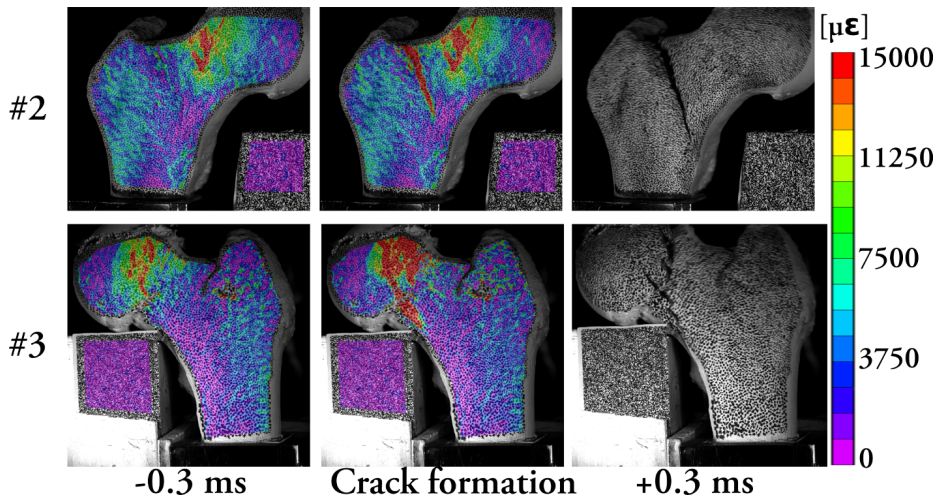


Figure 5.9: Evolution of the major principal strains for specimens #2 and #3 at the frames when the crack is formed. The strain data are superimposed to the raw images acquired by the master camera. Reprinted from paper III with permission from ASME.

5.2 CT-based FE models

5.2.1 Composite bones

The preliminary tests conducted on the six composite bones proved the validity of the proposed registration and validation approach. The approximately 50000 experimental data points per femur obtained from DIC were accurately registered over the FE models, and the linear regression analyses provided a high accuracy for the principal strains predicted along the whole anterior surface. One of the six composite bones was an outlier in the experimental data, showing a lower slope in the force-displacement curve [108]. When this composite bone was removed from the pooled set of validation data, the coefficient of determination, R^2 , was 0.91, with a slope of 0.94 and a NRMSE of 5% for an applied force of 3500 N. The analogous validation performed at the frame before fracture corroborated the validity of the validation method, even when the specimens were in a highly deformed state. The accuracy of the principal strain validation was slightly worse than in the

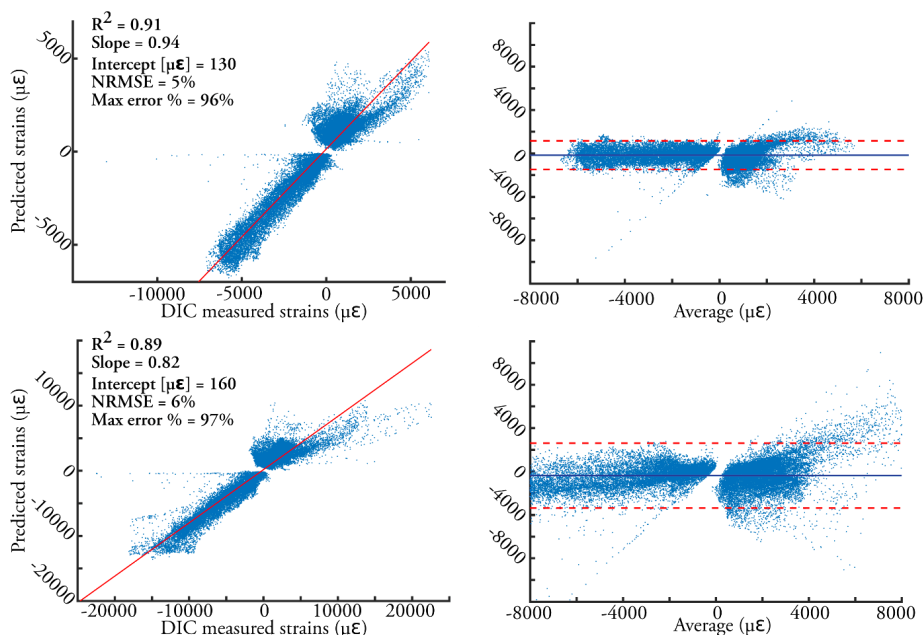


Figure 5.10: Scatter plot (left) and Bland-Altman plot (right) for the five composite bones (one outlier excluded after analysis of the force-displacement curves in [108]) when a force of 3500 N is applied (top), and at the last frame available before specimen fracture (bottom). The solid blue line in the Bland-Altman plot shows the mean value of the difference, with the red dotted lines showing the 95% confidence limits. Reprinted from paper II with permission from Elsevier.

3500 N case ($R^2 = 0.89$, slope = 0.82, NRMSE = 6%), likely due to the lack of any plasticity implemented in the FE models of the composite bones. Regression plots and Bland-Altman plots for both the 3500 N and close to fracture load cases are reported in figure 5.10.

5.2.2 Cadaver bones

The validation of the strain prediction accuracy was performed on approximately 1600 data points per specimen (4826 data points in total). The robust linear regression analysis at a load of 4 times the body weight gave a coefficient of determination of 0.94 (NRMSE = 9%), with a regression slope and intercept equal to 0.9 and 133 $\mu\epsilon$, respectively. The scatter plot of the FE predicted versus the DIC measured principal strains and the Bland-Altman plot are reported in figure 5.11 for the 3 specimens pooled. The results of the robust linear regression analyses are reported in table 5.2 for the three bones pooled as well as for each individual bone. The individual validation for each specimen (scatter and Bland-Altman plots reported in figure 5.12) always provided a coefficient of determination greater than 0.9, with slope close to unity, and intercept of a few hundred microstrains (see table 5.2).

The FE models were able to predict the femoral strength with a relative error of -1.5% for specimen #1, and +1.2% for specimen #2 (table 5.3). The standard error of the estimation (SEE) for the two specimens was 155 N. The femoral strength for specimen #3 could not be compared with the experimental measurements due to the slippage of the protective cap. This caused an unexpected change in the prescribed boundary conditions, which could not be accurately modelled in the FE models. The slippage of the cap is likely to have caused a stress concentration close to the rim of the cap itself, which ultimately produced an abnormal fracture mechanism. This speculation was corroborated by the peculiar fracture pattern exhibited by specimen #3 (figure 5.9), where the crack originated in the superolateral part of the femoral neck, close to the rim of the steel cap. The FE models predicted bone failure to

	3 bones pooled	Bone #1	Bone #2	Bone #3
R²	0.94	0.92	0.94	0.95
Slope	0.96	0.92	0.97	1.01
Intercept [$\mu\epsilon$]	133	144	174	79
NRMSE	9%	10%	11%	11%
Max error %	65%	46%	59%	83%

Table 5.2: Strain prediction accuracy at four times the body weight for the CT-based FE models, for the three bones pooled, and the three individual bones taken separately.

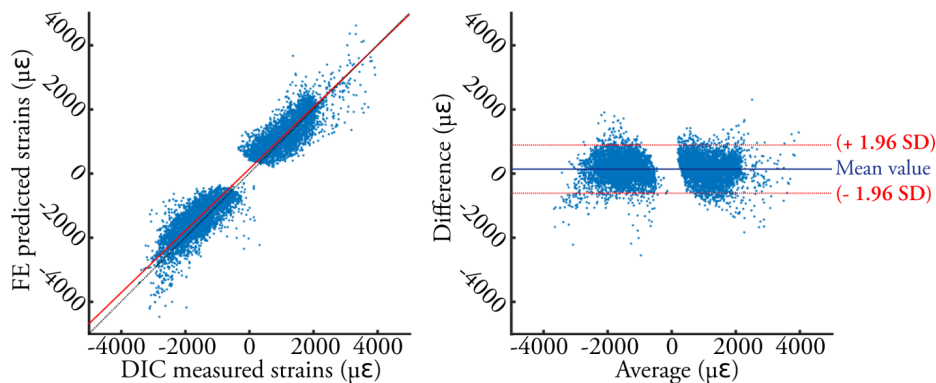


Figure 5.11: Scatter plot of the FE predicted principal strains versus the DIC measured strains (left), and Bland-Altman plot (right) for the 3 specimens pooled. The solid blue line in the Bland-Altman plot shows the mean value of the difference, with the red dotted lines showing the 95% confidence limits. Reprinted from paper IV with permission from Elsevier.

	Specimen #1	Specimen #2
Experimental strength [N]	13383	7856
Predicted strength [N]	13184	7947
Difference [%]	-1.5%	+1.2%

Table 5.3: Comparison of the predicted versus experimentally measured bone strength for specimens #1 and #2.

initiate under compression on the medial aspect of the femoral neck for all the specimens. The fracture onset predicted by the FE models appeared to be located very close (less than 1 cm away) to the fracture rim obtained during the ex vivo mechanical tests (figure 5.13).

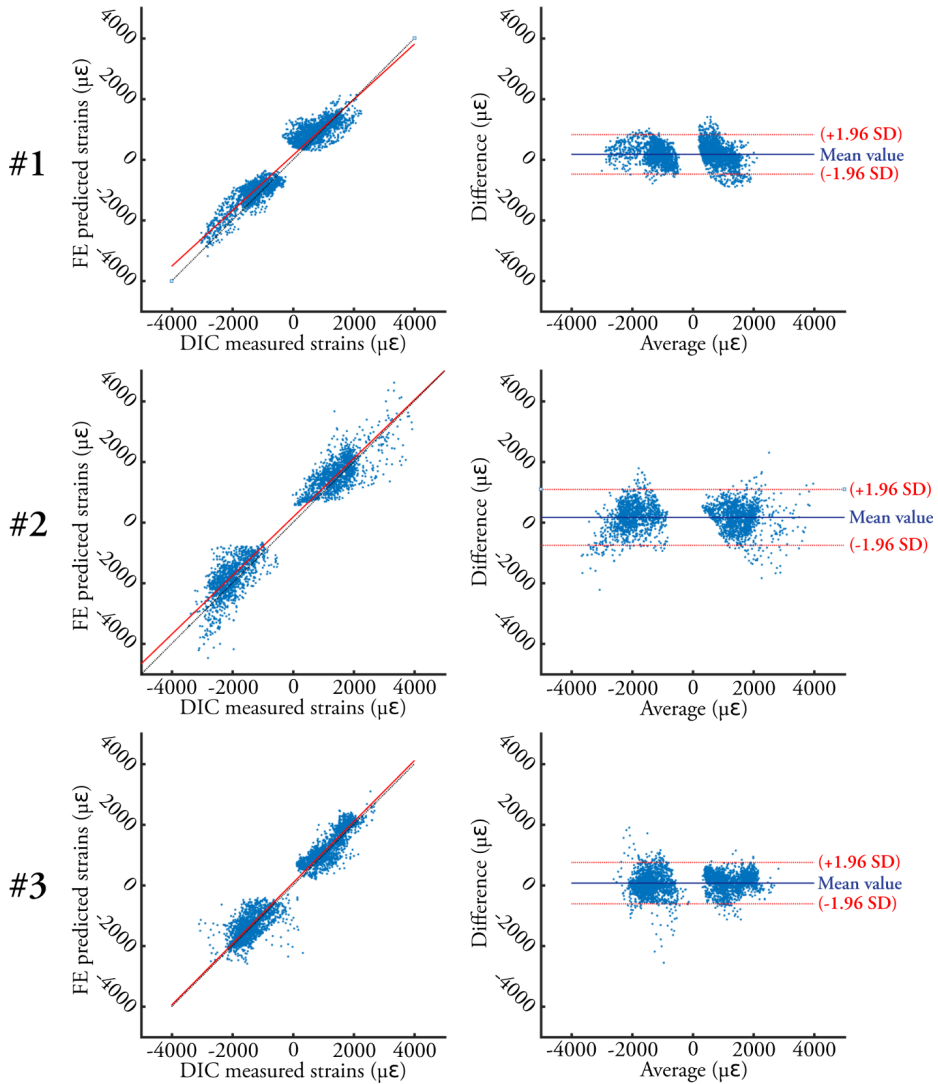


Figure 5.12: Scatter plots of the FE predicted principal strains versus the DIC measured strains (left column), and Bland-Altman plots (right column) for each of the three specimens tested. The solid blue line in the Bland-Altman plot shows the mean value of the difference, with the red dotted lines showing the 95% confidence limits. Reprinted from paper IV with permission from Elsevier.

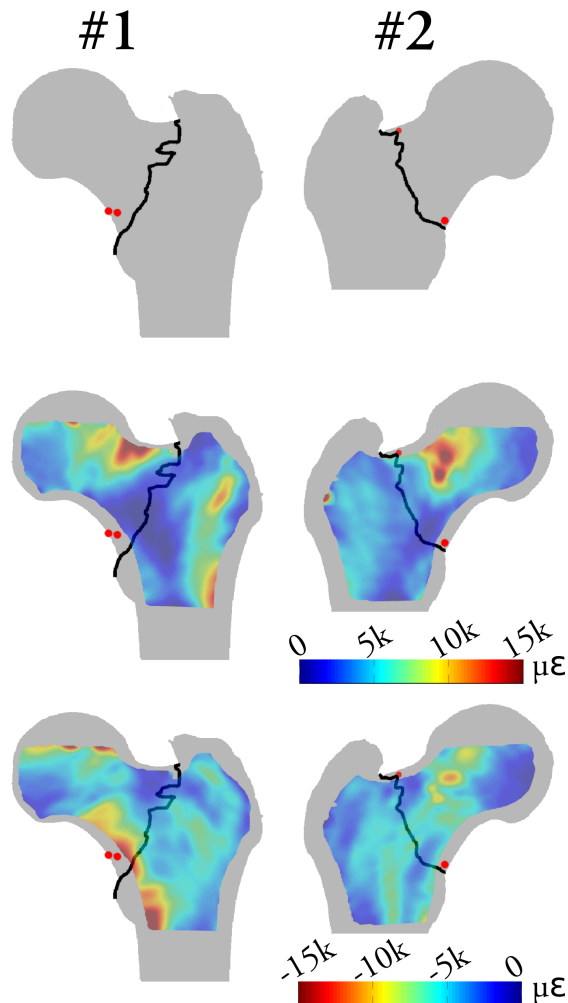


Figure 5.13: Graphical comparison of the experimentally obtained fracture rim (black line) and the FE predicted fracture onset (red dots). The major (central row) and minor (bottom row) principal strains detected with DIC at the frame before fracture are superimposed. For specimen #1, whose DIC recordings at fracture were not available due to a technical problem (see section 5.1.2), the strains for the last available frame are shown (for which the applied load was greater than 99% of the fracture load, estimated by comparing the DIC data with the internal recordings of the loading device during the experiments). Reprinted from paper IV with permission from Elsevier.

5.3 Combining SSAM and FE modelling

The validation of the strain prediction accuracy for the SSAM-based models was performed at a load corresponding to four times the subject's body weight. The results of the robust linear correlation analyses are presented in figure 5.14. The coefficient of determination was in all cases greater than 0.83, with a maximum of 0.92 for the *SSAM-based shape and BMD* model using the CT projection as the reference image. The NRMSE was around 10%, with a maximum of 16% for the

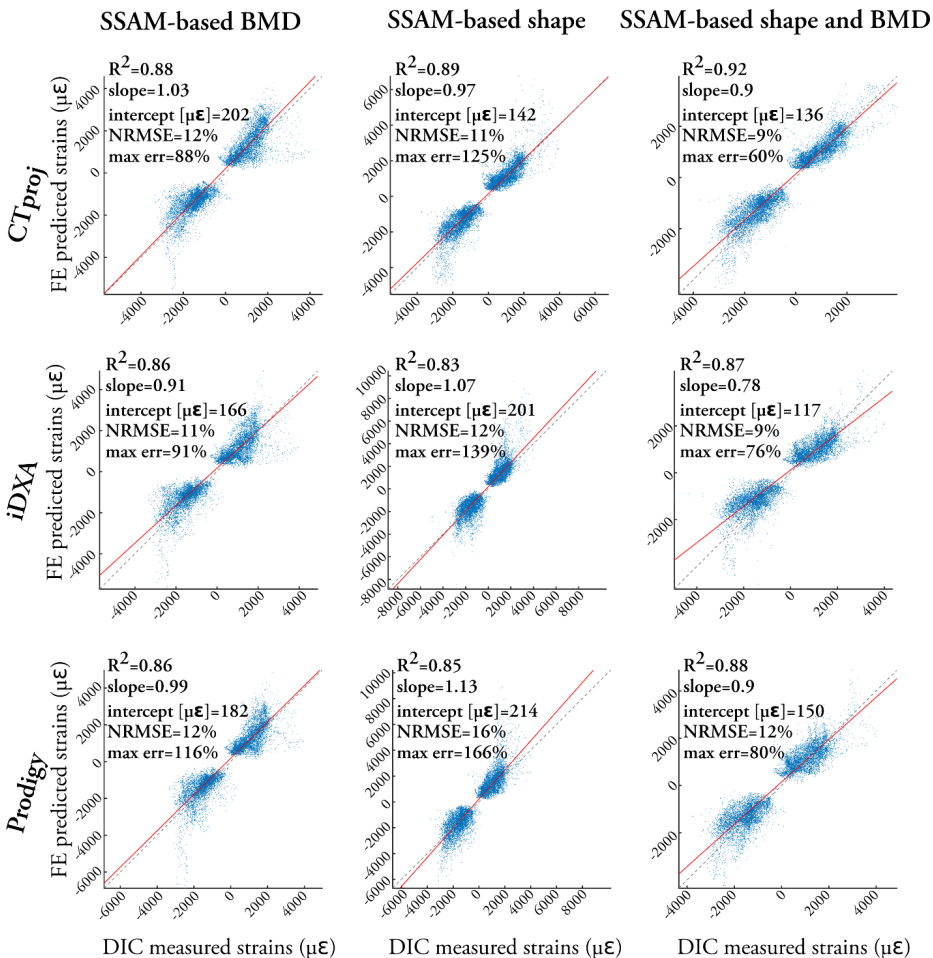


Figure 5.14: Scatter plot of the FE predicted principal strains versus the DIC measured strains for the three types of SSAM-based models built, and the three different types of 2D reference images used for the reconstruction. The results of the three proximal femurs are pooled together in each scatter plot.

	Bone #1			Bone #2			Bone #3		
	CTproj	iDXA	Prodigy	CTproj	iDXA	Prodigy	CTproj	iDXA	Prodigy
R²	0.90	0.90	0.90	0.84	0.83	0.83	0.92	0.89	0.89
Slope	1.00	0.91	0.92	1.03	0.99	1.08	1.03	0.85	0.97
Intercept [$\mu\epsilon$]	225	199	200	257	263	283	142	84	107
NRMSE	13%	11%	11%	19%	18%	20%	12%	12%	12%
Max error %	64%	69%	70%	89%	89%	113%	63%	58%	80%

Table 5.4: Strain prediction accuracy at four times the body weight for the *SSAM-based BMD* models of the three individual bones, for the three different types of 2D reference image.

	Bone #1			Bone #2			Bone #3		
	CTproj	iDXA	Prodigy	CTproj	iDXA	Prodigy	CTproj	iDXA	Prodigy
R²	0.89	0.82	0.82	0.89	0.88	0.88	0.91	0.79	0.83
Slope	0.88	1.00	1.04	0.98	1.03	1.11	1.07	1.22	1.23
Intercept [$\mu\epsilon$]	201	309	332	102	167	158	61	127	141
NRMSE	12%	18%	19%	13%	15%	18%	10%	13%	15%
Max error %	73%	188%	87%	125%	136%	108%	82%	134%	176%

Table 5.5: Strain prediction accuracy at four times the body weight for the *SSAM-based shape* models of the three individual bones, for the three different types of 2D reference image.

SSAM-based shape model using Prodigy as the reference image. The slope of the robust linear regression was always within $\pm 10\%$ from unity for all cases except two (*SAM-based shape* from Prodigy, and *SAM-based shape and BMD* from iDXA). The results of the robust linear regression analyses conducted for each individual bone are presented in table 5.4, 5.5, 5.6 for the *SSAM-based BMD*, *SSAM-based shape*, and *SSAM-based shape and BMD* cases, respectively. These results can be compared with the accuracy for the corresponding CT-based FE models reported in table 5.2.

The femoral strength predicted by the *SSAM-based* models was validated only for samples #1 and #2, due to the technical issues with sample #3, which were

	Bone #1			Bone #2			Bone #3		
	CTproj	iDXA	Prodigy	CTproj	iDXA	Prodigy	CTproj	iDXA	Prodigy
R²	0.88	0.84	0.86	0.94	0.89	0.9	0.92	0.87	0.88
Slope	0.81	0.76	0.88	0.90	0.74	0.86	0.98	0.86	0.99
Intercept [$\mu\epsilon$]	197	217	252	109	141	181	68	3	17
NRMSE	11%	14%	15%	10%	11%	13%	9%	8%	12%
Max error %	34%	37%	43%	51%	70%	61%	74%	72%	91%

Table 5.6: Strain prediction accuracy at four times the body weight for the *SSAM-based shape and BMD* models of the three individual bones, for the three different types of 2D reference image.

	Bone #1			Bone #2			SEE [N]
	CTproj	iDXA	Prodigy	CTproj	iDXA	Prodigy	
SSAM-based BMD	9858 (-26%)	11309 (-15%)	11007 (-18%)	7115 (-9%)	7789 (-1%)	5046 (-35%)	2267
SSAM-based shape	12776 (-4%)	9301 (-30%)	11983 (-18%)	7885 (+0.4%)	8525 (+8%)	7445 (-5%)	1975
SSAM-based shape and BMD	13106 (-2%)	13009 (-3%)	14820 (+11%)	9777 (+24%)	9203 (+17%)	8859 (+13%)	1215

Table 5.7: Femoral strength prediction accuracy for the SSAM-based FE models of specimens #1 and #2, for the three different types of 2D reference image.

explained in section 5.2. The SEE for the *SSAM-based shape and BMD* models was 1215 N, with an average absolute relative error of 12% ($\pm 8\%$, maximum absolute relative error 24%). All the results of the femoral strength validations for the SSAM-based models are reported in table 5.7. The femoral strength estimation was on average more accurate for the SSAM-based models built from CTproj (SEE = 1689 N) than for the models built from iDXA (SEE = 1974 N) and Prodigy (SEE = 1938 N). This is consistent with the greater information provided by the CTproj images compared to the DXA scans. Furthermore, the SSAM-based models built from CTproj showed a significantly higher accuracy in the shape reconstruction, as evidenced by the point-to-surface distance plots reported in figure 5.15. Most of the higher errors in the shape reconstruction were located in regions whose contribution to the mechanical behaviour of a femur is negligible, like the most superior tip of the greater trochanter. As the femoral neck is the most critical region when it comes to femoral fracture, the volumetric difference between the CT-based models and the SSAM-based models was calculated for the neck region only. The results are reported in table 5.8. When considering the results from figure 5.15 and table 5.8 together, it appears that the closer agreement between the femoral neck volume in

	Bone #1	Bone #2	Bone #3
CTproj	+9%	+10%	+9%
iDXA	+19%	+13%	-6%
Prodigy	+5%	+15%	+0.3%

Table 5.8: Difference in volume between the femoral neck region of the CT-based models and the SSAM-based models reconstructed from the three different reference images.

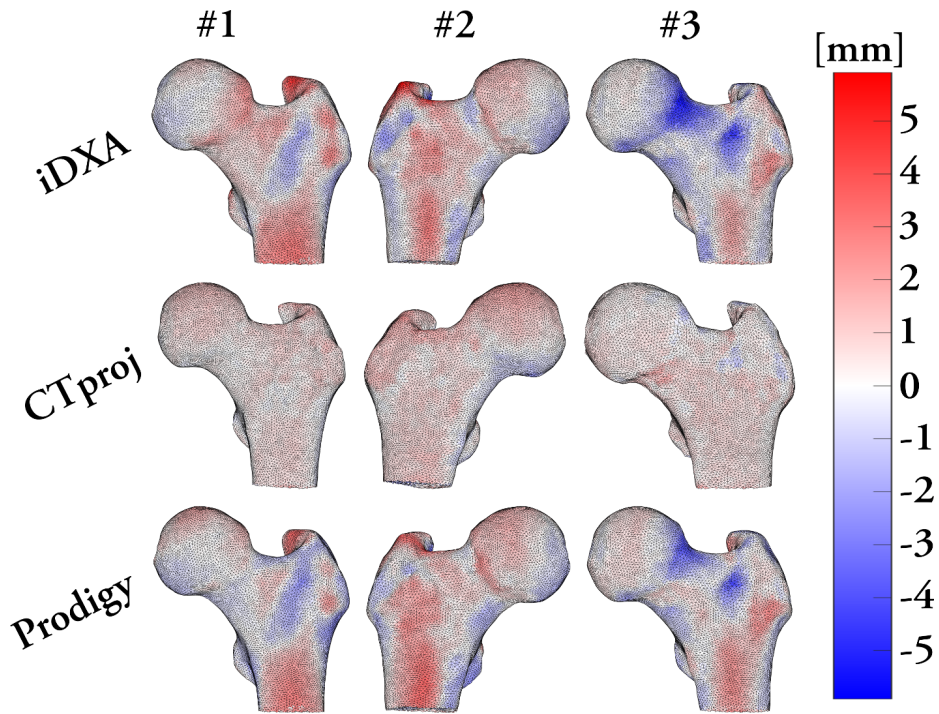


Figure 5.15: Point-to-surface distance between the different SSAM-based models, and the CT-based models described in section 4.3, for the three different femurs and the three types of reference image.

CT-based models and SSAM-based models from Prodigy is not accompanied by an equally high accuracy in the shape recovery, with errors as high as 3 mm in the neck region. Conversely, the good agreement (always within 10% difference) in the femoral neck volume for the SSAM-based models from CTproj was matched with a superior accuracy in the shape recovery. These results are consistent with the generally higher accuracy in both strain and femoral strength predictions exhibited by SSAM-based models obtained from CTproj images.

Chapter 6

Discussion

The aim of this thesis was to develop a subject-specific FE modelling procedure that can predict femoral strength using a single DXA scan. Towards this aim, the thesis work was divided into three main blocks, namely: collection of strain and femoral strength data from ex vivo mechanical tests, development of a subject-specific FE modelling procedure based on CT images, and development of a subject-specific FE modelling procedure based on the 2D to 3D reconstruction from a single DXA image using a SSAM.

The first block, the collection of experimental data from ex vivo mechanical tests, mainly aimed at creating a reliable and thorough set of data against which it was possible to validate the FE model predictions. The development of an accurate subject-specific FE modelling procedure from CT data aimed at defining a gold standard for the strain and femoral strength prediction. Finally, SSAM-based FE models were developed to predict strain and femoral strength from a single DXA image, thus allowing for a mechanistic prediction of bone strength that can provide added value to the current osteoporosis diagnostics.

The accuracy of the SSAM-based FE models was calculated by comparing the predicted strains with the measurements from the ex vivo tests. This accuracy was in turn compared to the gold standard, as represented by the CT-based FE models.

6.1 Collection of experimental measurements from ex vivo mechanical tests

The design of the ex vivo mechanical tests was based on the information collected during the feasibility studies performed on composite bones both experimentally (section 4.2, and [108]) and numerically (section 4.3.1). The aim was to collect accurate experimental data with high spatial resolution in a test whose boundary conditions were physiologically meaningful as well as accurately replicable in an FE simulation.

A loading configuration resembling single leg stance was chosen, based on its relative ease of implementation, and because it is one of the most commonly adopted configurations in literature [58, 70, 71, 123, 124]. 3D-surface DIC was used to measure the deformations, as it is a non-contact technique which allows to reconstruct the full-field strain distribution over the surface recorded by the cameras.

The noise from the strain measurements collected with DIC is an issue that has not been extensively addressed for bone mechanics applications [83, 108, 125]. Therefore, a control plate was placed on the side of the tested bone and used to assess the noise levels in the measurements. With the adopted settings for DIC calculation and data processing, strains in the order of 16-49 $\mu\epsilon$ were detected in the control plate for repeated acquisitions while the loading device was turned on, but not operating. The noise levels increased to 81-164 $\mu\epsilon$ when the loading device was operating, i.e., the control plate was moving vertically together with the constrained distal pot (figure 4.3). This is an interesting result, since most of the studies adopt repeated measurements of static objects to address noise in DIC strain data [108, 126], and the effect of rigid body movements have been evaluated using artificially displaced images [127, 128]. The obtained results evidence the need to assess the increased noise that results from the sample translation during the actual experiment and not only with simulated images.

The reduction of noise in the data obtained using DIC is generally pursued by implementing one or more filters. Typically, such filters act either on the input images (e.g., a low-pass filter can be used to reduce aliasing effects), or on the obtained strain field, with the latter approach reported to give the best results [126]. Filters acting on the strain field are typically implemented in the proprietary DIC software. However, this gives the user less control over the filtering parameters, and a limited range of choices in terms of filtering strategy. In the DIC software used for this thesis work (Vic 3D v7, Correlated Solutions, Inc.), the calculated strains are always smoothed using a local filter (i.e., the filter over the strains cannot be disabled). The implemented filter is a 90% centre-weighted Gaussian filter, for which the size of the smoothing window can be determined by the user (but with an allowed minimum size of 5 data points). In order to gain more control over the strain calculations, the displacement field was retrieved from the DIC software and different filtering and strain derivation techniques were tested using custom-written Matlab codes. The filtering strategy that gave the best results in removing the random noise between consecutive frames consisted in: (i) filtering the displacement vector for each tracked point using a low-pass filter with a cut-off frequency of 100 Hz, (ii) introducing the filtered displacement data back into the DIC software, and use them to derive the Green-Lagrangian strains, and (iii) filtering the obtained strains using a spatial decay filter of 5 pixel size. This procedure was used to calculate the strain field over the whole range of the loading curve, except for the last 50

frames before fracture. For the latter frames, no filtering over the displacements was applied. This choice was based on the need to get the highest possible resolution both in space and in time to extract relevant information about crack formation.

The measurements collected during the ex vivo mechanical tests showed that the chosen displacement rate of 15 mm/s resulted in a strain rate in the 3 virtual SGs of approximately 0.04 s^{-1} . This value is comparable to the strain rate values detected during in vivo studies, where strain rates in the order of $0.03\text{-}0.05 \text{ s}^{-1}$ were detected for high intensity activities such as jumping or running [129, 130]. Thus, it corroborates the physiological meaningfulness of the acquired measurements.

Using the implemented displacement rate, the tested bones showed a linear elastic behaviour up to fracture. The principal strains detected with DIC were highly correlated with the applied force: $R^2 > 0.96$ for the three virtual SGs, with 90% of the total data points showing an $R^2 > 0.9$ (average NRMSE = 12%). Most of the points showing a low linear correlation with the applied force were located either close to the constraints (where the strains are constantly very low, therefore not correlating with the increasing force), or in regions with high curvature (where the correlation quality can decrease during the test due to, e.g., shadowing effects). The linearity of principal strains versus applied force is in agreement with what was reported by Juszczak et al. [124] for femurs tested at a displacement rate of 3-30 mm/s. An additional evidence of the elastic behaviour of the femurs up to the macroscopic fracture was provided by the analysis of the residual strains after 0.08 seconds from the crack opening. In fact, all the strains were in the range of a few hundred microstrains (thus close to the noise levels in the control plate). Higher strains were instead detected in proximity of the fracture rim. Although DIC data in regions close to a discontinuity should be interpreted only qualitatively, this phenomenon suggests that plasticity is involved during bone damaging. This observation also corroborates the adoption of a bi-linear material model to predict femoral strength in FE models.

Bones #1 and #2 underwent a basicervical fracture, with a macroscopic crack opening on the superior aspect of the femoral neck and propagating approximately in parallel to the intertrochanteric line (figure 5.13). No clear fracture precursor could be identified by looking at the principal strain data in the frames before crack formation for neither bone #1 (at least until the camera recordings were available, the force at the time of the recording interruption was greater than 99% of the peak force) nor bone #2 (figure 5.9). Bone #3 underwent a sub-capital fracture, instead, with the crack propagating almost vertically. High strains could be located in the region where the fracture occurred a few milliseconds before the crack actually opened (figure 5.9). The fracture limit plots (figure 5.8) suggested that two cracks might have originated at different locations. A closer inspection of the video recordings showed that the protective steel cap glued on the femoral head actually slipped a few milliseconds before fracture. It is likely that the edge of the steel cap

hit the sub-capital region of the bone causing a damage that initiated the peculiar fracture pattern of bone #3. Surely, the slipping of the steel cap caused an unpredicted change in the prescribed boundary conditions. For this reason, the fracture load for bone #3 was not used to validate the FE model's accuracy in predicting femoral strength.

In summary, the developed ex vivo testing procedure was able to provide thousands of strain measurements collected at high frequency. These can be used to extensively validate the ability of the FE models to predict the strains for a single leg stance configuration, both in the elastic regime and up to the specimen fracture.

6.2 Development of a CT-based FE modelling procedure to predict femoral strength

The CT-based FE models were built with the aim of assessing the best accuracy achievable by FE models in terms of strain and femoral strength prediction. The validation was carried out for the 3 bones against the ex vivo measurements collected using DIC.

CT scans acquired ex vivo were used to build the CT-based FE models, using a procedure consisting of:

- Segmentation of the CT images
- Reverse engineering of the segmented geometry
- Meshing with tetrahedral elements
- Assignment of the inhomogeneous isotropic Young's moduli based on the calibrated HUs.

A similar procedure has been adopted in the past, giving a good accuracy in strain prediction both in configurations resembling single leg stance [131, 132] and a fall to the side [112]. However, in both cases the strain prediction accuracy was assessed against up to 16 measurements from SGs. In this study, the full-field strain distribution over the anterior surface of the femurs was obtained from DIC and used to more extensively validate the FE predictions. Finally, the femoral strength was predicted using a dedicated material model (figure 4.6) and compared to the peak force recorded during mechanical tests.

The principal strains were predicted with high accuracy ($R^2 = 0.94$, NRMSE = 9% for the three bones pooled, figure 5.11) for a load corresponding to four times the subject's BW. This accuracy was comparable to highest accuracy found in literature for FE models of human femurs in single leg stance ($R^2 = 0.95-0.97$, [132, 67]). The Bland-Altman plot for the three bones pooled (figure 5.11) did

not show any clear trend in the distribution, with the majority of the points lying within the 95% confidence limits.

Supported by the achieved accuracy in the prediction of principal strains, a strain-based material model to predict femoral strength was developed. The choice of using strains as limit values for the material model was motivated by the fact that limit strain values for both yield and fracture were proved to be independent of age, gender, and bone porosity [133, 134]. This feature is crucial when developing a criterion to predict femoral strength which should be equally accurate in a very heterogeneous group of patients. Besides, a simple strain limit criterion applied to linear FE models achieved a high coefficient of determination between predicted and experimental femoral strength (although the slope and intercept of the reported regression were statistically different from unity and zero, respectively) [135]. The developed material model included rate-dependence of the tangent modulus and different yield and failure strain limit values for tension and compression (figure 4.6). The material model was free from any internal parameter calibration, i.e., none of the acquired experimental measurements was used to adjust the implemented material properties. All the limit values were obtained from published studies that conducted mechanical testing on bone at the mesoscale level: yield strain values from Bayraktar et al., [117], ultimate strain and post-yield reduction of the tangent modulus were obtained from the data published by Reilly et al. [118], and the dependence of the tangent modulus from strain rate at the 0.06 power was assumed after Carter and Hayes [136]).

CT-based FE models implementing the developed material model predicted femoral strength with a relative error below 2% (SEE = 155 N). This accuracy is in line with the best results available in literature [137, 54]. These studies, however, used part of the available specimens as a training set to calibrate the limit values of the adopted failure criteria. The present CT-based FE models were instead based on published experimental data and did not use any internal parameter calibration.

The FE models predicted the crack to originate in the medial aspect of the femoral neck, which is mainly subjected to compressive strains in the prescribed loading configuration. Although the predicted fracture onset was very close to the experimental fracture rim (figure 5.13), the prediction of a fracture originating in the medial side is in contrast with the experimental high-speed video recordings, where the fracture seemed to originate in the lateral aspect of the femoral neck. It can be hypothesised that the fracture happened as a two-step process, in which an initial compressive failure in the medial side of the neck led to the opening of a macroscopic crack on the opposite side. An analogous failure mechanism was reported by de Bakker et al. [138] for femurs loaded in a configuration resembling a fall to the side. In that study, high-speed cameras were placed on the medial and lateral aspect of the neck, evidencing that bone failure occurred first on the lateral aspect of the neck (mainly subjected to compression in a fall to the side configura-

tion), and almost immediately resulted in a macroscopic crack on the medial side (subjected to tension in a fall to the side configuration). It is therefore possible that the same failure mechanism happened for femurs in single leg stance, with medial and lateral side inverted as a consequence of the different loading configuration.

In summary, the CT-based FE models were able to obtain a high accuracy for both strain and femoral strength, therefore representing a valuable benchmark to evaluate the performance of SSAM-based FE models on the same sample.

6.3 Development of SSAM-based FE models to predict femoral strength from DXA

The SSAM-based FE models were built with the aim of overcoming the limitation of the need of a CT scan to build a 3D subject-specific FE model that predicts femoral strength in individuals. Therefore, the FE modelling strategy described in section 3.2 was combined with the 3D reconstruction of shape and appearance that can be obtained by projecting a SSAM instance over a single DXA image [121].

Three different SSAM-based FE models were built: one implementing only the reconstructed bone shape (*SSAM-based shape* model), another implementing the reconstructed BMD only (*SSAM-based BMD* model), and the third implementing both shape and BMD as reconstructed from the DXA image (*SSAM-based shape and BMD* model). The idea was to quantify the individual effects of the shape (*SSAM-based shape* models) and BMD (*SSAM-based BMD* models) reconstruction errors on the accuracy of FE models obtained from the reconstruction of both shape and BMD from a DXA image (*SSAM-based shape and BMD* models).

The *SSAM-based shape and BMD* models predicted the principal strains with high accuracy against experimental data obtained with DIC (coefficient of determination 0.87, NRMSE below 12% for the three bones pooled together, figure 5.14). This accuracy is only slightly lower than that achieved by the CT-based FE models for the same specimens and the same load case (coefficient of determination 0.94, NRMSE of 9%, figure 5.11 and table 5.2).

When used to predict bone strength, *SSAM-based shape and BMD* models had a SEE of 1215 N for specimens #1 and #2 combined and the three different 2D reference images (average absolute error $12 \pm 8\%$, table 5.7). The CT-based models predicted bone strength with a SEE of 155 N and an average absolute error of 1%. The reduced accuracy for *SSAM-based shape and BMD* models can be ascribed to localised higher errors in the reconstruction of BMD combined with the adoption of a strain based fracture criterion, which does heavily depend on a correct estimation of the tangent modulus. Besides, two trends can be observed in the bone strength predictions. The first is that the models built using CTproj as the 2D reference image were more accurate (SEE = 1689 N) than the models built using iDXA (SEE

= 1974 N) or Prodigy (SEE = 1938 N). This trend is consistent with the higher signal-to-noise ratio of CTproj data than iDXA and Prodigy. The superior spatial resolution of iDXA (pixel size 0.25 x 0.3 mm) with respect to Prodigy (pixel size 1.05 x 0.6 mm), conversely, did not result in a superior prediction accuracy (table 5.2). The second trend is the higher SEE for *SSAM-based BMD* models with respect to *SSAM-based shape* models. This suggests that the reconstruction error for BMD is more influential than the reconstruction error for shape to the final bone strength prediction. However, further investigations are required to draw more definite conclusions on this aspect.

Previous studies have proposed to use 3D models reconstructed from a 2D reference image to improve the accuracy of fracture risk prediction [139, 97]. However, most of these studies used the reconstructed 3D models to measure 3D anatomical and densitometric parameters starting from a single 2D image. The collected parameters were then used as features to classify fractured subjects against non-fractured ones, and ultimately to complement the current epidemiological-based diagnostic tool [140, 141, 142].

Only a few studies used 3D models reconstructed from a 2D reference image to predict femoral strength using a mechanistic approach. Bryan et al. [102] estimated fracture risk using a mechanistic approach on 1000 femoral anatomies that were generated using a statistical model. The results of the FE analyses were finally used to identify geometrical or densitometric features that could help to classify the samples at high risk from those at low or moderate risk. However, this approach used material properties from CT scans, and no experimental validation could be provided, since the statistical tool was used to generate realistic shapes, not to reconstruct a specific anatomy based on its 2D reference image. Thevenot et al. [143] proposed a method to build 3D FE models from a radiographic image. The 3D shape was reconstructed using a shape template and a set of measurements that could be taken onto the radiographic image. The material properties were estimated based on the CT-based values of the bones in the training set and a homogeneity index derived from the target radiographic image. Using this approach, the femoral strength of 21 cadaver human femurs was predicted for a configuration resembling a fall to the side, reaching a remarkable accuracy (coefficient of determination of 0.63, SEE = 543 N). The results of the *SSAM-based shape and BMD* models proposed in this thesis are comparable to those obtained by Thevenot et al. in their study. The SEE of 1215 N achieved by the *SSAM-based shape and BMD* models was obtained for specimens whose average fracture load was 10620 N (table 5.3), tested in a configuration resembling single leg stance. The specimens tested by Thevenot et al. fractured at an average load of 3188 N (value extrapolated from the digitalisation of the data presented in figure 4 of [143]). The higher SEE of the *SSAM-based shape and BMD* models is therefore consistent with the specimens breaking at much higher load. When comparing the absolute error of the predic-

tion, the *SSAM-based shape and BMD* models had a maximum error of 24% (table 5.7), against a maximum error of 54% in Thevenot et al. (value extrapolated from the digitalisation of the data presented in figure 4 of [143]).

The results obtained by the *SSAM-based shape and BMD* models support the potential of SSAM-based FE models to provide a mechanistic contribution to fracture risk prediction in individuals, while maintaining DXA as the method to image the patients. Besides, the implementation of models using only the SSAM-based shape and only the SSAM-based BMD could help the future development of SSAM-based reconstructions by providing a quantitative estimation of the effect of the different reconstruction errors on the final model accuracy.

6.4 Limitations

The main limitations of this thesis are: (i) the limited sample size, (ii) the single loading configuration examined, (iii) the uncertainty in the localisation of the fracture onset, and (iv) the limited use of some of the data acquired with DIC.

Sample size

A limitation of this thesis work resides in the small size of the examined sample. With the exception of the feasibility studies conducted on six composite bones, all the other studies were conducted on three cadaver proximal femurs. Although many of the investigations conducted in this thesis resulted in highly accurate predictions, the low sample size limited the amount of statistical analyses that could be performed on them, and consequently the strength of the conclusions that could be drawn from the obtained results.

Strictly linked to the low sample size is the limitation concerning the reduced representativeness of the sample. All three cadaver proximal femurs came from male donors, of which one was of young age (table 4.1). This limitation was partly compensated by the adoption of strain limit values for the prediction of bone yield and failure together with an element-specific material mapping strategy from the calibrated CT-data. In fact, the differences in bone mechanical behaviour for different age groups are correlated to differences in tissue ash density [144, 134].

Originally, five cadaver proximal femurs were retrieved for the *ex vivo* mechanical tests. However, two of these specimens experienced an early failure of the distal epoxy embedding during the test, which resulted in a severe change in the prescribed boundary conditions. As a result, the experimental measurements on these two bones were of no practical use, and the two specimens were therefore discarded from all the studies. Following this, the distal epoxy embedding was reinforced for the remaining specimens whenever possible (section 4.2.1). While having experimental data from all the five specimens would have certainly been beneficial for

all the studies, that would not have changed the power of the performed statistical analyses. The collection of high numbers of cadaver bones is a common issue amongst many research groups. Validating SSAM-based FE models against experimental measurements could represent a partial solution to this issue, since it would allow the generation of thousands of synthetic bone instances whose shape and mechanical behaviour are representative of the real bone mechanical behaviour.

Loading configuration

A limitation which directly follows from the low sample size is that only one loading configuration has been tested. Numerical investigations showed that testing multiple loading conditions in both single-leg-stance and sideways fall configurations can improve the association between predicted bone strength and classification of fractured cases versus non-fractured [145]. However, this would require the FE models to be validated for different loading configurations. CT-based FE models built with a procedure analogous to the one proposed in section 4.3 accurately predict strains for a variety of sideways fall configurations in the elastic regime [112], and a simple strain limit criterion predicts the failure characteristics of proximal femurs in both stance and sideways fall [135]. While these two aspects give reasonable evidence that the CT-based models described in section 4.3 can accurately predict femoral strains and strength for a sideways fall configuration, the ability of SSAM-based models to produce adequately accurate predictions in a sideways fall configuration is yet to be proven.

One possibility to validate samples in multiple loading configurations is to perform non-destructive mechanical tests on the available specimens for different loading conditions [124, 109]. The absence of damage caused to the specimens during repeated non-destructive tests is typically assessed by monitoring the strains in real-time using SGs in order not to overcome a certain threshold value. While there is no consensus about the reliability of a non-destructiveness assessment based on a few SG measurements, DIC does not allow to measure strains in real-time, as DIC is calculated after the images have been acquired. Therefore, non-destructive tests were not performed on the available proximal femur anatomies, and this thesis focused on a single-leg-stance loading configuration only.

Localisation of fracture onset

Despite the extensive amount of data points collected, a definite answer on where, when and how fracture originates could not be provided. Two main reasons can be found for this, namely: (i) the frame rate adopted (3000 fps) not being high enough to capture the crack opening and propagation, and (ii) the DIC recordings covering only one anatomical aspect of the bones under test. The inability to localise the fracture onset during the experiments in turn affects the validation of the FE

results, as the prediction of the fracture onset due to a compressive failure of the medial side of the neck (section 6.2) could be neither confirmed, nor rejected.

Ideally, two pairs of faster cameras (9000 fps cameras have already been used in, e.g., [146]) should record the mechanical test, covering at least the two anatomical aspects that are more prone to fracture (for a typical configuration resembling single-leg-stance, the lateral and medial side of the femoral neck).

Usage of all the collected experimental measurements

One of the challenges that comes with collecting measurements using full-field techniques such as DIC is how to effectively process and present the huge amount of data collected. For the experiments described in section 4.2, and with the DIC parameters adopted, 10000 data points per specimen were collected at 3000 fps during a time span of about 0.5 s. Some new ways to show these data were proposed (e.g., virtual strain gages, fracture limit plots, maps of the principal strain directions, etc.), but most of the data acquired were still not presented. Although a single answer on how to use and effectively represent this huge amount of data cannot be provided, as that would depend on the study aims, the increasing adoption of full-field techniques in experimental bone mechanics is calling for new solutions to this issue.

The creation of reliable online platforms for sharing scientific datasets could allow different researchers to work on the same experimental data, thus making a broader use of the available measurements. Nevertheless, the question of how to make proper use of the huge amount of data coming from full-field measurements remains an open question within the biomechanics community.

6.5 Future perspectives

Short-term perspectives: continuation of this thesis work

The ideal continuation of this thesis work should address the limitations mentioned in the section above, with the aim to provide an improved ability to predict bone strength using SSAM-based reconstructed FE models.

Performing additional experimental mechanical tests in a configuration resembling a fall to the side would allow overcoming the limitations about the limited sample size and the single loading configuration inspected. An improved experimental design that allows simultaneous and synchronised camera recordings of two opposite aspects of the femoral neck would also help to elucidate the mechanisms leading to bone failure. The feasibility of an experimental design that provides reliable strain measurements in a sideways fall configuration is currently under evaluation using composite bones. New cadaver femoral samples are also collected to increase the size of the current sample.

Future works should also aim at providing a more seamless integration of the SSAM-based reconstruction with the FE analysis. With the perspective of a future clinical application in mind, the current procedure requiring a trained engineer to build the models and long computation times (about one day to predict femoral strength using a desktop PC) needs to be further refined. The computation time could be reduced by using hardware acceleration (e.g., GPU computing) and by refactoring the code. The level of automation could also be enhanced by developing the new codes for the SSAM-based reconstruction and the FE analysis as a unified module, and not as two separate components.

Last, the features of the SSAM-based reconstruction could also be enhanced. While recalling that the technical development of the SSAM-based reconstruction was not part of this thesis, a few enhancements could be proposed hereby. A first improvement would consist in re-building the SSAM using a higher number of samples in the training set. In the current implementation, 34 unpaired human proximal femur anatomies were used to build the SSAM (13 right and 21 left; 30 men and 4 women; age 50 ± 16 years, [121]). It is reasonable to hypothesise that re-building the SSAM on a higher number of samples would lead to an increased ability to reconstruct the 3D shape and density distribution. The possibility to build two separate SSAMs for men and women should also be explored. A potential improvement to the SSAM-based FE models could be represented by the addition of cortical thickness and anisotropy information.

The ability to reconstruct a longer portion of the femur than the one imaged in DXA could also be implemented. Such feature would allow the prescription of more physiological boundary conditions to the models, by means of allowing a better identification of the anatomical axes for the specific subject. An improved SSAM algorithm which can more accurately detect cortical density and cortical thickness as well as reconstruct missing parts of the femur is under active development, with the first preliminary results of this updated algorithm expected by the end of 2016.

The accuracy of the 3D reconstruction of shape and BMD distribution from DXA images has only been evaluated for DXA images acquired *ex vivo* [121]. Future works should therefore aim at evaluating the effect of factors typically occurring during *in vivo* DXA scans (e.g., in the presence of soft tissue) on the accuracy of the reconstructed shape and BMD distribution, and ultimately on the strength prediction accuracy of the *SSAM-based shape and BMD* models.

Long-term perspectives: the road to the clinics

The ultimate goal of applying FE models for osteoporosis diagnostics is to improve the accuracy of the fracture risk prediction. In this context, achieving an accurate and reliable estimation of femoral strength should be seen as a first step along the road that leads to clinical application. An ideal road to the clinical application could be defined by referring to the technology readiness levels (TRLs) table proposed by

TRL	Description of research and development activities
TRL1: Technical watch	Monitoring of fundamental technological innovations and discovery of fundamental biological mechanisms
TRL2: Basic technology research	Application of fundamental technological innovation to the quantification, prediction, and modification of fundamental biological mechanisms
TRL3: Research to prove feasibility	Demonstration of hypothesis testing and initial proof of concept in a limited number of in silico and in vitro models
TRL4: Technology demonstration	Demonstration of proof of concept and safety in a defined laboratory or animal model
TRL5: Technology demonstration	Preclinical studies, including good laboratory practices, animal safety and toxicity, are sufficient to support industrial application
TRL6: Technology demonstration	Phase 1 clinical trials: support to proceed to Phase 2 clinical trials; safety, usability, impact, accuracy on small cohort
TRL7: System /sub-system development	Phase 2 clinical trials: accuracy and efficacy on medium cohort; scalability and impact
TRL8: System test, launch, and operations	Phase 3 clinical trials: efficacy on large cohort; cost-benefit analysis, primary research for Health Technology Assessment
TRL9: Postmarketing studies and surveillance	Postmarketing studies and surveillance; registers, failure analysis, postmortem examinations

Table 6.1: Technology readiness levels (TRLs). Reprinted from Viceconti and Hunter [147].

Viceconti and Hunter [147] and reported in table 6.1. The technological improvements described in the previous section should bring the SSAM-based prediction of bone strength to the TRL5 stage. The road to the last stage of technology readiness level, TRL9, should therefore comprise the three phases of clinical trial:

- *Phase 1 clinical trial (TRL6)*: the greatest challenge to get to phase 1 clinical trial is to obtain clinical credibility [147]. Phase 1 clinical trials are normally conducted on 20-100 participants, and consist in a clinical research comparing the accuracy of the new technology with that of the current standard of care. Some studies tried to use FE-based strength prediction to classify fractured cases from control group on small clinical cohorts [148, 145, 93, 149, 150]. The results of these studies show a significant,

albeit non dramatic, increase of the predictive accuracy when using mechanistic predictions of bone strength. It has also been shown that the analysis of multiple loading conditions can significantly improve the association between FE-based strength prediction and fracture [145]. Therefore, the design of computer based experiments is expected to play a key role in further improving the predictive ability of FE-based fracture risk predictions. Moving from simpler comparative and parametric analyses to design of experiments and probabilistic approaches [151, 152]) can help to assess and reduce the sensitivity of the prediction, thus increasing the predictive ability.

- *Phase 2 clinical trial (TRL7)*: the second phase of clinical trial is performed on a higher number of participants compared to phase 1 (typically, a few hundred participants are involved). The aim of this phase is to verify the accuracy and efficacy on medium-sized cohorts, and to quantify the potential impact of the new technology on the clinical practice. A phase 2 clinical study could therefore adopt a mechanistic FE-based technology to assess the fracture risk at baseline for a medium-sized cohort. After the follow-up time, the predictive ability could be compared to the ability achieved by the current standard of care. The author of this thesis is not aware of any FE-based fracture risk prediction technology that was allowed to enter phase 2 of clinical trial at the time of writing.
- *Phase 3 clinical trial (TRL8)*: the biggest challenge for a technology that had reached TRL7 is typically the need to re-engineer the whole process in order to handle large volumes of data at low costs [147]. The process re-engineering will therefore aim at facilitating the integration and automation of the subject-specific modelling procedure [153]. Many subject-specific models require a considerable amount of pre- and post-processing by a trained operator with an engineering background. While this can be an acceptable solution during the development phase, it cannot be economically sustainable when the technology is adopted on a large-scale. In this perspective, the development of a mature SSAM-based FE modelling technology should contribute to greatly reduce the amount of work required by a trained engineer. Another aspect to be considered is the turnaround time [147]. The time of a fracture risk prediction obtained with FRAX is in the order of 15-45 minutes. The *SSAM-based shape and BMD* models would instead take 1-2 days to provide a prediction of bone strength with the current technology. A re-engineering of the technology should therefore aim at making the whole process faster, both by using hardware and software optimizations, and by considering a reduction of the computational complexity (e.g., implementing a simpler criterion to predict bone strength will worsen the strength prediction accuracy, but may not worsen the accuracy

of fracture risk prediction [154, 135])

Two large prospective cohorts will be used to perform clinical trials on the developed SSAM-based prediction of bone strength. The first cohort (Osteoporosis risk factor and Prevention, OSTPRE [155, 156]) includes about 2500 female subjects (age range 72-81 years, subjects being imaged with DXA at five year intervals starting from 1989), while the second prospective cohort (ManOS) includes about 2000 men (Osteoporotic fractures in men, MrOS, Swedish database only; age > 65 years when enrolled in the study, imaging with DXA at 4.5 year intervals [157, 158, 159]). The availability of these two large prospective cohorts for men and women will allow to undergo both phase 1 and phase 2 of the clinical trial, and to assess the ability to predict femoral strength and fracture risk on both men and women for two populations with high incidence of osteoporosis. As for phase 3 of the clinical trial, a solution to make the diagnosis faster and more cost-effective could be to introduce a multi-step screening, in which the subjects' BMD can be assessed with ultrasound first [160], and only those subjects who are judged to be at risk are further evaluated with SSAM-based FE analysis [161].

The road to the clinics has shown in the past to require a consistent amount of time and funding. At the same time, this road is expected to get easier to be covered in the future [147]. The overall design of a technology allowing to maintain the current standard of care in terms of imaging while providing a mechanistic prediction of fracture risk has a considerable potential of being successfully experimented in clinical trials, and to finally achieve a cost-effectiveness that could justify its adoption in clinical practice.

Chapter 7

Summary and Conclusions

In this thesis, a method to accurately predict femoral strength using FE models based both on CT images and on SSAM-reconstructed data from DXA was developed. The full-field surface strain distribution for cadaver femurs tested in a single leg stance configuration was collected and used to validate the FE predictions.

The main findings obtained during this thesis work are:

- *Digital image correlation can be used to extensively validate FE predictions:* DIC provides strain data for thousands of points covering one anatomical aspect of the femur, against the 10-15 measurements per bone obtained using strain gauges. The DIC data can be spatially registered over the FE models, and the validation can be performed by evaluating which experimental data points are within the sphere of interest of each finite element.
- *A low-pass filtering of the displacement field obtained with DIC can effectively reduce the noise levels in the strain data:* the noise in the DIC measurements is an aspect that needs to be considered, especially when elastic strains are examined. A control plate allowed to continuously assess the noise levels, and showed that filtering DIC displacements over time before deriving strains can be an effective solution to keep the noise levels low without losing spatial accuracy.
- *Femurs behave linearly elastic up to fracture when loaded at physiologically relevant strain rates:* the major and minor principal strains over the whole anterior surface of the femurs tested were highly linear with respect to the applied force. Evidences of plastic deformation were only found in proximity of the fracture rim, suggesting that local plastic damage is involved in the fracture mechanics.
- *CT-based FE models can accurately predict principal strains in human proximal femurs:* an accuracy comparable to the state of the art studies was obtained

when thousands of strain measurements from DIC were used to validate FE models. The high accuracy obtained over a broad portion of the femoral surface supports the adoption of a strain-based criterion to predict femoral strength.

- *A rate-dependent material model with strain limit values for yield and failure can predict femoral strength within 2% error:* the material model and fracture criterion implemented in the FE simulations used concepts and limit values taken from published experimental studies conducted at the mesoscale level, with no internal parameter calibration. Bone stiffening when loaded at higher strain rates was considered, as well as the tangent modulus reduction following yield. Both yield and failure were based on separate strain limit values for tensile and compressive behaviour.
- *FE models built from reconstructed DXA images can predict principal strains and femoral strength with only a slightly reduced accuracy:* the FE modelling procedure was combined with the 3D reconstruction of shape and BMD distribution obtained using a SSAM and a femur template. This allowed to build a 3D FE model starting from a single DXA image. The accuracy of both principal strains and femoral strength was only slightly lower than that obtained by CT-based FE models, showing the high potential of the SSAM-based FE models as a fracture predictor in clinical applications.

References

1. S. R. Cummings and L. J. Melton, "Epidemiology and outcomes of osteoporotic fractures.," *Lancet*, vol. 359, pp. 1761–7, may 2002.
2. L. J. Melton, E. A. Chrischilles, C. Cooper, A. W. Lane, and B. L. Riggs, "Perspective. How many women have osteoporosis?," *Journal of bone and mineral research : the official journal of the American Society for Bone and Mineral Research*, vol. 7, pp. 1005–10, sep 1992.
3. European Commission, "Population structure and ageing." http://ec.europa.eu/eurostat/statistics-explained/index.php/Population_structure_and_ageing, 2015 (accessed 2015-07-13).
4. World Health Organization, "Assessment of fracture risk and its application to screening for postmenopausal osteoporosis. Report of a WHO Study Group.," *World Health Organization technical report series*, vol. 843, pp. 1–129, jan 1994.
5. J. A. Kanis, F. Borgstrom, C. De Laet, H. Johansson, O. Johnell, B. Jonsson, A. Oden, N. Zethraeus, B. Pflieger, and N. Khaltayev, "Assessment of fracture risk.," *Osteoporosis international : a journal established as result of cooperation between the European Foundation for Osteoporosis and the National Osteoporosis Foundation of the USA*, vol. 16, pp. 581–9, jun 2005.
6. B. R. McCreadie and S. A. Goldstein, "Biomechanics of fracture: is bone mineral density sufficient to assess risk?," *J Bone Miner Res*, vol. 15, no. 12, pp. 2305–2308, 2000.
7. T. L. N. Järvinen, P. Kannus, and H. Sievänen, "Bone quality: Emperor's new clothes.," *Journal of musculoskeletal & neuronal interactions*, vol. 8, no. 1, pp. 2–9, 2007.

8. P. Geusens, T. van Geel, and J. van den Bergh, "Can Hip Fracture Prediction in Women be Estimated beyond Bone Mineral Density Measurement Alone?," *Therapeutic advances in musculoskeletal disease*, vol. 2, pp. 63–77, apr 2010.
9. C. Jiang, M. L. Giger, S. M. Kwak, M. R. Chinander, J. M. Martell, and M. J. Favus, "Normalized BMD as a predictor of bone strength," *Academic Radiology*, vol. 7, pp. 33–39, jan 2000.
10. J. C. Lotz, E. J. Cheal, and W. C. Hayes, "Fracture prediction for the proximal femur using finite element models: Part I—Linear analysis," *J Biomech Eng*, vol. 113, no. 4, pp. 353–360, 1991.
11. J. C. Lotz, E. J. Cheal, and W. C. Hayes, "Fracture prediction for the proximal femurs using finite element models: part II - Nonlinear analysis," *J Biomech Eng*, vol. 113, pp. 361–366, 1991.
12. D. D. Cody, G. J. Gross, F. J. Hou, H. J. Spencer, S. A. Goldstein, and D. P. Fyhrie, "Femoral strength is better predicted by finite element models than QCT and DXA," *J Biomech*, vol. 32, no. 10, pp. 1013–1020, 1999.
13. S. van den Munckhof and A. A. Zadpoor, "How accurately can we predict the fracture load of the proximal femur using finite element models?," *Clinical biomechanics (Bristol, Avon)*, vol. 449, jan 2014.
14. F. Taddei, I. Palmadori, W. R. Taylor, M. O. Heller, B. Bordini, A. Toni, and E. Schileo, "Safety factor of the proximal femur during gait: A population-based finite element study," *Journal of Biomechanics*, sep 2014.
15. W. B. Edwards and K. L. Troy, "Number crunching: how and when will numerical models be used in the clinical setting?," *Current osteoporosis reports*, vol. 9, pp. 1–3, mar 2011.
16. R. Marcus, D. Feldman, D. W. Dempster, M. Luckey, and J. A. Cauley, *Osteoporosis*. Academic Press, 4th ed., 2013.
17. B. Dawson-Hughes, "Commentary: A revised clinician's guide to the prevention and treatment of osteoporosis," *Journal of Clinical Endocrinology and Metabolism*, vol. 93, pp. 2463–2465, jul 2008.
18. S. Fujiwara, T. Nakamura, H. Orimo, T. Hosoi, I. Gorai, A. Oden, H. Johansson, and J. A. Kanis, "Development and application of a Japanese model of the WHO fracture risk assessment tool (FRAX™)," *Osteoporosis International*, vol. 19, pp. 429–435, apr 2008.

19. E. Siris, S. Baim, and A. Nattiv, "Primary care use of FRAX: absolute fracture risk assessment in postmenopausal women and older men.," *Postgraduate Medicine*, vol. 122, pp. 82–90 9p, jan 2010.
20. M. R. McClung, "To FRAX or not to FRAX," *Journal of Bone and Mineral Research*, vol. 27, pp. 1240–1242, jun 2012.
21. World Health Organization, "WHO Scientific Group on the Assessment of Osteoporosis at Primary Health Care Level," *World Health Organization*, 2004.
22. P. Augat, D. Weyand, S. Panzer, and T. Klier, "Osteoporosis prevalence and fracture characteristics in elderly female patients with fractures," *Archives of Orthopaedic and Trauma Surgery*, vol. 130, pp. 1405–1410, nov 2010.
23. J. A. Kanis, O. Johnell, C. De Laet, B. Jonsson, A. Oden, and A. K. Ogelsby, "International variations in hip fracture probabilities: implications for risk assessment.," *Journal of bone and mineral research : the official journal of the American Society for Bone and Mineral Research*, vol. 17, pp. 1237–1244, jul 2002.
24. O. Johnell and J. A. Kanis, "An estimate of the worldwide prevalence and disability associated with osteoporotic fractures.," *Osteoporosis international : a journal established as result of cooperation between the European Foundation for Osteoporosis and the National Osteoporosis Foundation of the USA*, vol. 17, pp. 1726–33, dec 2006.
25. I. Fogelman, "Oestrogen, the prevention of bone loss and osteoporosis.," *British journal of rheumatology*, vol. 30, pp. 276–281, aug 1991.
26. B. L. Riggs, "The mechanisms of estrogen regulation of bone resorption," *Journal of Clinical Investigation*, vol. 106, pp. 1203–1204, nov 2000.
27. J. Magaziner, E. M. Simonsick, T. M. Kashner, J. R. Hebel, and J. E. Kenzora, "Predictors of functional recovery one year following hospital discharge for hip fracture: a prospective study.," *Journal of gerontology*, vol. 45, pp. M101–7, may 1990.
28. G. S. Keene, M. J. Parker, and G. A. Pryor, "Mortality and morbidity after hip fractures," *BMJ*, vol. 307, pp. 1248–50, nov 1993.
29. C. L. Leibson, A. N. A. Tosteson, S. E. Gabriel, J. E. Ransom, and L. J. Melton, "Mortality, disability, and nursing home use for persons with and without hip fracture: A population-based study," *Journal of the American Geriatrics Society*, vol. 50, pp. 1644–1650, oct 2002.

30. B. L. Riggs and L. J. Melton, "The worldwide problem of osteoporosis: Insights afforded by epidemiology," *Bone*, vol. 17, pp. 505S–511S, nov 1995.
31. P. Kannus, J. Parkkari, S. Niemi, and M. Palvanen, "Epidemiology of osteoporotic ankle fractures in elderly persons in Finland," *Annals of Internal Medicine*, vol. 125, pp. 975–978, dec 1996.
32. J. D. Adachi, G. Loannidis, C. Berger, L. Joseph, A. Papaioannou, L. Pickard, E. A. Papadimitropoulos, W. Hopman, S. Poliquin, J. C. Prior, D. A. Hanley, W. P. Olszynski, T. Anastassiades, J. P. Brown, T. Murray, S. A. Jackson, A. Tenenhouse, and C. M. O. S. C. R. Group, "The influence of osteoporotic fractures on health-related quality of life in community-dwelling men and women across Canada," *Osteoporos Int*, vol. 12, no. 11, pp. 903–908, 2001.
33. C. Cooper, E. J. Atkinson, S. J. Jacobsen, W. M. O'Fallon, and L. J. Melton, "Population-based study of survival after osteoporotic fractures," *American journal of epidemiology*, vol. 137, pp. 1001–1005, may 1993.
34. J. Magaziner, E. Lydick, W. Hawkes, K. M. Fox, S. I. Zimmerman, R. S. Epstein, and J. R. Hebel, "Excess mortality attributable to hip fracture in white women aged 70 years and older," *American journal of public health*, vol. 87, pp. 1630–6, oct 1997.
35. H. G. Ahlborg, B. E. Rosengren, T. L. N. Järvinen, C. Rogmark, J.-A. Nilsson, I. Sernbo, and M. K. Karlsson, "Prevalence of osteoporosis and incidence of hip fracture in women—secular trends over 30 years," *BMC musculoskeletal disorders*, vol. 11, p. 48, 2010.
36. B. Gullberg, O. Johnell, and J. A. Kanis, "World-wide projections for hip fracture," *Osteoporosis international : a journal established as result of cooperation between the European Foundation for Osteoporosis and the National Osteoporosis Foundation of the USA*, vol. 7, pp. 407–13, jan 1997.
37. E. S. Siris, Y.-T. Chen, T. A. Abbott, E. Barrett-Connor, P. D. Miller, L. E. Wehren, and M. L. Berger, "Bone Mineral Density Thresholds for Pharmacological Intervention to Prevent Fractures," *Archives of internal medicine*, vol. 164, pp. 1108–1112, may 2004.
38. E. Sornay-Rendu, F. Munoz, P. Garnero, F. Duboeuf, and P. D. Delmas, "Identification of Osteopenic Women at High Risk of Fracture: The OFELY Study," *J Bone Miner Res*, vol. 20, pp. 1813–1819, oct 2005.
39. J. A. Pasco, E. Seeman, M. J. Henry, E. N. Merriman, G. C. Nicholson, and M. A. Kotowicz, "The population burden of fractures originates in women

- with osteopenia, not osteoporosis,” *Osteoporosis International*, vol. 17, no. 9, pp. 1404–1409, 2006.
40. P. Szulc, F. Munoz, F. Duboeuf, F. Marchand, and P. D. Delmas, “Bone mineral density predicts osteoporotic fractures in elderly men: the MINOS study,” *Osteoporosis international : a journal established as result of cooperation between the European Foundation for Osteoporosis and the National Osteoporosis Foundation of the USA*, vol. 16, pp. 1184–92, oct 2005.
41. K. B. Freedman, F. S. Kaplan, W. B. Bilker, B. L. Strom, and R. A. Lowe, “Treatment of osteoporosis: are physicians missing an opportunity?,” *The Journal of bone and joint surgery. American volume*, vol. 82-A, no. 8, pp. 1063–70, 2000.
42. E. S. Siris, P. D. Miller, E. Barrett-Connor, K. G. Faulkner, L. E. Wehren, T. A. Abbott, M. L. Berger, A. C. Santora, and L. M. Sherwood, “Identification and fracture outcomes of undiagnosed low bone mineral density in postmenopausal women: results from the National Osteoporosis Risk Assessment,” *JAMA : the journal of the American Medical Association*, vol. 286, pp. 2815–2822, dec 2001.
43. J. A. Kanis, A. Oden, O. Johnell, H. Johansson, C. De Laet, J. Brown, P. Burckhardt, C. Cooper, C. Christiansen, S. Cummings, J. A. Eisman, S. Fujiwara, C. Gluer, D. Goltzman, D. Hans, M. A. Krieg, A. La Croix, E. McCloskey, D. Mellstrom, L. J. Melton, H. Pols, J. Reeve, K. Sanders, A. M. Schott, A. Silman, D. Torgerson, T. Van Staa, N. B. Watts, and N. Yoshimura, “The use of clinical risk factors enhances the performance of BMD in the prediction of hip and osteoporotic fractures in men and women,” *Osteoporosis International*, vol. 18, pp. 1033–1046, aug 2007.
44. A. Unnanuntana, B. P. Gladnick, E. Donnelly, and J. M. Lane, “The assessment of fracture risk,” *The Journal of bone and joint surgery. American volume*, vol. 92, pp. 743–53, mar 2010.
45. T. L. N. Järvinen, J. Jokihäärä, P. Guy, M. Mba, P. Alonso-coello, G. S. Collins, K. Michaëlsson, and H. S. Scd, “Commentary Conflicts at the heart of the FRAX tool,” *CMAJ*, vol. 186, no. 3, pp. 165–167, 2014.
46. K. H. Rubin, T. Friis-Holmberg, A. P. Hermann, B. Abrahamsen, and K. Brixen, “Risk assessment tools to identify women with increased risk of osteoporotic fracture: Complexity or simplicity? A systematic review,” *Journal of Bone and Mineral Research*, vol. 28, pp. 1701–1717, aug 2013.

47. S. K. Sandhu, N. D. Nguyen, J. R. Center, N. A. Pocock, J. A. Eisman, and T. V. Nguyen, "Prognosis of fracture: Evaluation of predictive accuracy of the FRAX™ algorithm and Garvan nomogram," *Osteoporosis International*, vol. 21, no. 5, pp. 863–871, 2010.
48. S. L. Silverman and A. D. Calderon, "The utility and limitations of FRAX: A US perspective.," *Current osteoporosis reports*, vol. 8, pp. 192–7, dec 2010.
49. N. B. Watts, B. Ettinger, and M. S. LeBoff, "FRAX facts.," *Journal of bone and mineral research : the official journal of the American Society for Bone and Mineral Research*, vol. 24, pp. 975–9, jun 2009.
50. M. Viceconti, P. Hunter, and D. Hose, "Big data, big knowledge: big data for personalised healthcare," *IEEE Journal of Biomedical and Health Informatics*, vol. 2194, no. c, pp. 1–1, 2015.
51. N. S. Ottosen and H. Petersson, *Introduction to the finite element method*. Prentice Hall, 1992.
52. R. Huiskes and E. Chao, "A survey of finite element analysis in orthopedic biomechanics: The first decade," *Journal of Biomechanics*, vol. 16, pp. 385–409, jan 1983.
53. R. A. Brand, "Biographical sketch: julius wolff, 1836-1902.," *Clinical orthopaedics and related research*, vol. 468, pp. 1047–1049, apr 2010.
54. J. Koivumäki, J. Thevenot, P. Pulkkinen, V. Kuhn, T. Link, F. Eckstein, and T. Jämsä, "Ct-based finite element models can be used to estimate experimentally measured failure loads in the proximal femur," *Bone*, vol. 50, no. 4, pp. 824–829, 2012.
55. E. Schileo, F. Taddei, L. Cristofolini, and M. Viceconti, "Subject-specific finite element models implementing a maximum principal strain criterion are able to estimate failure risk and fracture location on human femurs tested in vitro," *Journal of Biomechanics*, vol. 41, no. 2, pp. 356–367, 2008.
56. Z. Yosibash and E. Priel, "p-FEMs for hyperelastic anisotropic nearly incompressible materials under finite deformations with applications to arteries simulation," *International Journal for Numerical Methods in Engineering*, vol. i, no. April, pp. 1152–1174, 2011.
57. E. Dall'Ara, B. Luisier, R. Schmidt, F. Kainberger, P. Zysset, and D. Pahr, "A nonlinear QCT-based finite element model validation study for the human femur tested in two configurations in vitro.," *Bone*, vol. 52, pp. 27–38, jan 2013.

58. J. H. Keyak, S. A. Rossi, K. A. Jones, and H. B. Skinner, "Prediction of femoral fracture load using automated finite element modeling," *Journal of biomechanics*, vol. 31, no. 2, pp. 125–133, 1998.
59. M. Viceconti and F. Taddei, "Automatic generation of finite element meshes from computed tomography data.," *Critical reviews in biomedical engineering*, vol. 31, pp. 27–72, jan 2003.
60. B. Helgason, E. Perilli, E. Schileo, F. Taddei, S. Brynjólfsson, and M. Viceconti, "Mathematical relationships between bone density and mechanical properties: a literature review.," *Clinical biomechanics (Bristol, Avon)*, vol. 23, pp. 135–46, feb 2008.
61. A. Natali and E. Meroi, "A review of the biomechanical properties of bone as a material," *Journal of Biomedical Engineering*, vol. 11, pp. 266–276, jul 1989.
62. M. Viceconti, S. Olsen, L.-P. Nolte, and K. Burton, "Extracting clinically relevant data from finite element simulations.," *Clinical Biomechanics (Bristol, Avon)*, vol. 20, pp. 451–4, jun 2005.
63. A. E. Anderson, B. J. Ellis, and J. A. Weiss, "Verification, validation and sensitivity studies in computational biomechanics.," *Computer methods in biomechanics and biomedical engineering*, vol. 10, pp. 171–84, jun 2007.
64. H. Henninger, S. Reese, A. Anderson, and J. Weiss, "Validation of computational models in biomechanics," *Proceedings of the Institution of Mechanical Engineers. Part H, Journal of engineering in medicine*, vol. 224, no. 7, pp. 801–812, 2010.
65. J. H. Keyak, H. B. Skinner, and J. A. Fleming, "Effect of force direction on femoral fracture load for two types of loading conditions," *J Orthop Res*, vol. 19, no. 4, pp. 539–544, 2001.
66. M. Bessho, I. Ohnishi, T. Matsumoto, S. Ohashi, J. Matsuyama, K. Tobita, M. Kaneko, and K. Nakamura, "Prediction of proximal femur strength using a CT-based nonlinear finite element method: differences in predicted fracture load and site with changing load and boundary conditions.," *Bone*, vol. 45, pp. 226–31, aug 2009.
67. Z. Yosibash, N. Trabelsi, and C. Milgrom, "Reliable simulations of the human proximal femur by high-order finite element analysis validated by experimental observations.," *Journal of Biomechanics*, vol. 40, pp. 3688–99, jan 2007.
68. E. S. Gurdjian and H. R. Lissner, "Mechanism of Head Injury as Studies by the Cathode Ray Oscilloscope Preliminary Report," *Journal of Neurosurgery*, vol. 1, no. 6, pp. 393–399, 1944.

69. V. L. Roberts, "Strain-gage techniques in biomechanics," *Experimental Mechanics*, vol. 6, pp. 19A–22A, mar 1966.
70. Y. H. Kim, J. S. Kim, and S. H. Cho, "Strain distribution in the proximal human femur. An in vitro comparison in the intact femur and after insertion of reference and experimental femoral stems.," *The Journal of bone and joint surgery. British volume*, vol. 83, pp. 295–301, mar 2001.
71. A. Aamodt, J. Lund-Larsen, J. Eine, E. Andersen, P. Benum, and O. S. Husby, "Changes in proximal femoral strain after insertion of uncemented standard and customised femoral stems," *The Journal of Bone and Joint Surgery*, vol. 83, pp. 921–929, aug 2001.
72. L. Cristofolini, M. Juszczuk, F. Taddei, R. E. Field, N. Rushton, and M. Viceconti, "Stress shielding and stress concentration of contemporary epiphyseal hip prostheses.," *Proceedings of the Institution of Mechanical Engineers Part H Journal of engineering in medicine*, vol. 223, no. 1, pp. 27–44, 2009.
73. J. Y. Rho and G. M. Pharr, "Effects of drying on the mechanical properties of bovine femur measured by nanoindentation.," *Journal of materials science. Materials in medicine*, vol. 10, pp. 485–8, aug 1999.
74. C. C. Perry, "Strain-gage reinforcement effects on orthotropic materials," *Experimental Techniques*, vol. 10, no. 2, pp. 20–24, 1986.
75. L. Cristofolini, M. Juszczuk, F. Taddei, and M. Viceconti, "Strain distribution in the proximal human femoral metaphysis.," *Proceedings of the Institution of Mechanical Engineers. Part H, Journal of engineering in medicine*, vol. 223, pp. 273–88, apr 2009.
76. M. M. Werneck, R. C. S. B. Allil, B. a. Ribeiro, and F. V. B. D. Nazaré, "A Guide to Fiber Bragg Grating Sensors," in *Current Trends in Short- and Long-period Fiber Gratings*, pp. 1–24, InTech, may 2013.
77. T. Fresvig, P. Ludvigsen, H. Steen, and O. Reikerås, "Fibre optic Bragg grating sensors: an alternative method to strain gauges for measuring deformation in bone.," *Medical engineering & physics*, vol. 30, pp. 104–8, jan 2008.
78. O. Reikeras, G. T. Aarnes, H. Steen, P. Ludvigsen, and G. Sagvolden, "Differences in external and internal cortical strain with prosthesis in the femur.," *The open orthopaedics journal*, vol. 5, pp. 379–84, jan 2011.
79. M. A. Sutton, J. J. Orteu, and H. Schreier, *Image Correlation for Shape, Motion and Deformation Measurements: Basic Concepts, Theory and Applications*. Springer, 2009.

-
80. G. Lionello and L. Cristofolini, "A practical approach to optimizing the preparation of speckle patterns for digital-image correlation," *Measurement Science and Technology*, vol. 25, p. 107001, oct 2014.
 81. M. Palanca, G. Tozzi, and L. Cristofolini, "The use of digital image correlation in the biomechanical area: a review," *International Biomechanics*, vol. 3, no. 1, pp. 1–21, 2016.
 82. J. Op Den Buijs and D. Dragomir-Daescu, "Validated finite element models of the proximal femur using two-dimensional projected geometry and bone density.," *Computer Methods and Programs in Biomedicine*, vol. 104, pp. 1–7, nov 2010.
 83. S. Gilchrist, P. Guy, and P. a. Crompton, "Development of an inertia-driven model of sideways fall for detailed study of femur fracture mechanics.," *Journal of biomechanical engineering*, vol. 135, p. 121001, dec 2013.
 84. H. F. Boehm, A. Horng, M. Notohamiprodjo, F. Eckstein, D. Burklein, A. Panteleon, J. Lutz, and M. Reiser, "Prediction of the fracture load of whole proximal femur specimens by topological analysis of the mineral distribution in DXA-scan images," *Bone*, vol. 43, no. 5, pp. 826–831, 2008.
 85. B. Helgason, S. Gilchrist, O. Ariza, J. D. Chak, G. Zheng, R. P. Widmer, S. J. Ferguson, P. Guy, and P. a. Crompton, "Development of a balanced experimental-computational approach to understanding the mechanics of proximal femur fractures.," *Medical engineering & physics*, vol. 36, pp. 793–799, mar 2014.
 86. B. K. Bay, T. S. Smith, D. P. Fyhrie, and M. Saad, "Digital volume correlation: Three-dimensional strain mapping using X-ray tomography," *Experimental Mechanics*, vol. 39, pp. 217–226, sep 1999.
 87. F. Gillard, R. Boardman, M. Mavrogordato, D. Hollis, I. Sinclair, F. Pierron, and M. Browne, "The application of digital volume correlation (DVC) to study the microstructural behaviour of trabecular bone during compression.," *Journal of the mechanical behavior of biomedical materials*, vol. 29, pp. 480–99, jan 2014.
 88. M. Palanca, G. Tozzi, L. Cristofolini, M. Viceconti, and E. Dall'Ara, "3D Local Measurements of Bone Strain and Displacement: Comparison of Three Digital Volume Correlation Approaches.," *Journal of biomechanical engineering*, mar 2015.

89. A. Hussein, P. Barbone, and E. Morgan, "Digital volume correlation for study of the mechanics of whole bones," *Procedia IUTAM*, vol. 4, pp. 116–125, 2012.
90. B. C. Roberts, E. Perilli, and K. J. Reynolds, "A Review on the Application of the Digital Volume Correlation Technique for the Measurement of Displacement and Strain Fields in Bone," *Journal of Biomechanics*, vol. 47, jan 2014.
91. L. Yang, N. Peel, J. A. Clowes, E. V. McCloskey, and R. Eastell, "Use of DXA-based structural engineering models of the proximal femur to discriminate hip fracture.," *Journal of bone and mineral research : the official journal of the American Society for Bone and Mineral Research*, vol. 24, pp. 33–42, jan 2009.
92. Y. Luo, Z. Ferdous, and W. D. Leslie, "Precision study of DXA-based patient-specific finite element modeling for assessing hip fracture risk.," *International journal for numerical methods in biomedical engineering*, vol. 29, pp. 615–29, may 2013.
93. L. Yang, L. Palermo, D. M. Black, and R. Eastell, "Prediction of incident hip fracture with the estimated femoral strength by finite element analysis of DXA Scans in the study of osteoporotic fractures.," *Journal of bone and mineral research : the official journal of the American Society for Bone and Mineral Research*, vol. 29, pp. 2594–600, dec 2014.
94. J. A. M. MacNeil, J. D. Adachi, D. Goltzman, R. G. Josse, C. S. Kovacs, J. C. Prior, W. Olszynski, K. S. Davison, and S. M. Kaiser, "Predicting fracture using 2D finite element modelling.," *Medical engineering & physics*, vol. 34, pp. 478–84, may 2012.
95. E. Dall'Ara, R. Eastell, M. Viceconti, D. Pahr, and L. Yang, "Experimental Validation of DXA-based Finite Element models for prediction of femoral strength," *Journal of the Mechanical Behavior of Biomedical Materials*, vol. 63, pp. 17–25, 2016.
96. N. Sarkalkan, H. Weinans, and A. A. Zadpoor, "Statistical shape and appearance models of bones," *Bone*, vol. 60, pp. 129–140, 2014.
97. I. Castro-Mateos, J. M. Pozo, T. F. Cootes, J. M. Wilkinson, R. Eastell, and A. F. Frangi, "Statistical shape and appearance models in osteoporosis," *Current Osteoporosis Reports*, vol. 12, pp. 163–173, jun 2014.
98. T. F. Cootes, C. J. Taylor, D. H. Cooper, and J. Graham, "Training Models of Shape from Sets of Examples," in *Training* (D. C. Hogg and R. D. Boyle, eds.), vol. 557, pp. 9–18, Springer-Verlag, 1992.

-
99. T. Cootes, C. Taylor, D. Cooper, and J. Graham, "Active Shape Models-Their Training and Application," *Computer Vision and Image Understanding*, vol. 61, pp. 38–59, jan 1995.
 100. T. Cootes and C. Taylor, "Statistical models of appearance for medical image analysis and computer vision," *Medical Imaging 2001*, pp. 236–248, 2001.
 101. T. Heimann and H.-P. Meinzer, "Statistical shape models for 3D medical image segmentation: a review.," *Medical image analysis*, vol. 13, pp. 543–63, aug 2009.
 102. R. Bryan, P. B. Nair, and M. Taylor, "Use of a statistical model of the whole femur in a large scale, multi-model study of femoral neck fracture risk.," *Journal of biomechanics*, vol. 42, pp. 2171–6, sep 2009.
 103. C. M. Langton, S. Pisharody, and J. H. Keyak, "Generation of a 3D proximal femur shape from a single projection 2D radiographic image.," *Osteoporosis international : a journal established as result of cooperation between the European Foundation for Osteoporosis and the National Osteoporosis Foundation of the USA*, vol. 20, pp. 455–61, mar 2009.
 104. S. P. Väänänen, J. S. Jurvelin, and H. Isaksson, "Estimation of 3D shape, internal density and mechanics of proximal femur by combining bone mineral density images with shape and density templates.," *Biomechanics and modeling in mechanobiology*, oct 2011.
 105. T. Whitmarsh, L. Humbert, M. De Craene, L. Del Rio Barquero, and A. Frangi, "Reconstructing the 3D Shape and Bone Mineral Density Distribution of the Proximal Femur from Dual-energy X-ray Absorptiometry.," *IEEE transactions on medical imaging*, jul 2011.
 106. S. Bonaretti, C. Seiler, C. Boichon, M. Reyes, and P. Buchler, "Image-based vs. mesh-based statistical appearance models of the human femur: Implications for finite element simulations," *Medical Engineering and Physics*, vol. 36, no. 12, pp. 1626–1635, 2014.
 107. A. Heiner, "Structural properties of fourth-generation composite femurs and tibias.," *Journal of Biomechanics*, vol. 41, no. 15, pp. 3282–3284, 2008.
 108. S. P. Väänänen, S. Amin Yavari, H. Weinans, A. A. Zadpoor, J. S. Jurvelin, and H. Isaksson, "Repeatability of digital image correlation for measurement of surface strains in composite long bones.," *Journal of biomechanics*, vol. 46, pp. 1928–32, jul 2013.

109. L. Zani, P. Erani, L. Grassi, F. Taddei, and L. Cristofolini, "Strain distribution in the proximal Human femur during in vitro simulated sideways fall," *Journal of Biomechanics*, vol. 48, no. 10, pp. 2130–2143, 2015.
110. M. Viceconti, F. Taddei, L. Montanari, D. Testi, A. Leardini, G. Clapworthy, and S. Van Sint Jan, "Multimod Data Manager: a tool for data fusion.," *Computer methods and programs in biomedicine*, vol. 87, pp. 148–59, aug 2007.
111. P. A. Yushkevich, J. Piven, H. C. Hazlett, R. G. Smith, S. Ho, J. C. Gee, and G. Gerig, "User-guided 3D active contour segmentation of anatomical structures: significantly improved efficiency and reliability.," *NeuroImage*, vol. 31, pp. 1116–28, jul 2006.
112. L. Grassi, E. Schileo, F. Taddei, L. Zani, M. Juszczuk, L. Cristofolini, and M. Viceconti, "Accuracy of finite element predictions in sideways load configurations for the proximal human femur.," *Journal of biomechanics*, vol. 45, pp. 394–399, nov 2012.
113. F. Taddei, E. Schileo, B. Helgason, L. Cristofolini, and M. Viceconti, "The material mapping strategy influences the accuracy of CT-based finite element models of bones: an evaluation against experimental measurements.," *Medical engineering & physics*, vol. 29, pp. 973–9, nov 2007.
114. F. Taddei, A. Pancanti, and M. Viceconti, "An improved method for the automatic mapping of computed tomography numbers onto finite element models.," *Medical Engineering & Physics*, vol. 26, no. 1, pp. 61–69, 2004.
115. E. F. Morgan, H. H. Bayraktar, and T. M. Keaveny, "Trabecular bone modulus–density relationships depend on anatomic site," *Journal of Biomechanics*, vol. 36, pp. 897–904, jul 2003.
116. D. T. Reilly and a. H. Burstein, "The elastic and ultimate properties of compact bone tissue.," *Journal of biomechanics*, vol. 8, pp. 393–405, jan 1975.
117. H. H. Bayraktar, A. Gupta, R. Y. Kwon, P. Papadopoulos, and T. M. Keaveny, "The Modified Super-Ellipsoid Yield Criterion for Human Trabecular Bone," *Journal of Biomechanical Engineering*, vol. 126, pp. 677–684, dec 2004.
118. D. Reilly and A. Burstein, "The mechanical properties of cortical bone," *The Journal of Bone & Joint Surgery*, vol. 56, no. 5, 1974.
119. J. M. Bland and D. G. Altman, "Measuring agreement in method comparison studies," *Statistical Methods in Medical Research*, vol. 8, pp. 135–160, apr 1999.

-
120. S. P. Väänänen, *Functional Imaging of Proximal Femur by Combining Dual Energy X-ray Imaging and Finite Element Simulations*. Academic dissertation, University of Eastern Finland, 2014.
 121. S. P. Väänänen, L. Grassi, G. Flivik, J. S. Jurvelin, and H. Isaksson, “Generation of 3D shape, density, cortical thickness and finite element mesh of proximal femur from a DXA image,” *Medical Image Analysis*, vol. 24, no. 1, pp. 125–134, 2015.
 122. A. Liu and B. Joe, “Relationship between tetrahedron shape measures,” *BIT*, vol. 34, no. 2, pp. 268–287, 1994.
 123. L. Cristofolini, M. Juszczuk, S. Martelli, F. Taddei, and M. Viceconti, “In vitro replication of spontaneous fractures of the proximal human femur,” *Journal of biomechanics*, vol. 40, pp. 2837–45, jan 2007.
 124. M. M. Juszczuk, L. Cristofolini, and M. Viceconti, “The human proximal femur behaves linearly elastic up to failure under physiological loading conditions,” *Journal of biomechanics*, vol. 44, pp. 2259–2266, jun 2011.
 125. H. Gustafson, G. Siegmund, and P. Cripton, “Comparison of Strain Rosettes and Digital Image Correlation for Measuring Vertebral Body Strain,” *Journal of Biomechanical Engineering*, vol. 138, p. 054501, mar 2016.
 126. J. Baldoni, G. Lionello, F. Zama, and L. Cristofolini, “Comparison of different filtering strategies to reduce noise in strain measurement with digital image correlation,” *The Journal of Strain Analysis for Engineering Design*, vol. 1, no. 15, 2016.
 127. B. Pan, J. Yuan, and Y. Xia, “Strain field denoising for digital image correlation using a regularized cost-function,” *Optics and Lasers in Engineering*, vol. 65, pp. 9–17, may 2015.
 128. Z. Gao, X. Xu, Y. Su, and Q. Zhang, “Experimental analysis of image noise and interpolation bias in digital image correlation,” *Optics and Lasers in Engineering*, vol. 81, pp. 46–53, 2016.
 129. D. B. Burr, C. Milgrom, D. Fyhrie, M. Forwood, M. Nyska, A. Finestone, S. Hoshaw, E. Saiag, and A. Simkin, “In vivo measurement of human tibial strains during vigorous activity,” *Bone*, vol. 18, pp. 405–10, may 1996.
 130. R. Al Nazer, J. Lanovaz, C. Kawalilak, J. D. Johnston, and S. Kontulainen, “Direct in vivo strain measurements in human bone—a systematic literature review,” *Journal of biomechanics*, vol. 45, pp. 27–40, jan 2012.

131. E. Schileo, F. Taddei, A. Malandrino, L. Cristofolini, and M. Viceconti, "Subject-specific finite element models can accurately predict strain levels in long bones.," *Journal of biomechanics*, vol. 40, pp. 2982–9, jan 2007.
132. E. Schileo, E. Dall'ara, F. Taddei, A. Malandrino, T. Schotkamp, M. Baleani, and M. Viceconti, "An accurate estimation of bone density improves the accuracy of subject-specific finite element models," *Journal of Biomechanics*, vol. 41, no. 11, pp. 2483–2491, 2008.
133. M. Ding, M. Dalstra, C. C. Danielsen, J. Kabel, I. Hvid, and F. Linde, "Age variations in the properties of human tibial trabecular bone.," *The Journal of bone and joint surgery. British volume*, vol. 79, no. 6, pp. 995–1002, 1997.
134. M. J. Mirzaali, J. Jakob Schwiedrzik, S. Thaiwichai, J. P. Best, J. Michler, P. K. Zysset, and U. Wolfram, "Mechanical properties of cortical bone and their relationships with age, gender, composition and microindentation properties in the elderly," *Bone*, dec 2015.
135. E. Schileo, L. Balistreri, L. Grassi, L. Cristofolini, and F. Taddei, "To what extent can linear finite element Models of Human femora predict failure under stance and fall loading configurations?," *Journal of Biomechanics*, vol. 47, pp. 3531–3538, sep 2014.
136. D. R. Carter and W. C. Hayes, "The compressive behavior of bone as a two-phase porous structure.," *The Journal of Bone and Joint Surgery*, vol. 59, no. 7, pp. 954–962, 1977.
137. M. Bessho, I. Ohnishi, J. Matsuyama, T. Matsumoto, K. Imai, and K. Nakamura, "Prediction of strength and strain of the proximal femur by a CT-based finite element method.," *Journal of Biomechanics*, vol. 40, pp. 1745–53, jan 2007.
138. P. M. de Bakker, S. L. Manske, V. Ebacher, T. R. Oxland, P. A. Crompton, and P. Guy, "During sideways falls proximal femur fractures initiate in the superolateral cortex: evidence from high-speed video of simulated fractures.," *Journal of biomechanics*, vol. 42, pp. 1917–25, aug 2009.
139. N. Sarkalkan, J. Waarsing, P. Bos, H. Weinans, and A. Zadpoor, "Statistical shape and appearance models for fast and automated estimation of proximal femur fracture load using 2D finite element models," *Journal of Biomechanics*, vol. 47, pp. 3107–3114, jul 2014.
140. J. S. Gregory, D. Testi, A. Stewart, P. E. Undrill, D. M. Reid, and R. M. Aspden, "A method for assessment of the shape of the proximal femur and its

- relationship to osteoporotic hip fracture.," *Osteoporosis international a journal established as result of cooperation between the European Foundation for Osteoporosis and the National Osteoporosis Foundation of the USA*, vol. 15, no. 1, pp. 5–11, 2004.
141. B. Schuler, K. D. Fritscher, V. Kuhn, F. Eckstein, T. M. Link, and R. Schubert, "Assessment of the individual fracture risk of the proximal femur by using statistical appearance models.," *Medical physics*, vol. 37, pp. 2560–71, jun 2010.
142. T. Whitmarsh, K. D. Fritscher, L. Humbert, L. M. del Rio Barquero, T. Roth, C. Kammerlander, M. Blauth, R. Schubert, and A. F. Frangi, "Hip fracture discrimination from dual-energy X-ray absorptiometry by statistical model registration," *Bone*, vol. 51, no. 5, pp. 896–901, 2012.
143. J. Thevenot, J. Koivumäki, V. Kuhn, F. Eckstein, and T. Jämsä, "A novel methodology for generating 3D finite element models of the hip from 2D radiographs," *Journal of Biomechanics*, vol. 47, no. 2, pp. 438–444, 2014.
144. C. Öhman, M. Baleani, C. Pani, F. Taddei, M. Alberghini, M. Viceconti, and M. Manfrini, "Compressive behaviour of child and adult cortical bone.," *Bone*, vol. 49, pp. 769–76, oct 2011.
145. C. Falcinelli, E. Schileo, L. Balistreri, F. Baruffaldi, B. Bordini, M. Viceconti, U. Albisinni, F. Ceccarelli, L. Milandri, A. Toni, and F. Taddei, "Multiple loading conditions analysis can improve the association between finite element bone strength estimates and proximal femur fractures: A preliminary study in elderly women.," *Bone*, jul 2014.
146. S. Gilchrist, K. Nishiyama, P. de Bakker, P. Guy, S. Boyd, T. Oxland, and P. Cripton, "Proximal femur elastic behaviour is the same in impact and constant displacement rate fall simulation," *Journal of Biomechanics*, vol. 47, pp. 3744–3749, jul 2014.
147. M. Viceconti and P. Hunter, "The Virtual Physiological Human: Ten Years After," *Annu. Rev. Biomed. Eng.*, vol. 18, pp. 103–23, 2016.
148. K. E. Naylor, E. V. McCloskey, R. Eastell, and L. Yang, "Use of DXA-based finite element analysis of the proximal femur in a longitudinal study of hip fracture.," *Journal of bone and mineral research : the official journal of the American Society for Bone and Mineral Research*, vol. 28, pp. 1014–21, may 2013.
149. K. K. Nishiyama, M. Ito, A. Harada, and S. K. Boyd, "Classification of women with and without hip fracture based on quantitative computed to-

- mography and finite element analysis,” *Osteoporosis International*, vol. 25, pp. 619–626, feb 2014.
150. M. Qasim, G. Farinella, J. Zhang, X. Li, L. Yang, R. Eastell, and M. Viceconti, “Patient-specific finite element estimated femur strength as a predictor of the risk of hip fracture: the effect of methodological determinants.,” *Osteoporosis international: a journal established as result of cooperation between the European Foundation for Osteoporosis and the National Osteoporosis Foundation of the USA*, vol. 27, pp. 2815–22, sep 2016.
 151. F. Taddei, S. Martelli, B. Reggiani, L. Cristofolini, and M. Viceconti, “Finite-element modeling of bones from CT data: sensitivity to geometry and material uncertainties.,” *IEEE transactions on bio-medical engineering*, vol. 53, pp. 2194–200, nov 2006.
 152. M. Taylor and P. J. Prendergast, “Four decades of finite element analysis of orthopaedic devices: Where are we now and what are the opportunities?,” *Journal of Biomechanics*, vol. 48, pp. 767–78, dec 2015.
 153. A. A. Zadpoor and H. Weinans, “Patient-specific bone modeling and analysis: The role of integration and automation in clinical adoption.,” *Journal of biomechanics*, vol. 48, pp. 750–760, dec 2015.
 154. A. Biewener, “Safety factors in bone strength,” *Calcified tissue international*, vol. 53, pp. 68–74, 1993.
 155. T. Rikkonen, K. Salovaara, J. Sirola, M. Tuppurainen, J. Jurvelin, R. Honkanen, E. Alhava, H. Kröger, and M. Kärkkäinen, “Physical activity slows femoral bone loss but promotes wrist fractures in postmenopausal women: A 15-year follow-up of the OSTPRE study,” *Journal of Bone and Mineral Research*, vol. 25, pp. 2332–2340, nov 2010.
 156. J. Saarelainen, V. Kiviniemi, H. Kröger, M. Tuppurainen, L. Niskanen, J. Jurvelin, and R. Honkanen, “Body mass index and bone loss among postmenopausal women: The 10-year follow-up of the OSTPRE cohort,” *Journal of Bone and Mineral Metabolism*, vol. 30, pp. 208–216, mar 2012.
 157. E. Orwoll, J. B. Blank, E. Barrett-Connor, J. Cauley, S. Cummings, K. Ensrud, C. Lewis, P. M. Cawthon, R. Marcus, L. M. Marshall, J. McGowan, K. Phipps, S. Sherman, M. L. Stefanick, and K. Stone, “Design and baseline characteristics of the osteoporotic fractures in men (MrOS) study - A large observational study of the determinants of fracture in older men,” *Contemporary Clinical Trials*, vol. 26, pp. 569–585, oct 2005.

-
158. H. Johansson, A. Odén, J. Kanis, E. McCloskey, M. Lorentzon, Ö. Ljunggren, M. K. Karlsson, E. Orwoll, Å. Tivesten, C. Ohlsson, and D. Mellström, “Low bone mineral density is associated with increased mortality in elderly men: MrOS Sweden.,” *Osteoporosis international : a journal established as result of cooperation between the European Foundation for Osteoporosis and the National Osteoporosis Foundation of the USA*, vol. 22, pp. 1411–8, may 2011.
 159. E. L. Ribom, D. Mellström, Ö. Ljunggren, and M. K. Karlsson, “Population-based reference values of handgrip strength and functional tests of muscle strength and balance in men aged 70-80 years,” *Archives of Gerontology and Geriatrics*, vol. 53, no. 2, pp. e114–7, 2011.
 160. J. P. Karjalainen, O. Riekkinen, J. Töyräs, J. S. Jurvelin, and H. Kröger, “New method for point-of-care osteoporosis screening and diagnostics,” *Osteoporosis International*, vol. 27, pp. 971–977, mar 2016.
 161. J. S. Jurvelin, S. P. Väänänen, M. K. H. Malo, L. Grassi, J. P. Karjalainen, O. Riekkinen, J. Töyräs, H. Isaksson, and H. Kröger, “Two-step diagnostics of osteoporosis and prediction of fracture risk,” in *Proceedings of the 21st congress of the European Society of Biomechanics*, 2015.

Paper I

Available online at www.sciencedirect.com

ScienceDirect

www.elsevier.com/locate/jmbbm

Review Article

Extracting accurate strain measurements in bone mechanics: A critical review of current methods



Lorenzo Grassi*, Hanna Isaksson

Department of Biomedical Engineering, and Department of Orthopedics, Lund University, Lund, Sweden

ARTICLE INFO

Article history:

Received 8 January 2015

Received in revised form

1 June 2015

Accepted 2 June 2015

Available online 11 June 2015

Keywords:

Strain

Femur

Validation

Strain gauges

Strain gages

Fibre Bragg grating

Digital image correlation

Digital volume correlation

ABSTRACT

Osteoporosis related fractures are a social burden that advocates for more accurate fracture prediction methods. Mechanistic methods, e.g. finite element models, have been proposed as a tool to better predict bone mechanical behaviour and strength. However, there is little consensus about the optimal constitutive law to describe bone as a material. Extracting reliable and relevant strain data from experimental tests is of fundamental importance to better understand bone mechanical properties, and to validate numerical models.

Several techniques have been used to measure strain in experimental mechanics, with substantial differences in terms of accuracy, precision, time- and length-scale. Each technique presents upsides and downsides that must be carefully evaluated when designing the experiment. Moreover, additional complexities are often encountered when applying such strain measurement techniques to bone, due to its complex composite structure.

This review of literature examined the four most commonly adopted methods for strain measurements (strain gauges, fibre Bragg grating sensors, digital image correlation, and digital volume correlation), with a focus on studies with bone as a substrate material, at the organ and tissue level. For each of them the working principles, a summary of the main applications to bone mechanics at the organ- and tissue-level, and a list of pros and cons are provided.

© 2015 Elsevier Ltd. All rights reserved.

Contents

1. Introduction	44
2. Approach	44
2.1. Strain gauges	45
2.1.1. Working principles	45
2.1.2. Most relevant studies	45

*Corresponding author. Tel.: +46 46 222 0655.

E-mail address: lorenzo.grassi@bme.lth.se (L. Grassi).

2.2.	Fibre Bragg grating sensors	46
2.2.1.	Working principles	46
2.2.2.	Most relevant studies	47
2.3.	Digital image correlation	47
2.3.1.	Working principles	47
2.3.2.	Most relevant studies	47
2.4.	Digital volume correlation	48
2.4.1.	Working principles	48
2.4.2.	Most relevant studies	48
3.	Discussion	49
3.1.	Strain gauges	49
3.2.	Fibre Bragg grating sensors	49
3.3.	Digital image correlation	50
3.4.	Digital volume correlation	51
4.	Conclusions	52
	References	52

1. Introduction

Understanding bone mechanical behaviour under different loading conditions is of great importance to prevent and treat bone fracture in individuals. Finite element (FE) models have been proposed as an automatic and mechanistic method to assess bone strength and fracture risk in individuals (Cody et al., 1999; Huiskes and Chao, 1983; Prendergast, 1997). However, there is no consensus about the optimal constitutive model and bone strength criterion to be implemented in such FE models (Natali and Meroi, 1989; Peng et al., 2006; Zysset, 2003; Helgason et al., 2008). This is because bone is a complex composite material, with properties that among other things change with time- and length-scale (Cristofolini et al., 2008; Ding and Dalstra, 1997). Treating bone fractures, e.g. in the form of total joint replacement or a fixation device, requires knowledge of the mechanical stimuli exerted by such devices, since bone can remodel itself in response to the local mechanical stimulation (Webster Müller, 2011; Robling et al., 2006). FE models can also help predicting the outcome of such surgical treatments if bone mechanical properties and strength are correctly modelled.

To identify the optimal material model for bone and account for the intrinsic inter- and intra-patient variability, the design of proper experiments with the aim of 1) better characterizing bone material properties, and 2) providing a validation benchmark for numerical investigations (Viceconti et al., 2005; Cristofolini et al., 2010; Anderson et al., 2007) is required. Depending on the specific aim, such experimental tests can be performed at different time- and length-scales. However, all the experiments need to extract reliable quantitative information about bone behaviour. Apart from recording the overall force and displacement during the experiment, usually displacements and strains can be measured at different locations over the tested samples. Depending on the required time, spatial resolution and the kind of mechanical tests performed, several techniques can be used to measure bone strain.

The continuous technological development provides new measurement tools with increased accuracy and precision. Consequently, the obtained strain data increases both in

resolution and number, from the first discrete measurements using extensometers, to the full-field reconstructions achieved today with optical methods. The technological development, however, does not guard against instrumentation misuse, and/or data misinterpretation. Methodological studies are available for each of the different strain measurement techniques (Klokova, 1978; Gillard et al., 2014; Kleckers, 2009; Bornert et al., 2009). Nevertheless, a vast majority of those was performed using flat, polished, and standardized specimens of polymeric or metallic materials. Human bones present additional complexities when it comes to strain measurements, mainly due to the geometry, surface roughness and humidity. As a consequence, additional care needs to be taken when measuring strains in human bones.

To our knowledge, an extensive review that covers the principal techniques for strain measurement with focus on human bone is lacking in the literature. Earlier reviews are either outdated and does therefore not include the latest developments (Pratt et al., 1979; Bedzinski and Tyndyk, 2000; Gdoutos et al., 1982; Ovryn, 1993), or limited to one single strain measurement technique (Roberts et al., 2014). Our aim is to provide a comprehensive review of the most commonly adopted methods to measure strains on bone, at a length scale of the organ- and tissue-level. The main methods of strain measurement adopted in bone biomechanics are reviewed, with their main applications, as well as their pros and cons. It is our intention that this manuscript should act as a reference guide for researchers who are designing a new experiment and need to choose the most suitable strain measurement method.

2. Approach

A first literature search was performed to identify the most relevant techniques for strain measurements on bone at the organ level. A review of some of the most relevant books on experimental biomechanics of bone (Miles and Tanner, 1992; An and Draughn, 1999) was made together with the analysis of the results of a “(strain OR measurement) AND bone” PubMed (<http://www.ncbi.nlm.nih.gov/pubmed/>) search. Four

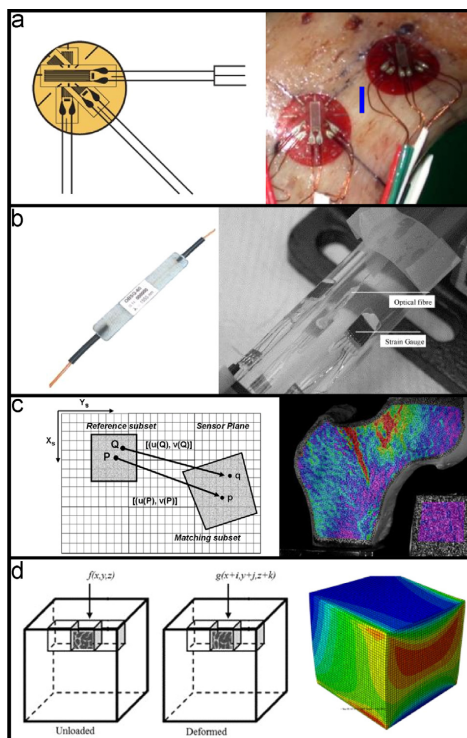


Fig. 1 – The four strain measurement techniques reviewed: a) strain gauges, b) fibre Bragg grating sensors, c) digital image correlation, and d) digital volume correlation. For each of these techniques, a schematic of the working principle is shown on the right, and an example of application to bone mechanics is reported on the left side. Parts of the figure are reprinted from Fresvig et al. (2008); Sutton (2007); Gillard et al. (2014) with permission of Elsevier, and Spie.

strain measurement techniques were identified (Fig. 1), as they were most frequently used in the spanned range of literature:

- strain gauges
- fibre Bragg grating sensors
- digital image correlation
- digital volume correlation

For each of the methods, a brief description of the principles, followed by a summary of the most relevant applications to bone biomechanics is provided. The cited studies were retrieved through a PubMed search, focusing on the applications of each technique on human bone samples at the organ-level length scale (Table 1). Where many studies on human bones were available, priority was

given to studies of the femur due to its high fracture incidence (Meling et al., 2009). A few studies investigating the micro-scale behaviour of bone were included for digital volume correlation, since the state-of-the-art studies with this technique were performed based on micro-CT data.

2.1. Strain gauges

The first application of bonded strain gauges (SG) was reported in 1938, and the first application to bone biomechanics dates only a few years later (Gurdjian and Lissner, 1944). Since then, SGs have been heavily used in bone biomechanics, and they are still considered the gold standard in bone strain measurement because of their accuracy and high frequency response.

2.1.1. Working principles

SGs measure the strains by reading the increase/decrease of the resistance of a metallic material when exposed to an external tensile/compressive force that elongates/contracts it. Given the original resistance of the material, R , its variation as a function of the applied strain, ϵ , is given by: $\Delta R/R = K_g \epsilon$, where K_g is the gauge factor, the coefficient expressing the SG sensitivity (Kyowa Electronic Instruments). A backing material carries deformation from the tested material to the electrical grid. SG typically have 3 differently oriented gauge grids (Fig. 1a). This so called “rosette” configuration allows to obtain 3 independent strain measurements in different directions, and thus determine the principal strains and principal strain orientations. An accurate strain measurement requires a proper bonding of the backing material to the specimen. Optimally, the surface for SG measurement should be chemically clean, with an appropriate roughness, a surface alkalinity corresponding to a pH of 7, and a visible gauge layout lines for locating and orienting the SG (Vishay Micro-Measurements, 2005). Bone does not have these features, and therefore different procedures have been adopted to optimize the bone surface for SG applications.

2.1.2. Most relevant studies

From the PubMed search, 239 publications were retrieved, where of four were considered most relevant. One additional study from a journal not indexed in PubMed (Roberts, 1966) was also reported (Table 1). Roberts (1966) defined a set of procedures to apply SGs on bone samples. These procedures included wiring, bonding, and waterproofing. The bone surface was prepared by removing all soft tissue and subsequently degreasing it with acetone, while body fluids were absorbed using sponges. SGs were bonded using cyanoacrylate or epoxy resins. Waterproofing was performed by coating the gauge top surface and wiring junctions with Glyptol and silicon rubber, whereas Teflon-insulated copper was used for wiring. As will be shown below, only minor modifications to this protocol have been introduced in the following 50 years.

Kim et al. (2001) investigated the strain distribution in the proximal human femur using SGs in response to the insertion of two different types of femoral stems. Ten 45° rosettes ($3 \times 1.25 \text{ mm}^2$ rectangular grid, $9 \times 9 \text{ mm}^2$ measuring grid carrier) were bonded to the proximal femora at four levels, namely at the calcar (medial side) and 2, 4, and 8 cm distal to the most caudal part of the femoral head. Bone surface was

Table 1 – Search criteria to retrieve the reviewed studies on PubMed. For each method, the search keywords used and the number of retrieved publications are reported, together with the detail of the eligible studies. Two publications non-indexed in PubMed were added in the strain gauges section.

	Keywords	Retrieved publications	Eligible	References
Strain gauges (SG)	(Gauge OR gage OR distribution) AND human AND (femur OR femurs OR femora) AND strain	239	4+1	Kim et al., 2001; Østbyhaug et al., 2009; Zani et al., 2015; Cristofolini et al., 2009 Extra: Roberts, 1966
Fibre Bragg grating sensors (FBGS)	(Bragg OR grating OR (optical AND (fibre OR fibre))) AND (bone OR femur OR femora) AND strain	26	2	Fresvig et al., 2008; Reikeras et al., 2011
Digital image correlation (DIC)	(Digital AND image AND correlation) AND (femur OR bone) AND (strain OR mechanics)	78	5	Gilchrist et al., 2013; Helgason et al., 2014; Grassi et al., 2014; Tang et al., 2015; Op Den Buijs and Dragomir-Daescu, 2011
Digital volume correlation (DVC)	(Digital AND volume AND correlation) AND (femur OR bone) AND (strain OR mechanics)	13	5	Gillard et al., 2014; Roberts et al., 2014; Hussein et al., 2012; Dall'Ara et al., 2014; Palanca et al., 2015

prepared for strain measurement by sandpapering, degreasing with acetone and drying in O₂ stream. An etchant was applied to the gauge site, and then rinsed with saline. SGs were bonded with two-component PMMA adhesive, and waterproofed using epoxy sealing. Femora were first tested in the intact configuration (900 N for all specimens), and then after the stem components insertion. A study adopting an almost identical procedure was proposed by Aamodt et al. (2001). Also, the same specimen preparation and strain gauge application procedure was adopted recently to investigate the different mechanical response of composite and cadaver femora (Basso et al., 2014).

A few years later, Østbyhaug et al. (2009) investigated the cortical strain pattern in response to insertion of two types of femoral stems. Twelve pairs of contralateral femora were obtained, and the stem was implanted randomly in the left or right femur. On each specimen, 10 strain-gauge rosettes (3 × 1.25 mm² rectangular grid, 9 × 9 mm² measuring grid carrier) were attached at four levels at the medial, lateral, and anterior aspects of the proximal femur. The bone surface was prepared for strain measurement by using acetone and etchant. The SGs were bonded using two-component PMMA adhesive, and subsequently waterproofed using a sealant.

In the same years, the group of Cristofolini and Viceconti performed several studies aimed at experimentally measuring the strain response of intact bones using SGs (Cristofolini et al., 2008, 2010; Zani et al., 2015). The strain distribution in the proximal human femoral metaphysis was measured in different configurations resembling single leg stance, using non-destructive tests (Cristofolini et al., 2009). A force corresponding to 75% of the body weight (BW) was applied, and bone was assumed to behave linearly until 2.5BW. Eleven triaxial stacked SGs (3 × 1.3 mm² rectangular grid, 10 × 10 mm² measuring grid carrier) were bonded to different locations (4 around the head, 3 around the neck, and 4 around the proximal diaphysis). The area for strain measurement was prepared by first degreasing it with ethanol, and then with a cocktail of acetone and 2-propanol. Then, the pores in the bone were filled, and the bone surface was waterproofed with two layers of polyurethane. Any excess of polyurethane was removed with fine sandpaper, and the SG bonded with cyanoacrylate glue. Finally, three layers of

polyurethane were applied over each SG to protect their electrical circuits from water. Strains were sampled at 100 Hz (with a low-pass cut-off of 10 Hz). Major principal strains, minor principal strains, and the angle of the principal strains were computed. The SG reinforcement effect (Perry, 1986) was estimated with FE analyses, and was found to vary from region to region, ranging from <1% up to 15%. Such effect was more pronounced where the cortex was thinner (reinforcement lower than 4% for bone thicker than 1 mm).

A similar approach was recently proposed by the same group for a sideways fall configuration (Zani et al., 2015). Sixteen SGs were bonded to one cadaver human femur, following the same protocol described above (one SG added on the lateral side of the femoral neck). Non-destructive tests were performed for 12 different sideways fall configurations, as well as in six different single leg stance configurations. Each of the non-destructive loading case was repeated six times. The specimens were eventually tested up to fracture in sideways fall. The study analyzed the repeatability of the measurements, showing that differences between different loading configurations were two-three orders of magnitude larger than the variability between repetitions of the same loading configuration.

2.2. Fibre Bragg grating sensors

Fibre Bragg gratings were discovered in 1978, with the first fibre Bragg grating sensors (FBGS) commercialized in 1995. Applications to bone biomechanics were reported in the late 2000s, with the aim of measuring strains at the interface between two materials, e.g. bone and a prosthesis. Such measurements would not be possible with traditional SGs, whose electrical circuitry would be damaged, or with optical methods, since the materials under examination are not transparent (Fresvig et al., 2008).

2.2.1. Working principles

A FBGS consists of a fibre with different refraction indexes in the inner and the outer core. Stretching an FBGS changes its grating period, resulting in a change in wavelength of the reflected ultraviolet light. This change in wavelength is

related to the change in the spatial period of the refractive index modulation using Bragg's law, which can be written in the form (Werneck et al., 2013): $\lambda_B = 2n_{\text{eff}}\Lambda$, where λ_B is the Bragg wavelength of the FBGS, n_{eff} is the effective refractive index of the fibre, and Λ is the periodicity of the grating. Thus, a longitudinal deformation can change both Λ and n_{eff} , the latter by the photo-elastic effect and the former by increasing the pitch of the grating. This causes a change in λ_B , which can be related to the applied longitudinal strain via: $\Delta\lambda_B/\lambda_B = (1 - \rho_e)\epsilon$. By knowing the photoelastic coefficient ρ_e , strains can be derived.

2.2.2. Most relevant studies

From the PubMed search, 26 publications were retrieved, where of 2 were considered relevant (Table 1). Fresvig et al. (2008) addressed the suitability of FBGSs for strain measurement on bones by comparing them with SGs. Tests were conducted on an acryl tube and on human femur diaphysis. Both were reduced to a cylindrical shape, and 4 SGs and 4 FBGSs were mounted with a 45° relative shift. The specimens were compressed step-wise, and the longitudinal strains from SGs and FBGSs were recorded. No significant differences were found between the measured strains on the acrylic tube (Pearson correlation coefficients between sensors ranged from 0.986–1.0) or the cylindrical bone sample (Pearson correlation coefficient from 0.629–0.999). However, the standard deviation of the difference between FBGSs was not provided, as the different sensors were not subjected to the same deformation due to alignment inaccuracies of both the gauge and loading axis.

Reikeras et al. (2011) continued from the conclusions of Fresvig et al. (2008), and used FBGSs to measure the strains at the implant-cortex interface of a cadaver femur with an implanted stem prosthesis. SGs were used to measure the strains on the external cortex. To prepare the bone for FBGS measurements, four shallow vertical ditches were made in the endosteal cortex (corresponding to the position and longitudinal direction of the rosette vertical SGs on the outside periosteal cortex). FBGSs were mounted in the ditches and bonded with cyanoacrylic adhesive. The stem of the prosthesis was not interfering with the FBGSs. The principal strains from the SGs were compared with the single direction strain measurements of the corresponding FBGSs, under the assumption of the principal strain direction being aligned with the vertical axis.

2.3. Digital image correlation

The first formulations of digital image correlation (DIC) to measure deformations are from 1980s (Sutton et al., 1983; Peters and Ranson, 1982). DIC was initially adopted for measurements of large displacements/strains. The evolution of digital imaging devices with high resolution and increased frame rate recently allowed DIC to be used to detect strains on the order of a few hundred microstrains. Thus, applications of DIC in the field of bone mechanics are very recent.

2.3.1. Working principles

Digital image correlation is a non-contact method where one digital image is mapped onto another digital image. The

images show the specimen that is tested, and the transformation field between the two images is used to retrieve the displacement field on the surface of the specimen. The transformation field is determined by maximizing a correlation coefficient. The latter is determined by examining pixel intensity array subsets on two or more corresponding images. The measurement accuracy of DIC can be affected by many factors, such as the size of the subset area used to match the same point in two images taken at different time points (Sutton et al., 2009), the step size (i.e., the number of pixels by which the subset is shifted to calculate the strain field) and, if used, the type of data smoothing/filtering adopted.

DIC measurements can be 2D (one camera used), or surface-3D (two cameras used in stereovision). The full 3D approach (where a 3D imaging device, e.g. an X-ray tomograph, is used) is referred as digital volume correlation (DVC), and is treated separately in this review.

2.3.2. Most relevant studies

From the PubMed search, 78 publications were retrieved, where of five were considered relevant (Table 1). Op Den Buijs and Dragomir-Daescu (2011) used 2D DIC to measure displacements and strains over 22 cadaver femora. The bones were tested in a configuration resembling a fall to the side, at a displacement rate of 100 mm/s up to fracture. Images were recorded with a high-speed video camera (1024 × 512 px, 6000 fps). However, results of the measured strains were only qualitatively presented for two representative femora. Also, no description of the applied speckle pattern (if any) and image correlation algorithm used for analysis was provided.

Gilchrist et al. (2013) assessed the capability of DIC to accurately measure strains on bones by comparing the strains measured by DIC to the measurements from SGs, considered as a gold standard. To do so, 20 human proximal femora were prepared with a strain rosette glued on the antero-superior femoral neck, and a speckle pattern was airbrushed over the same area. Femora were loaded to 50% of their predicted fracture load (determined using the method proposed by Boehm et al. (2008)) at 0.5 mm/s. Images were recorded at 100 fps with 1280 × 800 px (approx. 17 px/mm) resolution. Minor principal strains were used for validation. Results showed a good correlation (root mean square average difference 127 $\mu\epsilon$, standard deviation 239 $\mu\epsilon$), but also the presence of random image-to-image noise in the DIC data. The strains were only compared at one single location (anterior-superior aspect of the femoral neck), and at one time frame (corresponding to the maximal force in the test). Thereafter, DIC was used to measure strains in an impact simulator of sideways falls. However, DIC strain measurements recorded during the simulated fall on the side were not shown in the paper, and the authors only reported that strain fields calculated by DIC exhibited steep strain gradients, which were attributed to bone inhomogeneity.

Helgason et al. (2014) performed a drop tower test over one proximal human femur specimen in a sideways fall configuration. The impact between the 16.5 kg impactor and the specimen occurred at a 3.5 m/s speed. Two high-speed cameras recorded the proximal femur anteriorly and posteriorly (two separate 2D DIC set-up) at 9009 fps, 384 × 384 px (pixel pitch=0.25 mm). However, the strains measured were

only qualitatively compared to the predictions of FE models (minimum principal strains on the anterior surface shown), and no quantitative data was reported from the strain measurements.

Grassi et al. (2014) recently performed a study investigating the strain response of three human cadaver femora at physiological-like strain rates. Two high-speed (3000 fps) cameras were used in a surface 3D DIC scheme, and different correlation settings were used to analyze the whole load curve and the near-fracture behaviour. Those correlation settings were determined from an undeformed control plate which was used as a noise level reference during the tests. A data filtering method was developed, in which the obtained displacement vectors for each point were filtered in time using a low-pass filter. The filtered displacements were then used to calculate the strains. Digital SGs were identified and their output compared with literature. The evolution of the principal strain magnitude and direction was analyzed at different stages of the loading curve, and the collected data can act as a quantitative and comprehensive benchmark for numerical models.

Tang et al. (2015) investigated the mechanical behaviour of human cortical bone at the tissue level under shear. They used, among other techniques, 2D DIC to map the surface strains during the shear test. Polished $20 \times 5 \times 3 \text{ mm}^3$ bone samples with two V-shaped notches were obtained and tested under pure shear up to fracture at a 0.2 mm/min displacement rate. Strains were measured on a $3.6 \times 2.7 \text{ mm}^2$ section using an optical microscope equipped with a digital camera (4 fps). Use of optical microscope images together with the intrinsic micro-structural features of the polished samples provided a contrasted enough pattern in the acquired digital images, so no artificial speckle pattern was needed.

2.4. Digital volume correlation

Digital volume correlation (DVC) for tomographic datasets was first proposed by Bay et al. (1999). They proposed that the 2D-DIC concepts could be extended to match small sub-volumes of a tomographic reconstruction before and after undergoing loading to obtain a full volumetric field of 3D motions. DVC applications in bone mechanics are thus very recent.

2.4.1. Working principles

DVC is essentially the 3D extension of the 2D-DIC method. In 2D-DIC, a coefficient based on the summed difference of intensity values in a subset of a planar images is minimized. In DVC, the minimization is done on a 3D-subset where intensity values corresponding to (x,y,z) values are compared to a standard and the summed difference minimized using the predictive 3D displacement fields. Since tomographic attenuation-based images are used, a “white light” speckle pattern is not available, and DVC relies on naturally occurring patterns of the specimen to track changes in material features.

2.4.2. Most relevant studies

Thirteen publications were retrieved, where of five were relevant (Table 1). Since only a limited number of publications on

DVC in bone mechanics was available, some experimental studies performed on non-human bones were also included.

Roberts et al. (2014) recently reviewed the application of DVC on trabecular bone, with the aim of clarifying the role of the different correlation parameters on the outcome. The main conclusions are

- subset size is the most influential parameter in terms of measurement precision.
- A global correlation approach can reduce displacement measurement error compared to local techniques. This is accomplished by imposing continuity requirements, such that mapping of a single subset depends on mapping of adjacent regions.
- Since it is not possible to apply an artificial speckle pattern inside a specimen, the accuracy and precision of displacement and strain measurement are affected by the different bone micro-structure (e.g., bone volume fraction, trabecular number and separation, structure model index).

Hussein et al. (2012) used DVC to investigate the mechanics of 30 L1 vertebrae. To the authors' knowledge, this is the first and solely study reporting the usage of DVC on human bones at the organ level. The L1 segments were first preconditioned 10 times at 400 N, and were then imaged with a μCT . Step-wise 1 mm displacements were applied allowing 20 min relaxation time between steps. Samples were μCT scanned after each step ($\mu\text{CT}80$, Scanco Medical, $37 \mu\text{m}$ voxel size, 70 kVp, 114 mA, and 300 ms integration time). A final μCT scan was performed after fracture. A hexahedral mesh was created from the segmented vertebral geometries. The elements of the mesh defined the subsets used for DVC calculations. The correlation between subsets was calculated using a maximum likelihood method. Accuracy and precision were high when using simulated displacements (mean-bias error and root-mean-square error for the displacement about 0.025% and 0.35%, respectively). However, errors increased when real image data from repeated μCT acquisitions were used. This might have been due to imaging inaccuracies, such as X-ray beam fluctuations, or repositioning errors, which together led to a discrepancy between repeated measurements of $740 \pm 630 \mu\epsilon$ (0.58 ± 1.12 voxels displacement).

The need for accurate quantification of the measurement inaccuracies in DVC measurements was addressed by Gillard et al. (2014), with a study on porcine trabecular bone. Five repeated μCT scans were performed (HMX ST, Nikon Metrology, $24.6 \mu\text{m}$ voxel size, 105 kVp) on the same specimen, the first three without moving the sample, and the last two after shifting it by $125 \mu\text{m}$ in the vertical direction. DVC was calculated using a local approach (i.e., the shift of the pattern within each subset is independent from the shift of the neighbouring subsets) based on the fast Fourier transform (FFT). Strain resolutions ranging between $70 \mu\epsilon$ and $800 \mu\epsilon$ were reported when using the identified optimal correlation parameters (64 voxels sub-volume size, 50% overlap). More in detail, repeated scans without repositioning led to an accuracy (average strain) and precision (standard deviation of the strain) of 40 and $140 \mu\epsilon$, respectively. When the specimens

were repositioned between scans, the reported accuracy and precision were 250 and 750 $\mu\epsilon$, respectively. A significant decrease in the sub-volumes correlation was also reported when the trabeculae started to yield or fail. This led to unrealistic strain values, and the authors proposed to cut out points whose correlation values are below 0.9.

Dall'Ara et al. (2014) performed a methodological study aimed at evaluating precision and accuracy of DVC strain measurement on bovine cortical and trabecular bone specimens (3 mm in diameter, 29 mm in length) imaged with μ CT (Skyscan 1172, Bruker, 10 μm voxel size, 59–70 kV, 1180 ms exposure time). A custom global (i.e., the displacement of each subset is affected by the displacements of its neighbouring elements) DVC algorithm was used based on the ShIRT library (Barber and Hose, 2005) for deformable image registration. Briefly, an elastic registration algorithm was coupled to a FE simulation to calculate the strains in the mesh. Accuracy and precision were analyzed by comparing virtually displaced scans, repeated scans without any repositioning of the sample, and repeated scans taken after sample repositioning. The authors concluded that the main source of error was the intrinsic noise of the μ CT images. The error in the measurement could be decreased by increasing the size of the grid for strain calculation (a power law relationship between the two is reported), paying the price of decreased spatial resolution. For a grid size of 50 px, the accuracy and precision ranges reported were 425–692 $\mu\epsilon$ and 202–394 $\mu\epsilon$, respectively. Performing DVC on cortical bone resulted in a 10–25% decrease in the accuracy compared to trabecular bone with identical procedure. Therefore, the authors suggested that DVC strain measurements could be used to efficiently discriminate yielded from non-yielded regions. Reaching the accuracy needed to investigate the elastic regime required an increase of the grid size that would have ultimately reduced the spatial resolution too much.

Palanca et al. (2015) compared the performances of three different DVC algorithms on two cylindrical samples of cortical and trabecular bone, respectively. The samples were imaged with μ CT (Skyscan 1172, Bruker, 10 μm voxel size, 59–70 kV, 1180 ms exposure time). Most likely, the same datasets as in Dall'Ara et al. (2014) were used in this study. The three algorithms evaluated in this study were: two proprietary codes (LaVision Ltd, Germany) based on FFT and direct correlation (DC), respectively, and the ShIRT-based approach proposed in Dall'Ara et al. (2014). The comparison was performed in terms of strain accuracy (average strain) and precision (standard deviation), both against repeated scans without repositioning, and virtually displaced volumes. The FFT-based DVC exhibited a much faster computation time, but also the worst accuracy (one order of magnitude difference with respect to the other two methods) and precision. Both ShIRT- and DC-based DVC algorithm had accuracy and precision in the order of a few hundred micro-strains when the optimal parameters (50 voxels subset size) were adopted. In general, ShIRT-based DVC performed better than the other two algorithms, and the authors ascribed this to the global nature (which implies a continuity assumption) of the approach.

3. Discussion

The increasing number of studies aiming to model bone behaviour and bone fracture requires adequate validation methods. However, extracting relevant and accurate strain measurements from biomechanical experiments on bone is a challenge. The aim of the present review was to examine the most relevant literature regarding strain measurements on human bone samples *ex vivo*, with focus on the organ- and tissue-level. Each relevant technique was presented with an emphasis on the additional complexity introduced by having bone as the substrate material.

The comparison between experimental studies and different strain measurement techniques was somewhat impaired by the lack of a commonly defined metrics. In an attempt to compare the methods, we chose to report sampling frequency, spatial resolution, and strain accuracy for the studies where such data was available (Table 2). Please observe that the values for strain accuracy might have been defined in different ways for different techniques, and sometimes between different studies adopting the same technique. Therefore, references were provided for each reported value, and the reader is encouraged to check the referred papers to get a more detailed definition.

3.1. Strain gauges

SGs are often considered the gold standard for strain measurements on bone. However, obtaining accurate strain data with SGs is not trivial. Bone characteristics do not naturally meet the requirements for optimal SG adhesion (Vishay Micro-Measurements, 2005), and the procedures to optimize bone surface for SG measurements require training and skills. Moreover, SG measurement on bone presents intrinsic limitations. The first is the discreteness of the measurement. SGs can only record the average strain of the area to which they are bonded. The number of SGs that can be applied over a sample is limited by practical obstacles, e.g., limited presence of flat enough areas over the bone surface, electrical wires hindrance, etc. This results in having typically no more than 20 SGs applied over a proximal femur sample. Besides, the SG location has to be determined beforehand. Such position is usually determined either through numerical simulations, or by pursuing consistency with previous literature. This is an important limitation when the strains leading to, e.g., yielding or crack formation are investigated. Finally, SGs themselves have non-negligible stiffness, which leads to the so-called “reinforcement effect” (Perry, 1986). The entity of the reinforcement can be calculated theoretically under certain conditions (Beatty and Chewning, 1979; Ajovalasit et al., 2010), and has been estimated to be up to 15% on thin cortical sections of a femur using a validated FE procedure (Cristofolini et al., 2009).

3.2. Fibre Bragg grating sensors

The main advantages of FBGs are small size, light weight, biocompatibility, chemical inertness, and immunity to

Table 2 – Comparison of the performances of the four reviewed methods based on the reviewed studies. The spatial resolution was determined as the size of the excitation grids for the SG, and as the pixel/voxel size for DIC/DVC. Strain accuracy was reported when available (only indicative values).

	Sampling frequency [Hz]	Spatial resolution*	Type of measurement	Strain accuracy [$\mu\epsilon$]
Strain gauges	100 Hz (Cristofolini et al., 2009)	$3 \times 1.25 \text{ mm}^2$ grid size (Kim et al., 2001; Østbyhaug et al., 2009) $3 \times 1.3 \text{ mm}^2$ grid size (Cristofolini et al., 2009)	Contact, discrete	N/A
Optical Bragg grating fibre	60 Hz (Reikeras et al., 2011)	N/A	Contact, discrete	N/A
Digital image correlation	3000 Hz (Grassi et al., 2013) – 9216 Hz (Gilchrist et al., 2013) (100 Hz for DIC validation against SG (Gilchrist et al., 2013))	5 px/mm (Gilchrist et al., 2013; Helgason et al., 2014) – 10 px/mm (Grassi et al., 2014) (17 px/mm for DIC validation against SG (Gilchrist et al., 2013))	Non-contact, full-field	$\sim 33 \mu\epsilon$ in the standing control plate
Digital volume correlation	$\sim 3 \times 10^{-4}$ (estimated by the authors)	12–82 μm voxel size (Roberts et al., 2014)	Non-contact, full-field	740 $\mu\epsilon$ (Hussein et al., 2012) 20–250 $\mu\epsilon$ (Gillard et al., 2014) 10–792 $\mu\epsilon$ (Dall'Ara et al., 2014)

electromagnetic interference. Most of these qualities represent a significant advantage for in vivo application of FBGSs. As for the ex vivo applications, the main advantage of FBGSs is the absence of damageable electrical circuitry, that allows their positioning for example at the interface between two materials. This makes FBGSs a valuable option to investigate the strain response at the bone/implant interface. The potential of such application was shown by Reikeras et al. (2011), who found that deformations on the external cortex and the internal cortex at the bone/implant interface are not related. Thus, it is important to measure strains directly at the bone/implant interface to eventually improve implant design. Despite FBGSs are commercially available in a rosette configuration (thus being able to measure principal components of strain, analogously to SGs), the only two applications found in bone mechanics used single-fibre FBGSs. This represents a limitation to those studies, as the hypothesis of principal strains being aligned to the shaft axis is likely not to hold at the bone-implant interface.

A few studies have compared the accuracy of FBGSs and SGs, where SGs provided a higher precision (Werneck et al., 2013). Fresvig et al. (2008) reported non-significant differences between SG and FBGS, but a direct quantitative comparison was not provided. While SGs attain a high linearity in the response, FBGSs have a different sensitivity between positive and negative loads, and a very high sensitivity to temperature gradients (Kleckers, 2009). Di Sante et al. (2014) reported that the sensitivity values for FBGSs may differ significantly from the theoretical value for silica fibres, and recommended an in-situ calibration against a gold standard. Further development of the sensor technology, together with a more refined set-up for the application to bone material can possibly lead to an accuracy approaching that of SGs.

3.3. Digital image correlation

DIC has some advantages over the methods discussed above. First is the potential to obtain the full-field strain response of the bone, rather than a finite number of discrete strain measurements. A second advantage is the non-contact nature of DIC, which reduces the reinforcement effect to a minimum (or even completely eliminates it if no paint is applied (Tang et al., 2015)). Last, the rapid development of digital imaging technology results in the possibility of obtaining more accurate spatial and time resolved strain data. Despite these advantages, DIC has been scarcely used in ex vivo experiments, and no consensus exists on its reliability for bone mechanics. This is mostly due to the lack of methodological studies conducted with DIC on bone samples. Such studies are limited to 2D-DIC studies evaluated using synthetic images (Bornert et al., 2009; Amiot et al., 2013; Pan et al., 2009), thus not considering the spectrum of additional complexities introduced by testing human bone samples (e.g., non-planar, rough and wet surfaces, tracked using a 3D-surface DIC approach). Only Gilchrist et al. (2013) performed a validation of DIC on bone against one SG.

Most experimental studies using DIC adopted a 2D approach over femoral bone specimens (Op Den Buijs and Dragomir-Daescu, 2011; Helgason et al., 2014). This approach likely introduces significant artefacts in the measured strains as soon as the normal to the bone surface deviates from the optical axis of the camera. This limited the authors to a qualitative analysis of the measured DIC data. Such 2D DIC approach is instead suitable for studies involving regular shape, polished bone samples as in Tang et al. (2015). Another potential issue with DIC is linked to its continuum nature. DIC in its original formulation (Sutton et al., 2009) inherently

assumes that the object under consideration shows no strong discontinuities in displacement between consecutive images. This condition is clearly violated when a crack is formed on the specimen, and suggests additional care when dealing with DIC measurements from dynamic impact tests, such as in, e.g., (Gilchrist et al., 2013; Helgason et al., 2014). Thus, care must be taken to exclude regions where the continuum hypothesis is violated, unless extended DIC formulations are adopted (Nguyen et al., 2011; Roux et al., 2009). However, such extended DIC formulations are still under development, and out of the scope of the present review.

A proper application of DIC requires that the correlation parameters are optimized for that specific application. That implies that an a priori optimal set of parameters does not exist, nor does a univocal formula to calculate them. Some general guidelines about the choice of the correlation parameters (subset size, step size, and filtering) can be found in, e.g., Sutton et al. (2009). In simple terms, the larger a subset is, the more information it will contain, thus increasing the likelihood of obtaining a good correlation. On the other hand, an increase of the subset size leads to a decreased spatial resolution. Analogously, an increase of the step size will reduce the noise in the calculated strains, but will reduce the spatial resolution. Ultimately this results in the need to find an optimal trade-off between the parameters, which may require both experience and a considerable amount of trials.

One last concern with DIC is the determination of spatial resolution of the extracted displacement/strain field. The spatial resolution of DIC data is driven by the spatial resolution of the acquired images (in terms of px/mm ratio). However, the final resolution of the strain measurements depends on a number of other factors, like optical lens quality, marker size (Lionello and Cristofolini, 2014), and the correlation algorithm/parameters adopted. The absence of a univocal definition for the spatial resolution leads to that DIC spatial resolution is not reported, potentially impairing the clarity of the reported results, and the possibility to compare different studies.

3.4. Digital volume correlation

Digital volume correlation is the extension of 2D-DIC to the third spatial dimension. Thus, the same considerations as for DIC still holds. Although DVC can be performed on different type of 3D images (e.g. magnetic resonance, confocal microscopy, optical coherence tomography), applications to bone biomechanics at the organ and tissue level have only been reported using CT images. When compared to DIC with digital images, the use of X-ray tomographic reconstructions to calculate the strain field leads to two additional sources of noise, namely: (i) the noise of the tomographic images, which is generally higher than that of digital images, and (ii) that it is impossible to apply an artificial speckle pattern to enhance the correlation. The majority of studies adopting DVC on bone samples (Gillard et al., 2014; Roberts et al., 2014; Hussein et al., 2012), investigated bone mechanical properties at the tissue-level. This is because the trabecular bone at the tissue-level consists of a spongy network which is very well suitable for the calculation of a correlation coefficient between subsets of such network. The reported ranges of accuracy and precision for

DVC strain measurements on trabecular bone samples are 20–1280 $\mu\epsilon$ and 39–630 $\mu\epsilon$, respectively (extrapolated from Dall'Ara et al. (2014)). Only one DVC study investigated human bone at the organ level by scanning whole L1 vertebra samples (Hussein et al., 2012). However, the level of noise between repeated acquisitions of an undeformed sample was greater than $740 \pm 630 \mu\epsilon$. This value is only 10 times lower than the yield strain reported for trabecular bone in vertebrae (Kopperdahl and Keaveny, 1998), thus impairing the investigation of strains at physiological load levels. Dall'Ara et al. (2014) evidenced that both the precision and accuracy errors decrease with a power law as a function of the increasing size of the correlation window. However, increasing the size of the correlation window leads to a loss of spatial resolution. This poses the problem of finding the best compromise between spatial resolution and strain resolution for the designed study. The noise of the DVC measurements was also found to be related to the intrinsic noise of the tomographic images. Dall'Ara et al. (2014) also compared their accuracy and precision with those achieved by Gillard et al. (2014) when equivalent correlation parameters (two different DVC approaches were adopted in the two studies) were used. They found that the FFT-DVC approach in Gillard et al. (2014) achieved a better accuracy in the stationary test (i.e., repeated scans without repositioning), whereas the method by Dall'Ara et al. (2014) performed better in when the specimen was repositioned after the first scan.

The relevant issue of comparing the performances of different DVC algorithms on a common set of data was only recently addressed by Palanca et al. (2015). The study showed that a DVC approach implementing a continuity constraint between neighbouring subsets provided a higher strain accuracy and precision than local DVC approaches when evaluated using repeated scans without repositioning, in agreement with Roberts et al. (2014). Another important aspect that should be addressed is the optimal image resolution for DVC, i.e., what image resolution is good enough to achieve a high correlation between the subsets while not having an unnecessarily high X-ray dose or long scanning time. To our best knowledge, no study has addressed this question for bone samples yet.

The results reported in the evaluated DVC studies show that accuracy and precision are both around 200 $\mu\epsilon$ when a subset size corresponding to $\sim 700 \mu\text{m}$ is used (Dall'Ara et al., 2014). Thus, the strains during the elastic regime cannot be measured with a proper accuracy with current methodology. It is instead possible to successfully use DVC to discern yielded areas, and to measure strains around the yield point. However, it has to be observed that measuring over the yield point has other drawbacks. It is in fact not possible to obtain a good correlation value between excessively distorted subsets (Gillard et al., 2014).

In summary, DVC is a very powerful tool to explore the full field 3D strain distribution in bone samples. However, two main issues have to be solved: (i) the noise levels in μCT scans, and (ii) the time needed to acquire one μCT volume. As for the first issue, use of synchrotron-based tomographic scanners can possibly contribute to address such limitation in the immediate future. Although providing a limited field-of-view, synchrotron-based tomographic scanners allow for higher image resolutions and less noisy image due to the

higher brilliance and collimation of the X-ray source. As for the time needed to acquire one CT volume, this currently represents a severe limitation to DVC studies, as a full scan can take up to several hours. This means that the real time bone response, as well as creep and stress relaxation effects in bone cannot be investigated.

4. Conclusions

The scope of this review was to provide the means to decide which of the reviewed methods best fits the needs of the reader's experiment. It appears evident that no method is clearly superior to the others. However, the following conclusions can be drawn:

- Despite being old, SGs are still the gold standard when it comes to strain accuracy and measurement repeatability. They are recommended for accurate, discrete measurements in specific locations that can be a priori determined.
- FBGSs have lower precision and accuracy than SGs. FBGSs are recommended for regions where SG application is impaired by practical reasons. The interface between internal bone cortex and an artificial implant is a typical example of this.
- DIC presents advantages over SGs, including but not limited to the higher number of measurements, which allows for the reconstruction of full-field strain patterns. However, the estimation of the spatial resolution of DIC measurements is not trivial, and noise has to be handled with care. Therefore, future studies adopting DIC should report all the details of their procedure, especially including the parameters chosen to calculate the correlation coefficients (subset size, step size, etc.)
- Digital volume correlation can augment the knowledge in terms of internal strain distribution in bone in response to different loading conditions and when approaching yield. However, DVC is sensitive to noise in the obtained strain data. Such noise effects need to be controlled and measured in order to get a proper strain resolution. Moreover, the long acquisition time currently limits the usability to experiments where the real time strain response is not crucial.

REFERENCES

- Aamodt, A., Lund-Larsen, J., Eine, J., Andersen, E., Benum, P., Husby, O.S., 2001. Changes in proximal femoral strain after insertion of uncemented standard and customised femoral stems. *J. Bone Jt. Surg.* 83 (6), 921–929.
- Ajvalasit, A., Fragapane, S., Zuccarello, B., 2010. Local reinforcement effect of embedded strain gauges. *EPJ Web Conf.* 6.
- Amiot, F., Bornert, M., Doumalin, P., Dupré, J.-C., Fazzini, M., Orteu, J.-J., Poilâne, C., Robert, L., Rotinat, R., Toussaint, E., Watrisse, B., Wienin, J.S., 2013. Assessment of digital image correlation measurement accuracy in the ultimate error regime: main results of a collaborative benchmark. *Strain* 49 (6), 483–496.
- An Y., Draughn R., *Mechanical Testing of Bone and the Bone-Implant Interface*, 1999.
- Anderson, A.E., Ellis, B.J., Weiss, J.A., 2007. Verification, validation and sensitivity studies in computational biomechanics. *Comput. Methods Biomech. Biomed. Eng.* 10 (3), 171–184.
- Barber, D.C., Hose, D.R., 2005. Automatic segmentation of medical images using image registration: diagnostic and simulation applications. *J. Med. Eng. Technol.* 29 (2), 53–63.
- Basso, T., Klaksvik, J., Syversen, U., Foss, O.A., 2014. A biomechanical comparison of composite femurs and cadaver femurs used in experiments on operated hip fractures. *J. Biomech.* 47 (16), 3898–3902.
- Bay, B.K., Smith, T.S., Fyhrie, D.P., Saad, M., 1999. Digital volume correlation: three-dimensional strain mapping using X-ray tomography. *Exp. Mech.* 39 (3), 217–226.
- Beatty, M.F., Cheung, S.W., 1979. Numerical analysis of the reinforcement effect of a strain gage applied to a soft material. *Int. J. Eng. Sci.* 17 (7), 907–915.
- Bedzinski, R., Tynidy, M., 2000. Experimental methods of stress and strain analysis in orthopaedics biomechanics. *Acta Bioeng. Biomech.* 2 (2), 3–23.
- Boehm, H.F., Horng, A., Notohamiprodjo, M., Eckstein, F., Burklein, D., Panteleon, A., Lutz, J., Reiser, M., 2008. Prediction of the fracture load of whole proximal femur specimens by topological analysis of the mineral distribution in DXA-scan images. *Bone* 43 (5), 826–831.
- Bornert, M., Brémand, F., Doumalin, P., Dupré, J.-C., Fazzini, M., Grédiac, M., Hild, F., Mistou, S., Molimard, J., Orteu, J.-J., Robert, L., Surrel, Y., Vacher, P., Watrisse, B., 2009. Assessment of digital image correlation measurement errors: methodology and results. *Exp. Mech.* 49 (3), 353–370.
- Cody, D.D., Gross, G.J., Hou, F.J., Spencer, H.J., Goldstein, S.A., Fyhrie, D.P., 1999. Femoral strength is better predicted by finite element models than QCT and DXA. *J. Biomech.* 32 (10), 1013–1020.
- Cristofolini, L., Juszczak, M., Taddei, F., Viceconti, M., 2009. Strain distribution in the proximal human femoral metaphysis. *Proc. Inst. Mech. Eng. H* 223 (3), 273–288.
- Cristofolini, L., Schileo, E., Juszczak, M., Taddei, F., Martelli, S., Viceconti, M., 2010. Mechanical testing of bones: the positive synergy of finite-element models and in vitro experiments. *Philos. Trans. A: Math. Phys. Eng. Sci.* 368 (1920), 2725–2763.
- Cristofolini, L., Taddei, F., Baleani, M., Baruffaldi, F., Stea, S., Viceconti, M., 2008. Multiscale investigation of the functional properties of the human femur. *Philos. Trans. A: Math. Phys. Eng. Sci.* 366 (1879), 3319–3341.
- Dall'Ara, E., Barber, D., Viceconti, M., 2014. About the inevitable compromise between spatial resolution and accuracy of strain measurement for bone tissue: a 3D zero-strain study. *J. Biomech.* 47 (12), 2956–2963.
- Di Sante, R., Donati, L., Troiani, E., Proli, P., 2014. Reliability and accuracy of embedded fiber Bragg grating sensors for strain monitoring in advanced composite structures. *Met. Mater. Int.* 20 (3), 537–543.
- Ding, M., Dalstra, M., 1997. Age variations in the properties of human tibial trabecular bone. *J. Bone Joint Surg. Br.* 79, 995–1002.
- Fresvig, T., Ludvigsen, P., Steen, H., Reikerås, O., 2008. Fibre optic Bragg grating sensors: an alternative method to strain gauges for measuring deformation in bone. *Med. Eng. Phys.* 30 (1), 104–108.
- Gdoutos, E., Raftopoulos, D., Baril, J., 1982. A critical review of the biomechanical stress analysis of the human femur. *Biomaterials* 3, 2–8.
- Gilchrist, S., Guy, P., Cripton, P. a., 2013. Development of an inertia-driven model of sideways fall for detailed study of

- femur fracture mechanics. *J. Biomech. Eng.* 135 (12), 121001.
- Gillard, F., Boardman, R., Mavrogordato, M., Hollis, D., Sinclair, I., Pierron, F., Browne, M., 2014. The application of digital volume correlation (DVC) to study the microstructural behaviour of trabecular bone during compression. *J. Mech. Behav. Biomed. Mater.* 29, 480–499.
- Grassi, L., Väänänen, S.P., Amin Yavari, S., Weinans, H., Jurvelin, J. S., Zadpoor, A. a., Isaksson, H., 2013. Experimental validation of finite element model for proximal composite femur using optical measurements. *J. Mech. Behav. Biomed. Mater.* 21, 86–94.
- Grassi, L., Väänänen, S.P., Amin Yavari, S., Jurvelin, J.S., Weinans, H., Ristinmaa, M., Zadpoor, A.A., Isaksson, H., 2014. Full-field strain measurement during mechanical testing of the human femur at physiologically relevant strain rates. *J. Biomech. Eng.* 136 (11), 111010-1–111010-8.
- Gurdjian, E.S., Lissner, H.R., 1944. Mechanism of head injury as studies by the cathode ray oscilloscope preliminary report. *J. Neurosurg.* 1 (6), 393–399.
- Helgason, B., Gilchrist, S., Ariza, O., Chak, J.D., Zheng, G., Widmer, R.P., Ferguson, S.J., Guy, P., Crompton, P. a., 2014. Development of a balanced experimental-computational approach to understanding the mechanics of proximal femur fractures. *Med. Eng. Phys.* 36 (6), 793–799.
- Helgason, B., Perilli, E., Schileo, E., Taddei, F., Brynjólfsson, S., Viceconti, M., 2008. Mathematical relationships between bone density and mechanical properties: a literature review. *Clin. Biomech.* 23 (2), 135–146.
- Huiskes, R., Chao, E.Y.S., 1983. A survey of finite element analysis in orthopedic biomechanics: the first decade. *J. Biomech.* 16 (6), 385–409.
- Hussein, A., Barbone, P., Morgan, E., 2012. Digital volume correlation for study of the mechanics of whole bones. *Procedia IUTAM* 4, 116–125.
- Kim, Y.H., Kim, J.S., Cho, S.H., 2001. Strain distribution in the proximal human femur. An in vitro comparison in the intact femur and after insertion of reference and experimental femoral stems. *J. Bone Jt. Surg. Br.* 83 (2), 295–301.
- Kleckers T., Fibre Bragg sensors compared with electrical strain gauges for use in force measurement – Prospects and potentials, in: *Proceedings of the XIX IMEKO World Congress Fundamental and Applied Metrology*, 2009.
- Klokova, N.P., 1978. Metrological characteristics of resistance strain gauges and evaluation of deformation measurement errors. *Meas. Tech.* 21 (5), 640–649.
- Kopperdahl, D., Keaveny, T.M., 1998. Yield strain behavior of trabecular bone. *J. Biomech.* 31 (7), 601–608.
- Kyowa Electronic Instruments, Strain gage catalogue, pp. 1–100, Available at <http://www.kyowa-ei.com/eng/download/technical/strain_gages/pdf_index_001_eng.pdf>.
- Lionello, G., Cristofolini, L., 2014. A practical approach to optimizing the preparation of speckle patterns for digital-image correlation. *Meas. Sci. Technol.* 25 (10), 107001.
- Meling, T., Harboe, K., Søreide, K., 2009. Incidence of traumatic long-bone fractures requiring in-hospital management: a prospective age- and gender-specific analysis of 4890 fractures. *Injury* 40 (11), 1212–1219.
- Miles, A., Tanner, K., 1992. *Strain Measurement in Biomechanics*. Springer, Dordrecht, Netherlands.
- Natali, A.N., Meri, E.A., 1989. A review of the biomechanical properties of bone as a material. *J. Biomed. Eng.* 11 (4), 266–276.
- Nguyen, T.L., Hall, S.A., Vacher, P., Viggiani, G., 2011. Fracture mechanisms in soft rock: identification and quantification of evolving displacement discontinuities by extended digital image correlation. *Tectonophysics* 503 (1–2), 117–128.
- Op Den Buijs, J., Dragomir-Daescu, D., 2011. Validated finite element models of the proximal femur using two-dimensional projected geometry and bone density. *Comput. Methods Progr. Biomed.* 104 (2), 168–174.
- Østbyhaug, P.O., Klaksvik, J., Romundstad, P., Aamodt, A., 2009. An in vitro study of the strain distribution in human femora with anatomical and customised femoral stems. *J. Bone Jt. Surg. Br.* 91 (5), 676–682.
- Ovryn B., 1993. Whole-field displacement and strain measurements: application to biomechanics In: *Proceedings of the SPIE 1889, Holography, Interferometry, and Optical Pattern Recognition in Biomedicine III*, pp. 134–148.
- Palanca, M., Tozzi, G., Cristofolini, L., Viceconti, M., Dall'Ara, E., 2015. 3D local measurements of bone strain and displacement: comparison of three digital volume correlation approaches. *J. Biomech. Eng.* 137 (7), 071006.
- Pan, B., Qian, K., Anand, H.X., 2009. Two-dimensional digital image correlation for in-plane displacement and strain measurement: a review. *Meas. Sci. Technol.* 20 (6), 62001.
- Peng, L., Bai, J., Zeng, X., Zhou, Y., 2006. Comparison of isotropic and orthotropic material property assignments on femoral finite element models under two loading conditions. *Med. Eng. Phys.* 28 (3), 227–233.
- Perry, C.C., 1986. Strain-gage reinforcement effects on orthotropic materials. *Exp. Tech.* 10 (2), 20–24.
- Peters, W., Ranson, W., 1982. Digital imaging techniques in experimental stress analysis. *Opt. Eng.* 21 (3), 213427.
- Pratt, D.J., Bowker, P., Wardlaw, D., McLauchlan, J., 1979. Load measurement in orthopaedics using strain gauges. *J. Biomed. Eng.* 1 (4), 287–296.
- Prendergast, P., 1997. Finite element models in tissue mechanics and orthopaedic implant design. *Clin. Biomech.* 12 (6), 343–366.
- Reikeras, O., Aarnes, G.T., Steen, H., Ludvigsen, P., Sagvolden, G., 2011. Differences in external and internal cortical strain with prosthesis in the femur. *Open Orthop. J.* 5, 379–384.
- Roberts, B.C., Perilli, E., Reynolds, K.J., 2014. A review on the application of the digital volume correlation technique for the measurement of displacement and strain fields in bone. *J. Biomech.* 47 (5), 923–934.
- Roberts, V.L., 1966. Strain-gage techniques in biomechanics. *Exp. Mech.* 6 (3), 19A–22A.
- Robling, A.G., Castillo, A.B., Turner, C.H., 2006. Biomechanical and molecular regulation of bone remodeling. *Annu. Rev. Biomed. Eng.* 8, 455–498.
- Roux, S., Réthoré, J., Hild, F., 2009. Digital image correlation and fracture: an advanced technique for estimating stress intensity factors of 2D and 3D cracks. *J. Phys. D: Appl. Phys.* 42 (21), 214004.
- Sutton, M., Wolters, W., Peters, W., Ranson, W., McNeill, S., 1983. Determination of displacements using an improved digital correlation method. *Image Vis. Comput.* 1 (3), 133–139.
- Sutton, M.A., 2007. Three-dimensional digital image correlation to quantify deformation and crack-opening displacement in ductile aluminum under mixed-mode I/III loading. *Opt. Eng.* 46 (5), 051003.
- Sutton, M.A., Orteu, J.J., Schreier, H., 2009. *Image Correlation for Shape, Motion and Deformation Measurements: Basic Concepts, Theory and Applications*. Springer, USA.
- Tang, T., Ebacher, V., Crompton, P., Guy, P., McKay, H., Wang, R., 2015. Shear deformation and fracture of human cortical bone. *Bone* 71, 25–35.
- Viceconti, M., Olsen, S., Nolte, L.-P., Burton, K., 2005. Extracting clinically relevant data from finite element simulations. *Clin. Biomech.* 20 (5), 451–454.

- Vishay Micro-Measurements, 2005. Surface preparation for strain gage bonding. Application Note B-129-8.
- Webster, D., Müller, R., 2011. In silico models of bone remodeling from macro to nano – from organ to cell. Wiley Interdiscipl. Rev. Syst. Biol. Med. 3 (2), 241–251.
- Werneck M., Allil R., Ribeiro B., de Nazaré F., A Guide to Fiber Bragg Grating Sensors, pp. 1–24, 2013.
- Zani, L., Erani, P., Grassi, L., Taddei, F., Cristofolini, L., 2015. Strain distribution in the proximal Human femur during in vitro simulated sideways fall. J. Biomech..
- Zysset, P., 2003. A review of morphology–elasticity relationships in human trabecular bone: theories and experiments. J. Biomech. 36 (10), 1469–1485.

Paper II

Available online at www.sciencedirect.com

SciVerse ScienceDirect

www.elsevier.com/locate/jmbbm

Research Paper

Experimental validation of finite element model for proximal composite femur using optical measurements

Lorenzo Grassi^{a,*}, Sami P. Väänänen^b, Saber Amin Yavari^c, Harrie Weinans^{c,d},
Jukka S. Jurvelin^b, Amir A. Zadpoor^c, Hanna Isaksson^a

^aDivision of Solid Mechanics, and Department of Orthopedics, Lund University, Lund, Sweden

^bDepartment of Applied Physics, University of Eastern Finland, Kuopio, Finland

^cFaculty of Mechanical, Maritime, and Materials Engineering, Delft University of Technology, Delft, The Netherlands

^dDepartment of Orthopedics, Erasmus Medical Center, Rotterdam, The Netherlands

ARTICLE INFO

Article history:

Received 7 December 2012

Received in revised form

31 January 2013

Accepted 4 February 2013

Available online 19 February 2013

Keywords:

Digital image correlation

Composite femur

Finite element

Bone fracture

ABSTRACT

Patient-specific finite element models have been used to predict femur strength and fracture risk in individuals. Validation of the adopted finite element modelling procedure against mechanical testing data is a crucial step when aiming for clinical applications.

The majority of the works available in literature used data from strain gages to validate the model, thus having up to 15 experimental measurements. Optical techniques, such as digital image correlation, can help to improve the models by providing a continuous field of deformation data over a femoral surface. The main objective of this study was to validate finite element models of six composite femora against strain data from digital image correlation, obtained during fracture tests performed in quasi-axial loading configuration. The finite element models were obtained from CT scans, by means of a semi-automatic segmentation. The principal strains both during the elastic phase and close to the fracture were compared, and showed a correlation coefficient close to 0.9. In the linear region, the slope and intercept were close to zero and unity, while for the case when fracture load was simulated, the slope decreased somewhat. The accuracy of the obtained results is comparable with the state-of-the-art literature, with the significant improvement of having around 50,000 data points for each femur. This large number of measurements allows a more comprehensive validation of the predictions by the finite element models, since thousand of points are tracked along the femoral neck and trochanter region, i.e., the sites that are most critical for femur fracture. Moreover, strain measurement biases due to the strain gage reinforcement effect, were avoided. The combined experimental–numerical approach proved to be ready for application to *in-vitro* tests of human cadaver femurs, thus helping to develop a suitable mechanistic fracture risk criterion.

© 2013 Elsevier Ltd. All rights reserved.

*Corresponding author. Tel.: +46 46 222 79 92.

E-mail addresses: lorenzo.grassi@solid.lth.se, loregrassi@gmail.com (L. Grassi).

1. Introduction

Hip fractures are known to be a major trauma, especially affecting the elderly and resulting in a dramatic increase in patient morbidity and mortality (Roth et al., 2010). Hip fracture incidence increases exponentially with age (Burge et al., 2007) due to concurrent increase in fall rate (Berry and Miller, 2008; Parkkari et al., 1999) and decrease in bone strength (Courtney et al., 1995; Keaveny et al., 2010). Osteoporosis is a skeletal disease that causes an increased bone resorption, thus significantly reducing bone strength (Armas and Recker, 2012). Current methods for osteoporosis diagnosis (Cawthon et al., 2009; Svejme et al., 2012), or prediction of fracture risk (Kanis et al., 2005) that are mainly based on epidemiological parameters, are not sufficient to detect all at risk (Lekamwasam, 2010; Silverman and Calderon, 2010). For example, they lack characterization of spatial distribution of bone mineral density in all three dimensions. Subject-specific finite element (FE) models based on clinical imaging data have been proposed to overcome such limitation and assess bone strength (Cong et al., 2011; Schileo et al., 2008; Trabelsi et al., 2009; Viceconti et al., 2004). They provide a mechanistic model accounting for the 3D geometry of bone, its material property distribution, and also the different loading conditions.

The proposed FE models need to be validated thoroughly in the laboratory before being tested in clinical practice (Viceconti et al., 2005). Although several earlier studies using FE models have directly provided bone strength assessment using strain- or stress-based criteria (Keyak et al., 2001; Koivumäki et al., 2010), an *in-vitro* validation in terms of stress/strain prediction accuracy is required (Cristofolini et al., 2010). These previous studies achieved a high level of accuracy by validating their FE models with experimentally measured principal strains (Bessho et al., 2007; Taddei et al., 2007; Trabelsi et al., 2009). The determination coefficient between experimental measured principal strains and FE predicted strains reported in the above cited papers ranges from 0.92 (Bessho et al., 2007) to 0.96 (Trabelsi et al., 2009). Only Bessho et al. (2007) performed both experiments and FE simulations up to the fracture level, despite using a loading rate (0.5 mm/min) very far from an expected physiological value (Al Nazer et al., 2012).

Nevertheless, in the above-mentioned studies, the reported values for accuracy of bone strain prediction were calculated using a limited number of data points, i.e., up to 15 *in-vitro* measurements collected by using strain gauges (SG) during tests in quasi-axial loading configurations. Increasing the number of data points and acquiring strain distribution over the entire anatomical surface using thousand of measurements would allow for a more comprehensive validation of the FE models and improve the understanding of the tension/compression strain state occurring under loading.

Recently, optical techniques like digital image correlation (DIC) have been used to measure superficial strains over geometrically irregular surfaces (Chuang et al., 2011; Moerman et al., 2009; Szték et al., 2010), such as the surface of the human femur (Dickinson et al., 2011; Op Den Buijs and Dragomir-Daescu, 2011). The basic idea of DIC is to track the position of the same set of physical points shown in a reference image and in one (or more) deformed image.

Then, the recorded sets of coordinates can be used to calculate the strains, using different kind of algorithms (Bruck et al., 1989; Luu et al., 2011; Ma et al., 2012; Pan et al., 2012, 2009; Su and Anand, 2003). Although the first applications of DIC in material testing date back to 1985 (Bruck et al., 1989; Chu et al., 1985), the method has been introduced more recently in experimental biomechanics (Bay, 1995; Benecke et al., 2009; Ning et al., 2011; Verhulp et al., 2004; Zhang and Arola, 2004). One of the main advantages of DIC is the possibility to describe a continuous field of deformations by simultaneously tracking thousands of points on a surface. This technique can also mitigate the reinforcement due to the non-negligible stiffness of the sensor mounted onto (or embedded into) the tested material. This can be a particular issue when using SGs (Ajovalasit et al., 2010; Beatty and Chewning, 1979; Perry, 1986) on regions with low elastic modulus, such as the femoral neck surface.

To the authors knowledge, DIC has been adopted only a few times in combination with FE modelling for validation purposes of human femur mechanical behaviour, either using composite (Dickinson et al., 2011) or cadaver (Op Den Buijs and Dragomir-Daescu, 2011) specimens. Dickinson et al. (2011) tested one composite femur bone in quasi-axial configuration at different load magnitudes and recorded the strains using DIC. DIC data were averaged over a 5 mm² area, providing 25 measurements. The corresponding FE models were then validated in terms of von Mises strains. Op Den Buijs and Dragomir-Daescu (2011) acquired 2D DIC measurements from 22 cadaver human femora, and used the experimental data to validate 13 bi-dimensional FE models in terms of overall stiffness (9 specimens were used for tuning the simulation parameters). Therefore, there is currently no study in which FE results are validated against 3D principal strain measurements over an entire (that is, using thousand data points) surface of proximal femur. An evaluation of the principal strain would allow a better assessment of the tension/compression state with respect to von Mises strains. Furthermore, it would enable a direct comparison of the achieved strain prediction results with those reported in the literature (Bessho et al., 2007; Schileo et al., 2008; Trabelsi et al., 2011), and facilitate future developments of strain-based fracture criteria.

Recently, an extensive experimental benchmark employing optical strain measurements was performed by our group (Väänänen et al., 2012a). Six composite human femora were tested until fracture using a quasi-axial loading configuration, and a deformation gradient field was recorded with a DIC system. Composite bones include of a cortical part made of fiber-reinforced epoxy, and a cancellous part made of a solid rigid polyurethane foam, in order to mimic the mechanical properties of human bones. Use of composite femora instead of cadaver samples was preferred, since one of the objectives was to examine the extent of the reliability and repeatability of the DIC measurements. With composite femora we could isolate the effects of inter-individual variations in samples from the effects of the physical mechanism of deformation.

As a consequence, the aim of the present study was to provide a validation of a FE modelling technique against full-field surface principal strains measured by DIC over six similar composite human femur bones, using an automatic procedure for data spatial registration and comparison.

2. Material and methods

Six 4th generation medium-sized composite femur bones (model 3403, Sawbones, Pacific Research Laboratories Inc., Vashon, USA) were used. The composite bones were imaged with a CT scanner (SOMATOM Definition Flash, Siemens, Munich, Germany) in air, with a resolution ranging from 0.24 to 0.29 mm, and a slice thickness of 0.4 mm.

2.1. Experimental measurements

Details about the experimental measurements are minutely described in Väänänen et al. (2012a), and only briefly reported here. Femora were cut 15 cm below the minor trochanter and the distal end was embedded in an aluminium pot (height and diameter 5 cm, wall thickness 3 mm) that was filled with epoxy (Technovit 4071, Heraeus Kulzer, Wehrheim, Germany). The anterior aspect of each composite femur was painted with a white background spray layer, and a black random speckle pattern was applied with an airbrush. The resulting surface was dividable into about 50,000 uniquely traceable points. Each femur was loaded until fracture in a quasi-axial configuration, with a constant displacement rate of 1.0 mm/min (corresponding to a global strain rate of 0.0058 min^{-1}). The deformations were recorded throughout the whole mechanical testing process by two digital cameras (Limes Messtechnik und Software GmbH, Krefeld, Germany, resolution 4 Mpixel, maximum frame rate 7 Hz, image correlation processing done with Vic-3D 2007 software, Correlated Solutions, Inc., USA), at 4 frames per second, while the applied load was recorded at 15 frames per second by the uniaxial load cell (maximum load 20 kN, Zwick-Roell, Germany) placed on the upper effector of the loading machine.

2.2. Finite element modeling

Triangulated geometry and experimental reference system orientation of the composite bones were retrieved using a semi-automatic segmentation procedure based on an active contour method (Yushkevich et al., 2006). Non-Uniform Rational B-Splines (NURBS) models were created from the triangulated geometries through a reverse engineering process (Rhino v4.0, Robert McNeel & Associates, Seattle, USA), and meshes with 10-noded unstructured tetrahedral elements (average 148,894 nodes, 98,662 elements, mean element volume 2.75 mm^3) were built (Hypermesh v11.0, Altair Engineering, Inc., Troy, USA). Linear elastic transversely orthotropic material properties were applied, according to the material

data provided by the manufacturer (Table 1). The principal axes of orthotropy were modelled to be parallel to the anatomical shaft axis and neck axis in the shaft and neck region, respectively (Fig. 1). The shaft axis was determined as the line passing through the centroids of the two shaft sections: the first taken at the minor trochanter level and the second at the most distal level. To define the neck axis, an anatomical landmark corresponding to the centre of the femoral head was first determined as the centre of the largest

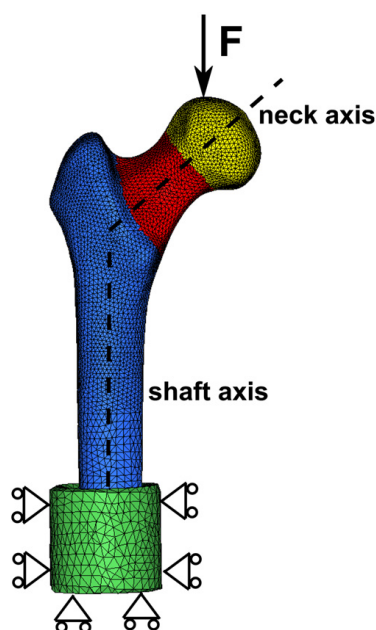


Fig. 1 – Material properties and boundary conditions in the FE model. Isotropic material properties were applied to the epoxy pot (depicted in green), the internal spongy material, and the femoral head region (in yellow). Orthotropic material properties were assigned to the femoral shaft (in blue) and neck (in red) region, with principal axes of orthotropy as shown. The force was applied on the top of the femoral head, while the distal epoxy was constrained to mimic the experimental conditions. (For interpretation of the references to color in this figure legend, the reader is referred to the web version of this article.)

Table 1 – Material properties for the cortical and cancellous part of the synthetic bone in use. Material property data are based on ASTM D-638, D-695, and D-1621 (<http://www.sawbones.com>).

	Cortical, longitudinal tensile	Cortical, longitudinal compressive	Cortical, transverse tensile	Cancellous, compressive
Density [g/cm^3]	1.64	1.64	1.64	0.27
Young's modulus [MPa]	16,000	16,700	10,000	155
Poisson's ratio	0.26	0.26	0.26	0.3

sphere that could be fitted into the femoral head. Then, the segmented dataset was rotated in order to align the neck region to the first axis of the CT reference system, and the centroid was calculated for all the segmented CT slices in the femoral neck region. The femoral neck axis was defined as the line passing through the centre of the femoral head, providing the best least-square fit of all the femoral neck slice centroids. The search was iterated until the location of the neck axis converged (Väänänen et al., 2011b). A custom Matlab (v7.12, The Mathworks, Inc., Natick, USA) code was used to identify the needed landmarks and anatomical axes for one femur, and to apply rigid registration of the coordinates of the landmarks in order to fit them to the geometries of all six femora.

A load of 3500 N was chosen for the FE modelling from the experimentally recorded linear region of the force-displacement curve. This load was chosen as it represented the end of the linear region of the curve in most of the samples. Additionally, the load at fracture from the mechanical test was analyzed for each bone (range 4719–6747 N). The load cases were applied to the FE models, and the simulations were solved using Abaqus standard solver (v6.9.1, Dassault Systemes HQ, Vélizy-Villacoublay, France).

2.3. Validation procedure

From the DIC measurements, a cloud of about 50,000 points over the anterior surface of each femur was available for deformation measurements. Each cloud was registered to the corresponding FE mesh, using a Matlab code based on a genetic optimization algorithm (mean node-to-node distance 0.8 mm, maximum node-to-node distance 3.9 mm). Experimental measurement points with a tracking quality parameter greater than two times the provided optimal value (2% of the total) were removed from the analysis according to the recommendations by the Vic-3D 2007 software guidelines. The DIC measurements were then averaged over a spherical volume of interest (VOI) to match the DIC points and FE mesh elements. First, the smallest sphere circumscribing each tetrahedral element was determined. From this, the VOI was defined as a spherical region

with the same coordinates of the centre, and with double the radius. Prediction accuracy was finally evaluated by comparing principal strains. Data from the six femurs were analyzed both separately and after pooling, and linear regression analysis between experimental and the FE calculated values was performed. Determination coefficient (R^2), slope and intercept, root mean square error (RMSE), and peak error of the FE predictions were calculated. Bland-Altman plots (Bland and Altman, 1999) were also calculated in order to provide a graphical interpretation of the agreement between experiments and FE prediction. Plots were drawn both for the 3500 N load and for the fracture load, and the 95% limit of agreement was depicted over each plot.

3. Results

3.1. Comparison of the 3500 N load case

When all 6 bones were pooled, the FE models predicted the experimentally measured principal strains at 3500 N load with a coefficient of determination, R^2 , of 0.87, a slope of 0.84 and an intercept close to zero (Fig. 2). RMSE was around 900 $\mu\epsilon$, with peak errors in the order of 96%, those circumscribed to only a few points (Fig. 2). The result for each individual bone highlighted some variation in the accuracy of strain prediction (Fig. 3). One of the six femora showed a lower slope (bone number 3, individual validations reported in Fig. 4). This bone was an outlier in the experimental results, and by removing it from the pooled data validation (please see subsequent discussion), values of correlation coefficient and slope were increased to 0.91 and 0.94, respectively, while the RMSE decreased to less than 700 $\mu\epsilon$ (Fig. 5).

3.2. Comparison of the fracture load case

When loading the bones until fracture, capacity of the FE model to predict the experimental findings decreased somewhat (Fig. 6). The slope of the linear correlation decreased to

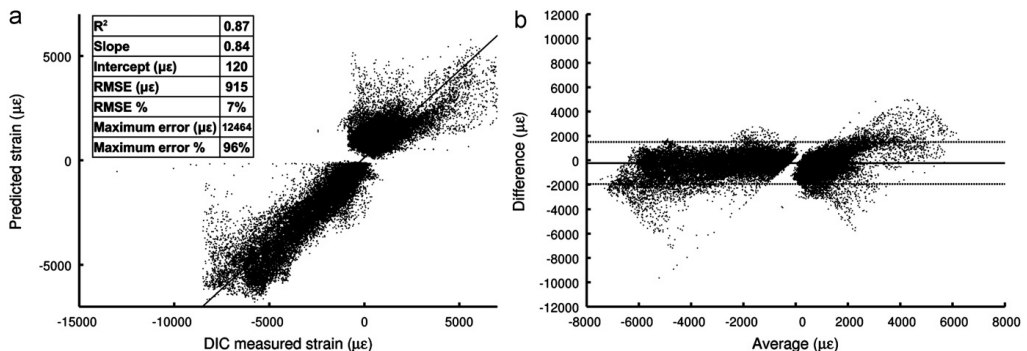


Fig. 2 – Prediction accuracy of the principal strains in the six bones pooled together at 3500 N load: linear correlation (a), and Bland-Altman plot (b). The dotted lines represent the 95% confidence interval.

0.76 for the six bones pooled, with correlation coefficient equal to 0.87. RMSE was 1800 $\mu\epsilon$, while the peak errors were in the same percentage order of magnitude as the results

obtained at 3500 N load (Fig. 6a). When removing the one outlier in experimental data from the validation, the slope was 0.82, with a correlation coefficient of 0.89 (Fig. 6c).

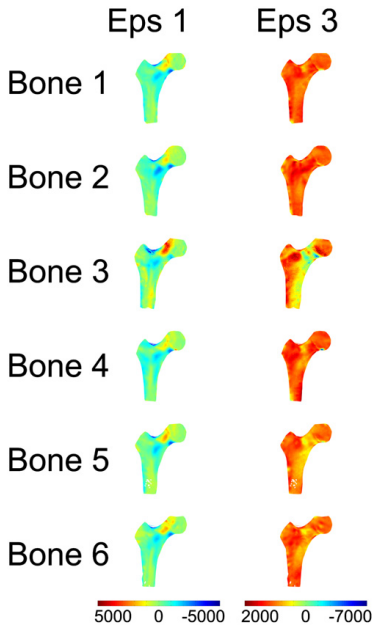


Fig. 3 – Maps for the prediction error in each femur for the first principal strain (μ strain, left column) and the third principal strain (μ strain, right column). (For interpretation of the references to color in this figure legend, the reader is referred to the web version of this article.)

4. Discussion

The aim of the present work was to develop an automatic procedure for reliable validation of subject-specific FE models against experimental measurements from a DIC system.

The proposed validation framework can directly take the results file of the FE simulation as an input and provide the accuracy metrics information as an output. 50,000 experimental measurements from each femur were collected for validation of the FE models, which brings it up to more than 600,000 measurements overall. This is, to the authors' knowledge, one of the greatest number of data points used for validation for this kind of application. The principal strains predicted by the FE simulations proved to be highly correlated with the experimental recordings from the DIC system. Determination coefficient was close to 0.9 for both the elastic region and the fracture load cases, with the slope and the intercept close to unity and zero, respectively, for 5 out of the 6 bones tested. RMSE was below 7% both at 3500 N and at the fracture load, while higher errors between FE predictions and experiments were circumscribed to a few points, as depicted in Fig. 3.

The validation results in this study in the elastic field region indicated only a minor worsening of the accuracy parameters with respect to the state-of-the-art literature (Bessho et al., 2007; Schileo et al., 2008; Trabelsi et al., 2009), which were obtained using less than 15 SG measurements from each cadaver bone tested. Those studies reported the coefficient of determination to be between 0.92 and 0.96 for the elastic field phase of bone mechanical behaviour. Excluding the outlier composite bone in the experiments,

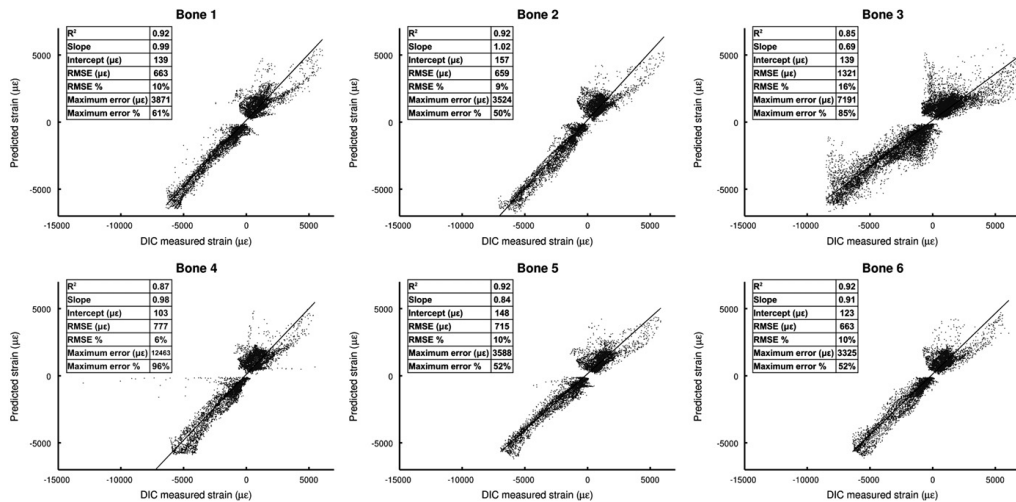


Fig. 4 – results of the linear regression analyses for each individual bone at 3500 N load.

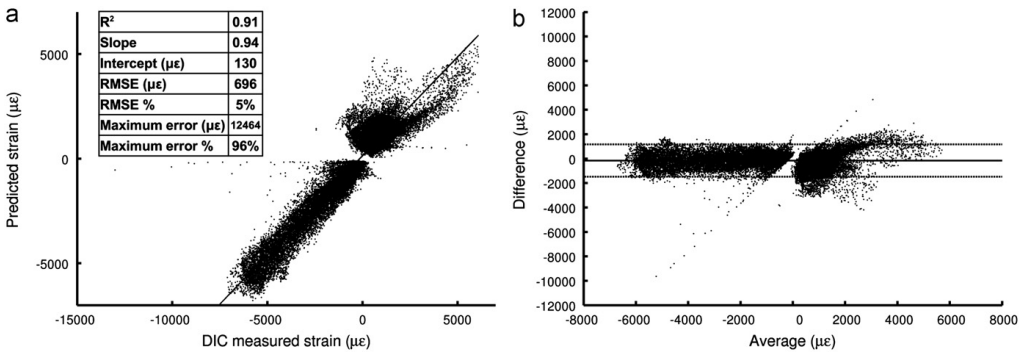


Fig. 5 – Prediction accuracy for the principal strains in five bones pooled together at 3500 N load. The experimental outlier, bone number 3 was left out from the validation. Linear correlation is depicted in (a), and Bland–Altman plot in (b). The dotted lines represent the 95% confidence interval.

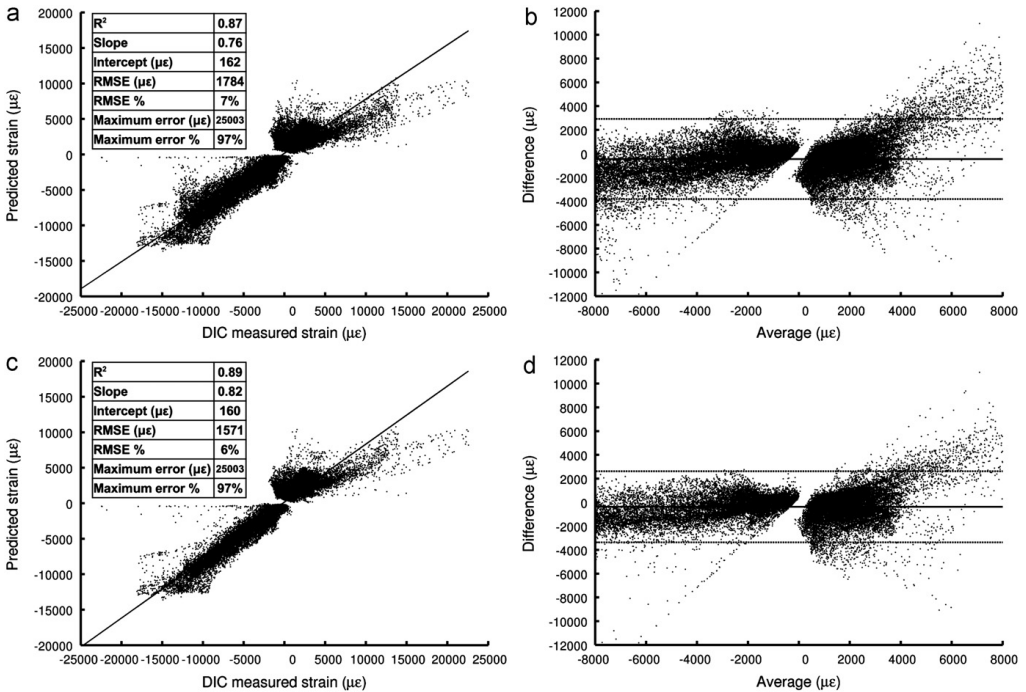


Fig. 6 – Linear correlation (a) and Bland–Altman plot (b) for the six bones pooled together when a load equivalent to the fracture load was applied to each specimen. The same plots are provided with the outlier bone excluded (linear correlation and Bland–Altman plot in (c) and (d) sector, respectively).

the present study reported a coefficient of determination of 0.91, with slope and intercept of the linear correlation very close to unity (0.94) and zero (130 µε), respectively. Inspection of the Bland–Altman plots (Figs. 2 and 5b) shows how specimen number 3 contributed to increase the standard

deviation between experiments and numerical calculation. Furthermore, after excluding bone 3 from the computation, the Bland–Altman plot for 5 bones (Fig. 5b) showed that almost all the points with negative compressive strains were within the confidence interval region, whereas in the

tensile strain region the points are only slightly more spread.

The advantage of our study is primarily the large number of measurements, which allowed us to perform a more comprehensive assessment of the FE predictions. By tracking thousand of points in the femoral neck and trochanter region, much more information is obtained from the sites of the femur that are most prone to fractures (Arakaki et al., 2011). The spatial resolution of DIC is greater than the resolution achievable with strain gages, thus it allows tracking of the peak strain values more accurately. Besides, strain measurement biases related to the SG reinforcement effect (Ajovalasit et al., 2010; Beatty and Cheung, 1979; Perry, 1986), are likely to be strongly mitigated by using only a thin paint layer. The Matlab-based validation framework provided automatic registration of the DIC cloud, averaging of the experimental measurements, and strain prediction accuracy parameters calculation.

Validation of the FE models at the fracture load was also provided. A reduction in the values of quality parameters was observed, as compared to the data at 3500 N. While the correlation coefficient was still around 0.9, the RMSE was twice the value obtained at 3500 N. Further, the measured strains were underestimated by 20%. This decrease in prediction agreement is likely to be due to the post-yield phenomena occurred during experiments in proximity of the fracture (Gardner et al., 2010; Zdero et al., 2010), which was not accounted for when developing the FE models. The difference between the slope of the cloud of positive strain points (first quadrant in Fig. 6), and slope of the cloud of negative strain points (third quadrant in Fig. 6) supports this hypothesis. Also when looking at the Bland–Altman plots for the fracture load case (Fig. 6b and d), the spread of the positive strain data appears to be more marked, thus corroborating the hypothesis of the occurrence of some plastic strain phenomena before the fracture.

To the authors' best knowledge the only comparable work available in literature was provided by Dickinson et al. (2011). With respect to the aforementioned work, and from an experimental perspective, the current work presented a much greater number of DIC measurements (50,000 measurements from each of the six composite femurs employed, instead of 1875 measurements from one composite bone) collected at a greater load magnitude (3500 N and fracture load, against a maximum applied load of 1200 N). From a computational point of view, a validation in terms of principal strains (instead of von Mises) is presented, thus permitting a more quantitative assessment of tension and compression behaviour. Last, the FE models presented in the present work achieved a higher strain prediction accuracy. Dickinson et al. (2011) reported a value of 0.86 for coefficient of determination (against 0.91 for the present study, when the outlier bone is excluded from the computation), with a slope of the regression line equal to 0.9 (0.94 in the present study). This improvement in the accuracy of strain prediction is likely to be due to the implementation of orthotropic material properties in the FE modelling procedure.

A similar study involving validation of femoral FE models against DIC data was also provided by Op Den Buijs and Dragomir-Daescu (2011), using human cadaver femora. Nevertheless, in that study the analysis was limited to 2D for both the FE models and the DIC recordings (only one video

camera was employed). Moreover, DIC measurements were used for validating models in terms of their stiffness, while experimentally measured strains were only qualitatively compared to the FE predicted strains.

Composite femur bones were employed in this study, since the scope was to evaluate the effectiveness, repeatability and automation of the modelling and validation procedures. Despite their synthetic nature, composite bones have a similar mechanical behaviour as cadaver bones (Cristofolini et al., 1996), while exhibiting a very low intra- and inter-specimen variability (Heiner, 2008). Use of the cadaver bones with great inter-sample variability (Cristofolini et al., 2009) could have been a significant source of uncertainties of the results obtained. Instead, use of six nearly identical composite bones provided better means to estimate variability in experimental findings, and their effect on the FE modelling procedure and accuracy. Thus, strong indications of the reliability and repeatability of both the experimental setup (Väänänen et al., 2012a) and the FE modelling and validation framework were provided, representing a fundamental milestone towards application of the proposed methodology in *in-vitro* testing on cadaver bones.

A limitation of the study is the presence of smaller areas or single points that experience very high errors. Those high errors are located either at the boundaries of the DIC cloud, or in proximity of regions with markedly high curvature. The same phenomenon was pointed out by Dickinson et al. (2011). Further tuning of the DIC acquisition parameters, speckle pattern, and hardware update are expected to reduce this problem.

As a second limitation, one of the six femurs reported a noteworthy underestimation of the FE predicted strains with respect to the experimental measurements. Analysis of the raw data from the mechanical tests indicated that mechanics of this particular bone was exceptional compared to that of the remaining five bones. It exhibited both loading and strain curves that were highly different. In particular, the strain levels at the same load magnitude were higher than in the other specimens (Väänänen et al., 2012a). This is most likely the reason why the reported slope in this bone is far from unity. However, further investigations are ongoing to better understand what exactly occurred in that specific composite bone specimen.

The lack of a more comprehensive modelling of the fracture data (including post-yield phenomena etc.), despite available experimental data at fracture should also be acknowledged as a limitation. However, we chose to focus the study on the data from all the samples at a fixed load magnitude of 3500 N. This was because at that load, all the bones were still behaving linearly. Modelling the post-yield material non-linearity of composite bones close to the fracture event was considered outside the scope of the present study, because the post-yield behaviour of composite bones is likely quite different from the post-yield behaviour of human bones.

Despite those limitations, the proposed combined experimental and numerical method proved to be ready for direct application in human cadaver bones testing. Validation of subject-specific FE models of human cadaver bones against DIC measurements has already been planned as a future work. This will allow an accurate tuning of the FE modelling

procedure, and also provide the means for a comprehensive analysis of the post-yield behaviour of human bones. Taken together, this will help to develop a reliable subject-specific fracture risk criterion.

Acknowledgements

Funding from the Swedish Research Council (2011-5064), the Crafoord foundation, Academy of Finland (14088), and University of Eastern Finland (929711) are gratefully acknowledged.

REFERENCES

- Ajvalasit, A., Fragapane, S., Zuccarello, B., 2010. Local reinforcement effect of embedded strain gauges. EPJ Web of Conferences, 6.
- Al Nazer, R., Lanovaz, J., Kawalilak, C., Johnston, J.D., Kontulainen, S., 2012. Direct in vivo strain measurements in human bone—a systematic literature review. *Journal of Biomechanics* 45, 27–40.
- Arakaki, H., Owan, I., Kudoh, H., Horizono, H., Arakaki, K., Ikema, Y., Shinjo, H., Hayashi, K., Kanaya, F., 2011. Epidemiology of hip fractures in Okinawa, Japan. *Journal of Bone and Mineral Metabolism* 29, 309–314.
- Armas, L., Recker, R.G., 2012. Pathophysiology of osteoporosis: new mechanistic insights. *Endocrinology and metabolism clinics of North America*, 41, 475–486.
- Bay, B.K., 1995. Texture correlation: a method for the measurement of detailed strain distributions within trabecular bone. *Journal of Orthopaedic Research: Official Publication of the Orthopaedic Research Society* 13, 258–267.
- Beatty, M.F., Chewing, S.W., 1979. Numerical analysis of the reinforcement effect of a strain gage applied to a soft material. *International Journal of Engineering Science* 17, 907–915.
- Benecke, G., Kerschmitzki, M., Fratzl, P., Gupta, H.S., 2009. Digital image correlation shows localized deformation bands in inelastic loading of fibrolamellar bone. *Journal of Materials Research* 24, 421–429.
- Berry, S.D., Miller, R.R., 2008. Falls: epidemiology, pathophysiology, and relationship to fracture. *Current Osteoporosis Reports* 6, 149–154.
- Bessho, M., Ohnishi, I., Matsuyama, J., Matsumoto, T., Imai, K., Nakamura, K., 2007. Prediction of strength and strain of the proximal femur by a CT-based finite element method. *Journal of Biomechanics* 40, 1745–1753.
- Bland, J.M., Altman, D.G., 1999. Measuring agreement in method comparison studies. *Statistical Methods in Medical Research* 8, 135–160.
- Bruck, H.A., McNeill, S.R., Sutton, M.A., Peters, W.H., 1989. Digital image correlation using Newton-Raphson method of partial differential correction. *Experimental Mechanics* 29, 261–267.
- Burge, R., Dawson-Hughes, B., Solomon, D.H., Wong, J.B., King, A., Tosteson, A., 2007. Incidence and economic burden of osteoporosis-related fractures in the United States, 2005–2025. *Journal of Bone and Mineral Research: The Official Journal of the American Society for Bone and Mineral Research* 22, 465–475.
- Cawthon, P.M., Ewing, S.K., McCulloch, C.E., Ensrud, K.E., Cauley, J.A., Cummings, S.R., Orwoll, E.S., 2009. Loss of hip BMD in older men: the osteoporotic fractures in men (MrOS) study. *Journal of Bone and Mineral Research: The Official Journal of the American Society for Bone and Mineral Research* 24, 1728–1735.
- Chu, T.C., Ranson, W.F., Sutton, M.A., 1985. Applications of digital-image-correlation techniques to experimental mechanics. *Experimental Mechanics* 25, 232–244.
- Chuang, S.-F., Chang, C.-H., Chen, T.Y.-F., 2011. Contraction behaviors of dental composite restorations—finite element investigation with DIC validation. *Journal of the Mechanical Behavior of Biomedical Materials* 4, 2138–2149.
- Cong, A., Buijs, J.O., Den, Dragomir-Daescu, D., 2011. In situ parameter identification of optimal density-elastic modulus relationships in subject-specific finite element models of the proximal femur. *Medical Engineering & Physics* 33, 164–173.
- Courtney, A.C., Wachtel, E.F., Myers, E.R., Hayes, W.C., 1995. Age-related reductions in the strength of the femur tested in a fall-loading configuration. *Journal of Bone and Joint Surgery. American Volume (Boston, MA)* 77, 387–395.
- Cristofolini, L., Juszczyc, M., Taddei, F., Viceconti, M., 2009. Strain distribution in the proximal human femoral metaphysis. *Proceedings of the Institution of Mechanical Engineers. Part H, Journal of Engineering in Medicine* 223, 273–288.
- Cristofolini, L., Schileo, E., Juszczyc, M., Taddei, F., Martelli, S., Viceconti, M., 2010. Mechanical testing of bones: the positive synergy of finite-element models and in vitro experiments. *Philosophical Transactions Series A, Mathematical, Physical, and Engineering Sciences* 368, 2725–2763.
- Cristofolini, L., Viceconti, M., Cappello, A., Toni, A., 1996. Mechanical validation of whole bone composite femur models. *Journal of Biomechanics* 29, 525–535.
- Dickinson, A.S., Taylor, A.C., Ozturk, H.M.B., 2011. Experimental validation of a finite element model of the proximal femur using digital image correlation and a composite bone model. *Journal of Biomechanical Engineering* 133, 014504.
- Gardner, M.P., Chong, A.C.M., Pollock, A.G., Wooley, P.H., 2010. Mechanical evaluation of large-size fourth-generation composite femur and tibia models. *Annals of Biomedical Engineering* 38, 613–620.
- Heiner, A.D., 2008. Structural properties of fourth-generation composite femurs and tibias. *Journal of Biomechanics* 41, 3282–3284.
- Kanis, J.A., Borgstrom, F., De Laet, C., Johansson, H., Johnell, O., Jonsson, B., Oden, A., Zethraeus, N., Pfleger, B., Khaltaev, N., 2005. Assessment of fracture risk. *Osteoporosis International* 16, 581–589.
- Keaveny, T.M., Kopperdahl, D.L., Melton, L.J., Hoffmann, P.F., Amin, S., Riggs, B.L., Khosla, S., 2010. Age-dependence of femoral strength in white women and men. *Journal of Bone and Mineral Research: The Official Journal of the American Society for Bone and Mineral Research* 25, 994–1001.
- Keyak, J.H., Skinner, H.B., Fleming, J.A., 2001. Effect of force direction on femoral fracture load for two types of loading conditions. *Journal of Orthopaedic Research* 19, 539–544.
- Koivumäki, J.E.M., Thevenot, J., Pulkkinen, P., Salmi, J.A., Kuhn, V., Lochmüller, E.-M., Link, T.M., Eckstein, F., Jämsä, T., 2010. Does femoral strain distribution coincide with the occurrence of cervical versus trochanteric hip fractures? An experimental finite element study. *Medical & Biological Engineering & Computing* 48, 711–717.
- Lekamwasam, S., 2010. Application of FRAX model to Sri Lankan postmenopausal women. *Journal of Clinical Densitometry: The Official Journal of the International Society for Clinical Densitometry* 13, 51–55.
- Luu, L., Wang, Z., Vo, M., Hoang, T., Ma, J., 2011. Accuracy enhancement of digital image correlation with B-spline interpolation. *Optics Letters* 36, 3070–3072.
- Ma, S., Zhao, Z., Wang, X., 2012. Mesh-based digital image correlation method using higher order isoparametric elements. *The Journal of Strain Analysis for Engineering Design* 47, 163–175.

- Moerman, K.M., Holt, C. a, Evans, S.L., Simms, C.K., 2009. Digital image correlation and finite element modelling as a method to determine mechanical properties of human soft tissue in vivo. *Journal of Biomechanics* 42, 1150–1153.
- Ning, J., Braxton, V.G., Wang, Y., Sutton, M.A., Wang, Y., Lessner, S.M., 2011. Speckle patterning of soft tissues for strain field measurement using digital image correlation: preliminary quality assessment of patterns. *Microscopy and Microanalysis* 17, 81–90 (The Official Journal of Microscopy Society of America, Microbeam Analysis Society, Microscopical Society of Canada).
- Op Den Buijs, J., Dragomir-Daescu, D., 2011. Validated finite element models of the proximal femur using two-dimensional projected geometry and bone density. *Computer Methods and Programs in Biomedicine* 104, 168–174.
- Pan, B., Asundi, A., Xie, H., Gao, J., 2009. Digital image correlation using iterative least squares and pointwise least squares for displacement field and strain field measurements. *Optics and Lasers in Engineering* 47, 865–874.
- Pan, B., Wu, D., Yu, L., 2012. Optimization of a three-dimensional digital image correlation system for deformation measurements in extreme environments. *Applied Optics* 51, 4409.
- Parkkari, J., Kannus, P., Palvanen, M., Natri, A., Vainio, J., Aho, H., Vuori, I., Jarvinen, M., 1999. Majority of hip fractures occur as a result of a fall and impact on the greater trochanter of the femur: a prospective controlled hip fracture study with 206 consecutive patients. *Calcified Tissue International* 65, 183–187.
- Perry, C.C., 1986. Strain-gage reinforcement effects on orthotropic materials. *Experimental Techniques* 10, 20–24.
- Roth, T., Kammerlander, C., Gosch, M., Luger, T.J., Blauth, M., 2010. Outcome in geriatric fracture patients and how it can be improved. *Osteoporosis International* 21, S615–S619.
- Schileo, E., Dall'ara, E., Taddei, F., Malandrino, A., Schotkamp, T., Baleani, M., Viceconti, M., 2008. An accurate estimation of bone density improves the accuracy of subject-specific finite element models. *Journal of Biomechanics* 41, 2483–2491.
- Silverman, S.L., Calderon, A.D., 2010. The utility and limitations of FRAX: a US perspective. *Current Osteoporosis Reports* 8, 192–197.
- Su, C., Anand, L., 2003. A New Digital Image Correlation Algorithm for Whole-field Displacement Measurement. In: *Proceedings Singapore-MIT Alliance Symposium of Innovation in Manufacturing Systems and Technology*.
- Svejme, O., Ahlborg, H.G., Nilsson, J.-Å., Karlsson, M.K., 2012. Early menopause and risk of osteoporosis, fracture and mortality: a 34-year prospective observational study in 390 women. *BJOG: An International Journal of Obstetrics and Gynaecology* 119, 810–816.
- Sztfek, P., Vanleene, M., Olsson, R., Collinson, R., Pitsillides, A. a, Shefelbine, S., 2010. Using digital image correlation to determine bone surface strains during loading and after adaptation of the mouse tibia. *Journal of Biomechanics* 43, 599–605.
- Taddei, F., Schileo, E., Helgason, B., Cristofolini, L., Viceconti, M., 2007. The material mapping strategy influences the accuracy of CT-based finite element models of bones: an evaluation against experimental measurements. *Medical Engineering & Physics* 29, 973–979.
- Trabelsi, N., Yosibash, Z., Milgrom, C., 2009. Validation of subject-specific automated p-FE analysis of the proximal femur. *Journal of Biomechanics* 42, 234–241.
- Trabelsi, N., Yosibash, Z., Wutte, C., Augat, P., Eberle, S., 2011. Patient-specific finite element analysis of the human femur-A double-blinded biomechanical validation. *Journal of Biomechanics* 44, 1666–1672.
- Verhulp, E., Van Rietbergen, B., Huiskes, R., 2004. A three-dimensional digital image correlation technique for strain measurements in microstructures. *Journal of Biomechanics* 37, 1313–1320.
- Viceconti, M., Davinelli, M., Taddei, F., Cappello, A., 2004. Automatic generation of accurate subject-specific bone finite element models to be used in clinical studies. *Journal of Biomechanics* 37, 1597–1605.
- Viceconti, M., Olsen, S., Nolte, L.-P., Burton, K., 2005. Extracting clinically relevant data from finite element simulations. *Clinical Biomechanics (Bristol, Avon)* 20, 451–454.
- Väänänen, S.P., Amin Yavari, S., Zadpoor, A.A., Weinans, H., Jurvelin, J.S., Isaksson, H., 2012a. Measurement of surface strain distribution in composite femora using digital image correlation. In: *Proceedings of the 18th Congress of the European Society of Biomechanics*. Lisbon.
- Väänänen, S.P., Jurvelin, J.S., Isaksson, H., 2012b. Estimation of 3D Shape, Internal Density and Mechanics of Proximal Femur by Combining Bone Mineral Density Images with Shape and Density Templates. *Biomechanics and Modeling in Mechanobiology* 11, 791–800.
- Yushkevich, P.A., Piven, J., Hazlett, H.C., Smith, R.G., Ho, S., Gee, J.C., Gerig, G., 2006. User-guided 3D active contour segmentation of anatomical structures: significantly improved efficiency and reliability. *NeuroImage* 31, 1116–1128.
- Zdero, R., Shah, S., Mosli, M., Schemitsch, E.H., 2010. The effect of load application rate on the biomechanics of synthetic femurs. *Proceedings of the Institution of Mechanical Engineers. Part H, Journal of Engineering in Medicine* 224, 599–605.
- Zhang, D., Arola, D.D., 2004. Applications of digital image correlation to biological tissues. *Journal of Biomedical Optics* 9, 691–699.

Paper III

Lorenzo Grassi

Division of Solid Mechanics,
Lund University,
Lund 22363, Sweden;
Department of Biomedical Engineering,
Lund University,
BMC D13, Sölvegatan 19,
Lund 22184, Sweden
e-mail: lorenzo.grassi@bme.lth.se

Sami P. Väänänen

Department of Applied Physics,
University of Eastern Finland,
Kuopio 70211, Finland

Saber Amin Yavari

Faculty of Mechanical, Maritime, and
Materials Engineering,
Delft University of Technology,
Delft 2628 CD, The Netherlands

Jukka S. Jurvelin

Department of Applied Physics,
University of Eastern Finland,
Kuopio 70211, Finland

Harrie Weinans

Faculty of Mechanical, Maritime, and
Materials Engineering,
Delft University of Technology,
Delft 2628 CD, The Netherlands;
Department of Orthopaedics,
UMC Utrecht 3508 GA, The Netherlands

Matti Ristinmaa

Division of Solid Mechanics,
Lund University,
Lund 22363, Sweden

Amir A. Zadpoor

Faculty of Mechanical, Maritime, and
Materials Engineering,
Delft University of Technology,
Delft 2628 CD, The Netherlands

Hanna Isaksson

Division of Solid Mechanics,
Lund University,
Lund 22363, Sweden;
Department of Biomedical Engineering,
Lund University,
Lund 22184, Sweden;
Department of Orthopaedics,
Lund University,
Lund 22184, Sweden

Full-Field Strain Measurement During Mechanical Testing of the Human Femur at Physiologically Relevant Strain Rates

*Understanding the mechanical properties of human femora is of great importance for the development of a reliable fracture criterion aimed at assessing fracture risk. Earlier *ex vivo* studies have been conducted by measuring strains on a limited set of locations using strain gauges (SGs). Digital image correlation (DIC) could instead be used to reconstruct the full-field strain pattern over the surface of the femur. The objective of this study was to measure the full-field strain response of cadaver femora tested at a physiological strain rate up to fracture in a configuration resembling single stance. The three cadaver femora were cleaned from soft tissues, and a white background paint was applied with a random black speckle pattern over the anterior surface. The mechanical tests were conducted up to fracture at a constant displacement rate of 15 mm/s, and two cameras recorded the event at 3000 frames per second. DIC was performed to retrieve the full-field displacement map, from which strains were derived. A low-pass filter was applied over the measured displacements before the crack opened in order to reduce the noise level. The noise levels were assessed using a dedicated control plate. Conversely, no filtering was applied at the frames close to fracture to get the maximum resolution. The specimens showed a linear behavior of the principal strains with respect to the applied force up to fracture. The strain rate was comparable to the values available in literature from *in vivo* measurements during daily activities. The cracks opened and fully propagated in less than 1 ms, and small regions with high values of the major principal strains could be spotted just a few frames before the crack opened. This corroborates the hypothesis of a strain-driven fracture mechanism in human bone. The data represent a comprehensive collection of full-field strains, both at physiological load levels and up to fracture. About 10,000 points were tracked on each bone, providing superior spatial resolution compared to ~15 measurements typically collected using SGs. These experimental data collection can be further used for validation of numerical models, and for experimental verification of bone constitutive laws and fracture criteria. [DOI: 10.1115/1.4028415]*

Introduction

The femur is the bone in the human body that is most frequently fractured [1,2]. Aside from the femur fractures that result from high-energy impacts, such as car accidents, there is a continuously increasing number of fractures occurring after low-energy or no

impact [3]. Many of these occurrences are due to osteoporosis. Most femoral fractures occur in the proximal region [2], and result in a dramatic increase in patient morbidity and mortality [4]. In clinical practice, the fracture risk is currently estimated based on the bone mineral density values and use of statistical tools that account for clinical risk factors [5]. These methods have the advantage of being easy to access and administer, but they also have severe limitations [6,7]. One limitation is that the bone geometry and mechanical properties are poorly considered in these methods. However, bone mechanical properties are highly

Manuscript received May 8, 2014; final manuscript received August 13, 2014; accepted manuscript posted August 27, 2014; published online September 17, 2014. Assoc. Editor: David Corr.

correlated with fracture risk in individuals [8,9]. Therefore, the mechanics of femoral neck fractures have been investigated through ex vivo experiments, with the aim of directly providing information on the bone mechanical properties [10,11], and of complementing numerical studies [12]. Most previous studies conducting mechanical ex vivo tests on proximal femora measured the structural properties [13] and/or the strain levels in a few predetermined locations using SGs [14].

DIC is a noncontact method that acquires digital images of an object and performs image analysis to extract full-field shape, deformation and/or motion measurements [15]. The use of DIC for full-field strain measurements during mechanical testing of long bones has been introduced only recently. Dickinson et al. explored the potential of DIC as a tool for strain measurement using a synthetic composite bone with the aim to be used for validation for numerical studies [16]. The strain prediction accuracy was comparable to that in previous literature; however, the validation was performed against 25 measurements from as many selected spots, and not against the full-field data. Other studies, e.g., Op Den Buijs and Dragomir Daescu [17], used 2D DIC to measure strains, thus allowing only qualitative evaluation of the obtained measurements. Gilchrist et al. used high-speed cameras and DIC to measure strains on proximal human femora under a simulated fall on a side [18]. The reliability of DIC strain measurements on human femora was also determined by a direct comparison with SG data. Our research group recently performed some experiments using DIC, with the aim of addressing the strain measurement repeatability using synthetic bones [19], and to investigate the compression behavior and fracture mechanism of rat bones [20]. However, no studies have investigated the full-field strain response of ex vivo human femora at a strain rate compatible with those found during normal daily activities, e.g., walking or single leg stance. Thus, the aim of the present study was to investigate the mechanical response of cadaver proximal femora up to fracture in a configuration resembling single leg stance, using a 3D-surface DIC system equipped with high-speed cameras.

Material and Methods

Material. Three fresh-frozen proximal cadaver femora were obtained from Kuopio University Hospital through an ethically approved protocol (ethical permission by National Authority for Medicolegal Affairs 5783/2004/044/07). Computed tomography (CT) scans were obtained (Siemens Definition AS64, Siemens AG, Germany, $0.4 \times 0.4 \times 0.6$ mm voxel size) of each specimen to exclude the presence of fractures or other abnormalities. None of the donors had any history of musculoskeletal disorders. The height, weight, sex, and age at death of the donors are reported in Table 1. Soft tissues were removed from the femora by using scalpels and fine sandpaper. During the imaging and mechanical testing phase, the femora were kept in plastic boxes partly filled with phosphate buffered saline solution to preserve tissue hydration when not in use, and put back in the freezer afterward.

Specimen Preparation. The anatomical planes were identified from the proximal femur geometry to ensure a consistent alignment between the three specimens. Bones were resected 5.5 cm below the minor trochanter and leaned on the anterior side on a flat surface. The three contact points located on the femoral head,

greater trochanter and shaft defined the anterior plane for each femur (Fig. 1, red circles). The shaft axis was then defined as the line connecting the most lateral points of the femur at the minor trochanter level and at the distal cutting region level (Fig. 1, blue triangles). Following the defined reference frame, the distal part of each specimen was inserted in a custom-made, stainless steel holder that was subsequently filled with cold-cured epoxy resin (Technovit[®] 4071, Heraeus Kulzer, Germany). The height of the epoxy pot was 2.5 cm for specimen #3, whilst the other two specimens required a 5 cm tall pot in order to avoid relative movements during the mechanical test. To prevent local crushing, the superior part of the femoral head was covered with a stainless steel cap, which was applied over the femoral head using epoxy (Fig. 1).

Each specimen was optimized for camera recordings and DIC measurements by applying a matt white background over the anterior surface using a solvent-based spray paint (Gamma, The Netherlands). After the white paint dried, a black random speckle pattern was manually applied using a permanent marker. This ensured a high repeatability in terms of speckle size, and an enhanced contrast between the speckle and the background. Following the practical recommendations from Sutton [15, Chap. 10], speckles should be sampled by at least a 3 by 3 pixel array to minimize oversampling. With the adopted camera settings (reported in the next section), and aiming at obtaining a 6 by 6 pixel speckle size, the physical speckle size was set to a minimum of 0.6×0.6 mm.

Mechanical Testing. Two high-speed cameras (Fastcam SA1.1, Photron, Inc.) with 1 Mpx resolution were used to record the test at 3000 frames per second (fps). With the adopted parameters for DIC recording (pan angle 29 deg, baseline camera distance 280 mm), a spatial resolution of approximately 0.1 mm/px was achieved. Two high-intensity cold light sources (DX15, Hedler GmbH, Germany) were used to enhance the light to allow camera recordings with a short shutter time and high aperture settings.

Mechanical tests were performed with a single monotonic ramp at 15 mm/s up to the macroscopic failure of each specimen. The distal pot was rigidly mounted on the moving part of the loading machine (5500 R, Instron, Inc.), and the contact point with the steel cap placed over the femoral head was greased to minimize

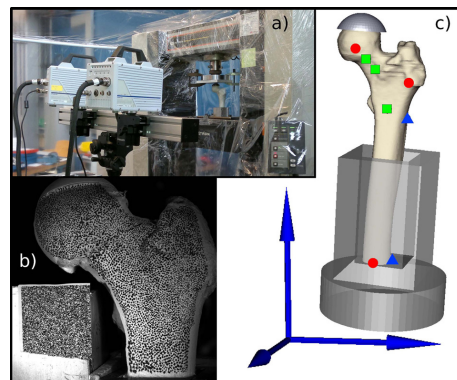


Fig. 1 (a) Experimental setup. (b) A raw image from the master DIC camera, showing one sample with its control plate. (c) Sketch of the specimen preparation. Frontal plane was defined by the three contact points on the frontal side of the femur, depicted with red circles. The shaft axis was defined by the two most lateral points at the smaller trochanter level and at the cutting plane level, respectively (blue triangles). This reference system was used to guide the insertion of the distal pot, and the application of the protective cap on the femoral head. The position of the three virtual SGs is shown with green squares.

Table 1 Patient information (sex, age at death, height/weight, and leg side) for the three specimens tested

Specimen ID	Sex (M/F)	Age (yr)	Height (cm)	Weight (kg)	Side (L/R)
#1	M	22	186	106	L
#2	M	58	183	85	R
#3	M	58	183	112	L

the friction and avoid undesired load components. A load cell (maximum axial load 100 kN, accuracy 0.5% of the reading within 1/500th of the load cell capacity, Instron, Inc.) measured the contact force at the femoral head. The analog recordings of the applied displacement and resulting force from the loading machine were sampled at the same recording frequency of the cameras, and converted to a digital signal using a digital acquisition module (Isi-DAQ-STD-8D, Isi-Sys GmbH, Germany). This digital acquisition module was taking both the analog data from the loading machine and the clock digital signal from the master camera as an input, and providing synchronized measurements of the measured force and displacement as a digital output signal to a computer equipped with the control software (Vic-3D 2010, Correlated Solutions, Inc.). During the tests, a control plate of approximately 35 × 35 mm size with a speckle pattern applied with a sticker was rigidly connected to the moving part of the loading machine to serve as a zero reference for control and analysis of systematic errors and random noise (Fig. 1).

Image Correlation. After the mechanical testing, the DIC of the recorded images was calculated for each specimen (Vic-3D v7, Correlated Solutions, Inc.) to obtain a discrete displacement field for each recorded frame. A triangularization process analogous to the one used in the finite element method retrieved strains from this discrete displacement field [15]. Two different sets of parameters were used for the DIC and strain calculation, called prefracture and near-fracture. The prefracture parameter set was applied to all frames before the fracture, i.e., before the crack formation was noticeable with the naked eye. The near-fracture parameter set was applied to 100 frames preceding and following the crack opening frame, i.e., 50 frames before and 50 frames after fracture. The two DIC parameter sets were defined as follows:

- Prefracture: DIC was calculated with a subset size (that is, the size of the area used to evaluate the gray level pattern) of 25 px and a step size (defined as the number of pixels by which the subset is shifted to calculate the displacement field) of 5 px. All the frames were compared to the same specimen reference picture, taken in the undeformed configuration. The displacement vector at each recorded point was filtered using a low-pass filter at a cut-off frequency of 100 Hz to remove high-frequency vibration components. Green-Lagrangian strains were then calculated from the filtered displacement field using a spatial decay filter of 5 px size.
- Near-fracture: DIC was calculated with subset size = 25 px, step size = 1 px, and no filters were applied to the obtained displacement. The Green-Lagrangian strains were calculated with the same spatial decay filter as in the prefracture mode.

DIC Postprocessing. To enable comparison with literature, the location of three virtual SGs was identified over the measured field at the femoral head, neck and diaphysis level [21], as shown in Fig. 1 (green squares). The 3D shape of each specimen was obtained by semi-automatic segmentation of the CT datasets (Seg3D2, CIBC, University of Utah), and spatially registered to fit with the DIC point clouds, using a MATLAB (v8.1, The Mathworks, Inc.) code based on a genetic optimization algorithm. The position of the virtual SGs was identified over the registered 3D models using a multimodal data software [22]. The strains in those three locations were averaged over a 3 mm² area to reproduce the output of a SG typically used in previous tests. The calculated principal strains were then plotted against the applied force. The strain rate at the three virtual SGs location was also evaluated with a custom-written MATLAB code. Moreover, the evolution of the principal strain magnitude and orientation was investigated for several representative loads: 75%, 100%, and 150% of the body weight (BW), and at the frame immediately before fracture. The latter was defined as the last frame in the time series where a crack was not visible with the naked eye.

The noise levels were benchmarked against the control plate placed on a side of the specimen under test (Fig. 1). This plate was rigidly connected to the distal holder of the femur, moving together

with it during the test. As no force was applied onto this plate, a constant null strain should theoretically be obtained from its DIC displacement field. Thus, the average and the maximum values of the major principal strain detected by the DIC algorithm on this control plate were evaluated before and during the test, and taken as an indication of the noise level of the measurements.

Using the data from the near-fracture parameter set, the peak strains at fracture were measured, and the crack evolution was plotted. Fracture limit diagrams were produced, showing the principal strain components at the fracture instant, with the aim of identifying a possible fracture precursor, as they provided some useful information in previous studies on rat bones [20]. The residual strains in the femora 0.08 s after fractures were also evaluated to provide a qualitative estimation of the amount of plastic phenomena that occurred.

Results

“Global” Measurements. The coefficient of determination (R^2) of the displacement–time curves was greater than 0.99 for all tests, and the corresponding normalized root mean square error (NRMSE) was smaller than 11%. Each mechanical test took approximately 0.5 s. The force–displacement curves for the three femora exhibited a sudden drop after the maximum force had been reached (Fig. 2). The coefficient of determination for all the force–displacement curves was equal to or higher than 0.99 up to the maximum recorded force. The maximum force recorded for the three specimens was 13,383 N, 7856 N, and 9080 N, respectively.

DIC Noise. Using the prefracture parameter set, the average major principal strain detected on the control plate in the resting mode (i.e., with loading machine turned on but not operating) was $31 \pm 22 \mu\epsilon$, $49 \pm 30 \mu\epsilon$, and $16 \pm 12 \mu\epsilon$ for the three specimens, respectively. The corresponding maximum recorded values of the major principal strain were $142 \mu\epsilon$, $361 \mu\epsilon$, and $51 \mu\epsilon$, respectively. When the mechanical test was ongoing, the values raised to $164 \pm 27 \mu\epsilon$, $106 \pm 29 \mu\epsilon$, and $81 \pm 19 \mu\epsilon$, respectively. The maximum recorded major principal strains during test were $593 \mu\epsilon$, $659 \mu\epsilon$, and $532 \mu\epsilon$, respectively.

Simulated Strain Gauges. The strain data from the simulated SGs show a linear-wise behavior with respect to the applied force until fracture (Fig. 3). The linear correlation coefficient was greater than 0.96 (NRMSE smaller than 19%) for all the SGs from all the specimens, except for one SG in specimen #1 and #2, whose positions were set too close to the distal pot (Table 2). As a consequence, the strains were measured over a substantially undeformed region, thus weakly correlating with the increasing applied force. The strain rate calculated from the virtual SGs varied between the different SG locations, with the greatest values constantly located at the femoral head or neck. For all tested

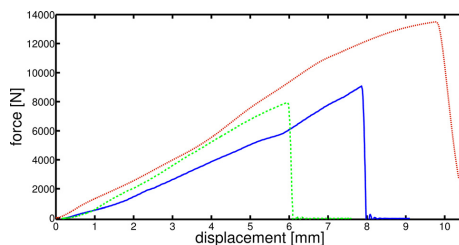


Fig. 2 Force–displacement curves for the three specimens tested. Specimen #1 is shown in red (dotted line), #2 in green (dashed line), and #3 in blue (continuous line).

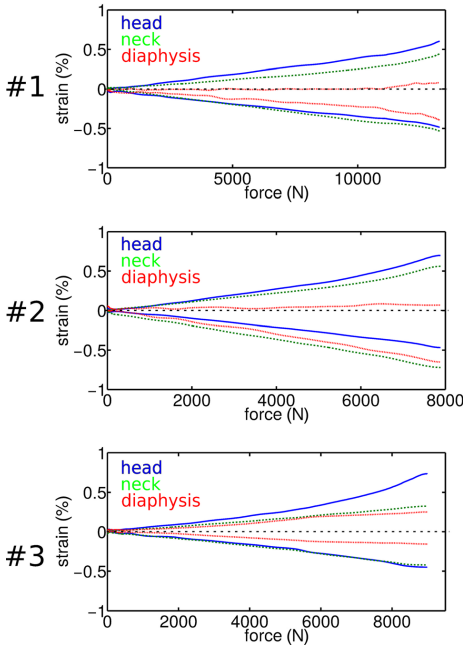


Fig. 3 Evolution of the major (positive sector) and minor (negative sector) principal strains, as a function of the applied force, in the simulated SGs for the three femora. The strain gage on the head is depicted in blue (continuous line), the one on the neck in green (dashed line), and the one at the diaphysis level in red (dotted line).

specimens, the maximum value of the strain rate was recorded just before the fracture with magnitudes ranging between 0.032 and 0.053 s^{-1} .

Strain Linearity. The linear correlation of the principal strains with respect to the applied force was investigated also over the whole cloud of measurements. Pooling the principal strains of the three specimens, 91% of the points had a coefficient of determination greater than 0.9 (average NRMSE for these points $12\% \pm 7\%$, maximum NRMSE = 32%), and 81% had a coefficient of

determination greater than 0.95 (average NRMSE for these points = $11\% \pm 5\%$, maximum NRMSE = 22%).

Principal Strains Magnitude and Direction. The major and minor principal strain directions did not change noticeably during the test as the applied force increased (Figs. 4 and 5, respectively). However, a more uniform alignment of the principal directions was observed with increasing force levels. The corresponding major and minor principal strain magnitudes consistently increased (in absolute value) with the increasing levels of the applied load (Figs. 6 and 7, respectively).

Fracture Limit. Due to a technical problem with the camera trigger, the video recordings of specimen #1 were interrupted just a few frames before the fracture. Thus, results at fracture can only be presented for specimens #2 and #3. The frames closest to the crack formation and propagation were isolated, and the evolution of the major principal strain during those frames is depicted in Fig. 8. The fracture limit plots indicate that tensile strains dominate over compressive strains in the anterior surface of the femora at fracture (Fig. 9). The points with the highest sum of the absolute value of the major and minor principal strains are consistently located where the cracks are subsequently formed in 0.3 ms (Fig. 9, black points).

Residual Strains. The residual strains 0.08 s after the crack opening were in the order of a few hundred microstrains. High strain levels (greater than $1000 \mu\epsilon$) were found only in the crack region. Mean and median values of the residual principal strains are reported in Table 3.

Discussion

The aim of the present study was to investigate the mechanical behavior of human femora both under physiological loading and at fracture, using DIC to measure the strain response at the surface during ex vivo mechanical testing.

The noise in the DIC measurements was evaluated during the postprocessing phase using a control plate, rigidly joined to the moving part of the loading machine but not subjected to any deformation. A constant null strain should theoretically be detected by DIC on the control plate. This does not happen in reality, where hardware intrinsic limitations and external disturbances might add undesired components to the measured signals [23]. The latter will add noise to the calculated strains; the strains detected over the undeformed control plate can thus be taken as an indication of such noise component. High-frequency oscillations, likely caused by vibration of the loading machine, can generate noise in the DIC displacement field. This noise was more pronounced along the out-of-plane direction of the cameras, likely due to the intrinsic limitations in the stereographic reconstruction. The noise is further amplified when deriving the strains. A low-

Table 2 Linear regression data for the simulated SGs at different positions (H = femoral head, N = femoral neck, D = proximal diaphysis) for the three specimens tested

Specimen number	SG position	R^2		NRMSE (%)		Slope ($\mu\epsilon/\text{N}$)		Intercept ($\mu\epsilon/\text{N}$)	
		ϵ_1	ϵ_2	ϵ_1	ϵ_2	ϵ_1	ϵ_2	ϵ_1	ϵ_2
1	H	0.99	0.99	0.92	0.95	0.40	-0.35	73.7	-58.7
1	N	0.98	0.99	0.86	0.97	0.28	-0.39	20.0	-13.9
1	D	0.58	0.98	0.35	0.87	0.03	-0.24	-49.5	-75.1
2	H	0.99	0.99	0.88	0.90	0.77	-0.54	23.1	-121.0
2	N	0.98	0.99	0.86	0.96	0.61	-0.90	69.4	-93.7
2	D	0.51	0.99	0.30	0.94	0.08	-0.77	145.0	-98.8
3	H	0.96	0.99	0.81	0.90	0.63	-0.46	54.6	-13.8
3	N	0.99	0.99	0.93	0.94	0.34	-0.46	96.2	-30.6
3	D	0.99	0.98	0.90	0.87	0.29	-0.18	20.5	-37.6

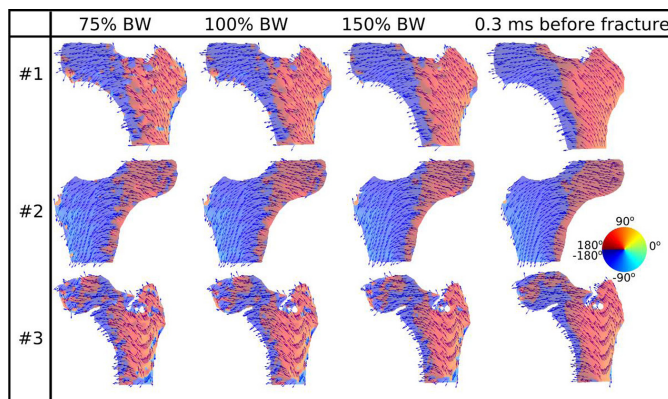


Fig. 4 The orientation of the major principal strain direction for the three femora at four different load levels, defined by 75%, 100%, and 150% of the BW, and at the frame immediately before the crack formation. Only a subsampling of the points was depicted with arrows, and the direction of the other points is indicated by the background color of the femur, according to the legend on the right.

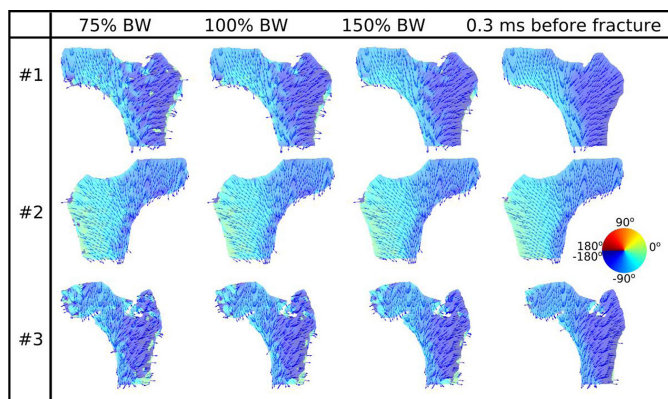


Fig. 5 The orientation of the minor principal strain direction for the three femora at four different load levels, defined by 75%, 100%, and 150% of the BW, and at the frame immediately before the crack formation. Only a subsampling of the points was depicted with arrows, and the direction of the other points is indicated by the background color of the femur, according to the legend on the right.

pass filter was thus applied on the DIC displacement data in the prefraction stage, before strain derivation. This reduced the noise levels in the control plate to $\sim 100 \mu\epsilon$. The strain levels from the control plate define the worst case scenario, since the plate was located on one side of the camera field of view, and all the camera and lighting settings were specifically optimized to best capture the surface of the femur. However, the derivation of strains for the crack propagation phase was conducted without any previous filtering, to get the maximum time and spatial resolution.

Our findings show that the chosen displacement rate corresponded to a strain rate in the virtual strain gages of $\sim 0.04 \text{ s}^{-1}$, which is comparable to the values found in literature from in vivo strain measurements during physiological activities like walking and running [24,25].

The tested specimens revealed a linear behavior in terms of strain levels on the surface against applied force ($R^2 > 0.96$ for the virtual SGs, and $R^2 > 0.9$ for over 90% of the measurements, with average NRMSE of 12%). Points with low correlation were located at the boundaries of the DIC cloud, where uncertainties in the strain calculation may arise related to the adopted algorithm [15], and close to the holding pot, where negligible strains were measured throughout the test, thus weakly correlating with the increasing force. These results corroborate the findings by Juszczak et al. [11], who reported a linear correlation between principal strains and applied force on a limited set of anatomical locations, using SGs. Our results provide a significant complement to them by showing that the linear correlation extends to the whole anterior surface of the femur, with about

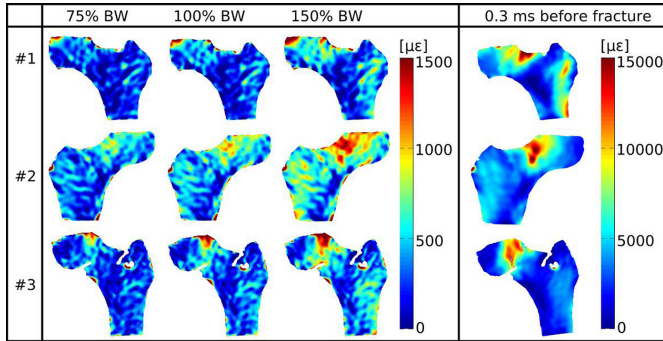


Fig. 6 Major principal strain distribution for the three femora at four different load levels, defined by 75%, 100%, and 150% of the BW, and at the frame immediately before the crack formation

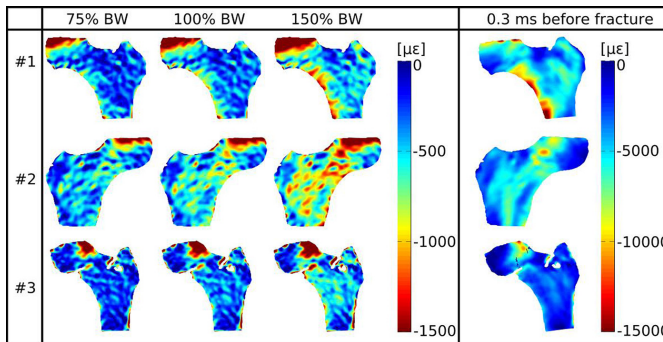


Fig. 7 Minor principal strain distribution for the three femora at four different load levels, defined by 75%, 100%, and 150% of the BW, and at the frame immediately before the crack formation

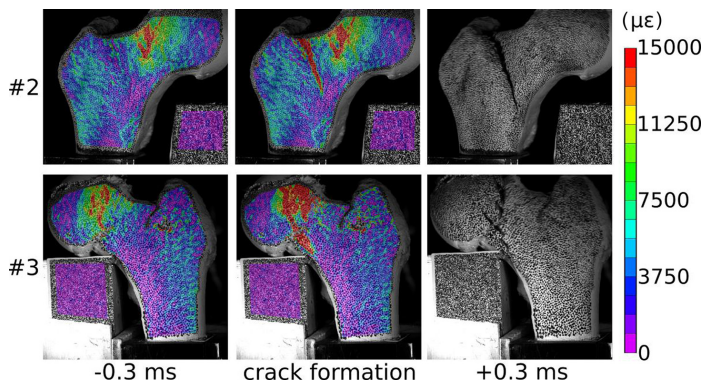


Fig. 8 Crack formation and propagation for specimens #2 and #3: the major principal strain distribution is superimposed on the raw pictures recorded. The major principal strains after the crack opened are not shown, as the fast surface motion resulted in a slightly out-of-focus picture. This impaired the correct image correlation.

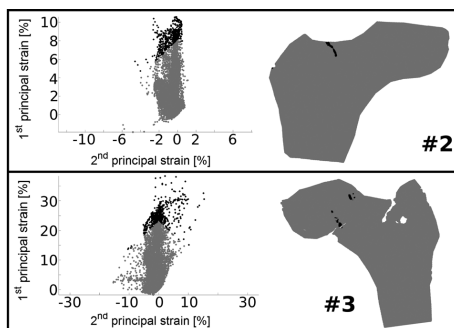


Fig. 9 Fracture limit plot for specimens #2 and #3 at the last frame before the crack is detected. The 5% of the points with a higher sum of the principal strains is evidenced in black in the plots (left), and their anatomical location is shown with the same color (right).

Table 3 Median and average value of the residual strains measured in specimen #2 and #3 0.08 s after the crack was noticed

Specimen number	Principal strain	Median ($\mu\epsilon$)	Average ($\mu\epsilon$)
2	ϵ_1	153.3	338.9
2	ϵ_2	238.6	433.4
3	ϵ_1	328.6	760.1
3	ϵ_2	318.6	559.6

10,000 points per specimen tracked using an optical full-field technique.

The linear, macroscopically elastic, behavior of the tested specimens up to fracture is also corroborated by the analysis of the residual strains measured 0.08 s after fracture. The strains were in the order of a few hundred microstrains, with higher strains confined in proximity of the fracture rim where small localized plastic phenomena are likely to happen.

The major and minor principal strain directions formed a pattern that corresponds to the classic theory of Wolff's law [26], such that the "principal tensile group" and the "principal compressive group" are clearly visible in the results (Figs. 4, 5, and 10). The principal strain directions (Figs. 4 and 5) aligned more with those identified by Wolff, for higher loads. This means that the surface strains of a human femur subjected to a single stance-like load have principal orientations that tend to follow the internal trabecular orientation. Thus, our results confirm the significant contribution of trabecular bone to load bearing. These results are also in agreement with the principal directions of anisotropy found through a Gradient Structure Tensor analysis of clinical CT scans [27], and when implementing anisotropy in finite element models [28].

The fracture event lasted for less than ~ 1 ms after the first crack formation was seen in the camera recordings. Specimen #3 underwent a subcapital fracture, and a cloud of points with high major principal strains ($>15,000 \mu\epsilon$) was present in the fracture region several milliseconds before the crack actually formed. This cloud constantly expanded and increased in magnitude until the crack abruptly formed and propagated. The major principal strain can thus be seen as a good fracture predictor for this case, in agreement with previous experimental and numerical studies [29]. The fracture limit plot in Fig. 9 (bottom) also corroborates this hypothesis, i.e., the cracked region exhibited the highest values of tensile strains. Specimen #2 underwent a different kind of fracture, which can be classified as a basi-cervical femur fracture. The fracture onset was located on the superior aspect of the femoral neck and

the crack propagated almost parallel to the intertrochanteric line. No clear fracture precursor was found in this case, as only a small region where high strains concentration could be spotted in the fracture region before the crack opened, whilst a wide region with high major principal strains was present in the subcapital region without giving rise to a crack. This suggests that the crack actually originated in a region out of the field of view of the recording system, most likely in the superior aspect of the neck, which was only partly covered by the cameras due to its high curvature. Then, DIC captured the fracture propagating over the camera field of view, where a combination of high tensile and compressive strains was driving the crack propagation, as shown in Fig. 9 (top).

To our knowledge, this is the first study conducting comprehensive mechanical tests up to fracture on human cadaveric bones using high frame rate DIC to evaluate the full-field response at physiologically relevant strain rates. Dickinson et al. [16] and Väänänen et al. [19] tested synthetic femoral bones, which resulted in conclusions only related to the feasibility of DIC over such geometries. Testing cadaveric specimens involves additional challenges related to tissues hydration and preservation, and to the presence of small anatomical features on the surface (such as microholes, protuberances and wrinkles) that are not reproduced in synthetic femora. Mechanical tests on cadaver femora using DIC were performed by Op Den Buijs and Dragomir-Daescu [17]. However, only one video camera was used for DIC recordings, meaning that only 2D strain measurement was possible. That is likely to adversely affect the accuracy of the measurements in high curvature regions. Moreover, only qualitative analysis of the strain data was provided, as only the global bone stiffness was evaluated quantitatively. Gilchrist et al. [18] investigated the femur behavior during fall on the side, while our study aimed at evaluating a physiological loading condition such as single leg stance.

Compared to literature where SGs are used, the advantage of DIC is in the higher number of measurements, i.e., about 10,000 measurement points with the prefracture parameter set, against 10–15 measurements typically obtained with SGs. This allows us to obtain a full-field deformation measurement over the recorded bone surface. Moreover, DIC measurements are noncontact, practically eliminating the reinforcement effect that could be significant when using SGs over thin surfaces [30].

The main limitation with the present study is the low number ($n=3$) of tested cadaveric femora, which prevents us from doing a reliable statistical analysis. All three specimens came from male donors, of which one young and two middle aged (Table 1), thus they do not cover the variability in the population in terms of femoral size, cortical thickness, and bone density. However, the main

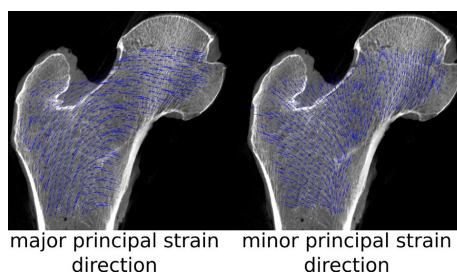


Fig. 10 The orientation of the major and minor principal strain directions for specimen #2 at the frame immediately before the crack formation. The orientations are reported over a sagittal section of the femur obtained with a high-resolution CT scanner (Verity CT scanner, Planmex, Finland). The CT images and the full-field orientation data were coregistered manually, with aim of qualitatively showing the correspondence between the principal strain directions on the bone surface, and the internal trabecular orientation.

findings of the study in terms of fracture toughness at a physiological strain rate are not affected by this, since aging is believed to result in increasing the brittleness in mechanical behavior of bone [31].

Another limitation is the slightly different boundary conditions applied to specimen #3, since the other two specimens required a deeper epoxy potting in order to achieve stability inside the holder. At first, a 2.5 cm tall pot was built also for specimens #1 and #2. However, it was judged to be too weak. Thus, we believed it was safer to reinforce the epoxy pot by adding 2.5 cm extra material, in order to eliminate the risk of possible mechanical instabilities. The greater stability of specimen #3, in comparison to the other two was probably related to its significantly greater shaft diameter that almost filled the base of the distal steel box. However, these differences in the distal holding level should not affect the mechanical behavior significantly, since similar fracture patterns have been found in a multitude of previous studies using very different boundary conditions.

A final limitation is the frame rate of the camera recordings. Despite being high for the currently available technology (3000 fps), it only allowed us to record 3–4 frames of the crack opening and propagation at the adopted displacement rate. Future studies should aim at adopting even higher frame rates and expanding the field covered by the DIC. The latter point can be addressed, for example by using a second pair of cameras pointing at the posterior side of the femur.

In summary, the developed ex vivo testing protocol was able to provide a detailed high-frequency strain mapping of the whole femoral surface, including also the fracture region. The collected data showed a linear behavior of the proximal human femora when loaded up to fracture at a physiologically relevant strain rate, suggesting that the principal strains at the surface can represent a reliable fracture discriminant. The full-field collection of displacement and deformation measurements will also act as an extensive benchmark for subject-specific finite element models of proximal femur [32,33].

Acknowledgment

The authors would like to acknowledge Peter Mäckel on behalf of Isi-Sys GmbH, Germany, for the technical help provided before, during and after the test. The first author would also like to personally thank Lorenzo Zani for the valuable discussion regarding many practical aspects of bone testing. The present study was funded by the Swedish Research Council (2011-5064), Crafoord foundation, (Grant No. 20120752, and Grant No. 20120632 for the Vic-3D software license), Academy of Finland (14088), Finnish National Doctoral Program of Musculoskeletal Disorders and Biomaterial, and University of Eastern Finland (929711).

Nomenclature

fps = frame rate, expressed in frames per second
 ms = time, expressed in milliseconds
 R^2 = coefficient of determination
 ε_1 = major principal strain
 ε_2 = minor principal strain
 $\mu\varepsilon$ = strain, expressed in microstrains (strain $\times 10^{-6}$)

References

- [1] Brauer, C. A., Coca-Perrailon, M., Cutler, D. M., and Rosen, A. B., 2009, "Incidence and Mortality of Hip Fractures in the United States," *JAMA*, **302**(14), pp. 1573–1579.
- [2] Meling, T., Harboe, K., and Søreide, K., 2009, "Incidence of Traumatic Long-Bone Fractures Requiring In-Hospital Management: A Prospective Age- and Gender-Specific Analysis of 4890 Fractures," *Injury*, **40**(11), pp. 1212–1219.
- [3] Cauley, J. A., 2013, "Public Health Impact of Osteoporosis," *J. Gerontol., Ser. A*, **68**(10), pp. 1243–1251.
- [4] Roth, T., Kammerlander, C., Gosch, M., Luger, T. J., and Blauth, M., 2010, "Outcome in Geriatric Fracture Patients and How It Can be Improved," *Osteoporos. Int.*, **21**(Suppl 4), pp. S615–S619.
- [5] Kanis, J. A., Borgstrom, F., De Lact, C., Johansson, H., Johnell, O., Jonsson, B., Oden, A., Zethraeus, N., Pflieger, B., and Khaltaev, N., 2005, "Assessment of Fracture Risk," *Osteoporos. Int.*, **16**(6), pp. 581–589.
- [6] Silverman, S. L., and Calderon, A. D., 2010, "The Utility and Limitations of FRAX: A US Perspective," *Curr. Osteoporos. Rep.*, **8**(4), pp. 192–197.

- [7] Lekamwasam, S., 2010, "Application of FRAX Model to Sri Lankan Postmenopausal Women," *J. Clin. Densitom.*, **13**(1), pp. 51–55.
- [8] Amin, S., Kopperdhal, D. L., Melton, L. J., Achenbach, S. J., Therneau, T. M., Riggs, B. L., Keaveny, T. M., and Khosla, S., 2011, "Association of Hip Strength Estimates by Finite-Element Analysis With Fractures in Women and Men," *J. Bone Miner. Res.*, **26**(7), pp. 1593–1600.
- [9] Szulc, P., Duboeuf, F., Schott, A. M., Dargent-Molina, P., Meunier, P. J., and Delmas, P. D., 2006, "Structural Determinants of Hip Fracture in Elderly Women: Re-Analysis of the Data From the EPIDOS Study," *Osteoporos. Int.*, **17**(2), pp. 231–236.
- [10] Currey, J., 2009, "Measurement of the Mechanical Properties of Bone: A Recent History," *Clin. Orthop. Relat. Res.*, **467**(8), pp. 1948–1954.
- [11] Juszczak, M. M., Cristofolini, L., and Viceconti, M., 2011, "The Human Proximal Femur Behaves Linearly Elastic Up to Failure Under Physiological Loading Conditions," *J. Biomech.*, **44**(12), pp. 2259–2266.
- [12] Cristofolini, L., Schileo, E., Juszczak, M., Taddei, F., Martelli, S., and Viceconti, M., 2010, "Mechanical Testing of Bones: The Positive Synergy of Finite-Element Models and in vitro Experiments," *Philos. Trans. R. Soc., A*, **368**(1920), pp. 2725–2763.
- [13] Lochmüller, E. M., Groll, O., Kuhn, V., and Eckstein, F., 2002, "Mechanical Strength of the Proximal Femur as Predicted From Geometric and Densitometric Bone Properties at the Lower Limb Versus the Distal Radius," *Bone*, **30**(1), pp. 207–216.
- [14] Cristofolini, L., Conti, G., Juszczak, M., Cremonini, S., Van Sint Jan, S., and Viceconti, M., 2010, "Structural Behaviour and Strain Distribution of the Long Bones of the Human Lower Limbs," *J. Biomech.*, **43**(5), pp. 826–835.
- [15] Sutton, M. A., Orteu, J. J., and Schreier, H., 2009, *Image Correlation for Shape, Motion and Deformation Measurements: Basic Concepts, Theory and Applications*, Springer, New York.
- [16] Dickinson, A. S., Taylor, A. C., Ozturk, H., and Browne, M., 2011, "Experimental Validation of a Finite Element Model of the Proximal Femur Using Digital Image Correlation and a Composite Bone Model," *ASME J. Biomech. Eng.*, **133**(1), p. 014504.
- [17] Op Den Buijs, J., and Dragomir-Daescu, D., 2011, "Validated Finite Element Models of the Proximal Femur Using Two-Dimensional Projected Geometry and Bone Density," *Comput. Methods Programs Biomed.*, **104**(2), pp. 168–174.
- [18] Gilchrist, S., Guy, P., and Crompton, P. A., 2013, "Development of an Inertia-Driven Model of Sideways Fall for Detailed Study of Femur Fracture Mechanics," *ASME J. Biomech. Eng.*, **135**(12), p. 121001.
- [19] Väänänen, S. P., Amin Yavari, S., Weinans, H., Zadpoor, A. A., Jurvelin, J. S., and Isaksson, H., 2013, "Repeatability of Digital Image Correlation for Measurement of Surface Strains in Composite Long Bones," *J. Biomech.*, **46**(11), pp. 1928–1932.
- [20] Amin Yavari, S., van der Stok, J., Weinans, H., and Zadpoor, A. A., 2013, "Full-Field Strain Measurement and Fracture Analysis of Rat Femora in Compression Test," *J. Biomech.*, **46**(7), pp. 1282–1292.
- [21] Cristofolini, L., Juszczak, M., Taddei, F., and Viceconti, M., 2009, "Strain Distribution in the Proximal Human Femoral Metaphysis," *Proc. Inst. Mech. Eng. H*, **223**(3), pp. 273–288.
- [22] Viceconti, M., Taddei, F., Montanari, L., Testi, D., Leardini, A., Clapworthy, G., and Van Sint Jan, S., 2007, "Multimod Data Manager: A Tool for Data Fusion," *Comput. Methods Programs Biomed.*, **87**(2), pp. 148–159.
- [23] Bornert, M., Brémand, F., Doumalin, P., Dupré, J.-C., Fazzini, M., Grédiac, M., Hild, F., Mistou, S., Molimard, J., Orteu, J.-J., Robert, L., Surrel, Y., Vacher, P., and Wattrisse, B., 2008, "Assessment of Digital Image Correlation Measurement Errors: Methodology and Results," *Exp. Mech.*, **49**(3), pp. 353–370.
- [24] Burr, D. B., Milgrom, C., Fyhrich, D., Forwood, M., Nyska, M., Finestone, A., Hoshaw, S., Saig, E., and Simkin, A., 1996, "In Vivo Measurement of Human Tibial Strains During Vigorous Activity," *Bone*, **18**(5), pp. 405–410.
- [25] Al Nazer, R., Lanovaz, J., Kawalilak, C., Johnston, J. D., and Kontulainen, S., 2012, "Direct In Vivo Strain Measurements in Human Bone—A Systematic Literature Review," *J. Biomech.*, **45**(1), pp. 27–40.
- [26] Wolff, J., 1986, *The Law of Bone Remodeling* (Translation of the German 1892 ed.), Springer, Berlin, Germany.
- [27] Kersh, M. E., Zysset, P. K., Pahr, D. H., Wolfram, U., Larsson, D., and Pandey, M. G., 2013, "Measurement of Structural Anisotropy in Femoral Trabecular Bone Using Clinical-Resolution CT Images," *J. Biomech.*, **46**(15), pp. 2659–2666.
- [28] San Antonio, T., Ciaccia, M., Müller-Karger, C., and Casanova, E., 2012, "Orientation of Orthotropic Material Properties in a Femur FE Model: A Method Based on the Principal Stresses Directions," *Med. Eng. Phys.*, **34**(7), pp. 914–919.
- [29] Schileo, E., Taddei, F., Cristofolini, L., and Viceconti, M., 2008, "Subject-Specific Finite Element Models Implementing a Maximum Principal Strain Criterion are Able to Estimate Failure Risk and Fracture Location on Human Femurs Tested In Vitro," *J. Biomech.*, **41**(2), pp. 356–367.
- [30] Perry, C. C., 1986, "Strain-Gage Reinforcement Effects on Orthotropic Materials," *Exp. Tech.*, **10**(2), pp. 20–24.
- [31] Malo, M. K. H., Rohrbach, D., Isaksson, H., Töyräs, J., Jurvelin, J. S., Tamminen, I. S., Kröger, H., and Raam, K., 2013, "Longitudinal Elastic Properties and Porosity of Cortical Bone Tissue Vary With Age in Human Proximal Femur," *Bone*, **53**(2), pp. 451–458.
- [32] Grassi, L., Väänänen, S. P., Amin Yavari, S., Weinans, H., Jurvelin, J. S., Zadpoor, A. A., and Isaksson, H., 2013, "Experimental Validation of Finite Element Model for Proximal Composite Femur Using Optical Measurements," *J. Mech. Behav. Biomed. Mater.*, **21**(1), pp. 86–94.
- [33] Poelert, S., Valstar, E., Weinans, H., and Zadpoor, A. A., 2013, "Patient-Specific Finite Element Modeling of Bones," *Proc. Inst. Mech. Eng. H*, **227**(4), pp. 464–478.

Paper IV



Contents lists available at ScienceDirect

Journal of Biomechanics

journal homepage: www.elsevier.com/locate/jbiomech
www.JBiomech.com

Short communication

How accurately can subject-specific finite element models predict strains and strength of human femora? Investigation using full-field measurements

Lorenzo Grassi^{a,*}, Sami P. Väänänen^b, Matti Ristinmaa^c, Jukka S. Jurvelin^{b,d}, Hanna Isaksson^a

^a Department of Biomedical Engineering, Lund University, Sweden^b Department of Applied Physics, University of Eastern Finland, Finland^c Division of Solid Mechanics, Lund University, Sweden^d Diagnostic Imaging Center, Kuopio University Hospital, Finland

ARTICLE INFO

Article history:

Accepted 12 February 2016

Keywords:

Finite element

Human femur

Experimental validation

Bone strength

ABSTRACT

Subject-specific finite element models have been proposed as a tool to improve fracture risk assessment in individuals. A thorough laboratory validation against experimental data is required before introducing such models in clinical practice. Results from digital image correlation can provide full-field strain distribution over the specimen surface during in vitro test, instead of at a few pre-defined locations as with strain gauges. The aim of this study was to validate finite element models of human femora against experimental data from three cadaver femora, both in terms of femoral strength and of the full-field strain distribution collected with digital image correlation. The results showed a high accuracy between predicted and measured principal strains ($R^2=0.93$, RMSE=10%, 1600 validated data points per specimen). Femoral strength was predicted using a rate dependent material model with specific strain limit values for yield and failure. This provided an accurate prediction (< 2% error) for two out of three specimens. In the third specimen, an accidental change in the boundary conditions occurred during the experiment, which compromised the femoral strength validation. The achieved strain accuracy was comparable to that obtained in state-of-the-art studies which validated their prediction accuracy against 10–16 strain gauge measurements. Fracture force was accurately predicted, with the predicted failure location being very close to the experimental fracture rim. Despite the low sample size and the single loading condition tested, the present combined numerical–experimental method showed that finite element models can predict femoral strength by providing a thorough description of the local bone mechanical response.

© 2016 Elsevier Ltd. All rights reserved.

1. Introduction

Fragility fractures due to osteoporosis are a huge problem in Western society (Burge et al., 2007). Pharmacological treatment can increase strength of osteoporotic bones and reduce fracture risk (Kanis et al., 2013) but should be targeted to individuals whose risk of fracture is highest (Lindsay et al., 2005).

Osteoporosis is diagnosed based on bone mineral density measured in the proximal femur or lumbar spine using Dual-Energy X-ray absorptiometry. By including epidemiological parameters, fracture risk is estimated (Cummings et al., 2006;

Kanis et al., 2005). This method has a relatively poor accuracy (30% false negatives (Järvinen et al., 2005; McCreddie and Goldstein, 2000)), and is ethnic-specific (Watts et al., 2009). Subject-specific finite element (FE) models from computed tomography (CT) scans can increase the prediction accuracy by providing a comprehensive description of the bone's mechanical response. Although the prediction accuracy is considerably high both for strains ($R^2 > 0.95$ (Schileo et al., 2008; Yosibash et al., 2007)) and femoral strength (standard error of estimation(SEE) < 400 N (Koivumäki et al., 2012)), FE models have not yet been introduced in clinical practice. This is due to several reasons including concerns about validation (Henninger et al., 2010; Viceconti et al., 2005). Typically, validation against ex-vivo measurements with strain-gauges is performed. This limits the data to ~10–15 measurements at pre-selected spots (Grassi and Isaksson, 2015). Optical methods like digital image

* Correspondence to: Department of Biomedical Engineering, Lund University BMC D13, 221 84 Lund, Sweden. Tel.: +46 46 222 06 55.
E-mail address: lorenzo.grassi@bme.lth.se (L. Grassi).

correlation (DIC) (Gilchrist et al., 2013; Helgason et al., 2014; Op Den Buijs and Dragomir-Daescu, 2011) provide a more comprehensive validation benchmark. We recently collected DIC measurements at a physiological loading rate on three femora (Grassi et al., 2014), suited for reliable validation of FE models.

Therefore, the aim of the present study was to predict fracture load in human femora using subject-specific FE models. Validation was performed for strains calculated with FE against strains measured experimentally with DIC, and for femoral strength calculated with FE against the maximum force recorded experimentally.

2. Material and methods

Three male cadaver human proximal femora were harvested fresh at Kuopio University Hospital, Finland (ethical permission 5783/2004/04/07). None of the donors had any reported musculoskeletal disorder. Height, weight, sex and age at death are reported in Table 1. The specimens were CT scanned (Definition AS64, Siemens AG, 0.4 × 0.4 × 0.6 mm voxel size).

2.1. Mechanical testing

The three femora were mechanically tested to failure in a single-leg-stance configuration, and strains were measured using DIC. The experimental protocol was reported in detail by Grassi et al. (2014). Briefly, the specimens were cleaned and resected 5.5 cm below the minor trochanter. The femoral shaft below the minor trochanter was embedded in epoxy and constrained. A stainless steel cap was applied on the femoral head to distribute the load and avoid local crushing. The gap between the cap and the femoral head was filled with epoxy. The anterior surface was prepared for DIC by applying a random black speckle pattern over a matt white background. Mechanical tests were performed in a single-leg-stance configuration, with the load applied on the femoral head parallel to the shaft axis. Specimens were loaded at 15 mm/s until macroscopic failure. DIC was performed on the acquired images (two Fastcam SA1.1, Photron, Inc., 3000 frames per second; VIC 3D v7, Correlated Solutions, Inc., 25 px subset, 5 px step, 100 Hz low-pass displacement filter), and the Green-Lagrange strains were retrieved at each frame (~10,000 uniquely traceable points per specimen) (Grassi et al., 2014).

2.2. Finite element modelling

FE models were generated using a consolidated procedure (Grassi et al., 2013; Schileo et al., 2008). Femur geometry was semi-automatically segmented from CT (threshold, dilation/erosion, and manual correction, Seg3D2, University of Utah). The geometries were reverse-engineered (Rhinozeros 4.0, Robert McNeel & Associates, USA, and RhinoResurf, Resurf3d, China), and a second-order tetrahedral mesh (~140,000 nodes, ~100,000 elements, Hypermesh v13.0, Altair Engineering) was created. Elements in the epoxy pot were assigned an isotropic Young's modulus of 2.5 GPa, (Technovit 4071, Heraeus Kulzer). Elements belonging to the femur were assigned Young's modulus based on the Hounsfield Unit (HU) values. CT images were reconstructed using a sharp convolution kernel (B60f). Each axial slice was filtered using a mean filter of 4 × 4 px size to compensate for the HU over-estimation due to this kernel. Bonemat_V3 (Taddei et al., 2007) assigned inhomogeneous isotropic material properties to the elements, based on the HU values of the volume enclosed by each element. HU values were converted to equivalent radiological density (Model 3CT, Mindways Inc.), and the Young's modulus was derived using the relationships proposed by Schileo et al. (2008). Poisson's ratio was set to 0.4 (Reilly and Burstein, 1975). The geometry of the epoxy pot was used to identify the experimental reference system (Fig. 1). The load was equally distributed among the 10 most superior surface nodes on the femoral head. FE simulations were solved using Abaqus (v6.12-4, Dassault Systèmes).

Table 1

Patient information (sex, age at death, height, weight, and leg side) for the three specimens used in this study.

Specimen ID	Sex (M/F)	Age [years]	Height [cm]	Weight [kg]	Side (L/R)
#1	M	22	186	106	L
#2	M	58	183	85	R
#3	M	58	183	112	L

2.3. Strain prediction accuracy

Strain prediction accuracy was evaluated at a force of four times the body weight (BW). The predicted principal strains were compared to DIC measurements. A registration and data comparison method was adopted, based on a procedure that earlier provided good results for composite bones (Grassi et al., 2013). The DIC point cloud was registered over the FE model using an iterative closest point approach. For each surface element, the smallest sphere circumscribing it was calculated. All DIC data lying within the sphere were averaged, and the obtained value compared to the FE element strain. A robust regression analysis with bisquare weighting function of the major and minor principal strain magnitudes was performed to assess the accuracy. Bland–Altman plots (Bland and Altman, 1999) provided a visual interpretation of the agreement between predicted and measured principal strains.

2.4. Femoral strength prediction accuracy

The FE models implemented a rate-dependent material model, with different strain limit values for yield and failure (Fig. 2). Each element was assigned its specific initial modulus (E_{elem}^{ref}) as described above. A strain rate correction factor: $SRCF_{elem} = (\dot{\epsilon}_{elem}^{ref} / \dot{\epsilon}_{elem}^{ref})^{0.006}$ was defined, where $\dot{\epsilon}_{elem}$ is the absolute major principal strain rate, and $\dot{\epsilon}_{elem}^{ref}$ is the strain rate at which yield values and density-elasticity relationship were obtained (5000 $\mu\epsilon/s$ (Bayraktar et al., 2004; Morgan et al., 2003)). The tangent modulus was defined as: $E_{elem}(SRCF) = SRCF_{elem} * E_{elem}^{ref}$.

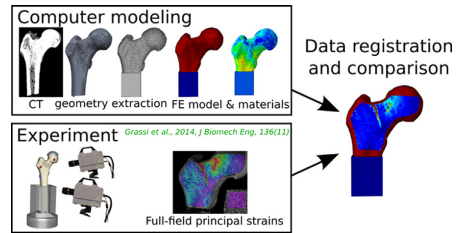


Fig. 1. Overview of the study. Top left: the subject-specific FE models were built starting from the CT scan through a process of segmentation, reverse engineering, tetrahedral meshing, and material property mapping based on the calibrated CT values. The origin of the experimental reference system was set in a base corner of the epoxy pot, with x-axis and y-axis aligned to horizontal and vertical side, respectively. The load was applied along the negative y-direction on the femoral head. Bottom left: schematic of the experimental setup. The specimens were tested until fracture in a single-leg-stance position, and deformations measured using 3D surface digital image correlation (Grassi et al., 2014). Right: the FE predictions were compared to the measured principal strains by registering the experimental point cloud over the FE model, and then averaging the experimental values within each element's volume of interest.

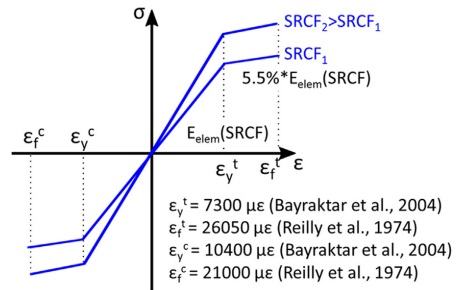


Fig. 2. The material model implemented in the FE models to predict bone strength. The response was strain rate dependent, according to the defined strain rate correction factor (SRCF). The behaviour of one element for two different values of SRCF is shown in the stress strain diagram. Bone strength was predicted using threshold strain values for yield (ε_y) and failure (ε_f). Different thresholds were chosen for tension ("t" superscript) and compression ("c" superscript). The post-yield modulus was set to 5.5% of the modulus in the elastic range, as extrapolated from the measurements reported by Reilly et al. (1974).

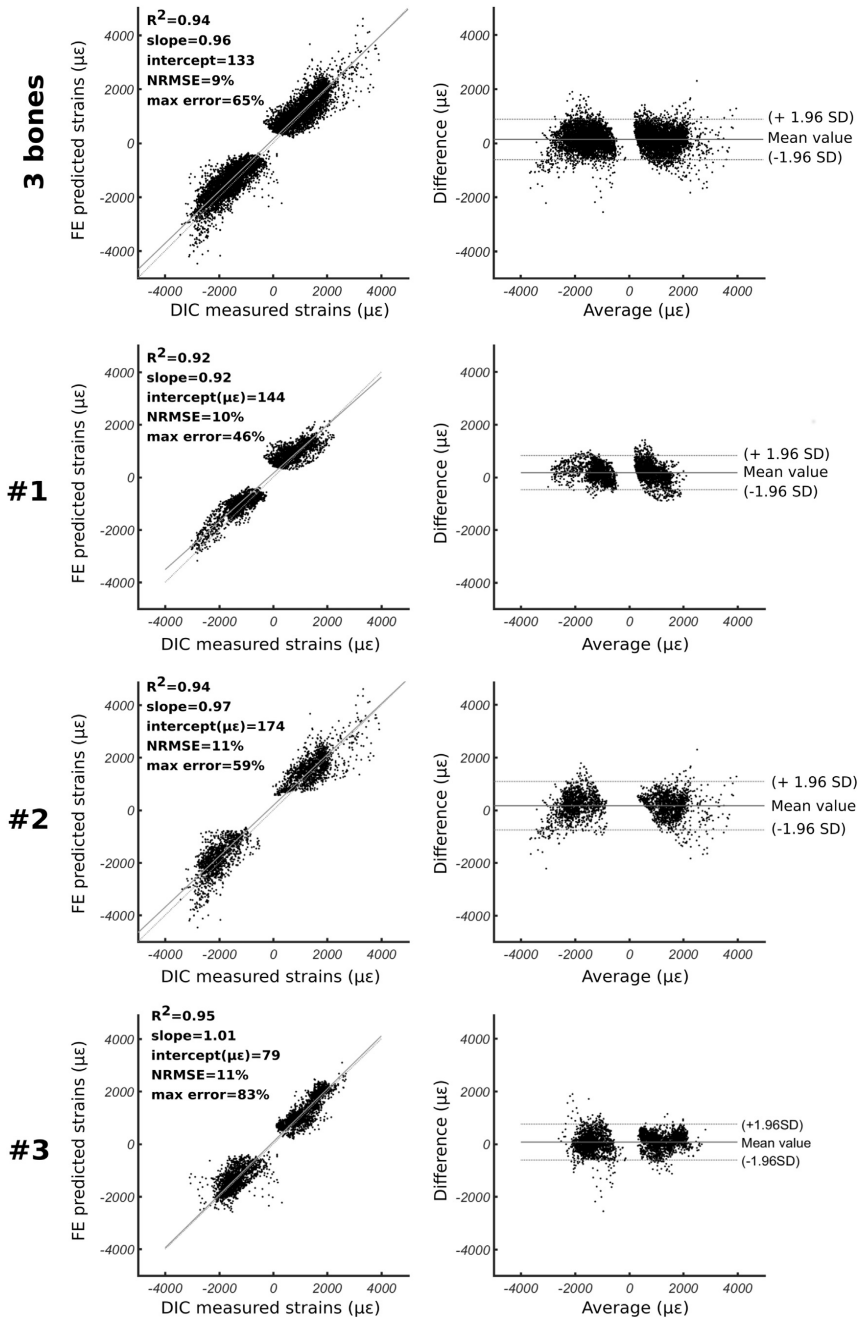


Fig. 3. Prediction accuracy for the principal strains for the three bones pooled (top) and for each bone separately (row 2–4). The applied force was 4 times the subjects' body weight. The robust linear regression analyses are shown on the left, and Bland–Altman plots on the right. The dotted lines represent the 95% confidence interval.

Different limit strain values in tension (major principal strains) and compression (minor principal strains) were implemented for yield and failure. When element strain exceeded the yield strain limit (10,400 $\mu\epsilon$ compression, 7300 $\mu\epsilon$ tension (Bayraktar et al., 2004)), the modulus was reduced to 5.5% of the tangent modulus (Reilly et al., 1974), and the simulation continued. An element was considered failed when the ultimate strain limit was exceeded (21,000 $\mu\epsilon$ compression, 26,050 $\mu\epsilon$ tension (Reilly et al., 1974)).

The FE analysis was conducted by applying consecutive 0.05 mm increments, with the time increment tuned to 15 mm/s displacement rate. The specimen was considered failed when the first element failed, and the applied force taken as the predicted femoral strength. This value was compared to the maximum force recorded during the experiment. Relative error and SEE were reported. The predicted fracture onset location was qualitatively compared to the experimental fracture rim.

3. Results

3.1. Strain prediction accuracy

For the three bones pooled (4826 data points), principal strains magnitudes were predicted with a determination coefficient (R^2) of 0.94. The regression slope was 0.96, and the intercept 133 $\mu\epsilon$. The normalised root mean square error (NRMSE) was 9%. The predicted versus measured principal strains and the Bland–Altman plot are reported in Fig. 3. When validating each bone individually (Fig. 3), R^2 was always > 0.9 , with slope and intercept close to 1 and 0, respectively.

3.2. Femoral strength prediction accuracy

Femoral strength was predicted with an error of -1.5% and $+1.2\%$ for bone #1 and #2, respectively (SEE=155 N, Table 2). Femoral strength for the third specimen could not be validated because the cap slipped experimentally, which changed the prescribed boundary conditions. FE models predicted failure to initiate in compression on the medial aspect of the neck. The predicted fracture onset was < 1 cm away from the experimental fracture line (Fig. 4).

4. Discussion

This study aimed to assess the ability of subject-specific FE models to predict principal strains and femoral strength in human femora. This is, to our knowledge, the first study reporting a strain-fracture load FE validation against full-field strain measurements at physiologically relevant strain rates (maximum strain rate $0.032\text{--}0.053\text{ s}^{-1}$ (Grassi et al., 2014)).

Strains were predicted with a high accuracy ($R^2=0.94$, NRMSE=9%), comparable to the highest reported for human femora in analogous loading configurations ($R^2=0.95\text{--}0.97$ (Schileo et al., 2008; Yosibash et al., 2007)). The strain accuracy in those studies was obtained against ~ 10 measurements. In this study, ~ 1600 measurements covering the femur anterior surface (Grassi et al., 2014) were used. This corroborates the validity of our FE modelling approach, and represents one of the strengths of this study. The majority of the points laid within the confidence limits

Table 2
Bone strength of the two specimens used in this study as measured during the experiments (Grassi et al., 2014), and predicted using FE models.

	Bone #1	Bone #2
Experimental strength [N]	13,383	7856
Predicted strength [N]	13,184	7947
Difference [%]	-1.5%	$+1.2\%$

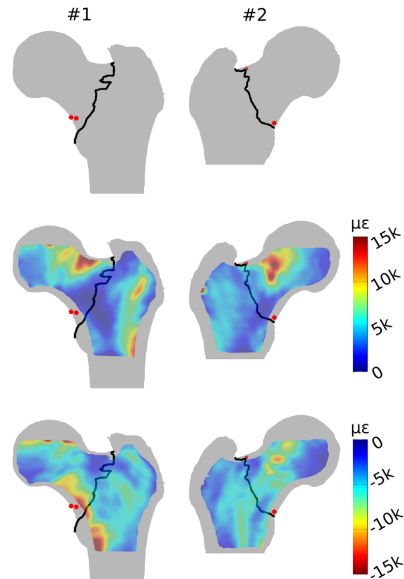


Fig. 4. Top: graphical comparison of the experimentally obtained fracture rim (black) with the fracture onset location predicted by the FE models (red). Middle: the experimentally measured major principal strains at 0.3 ms before a crack was detected in the DIC images are superimposed to the fracture rim and the predicted fracture onset. Bottom: the experimentally measured minor principal strains at 0.3 ms before a crack was detected in the DIC images are superimposed to the fracture rim and the predicted fracture onset. (For interpretation of the references to colour in this figure legend, the reader is referred to the web version of this article.)

of the Bland–Altman plots, with no observable trends in the distribution (Fig. 3).

Rate-dependent material with strain limit values for yield and failure was implemented. Limit values were taken from literature (Bayraktar et al., 2004; Reilly and Burstein, 1974). SRCF was defined, similar to Schileo et al. (2014). However, they applied a constant SRCF to all elements. In our implementation, SRCF was calculated for each element, and updated at every time increment, thus more realistically describing the rate dependency of bone.

Femoral strength was accurately predicted for the first two specimens (-1.5% and $+1.2\%$). SEE was comparable to the best published results (Bessho et al., 2007; Koivumäki et al., 2012). The latter were obtained using some specimens to train the models and identify the optimal strain/stress limit values, and validating the predictions over the remaining specimens. Our approach is instead free from internal parameter calibration, and uses limit values from experiments investigating bone properties at the mesoscale level.

Fracture load was not validated for the third specimen, since the cap slipped during the experiment. As a result, specimen #3 exhibited a peculiar fracture pattern: the crack originated close to the rim of the cap and propagated vertically (Grassi et al., 2014).

Failure onset was predicted on the medial aspect of the neck, a region mainly in compression. The onsets were close to the experimental fracture rim (Fig. 4). The experimental images show the crack originating on the superolateral aspect of the neck (Grassi et al., 2014), which is predominantly loaded in tension. We hypothesised that macroscopic crack formation was a consequence of a compressive failure of the medial side of the neck, occurring

fractions of milliseconds before the crack formation. A similar two-step failure mechanism has been reported for femora in side-fall (de Bakker et al., 2009). There, high-speed cameras placed on the medial and lateral aspect showed a two-step failure, where the first failure was in compression on the superolateral aspect. The macroscopic crack occurred immediately after on the contralateral side. An analogous mechanism, with medial and lateral side inverted due to the different loading direction, can very well occur in single-leg-stance. In our experiment, no video recordings of medial and lateral side were available, leaving the question about fracture onset unanswered. Future experiments investigating bone fracture should, whenever possible, use more cameras covering a broader area.

This study is limited by its small sample size, with three specimens tested. A second limitation regards specimen #3, whose fracture load could not be validated due to the cap slippage. Nevertheless, the strain response for specimen #3 was analysed at 4BW, since slippage occurred later. Specimen #3 showed a very high strain accuracy ($R^2=0.94$, slope=0.99, Fig. 3), which corroborates the accuracy of the proposed FE modelling approach in predicting femoral mechanical behaviour. The single loading direction investigated is also limiting. Future works will aim at extending our combined experimental/numerical approach to sideways fall configuration.

In summary, a simple subject-specific FE modelling technique, free from internal parameter calibration, accurately predicted the mechanical behaviour of human femora in a single-leg-stance configuration, both in terms of strain response and fracture load. These results support the translation of FE into clinical studies, where the predicted bone strength could complement epidemiological parameters in fracture risk estimation.

Conflict of interest statement

None of the authors had conflict of interest to declare.

Acknowledgements

The authors wish to thank Aleksandra Turkiewicz for the help with the statistical analysis. The study was supported by the Swedish Research Council (2011-5064), Swedish Foundation for Strategic Research, Finnish Cultural Foundation and University of Eastern Finland (929711) strategic funding.

References

- Bayraktar, H.H., Morgan, E.F., Niebur, G.L., Morris, G.E., Wong, E.K., Keaveny, T.M., 2004. Comparison of the elastic and yield properties of human femoral trabecular and cortical bone tissue. *J. Biomech.* 37, 27–35. [http://dx.doi.org/10.1016/S0021-9290\(03\)00257-4](http://dx.doi.org/10.1016/S0021-9290(03)00257-4).
- Bessho, M., Ohnishi, I., Matsuyama, J., Matsumoto, T., Imai, K., Nakamura, K., 2007. Prediction of strength and strain of the proximal femur by a CT-based finite element method. *J. Biomech.* 40, 1745–1753. <http://dx.doi.org/10.1016/j.jbiomech.2006.08.003>.
- Bland, J.M., Altman, D.G., 1999. Measuring agreement in method comparison studies. *Stat. Methods Med. Res.* 8, 135–160. <http://dx.doi.org/10.1177/096228029900800204>.
- Burge, R., Dawson-Hughes, B., Solomon, D.H., Wong, J.B., King, A., Tosteson, A., 2007. Incidence and economic burden of osteoporosis-related fractures in the United States, 2005–2025. *J. Bone Miner. Res.* 22, 465–475. <http://dx.doi.org/10.1359/jbmr.061113>.

- Cummings, S.R., Cawthon, P.M., Ensrud, K.E., Cauley, J.A., Fink, H.A., Orwoll, E.S., 2006. BMD and risk of hip and nonvertebral fractures in older men: a prospective study and comparison with older women. *J. Bone Miner. Res.* 21, 1550–1556. <http://dx.doi.org/10.1359/jbmr.060708>.
- de Bakker, P.M., Manske, S.L., Ebacher, V., Oxland, T.R., Crompton, P.A., Guy, P., 2009. During sideways falls proximal femur fractures initiate in the superolateral cortex: evidence from high-speed video of simulated fractures. *J. Biomech.* 42, 1917–1925. <http://dx.doi.org/10.1016/j.jbiomech.2009.05.001>.
- Gilchrist, S., Guy, P., Crompton, P.A., 2013. Development of an inertia-driven model of sideways fall for detailed study of femur fracture mechanics. *J. Biomech. Eng.* 135, 121001. <http://dx.doi.org/10.1115/1.4025390>.
- Grassi, L., Isaksson, H., 2015. Extracting accurate strain measurements in bone mechanics: a critical review of current methods. *J. Mech. Behav. Biomed. Mater.* 50, 43–54. <http://dx.doi.org/10.1016/j.jmbm.2015.06.006>.
- Grassi, L., Väänänen, S.P., Amin Yavari, S., Jurvelin, J.S., Weinans, H., Ristinmaa, M., Zadpoor, A.A., Isaksson, H., 2014. Full-field strain measurement during mechanical testing of the human femur at physiologically relevant strain rates. *J. Biomech. Eng.* 136, <http://dx.doi.org/10.1115/1.4028415>.
- Grassi, L., Väänänen, S.P., Amin Yavari, S., Weinans, H., Jurvelin, J.S., Zadpoor, A.A., Isaksson, H., 2013. Experimental validation of finite element model for proximal composite femur using optical measurements. *J. Mech. Behav. Biomed. Mater.* 21, 86–94. <http://dx.doi.org/10.1016/j.jmbm.2013.02.006>.
- Helgason, B., Gilchrist, S., Ariza, O., Chak, J.D., Zheng, G., Widmer, R.P., Ferguson, S.J., Guy, P., Crompton, P., 2014. Development of a balanced experimental–computational approach to understanding the mechanics of proximal femur fractures. *Med. Eng. Phys.* 36, 793–799. <http://dx.doi.org/10.1016/j.medengphy.2014.02.019>.
- Henninger, H., Reese, S., Anderson, A., Weiss, J., 2010. Validation of computational models in biomechanics. *Proc. Inst. Mech. Eng. H* 224, 801–812.
- Järvinen, T.L.N., Sievänen, H., Jokihäärä, J., Einhorn, T.A., 2005. Revival of bone strength: the bottom line. *J. Bone Miner. Res.* 20, 717–720.
- Kanis, J.A., Borgstrom, F., De Laet, C., Johansson, H., Johnell, O., Jonsson, B., Oden, A., Zethraeus, N., Pfeleger, B., Khaltaev, N., 2005. Assessment of fracture risk. *Osteoporos. Int.* 16, 581–589. <http://dx.doi.org/10.1007/s00198-004-1780-5>.
- Kanis, J.A., McCloskey, E.V., Johansson, H., Cooper, C., Rizzoli, R., Reginster, J.-Y., 2013. European guidance for the diagnosis and management of osteoporosis in postmenopausal women. *Osteoporos. Int.* 24, 23–57. <http://dx.doi.org/10.1007/s00198-012-2074-y>.
- Koivumäki, J.E.M., Thevenot, J., Pulkkinen, P., Kuhn, V., Link, T.M., Eckstein, F., Jämsä, T., 2012. Ct-based finite element models can be used to estimate experimentally measured failure loads in the proximal femur. *Bone* 50, 824–829. <http://dx.doi.org/10.1016/j.bone.2012.01.012>.
- Lindsay, R., Pack, S., Li, Z., 2005. Longitudinal progression of fracture prevalence through a population of postmenopausal women with osteoporosis. *Osteoporos. Int.* 16, 306–312. <http://dx.doi.org/10.1007/s00198-004-1691-5>.
- McCreadie, B.R., Goldstein, S.A., 2000. Biomechanics of fracture: is bone mineral density sufficient to assess risk? *Bone Min.* Res. 15, 2305–2308.
- Morgan, E.F., Bayraktar, H.H., Keaveny, T.M., 2003. Trabecular bone modulus–density relationships depend on anatomic site. *J. Biomech.* 36, 897–904.
- Op Den Buijs, J., Dragomir-Daescu, D., 2011. Validated finite element models of the proximal femur using two-dimensional projected geometry and bone density. *Comput. Methods Programs Biomed.* 104, 168–174. <http://dx.doi.org/10.1016/j.cmpb.2010.11.008>.
- Reilly, D., Burstein, A., 1974. The mechanical properties of cortical bone. *J. Bone Jt. Surg.*, 56.
- Reilly, D., Burstein, A., Frankel, V., 1974. The elastic modulus for bone. *J. Biomech.* 7, 271–275.
- Reilly, D.T., Burstein, A.H., 1975. The elastic and ultimate properties of compact bone tissue. *J. Biomech.* 8, 393–405. [http://dx.doi.org/10.1016/0021-9290\(75\)90075-5](http://dx.doi.org/10.1016/0021-9290(75)90075-5).
- Schileo, E., Balistreri, L., Grassi, L., Cristofolini, L., Taddei, F., 2014. To what extent can linear finite element models of human femora predict failure under stance and fall loading configurations? *J. Biomech.* 47, 3531–3538. <http://dx.doi.org/10.1016/j.jbiomech.2014.08.024>.
- Schileo, E., Dall'ara, E., Taddei, F., Malandrino, A., Schotkamp, T., Baleani, M., Viceconti, M., 2008. An accurate estimation of bone density improves the accuracy of subject-specific finite element models. *J. Biomech.* 41, 2483–2491.
- Taddei, F., Schileo, E., Helgason, B., Cristofolini, L., Viceconti, M., 2007. The material mapping strategy influences the accuracy of CT-based finite element models of bones: an evaluation against experimental measurements. *Med. Eng. Phys.* 29, 973–979. <http://dx.doi.org/10.1016/j.medengphy.2006.10.014>.
- Watts, N.B., Ettinger, B., LeBoff, M.S., 2009. FRAX facts. *J. Bone Miner. Res.* 24, 975–979. <http://dx.doi.org/10.1359/jbmr.090402>.
- Viceconti, M., Olsen, S., Nolte, L.-P., Burton, K., 2005. Extracting clinically relevant data from finite element simulations. *Clin. Biomech.* 20, 451–454. <http://dx.doi.org/10.1016/j.clinbiomech.2005.01.010>.
- Yosibash, Z., Trabelsi, N., Milgrom, C., 2007. Reliable simulations of the human proximal femur by high-order finite element analysis validated by experimental observations. *J. Biomech.* 40, 3688–3699. <http://dx.doi.org/10.1016/j.jbiomech.2007.06.017>.

Paper V

Prediction of Femoral Strength Using 3D Finite Element Models Reconstructed from DXA Images: Validation Against Experiments

Lorenzo Grassi¹, Sami P. Väänänen^{2,3}, Matti Ristinmaa⁴, Jukka S. Jurvelin^{2,5}, Hanna Isaksson¹

¹ Department of Biomedical Engineering, Lund University, Sweden

² Department of Applied Physics, University of Eastern Finland, Finland

³ Department of Orthopaedics, Traumatology and Hand Surgery, Kuopio University Hospital, Finland

⁴ Division of Solid Mechanics, Lund University, Sweden

⁵ Diagnostic Imaging Center, Kuopio University Hospital, Finland

ABSTRACT

Computed tomography (CT)-based finite element (FE) models may improve the current osteoporosis diagnostics and prediction of fracture risk by providing an estimate for femoral strength. However, the need for a CT scan, as opposed to the conventional use of dual energy X-ray absorptiometry (DXA) for osteoporosis diagnostics, is considered a major obstacle. The 3D shape and bone mineral density (BMD) distribution of a femur can be reconstructed using a statistical shape and appearance model (SSAM) and the DXA image of the femur. Then, the reconstructed shape and BMD could be used to build FE models to predict bone strength. Since high accuracy is needed in all steps of the analysis, this study aimed at evaluating the ability of a 3D FE model built from one 2D DXA image to predict the strains and fracture load of human femora.

Three cadaver femora were retrieved, for which experimental measurements from ex vivo mechanical tests were available. FE models were built using the SSAM-based reconstructions: using only the SSAM-reconstructed shape, only the SSAM-reconstructed BMD distribution, and the full SSAM-based reconstruction (including both shape and BMD distribution). When compared to experimental data the SSAM-based models predicted accurately principal strains (coefficient of determination >0.83, normalised root mean square error <16%) and femoral strength (standard error of the estimate 1215 N). These results were only slightly inferior to those obtained with CT-based FE models, but with the considerable advantage of the models being built from DXA images. In summary, the results support the feasibility of SSAM-based models as a practical tool to introduce FE-based bone strength estimation in the current fracture risk diagnostics.

Keywords: Statistical shape model, statistical appearance model, Finite element, Proximal femur, Validation

Corresponding author: Lorenzo Grassi,

Department of Biomedical Engineering, Lund University, BMC D13, 221 84 Lund, Sweden

Email: lorenzo.grassi@bmc.lth.se

Telephone: +46 46 222 06 55

INTRODUCTION

Fragility fractures represent a major concern in the modern Western society, with both fracture incidence and associated economic burden continuously increasing (Burge et al. 2007). The majority of low-energy trauma fractures can be ascribed to bone weakness due to osteoporosis (Johnell and Kanis 2006). While pharmacological treatments can increase the strength of osteoporotic bone and reduce the risk of fracture (Kanis et al. 2013), the identification of the subjects at high risk of fracture remains an issue. The methods currently adopted in the clinical practice are based on measurement of bone mineral density (BMD) using dual-energy X-ray absorptiometry (DXA), often complemented by epidemiological and statistical parameters (Kanis et al. 2005; Cummings et al. 2006). These methods are limited in their ability to accurately diagnose osteoporosis (30% false negatives (Järvinen et al. 2005; Järvinen et al. 2014)), with the epidemiological and statistical tools often not being general enough, due to their ethnic-specificity (Watts et al. 2009; Lekamwasam 2010; Silverman and Calderon 2010).

Subject-specific finite element (FE) models have the potential to improve the accuracy of fracture risk predictions by providing an accurate estimate for bone strength, together with a comprehensive and local characterization of the mechanical response of bone under different loading conditions. Although FE models can predict femoral strength more closely, as compared to BMD based on DXA images (Cody et al. 1999), they are still not used in the clinics to predict fracture risk. One reason for this is that the majority of the proposed FE modelling techniques is based on computed tomography (CT) datasets. When compared to DXA, CT has higher operational cost and provides a higher radiation dose to the patients (Kanis 2002). Subject-specific FE models from DXA images would overcome this issue, enabling also the possibility of conducting clinical trials in parallel with the current diagnostics. When building FE models from DXA images, the two main approaches are: (i) construction of two-dimensional FE models using the planar image provided by the DXA instrument (Op Den Buijs and Dragomir-Daescu 2010; MacNeil et al. 2012; Sarkalkan et al. 2014a; Yang et al. 2014; Dall'Ara et al. 2016), and (ii) use of statistical tools (most often based on principal component analysis, PCA) to reconstruct the 3D shape and BMD distribution from a planar DXA image, and use the reconstructed information to perform a 3D FE analysis (Langton et al. 2009; Whitmarsh et al. 2011; Väänänen et al. 2015). Two-dimensional FE models based on DXA may accurately predict femoral strength (Yang et al. 2014; Dall'Ara et al. 2016), but cannot overcome the limitations inherent to their two-dimensional nature, such as the inability to test the bone in out-of-plane direction or to localize the point where the fracture originates. The 3D shape and BMD reconstruction from a 2D image using statistical tools has the potential to overcome these issues. The accuracy in the reconstruction of both shape and BMD has reached remarkable levels (average shape reconstruction error 1.4 mm, mean absolute difference of the reconstructed volumetric BMD 185 mg/cm³ (Väänänen et al. 2015)).

However, to the authors' best knowledge, no 3D FE models obtained from statistical reconstruction of a DXA image have been confirmed to accurately predict the mechanical behaviour of human femora, and ultimately the bone strength (Sarkalkan et al. 2014b; Castro-Mateos et al. 2014). Bryan et al. (2009) used a statistical model to generate 1000 realistic femur anatomies and estimate their fracture

risk in a configuration resembling a postero-lateral fall. However, the generated models used material properties from CT data, and no direct validation could be provided, since the models were randomly generated. Whitmarsh et al. (2012) used a statistical reconstruction of shape and BMD from DXA images to discriminate hip fracture cases. The contribution of the reconstructed models was restricted to the extraction of three-dimensional anatomical shape and density parameters. These were used as additional risk factors to improve the accuracy of the discrimination. Thus, no actual FE analyses of the mechanical behaviour of the reconstructed models were performed. Grassi et al. (2014a) evaluated the ability of PCA-based finite element models to predict the mechanical behaviour of 8 human femora. A high correlation was found between the strains predicted by the reconstructed PCA-based models and those measured during analogous experimental tests on the same specimens. However, the PCA-based models were reconstructed against 3D CT data, and no validation of femoral strength was provided. Thevenot et al. (2014) proposed a specific method to construct 3D FE models of proximal femora from a single radiograph, using a shape template and a set of geometrical parameters that were measured from the radiograph. The models were used to predict femoral strength on 21 samples in a condition resembling a fall to the side, showing a promising accuracy (coefficient of determination = 0.64, standard error of the estimate = 543 N). The material properties for the models were estimated based on the CT-based values of the training set bones and a homogeneity index derived from the radiograph. Therefore, the subject-specific BMD distribution was not taken into account, which can be a limitation when samples with BMD significantly different from that of the seven bones of the training set are examined. Recently, Bonaretti et al. (2014) created statistical models of shape and appearance using both an image-based approach (i.e., the result of the reconstruction is a volumetric image) and a mesh-based approach (i.e., a FE-ready mesh is reconstructed and used to store the shape and appearance information in the statistical model), and their strain predictions were compared to those of FE models built from segmentation of the original CT images. Both image-based and mesh-based approaches predicted similar principal strains when compared to the CT-based models, but with the mesh-based approach being more compact (i.e., requiring less modes of variation to provide an accurate reconstruction) and significantly less computationally intensive. The study concluded that image-based approaches were preferred, since some severely distorted elements were found when using the mesh-based approach. However, element distortion can be mitigated by using a mesh relaxation algorithm, and by implementing a modified cost function for bone reconstruction (Väänänen et al. 2015).

Recently, our group presented a mesh-based statistical shape and appearance model (SSAM) to reconstruct shape and BMD of a proximal femur from a single DXA image (Väänänen et al. 2015), as well as a subject-specific FE modelling procedure from CT scans to predict strain and strength of human proximal femora (Grassi et al. 2016). The latter study was validated against a set of full-field experimental measurements collected using digital image correlation (DIC) (Grassi et al. 2014b). In the present study, subsequently, we aimed at evaluating the ability of a SSAM-based FE model to accurately predict strains and strength in human femora. The results were validated against experimental DIC data, and compared to the performance of analogous CT-based FE model.

MATERIAL AND METHODS

Materials. Three male cadaver human femora, harvested fresh at Kuopio University Hospital, Finland (ethical permission 5783/2004/044/07) were used for this study. Height, weight, sex, BMD at the femoral neck, and age at death are presented in table 1. None of the donors had any reported musculoskeletal disease. The specimens were scanned both with CT (Somatom Definition AS64, Siemens AG, 0.4 x 0.4 x 0.6 mm voxel size) and with two DXA devices (Lunar Prodigy and Lunar iDXA, GE Healthcare, pixel size 1.05 x 0.60 mm and 0.25 x 0.3 mm, respectively). For all specimens, experimental strain measurements were obtained from mechanical tests performed up to fracture in a configuration resembling single leg stance. The force versus displacement curves were acquired from the loading device, while the full-field strain distribution was acquired using DIC (Grassi et al. 2014b).

Specimen ID	Sex (M/F)	Age [years]	Height [cm]	Weight [kg]	Neck BMD [g/cm ³]	Side (L/R)
#1	M	22	186	106	1.16	L
#2	M	58	183	85	0.6	R
#3	M	58	183	112	0.89	L

Table 1: Patient information (sex, age at death, height, weight, BMD at femoral neck and leg side) for the three samples used in this study.

Creation of the models. The SSAM has been thoroughly described earlier (Väänänen et al. 2015), and is only briefly summarized here. A training set of 34 proximal femur anatomies was retrieved. The samples were segmented, and their average shape was calculated. A template mesh of the average shape was generated (1.6 million tetrahedral elements, Hypermesh 11.0, Altair Engineering, Inc.) and morphed over the shape of each bone in the training set. A Matlab (The Mathworks, Inc.) re-implementation of Bonemat_V2 (Taddei et al. 2007; Venäläinen et al. 2016) was used to map bone density over each morphed mesh based on the underlying calibrated CT values. The SSAM was created by performing the singular value decomposition of a matrix containing the nodal coordinates of each morphed tetrahedral mesh and the density values for each element, arranged column-wise. The reconstruction of a femur from its 2D image was performed by using a genetic algorithm to register the SSAM to the 2D reference image. A digital reconstructed radiography (DRR) was generated at each iteration round by projecting the SSAM instance onto the coronal plane. The cost function of the genetic algorithm was given by the sum of three components: the sum of absolute difference of the areal BMD between DRR and the 2D reference image, the mesh quality of the instance (Liu and Joe 1994), and the anatomical positioning. For each of the present samples, the reconstruction was performed using three different 2D reference images, namely: 2D projection of the CT image along the antero-posterior plane (hereafter referred to as CTproj), the DXA image obtained with Lunar Prodigy (lower resolution, hereafter referred to as Prodigy), and the DXA image obtained with Lunar iDXA (higher resolution, hereafter referred to as iDXA).

The CT-based FE modelling procedure has also been previously described in detail (Grassi et al. 2016). Briefly, the femur geometry was retrieved through semi-automatic segmentation of the CT images. The geometry was converted to Non-Uniform Rational B-Splines and meshed ($\sim 100k$ elements, Hypermesh v13.0). Inhomogeneous isotropic Young's moduli were assigned using Bonemat_V3 (Taddei et al. 2007) and a set of empirical relationships to link radiological density to the modulus of elasticity (Schileo et al. 2008).

The CT-based FE modelling procedure was combined with the SSAM and the reconstruction algorithm to build subject-specific FE models from a single DXA image. For each sample three different reference images were used for reconstruction (CTproj, iDXA, Prodigy). Three different models were built for each of the three samples (#1, #2, and #3), and for each of the three reference images used for reconstruction:

- i) A FE model obtained using the CT-based geometry (considered as the true bone shape), and the bone density as estimated from the SSAM-based reconstruction of the DXA image. This model will be referred to as *SSAM-BMD*.
- ii) A FE model obtained using the estimated bone geometry as reconstructed by registering the SSAM on the DXA image, and the bone density from calibrated CT-values (considered as the true bone density distribution). This model will be referred to as *SSAM-shape*.
- iii) A FE model obtained using both the estimated geometry and the estimated bone density as reconstructed by registering the SSAM on the DXA image. This model will be referred to as *SSAM-shape & BMD*.

The rationale behind these three models was to evaluate the individual effects of each step in the shape (*SSAM-shape* models) and BMD reconstruction (*SSAM-BMD* models) on the final accuracy obtained by models implementing both shape and BMD as reconstructed by registering the SSAM on the DXA image (*SSAM-shape & BMD* models).

The *SSAM-BMD* models were created as follows: the CT-based FE meshes used in (Grassi et al. 2016) were retrieved, and the bone density distribution was mapped based on the reconstructed BMD obtained by registration of the SSAM on the DXA image. Therefore, the model obtained by registering the SSAM on the DXA image (hereafter referred to as SSAM-based mesh) was first registered and then morphed to the CT-based geometry. The BMD in the SSAM-based mesh was presented as a three-dimensional step-function according to the element borders. Then, the BMD was captured into the target CT-based mesh by integrating the function over each element in the target mesh. As a result, the density at each element was given by the average of the densities in the SSAM-based mesh, weighted by the volume of intersection between the element itself with each element of the SSAM-based mesh. Young's moduli were retrieved from density values using the same density-elasticity relationship as adopted for CT-based FE models. After the mapping, a two-step compensation process was applied, where: (i) the modulus of elasticity of the surface elements was derived as the maximum between the mapped value and the moduli of the neighbouring elements that were not surface elements

as well, and (ii) the allowed maximum modulus of elasticity for the model was set to 22 GPa (Bayraktar et al. 2004), while the minimum modulus of elasticity for the surface elements was set to 5 GPa (assuming very thin cortex and consequently a Young's modulus corresponding to that of the underlying trabecular bone (Rho et al. 1993)). The whole registration, warping, and density mapping procedure was implemented in Matlab.

The *SSAM-shape* models were created by taking the geometry of the SSAM-based mesh. The geometry was meshed using Hypermesh (v14.0, Altair, Inc.), using the same parameters adopted in Grassi et al. (2016) (element size 1.5 mm on the femoral neck, 2 mm elsewhere, ~100k tetrahedral elements). The mesh was then registered to the CT reference system, and the bone density values were assigned based on the underlying CT-values using Bonemat_V3 (Taddei et al. 2007). The geometry of the SSAM-based mesh included a smaller portion of the bone than the femoral segment imaged with CT. In order to create *SSAM-shape* models with the same length as that of the CT-based models, the missing distal part of the shaft and the epoxy pot from the CT-based models were connected to the model using tie connections in Abaqus (v2016, Dassault Systèmes). These procedures were implemented in Matlab. An example of the model is shown in figure 1.

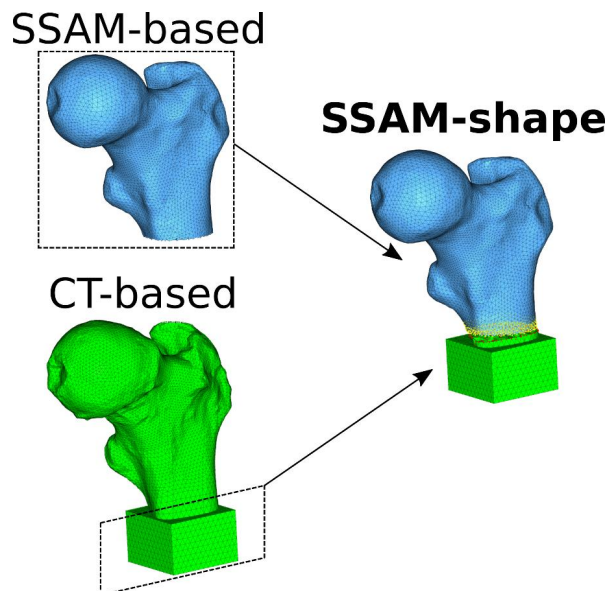


Figure 1: Schematic of the generation of the FE models implementing the SSAM-based shape (*SSAM-shape* and *SSAM-shape* & BMD models): the model produced by the SSAM-based reconstruction (depicted in blue, left side) present a shorter shaft than the actual sample, as reconstructed by segmentation of its CT scan (CT-based model depicted in green, left side). In order to test the SSAM-shape based models while keeping the exact same boundary conditions as in the experiments (Grassi et al. 2014) and in the CT-based FE models (Grassi et al. 2016), the most distal part of the CT-based FE model was added to the SSAM-based FE model, and connected to it using tie constraints (Abaqus v2016, Dassault Systèmes). The distal cut region of the SSAM-based FE model (yellow points) was thus rigidly connected to the cutting region of the CT-based FE model (red points).

The *SSAM-shape* & *BMD* models were created by taking the shape of the reconstructed SSAM-based models, analogously to what described for the *SSAM-shape* models, as well as including the bone density from the reconstructed SSAM-based models, using the procedure described for the *SSAM-BMD* models.

Performance comparison. In order to evaluate the performance of each of the models created, identical boundary conditions to those in the experiments (Grassi et al. 2014b) and in the CT-based FE models (Grassi et al. 2016) were applied. The ability of the models to predict the mechanical behaviour of bone was then evaluated both in terms of strain prediction accuracy, and of ability to predict femoral strength.

To assess the strain prediction accuracy, a force equal to four times the body weight (BW) of the subject was applied onto the femoral head, equally distributed among the 10 most superior nodes on the surface. The principal strain patterns were then obtained and compared to principal strains measured experimentally with DIC. To do this, the DIC cloud was registered over the FE model using an iterative closest point algorithm. When the model had its shape retrieved from SSAM reconstruction (*SSAM-shape* and *SSAM-shape* & *BMD* models), a point to surface projection of the DIC points over the FE model was performed. For each surface element of the FE models, the smallest sphere circumscribing it was calculated. All DIC data within that sphere were averaged, and the obtained experimental value was compared to the FE element strain. A robust regression analysis with bi-square weighting function of the major and minor principal strain magnitudes was finally performed. The coefficient of determination, slope, intercept, normalized root mean square error (NRMSE) and maximum error were reported for each robust regression. The same accuracy parameters obtained earlier by the CT-based FE models (Grassi et al. 2016) are also reported to allow for a comparison between the proposed SSAM-based models and the state of the art.

To validate femoral strength prediction, a rate-dependent material model, with different strain limit values for yield and failure, was used (Grassi et al. 2016). The material model and failure criterion are depicted in figure 2. The FE analyses were conducted in displacement control with consecutive 0.05 mm increments. The sum of the reaction forces at the increment where the first element of the model failed was calculated to indicate the predicted femoral strength. The simulation time was adjusted to provide a displacement rate of 15 mm/s, identical to the value used in the experimental mechanical tests. The predicted and experimental femoral strength data were compared in terms of relative error and standard error of the estimate (SEE). Again, the accuracy of the strength prediction achieved by CT-based FE models (Grassi et al. 2016) was presented to enable immediate comparison.

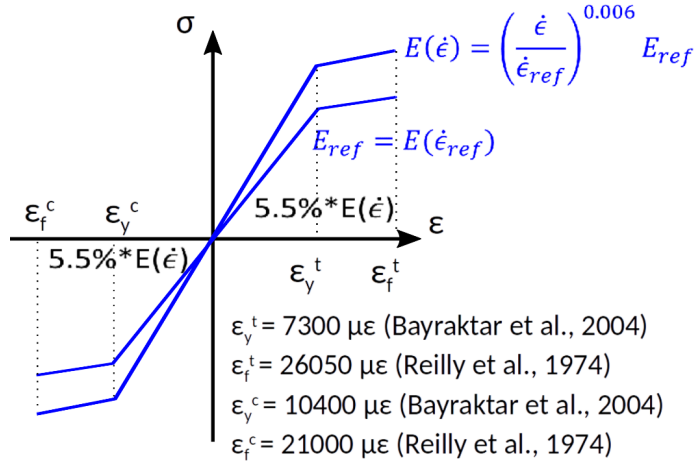


Figure 2: Diagram showing the material model implemented to predict femoral strength, as proposed first in (Grassi et al. 2016). Each element is assigned a modulus of elasticity which applies for the reference strain rate (5000 $\mu\epsilon/s$, consistently with the strain rate used to experimentally obtain the density-elasticity relationships (Morgan et al. 2003) and yield limit values (Bayraktar et al. 2004) used in this model). The strain rate was then constantly updated for each element during the simulation, and its modulus of elasticity according to relationship for $E(\dot{\epsilon})$ shown in figure. Yield and failure were defined by separate thresholds for tension and compression. When an element reached the yield state, its modulus of elasticity was reduced to $0.55 * E(\dot{\epsilon})$, and the simulation proceeded. The simulation was stopped when the first surface element reached the failed state, and the applied force at that stage taken as the predicted femoral strength.

The error in the shape reconstruction was also assessed. The distance between the nodes of the *SSAM-shape* models and the surface of the CT-based models was calculated. In addition, the volumetric difference between the *SSAM-shape* and CT-based models was calculated limited to the femoral neck region.

RESULTS

The results of the robust regression analyses for the principal strains predicted at 4 BW are reported in figure 3 for the three bones pooled of the *SSAM-BMD*, *SSAM-shape*, and *SSAM-shape* \leftrightarrow *BMD* models. The coefficient of determination was always greater than 0.83, while the slope was within $\pm 10\%$ from unity for all but two cases (*SSAM-shape* models from Prodigy images, and *SSAM-shape* \leftrightarrow *BMD* models from iDXA images).

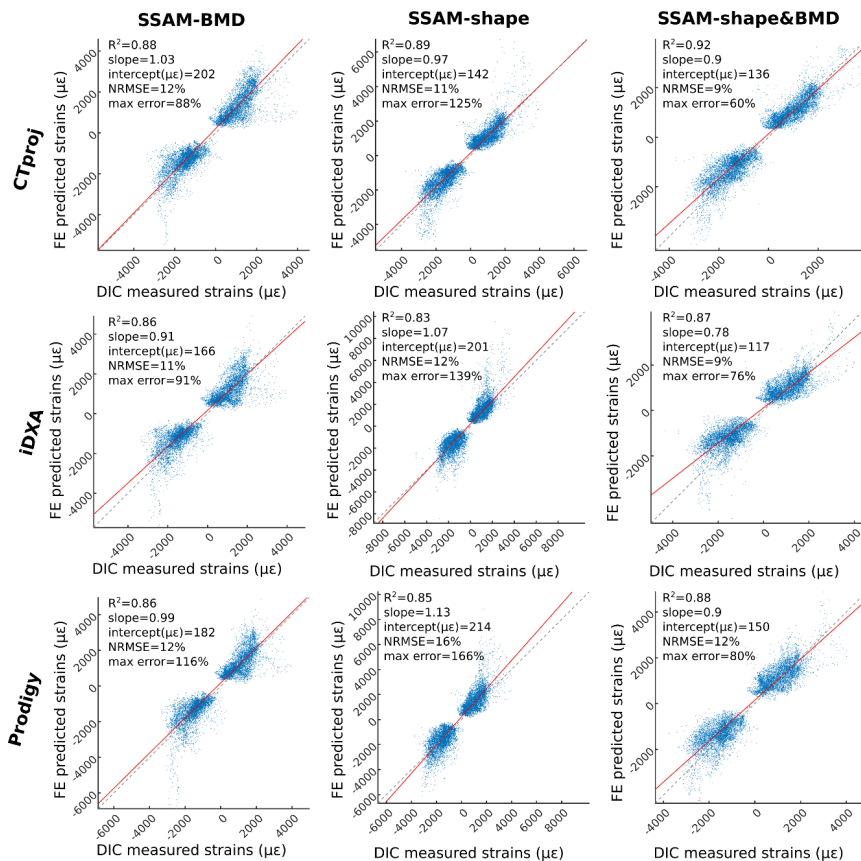


Figure 3: Prediction accuracy for the major and minor principal strains for SSAM-BMD (1st column), SSAM-shape (2nd column), and SSAM-shape & BMD (3rd column) models of the three bones pooled together. From top to bottom, the accuracy results are plotted for the models using CT projection, iDXA, and Prodigy images for the SSAM-based reconstructions.

The coefficient of determination was consistently higher for the models using the CT projection for the reconstruction, followed by those using Prodigy images. The models based on the use of iDXA images showed the lowest values. For comparison, the analogous robust regression analysis for the CT-based models (Grassi et al. 2016) when the data on three bones were pooled provided an R^2 of 0.94, with a slope of 0.96 (intercept = 133 $\mu\epsilon$), NRMSE = 9%, with a maximum estimation error of 65%.

		bone #1			bone #2			bone #3		
		CTproj	iDXA	Prodigy	CTproj	iDXA	Prodigy	CTproj	iDXA	Prodigy
SSAM-BMD	R²	0.9	0.9	0.9	0.84	0.83	0.83	0.92	0.89	0.89
	slope	1	0.91	0.92	1.03	0.99	1.08	1.03	0.85	0.97
	Intercept ($\mu\epsilon$)	225	199	200	257	263	283	142	84	107
	NRMSE	13%	11%	11%	19%	18%	20%	12%	12%	12%
	max error%	64%	69%	70%	89%	89%	113%	63%	58%	80%
SSAM-shape	R²	0.89	0.82	0.82	0.89	0.88	0.88	0.91	0.79	0.83
	slope	0.88	1	1.04	0.98	1.03	1.11	1.07	1.22	1.23
	Intercept ($\mu\epsilon$)	201	309	332	102	167	158	61	127	141
	NRMSE	12%	18%	19%	13%	15%	18%	10%	13%	15%
	max error%	73%	188%	87%	125%	136%	108%	82%	134%	176%
SSAM-shape & BMD	R²	0.88	0.84	0.86	0.94	0.89	0.9	0.92	0.87	0.88
	slope	0.81	0.76	0.88	0.9	0.74	0.86	0.98	0.86	0.99
	intercept ($\mu\epsilon$)	197	217	252	109	141	181	68	3	17
	NRMSE	11%	14%	15%	10%	11%	13%	9%	8%	12%
	max error%	34%	37%	43%	51%	70%	61%	74%	72%	91%
CT-based (Grassi et al. 2016)	R²		0.92			0.94			0.95	
	slope		0.92			0.97			1.01	
	intercept ($\mu\epsilon$)		144			174			79	
	NRMSE		10%			11%			11%	
	max error%		46%			59%			83%	

Table 2: Prediction accuracy for the major and minor principal strains for SSAM-BMD models of the three bones taken individually. For each bone, the accuracy obtained using the three different 2D reference images (CT projection, iDXA, and Prodigy) for the SSAM-based reconstruction is reported. The accuracy parameters reported by Grassi et al. (2016) for the CT-based models were also reported in the last row to allow for an easy comparison.

The individual validation of the single bones demonstrated a coefficient of determination greater than 0.79 for all cases and a NRMSE always below 20%, as shown in table 2 for the *SSAM-BMD*, *SSAM-shape*, and *SSAM-shape & BMD* models. The slope was generally close to unity, with a few exceptions: the slope was underestimated by 14-26% for the *SSAM-shape & BMD* models using iDXA images for the reconstruction. On the other hand, the slope of SSAM-shape models for bone #3 was overestimated by 22% and 23% when using iDXA and Prodigy images for reconstruction, respectively. The previous results of the analogous individual validations for the CT-based FE models in Grassi et al. (2016) are also reported in table 2. Due to a technical problem during the mechanical test, the femoral strength could not be validated for bone #3 (please see (Grassi et al. 2016)). The SEE for the *SSAM-shape & BMD* models (pooling the models from the three 2D reference images) was 1215 N (table 3). Typically, more accurate strength estimations were obtained when using CTproj data as the 2D reference image (SEE = 1689 N, against SEE equal to 1974 N and 1938 N for iDXA and Prodigy data, respectively).

	Bone #1			Bone #2			SEE [N]
	CTproj	iDXA	Prodigy	CTproj	iDXA	Prodigy	
SSAM-BMD	9858 (-26%)	11309 (-15%)	11007 (-18%)	7115 (-9%)	7789 (-1%)	5046 (-35%)	2267
SSAM-shape	12776 (-4%)	9301 (-30%)	10983 (-18%)	7885 (+0.4%)	8525 (+8%)	7445 (-5%)	
SSAM-shape & BMD	13106 (-2%)	13009 (-3%)	14820 (+11%)	9777 (+24%)	9203 (+17%)	8859 (+13%)	1215
CT-based (Grassi et al. 2016)	13184 (-1%)			7947 (+1%)			155
Experimentally measured (Grassi et al. 2014b)	13383			7856			-

Table 3: Femoral strength prediction accuracy for bones #1 and #2, for the three different FE models (SSAM-BMD, SSAM-shape, and SSAM-shape & BMD), each of them built for the three different 2D reference images (CT projection, iDXA, and Prodigy). The relative error to the actual femoral strength measured experimentally (Grassi et al. 2014b) is reported between parentheses. The strength prediction accuracy reported by Grassi et al. (2016) for the CT-based models was also reported in the last row to allow for an easy comparison.

The shape reconstructions performed over CTproj evidenced a higher accuracy in boundary recovery than those based on iDXA and Prodigy images (figure 4). Higher reconstruction errors were generally localized in regions with negligible contribution to the mechanical behaviour of femora, such as the tip of the greater trochanter. The volumetric difference at the femoral neck, calculated between the SSAM-shape and CT-based models (table 4), highlighted the reconstruction error in a region with crucial mechanical contribution under the single leg stance configuration.

	Bone #1	Bone #2	Bone #3
CTproj	9%	10%	9%
iDXA	19%	13%	-6%
Prodigy	5%	15%	0.3%

Table 4: Relative change between the volume of the femoral neck of the SSAM-shape models and the CT-based models (here considered as the true value), for the three different types of 2D reference image (CT projection, iDXA, and Prodigy). Positive values indicate that the SSAM-reconstructed shape is bigger.

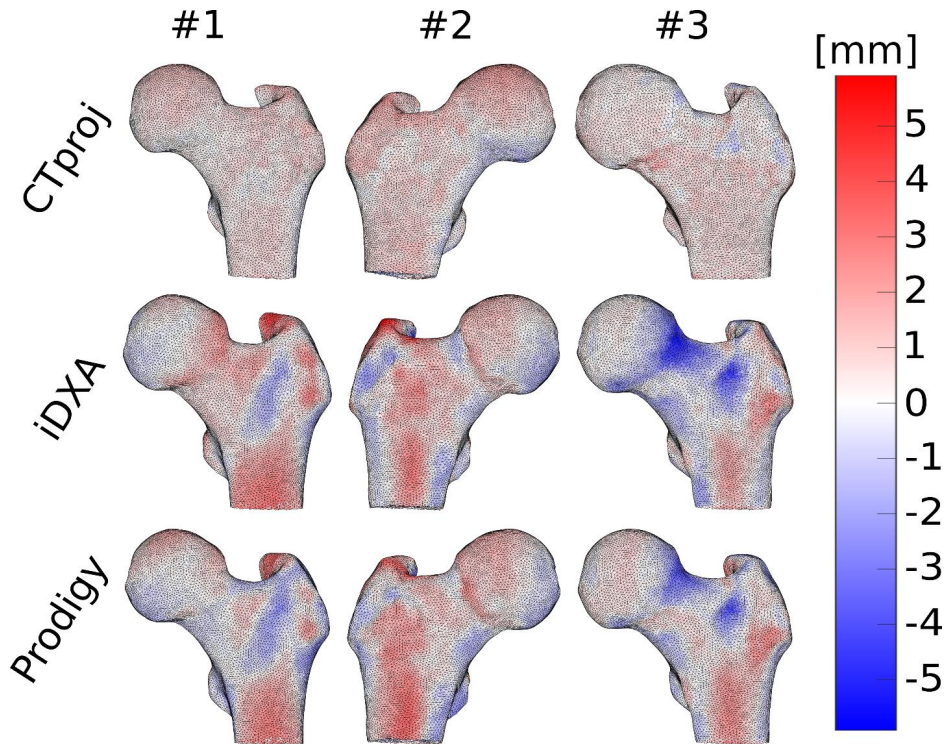


Figure 4: Error in the shape reconstruction for the three different femora (from left to right, bone #1, #2, and #3) and the different types of images (from top to bottom, CT projection, iDXA, and Prodigy) used for the SSAM-based reconstruction.

DISCUSSION

This study posed the main question of how accurately a 3D FE model reconstructed from a single DXA image and a SSAM could predict tissue strains and strength of proximal femur. The gold standard method, CT-based 3D FE model, was applied as a reference. To properly answer this question, it is necessary to understand the relative contribution of the different factors (bone shape, BMD distribution, local reconstruction errors, etc.) to the prediction accuracy. To this aim, three different models were built, implementing the reconstructed bone shape only (*SSAM-shape* models), the reconstructed BMD distribution only (*SSAM-BMD* models), and the combination of these two (*SSAM-shape & BMD* models).

The *SSAM-shape & BMD* models predicted strains with high accuracy (coefficient of determination > 0.87 , NRMSE $< 12\%$ for the three bones pooled, figure 3), when validated against thousands of experimental strain measurements per bone collected with DIC. CT-based FE models obtained a

coefficient of determination of 0.94, with a NRMSE of 9% for the same set of samples and experimental data (Grassi et al. 2016). Our present results on accuracy were only slightly lower. Nevertheless, *SSAM-shape & BMD* models reconstructed using iDXA significantly underestimated the strain levels (slope of the robust linear regression = 0.78). The inaccuracy was mostly related to bones #1 and #2 (*SSAM-shape & BMD* models from iDXA, table 2). By implementing only the shape and only the BMD from the SSAM reconstruction we can explain how to the strain underestimation occurred for these two cases. When implementing only *SSAM-BMD* (*SSAM-BMD* models from iDXA, table 2) and *SSAM-shape* (*SSAM-shape* models from iDXA, table 2), both samples exhibited a slope close to unity. However, due to the shape reconstruction error, the volume in the femoral neck region was overestimated by 13-19% (iDXA values, figure 4 and table 4). Therefore, a correct reconstruction of the material properties was associated with a femoral neck that was 13-19% bigger in volume than the CT-based one, which led to a stiffer femoral neck and ultimately underestimated the principal strains for the iDXA cases. This reveals that the accuracy in the shape reconstruction from SSAM models should be evaluated not only in terms of the absolute point-to-surface distance, but also in terms of the capacity to preserve the actual volumes of the different anatomical compartments (femoral neck first, but also femoral head, and shaft).

The *SSAM-shape & BMD* models predicted femoral strength with a SEE of 1215 N and a maximum absolute relative error of 24% (table 3). The CT-based models predicted femoral strength with a SEE of 155 N and a maximum absolute relative error of 1.5% for the same set of data (Grassi et al. 2016). The accuracy data on femoral strength (table 3) were scattered. Typically, femoral strength was predicted with high accuracy, but also some outliers with lower accuracy were found in the data. At least two main trends were observed, namely: (i) the models built using CTproj as 2D reference image were more accurate than those built with iDXA and Prodigy. This was consistent with the fact that CTproj data had a higher signal-to-noise ratio than DXA images. The different spatial resolution between iDXA (pixel size 0.25 x 0.3 mm) and Prodigy (pixel size 1.05 x 0.6 mm) was not found to affect the accuracy of the SSAM-based models, instead (ii) the *SSAM-BMD* models had a higher SEE than the *SSAM-shape* models. This evidence suggested that the error in the reconstruction of BMD, and consequently of the material properties, influenced the outcome more than the error in the shape reconstruction. Consistent to this finding, Bonaretti et al. (2014) found that the mesh-based SSAM reconstructions (like the one used in this study) are less accurate than the image-based SSAM reconstructions in estimating the original bone density distribution. This was also consequent to the fact that a strain based criterion, thus strongly dependent on the correctly estimated value for modulus of elasticity, was adopted for the calculation of femoral strength.

This is, to our best knowledge, the first study evaluating the ability of a FE model built from a statistical-based reconstruction to predict strains and femoral strength of human proximal femora anatomies against direct ex vivo measurements. A validation in terms of strain prediction accuracy was already proposed (Grassi et al. 2014a). However, the femoral strength was not evaluated and, more importantly, the PCA-based reconstruction was performed over the 3D CT data (Grassi et al. 2014a). This limited the applicability of the study to the reconstruction of synthetic anatomies aimed at exploring the effects of anatomical variability. In the present study the FE models were reconstructed

from two-dimensional reference images, thus making them suitable for subject-specific estimation of fracture risk. Earlier, Thevenot et al. (2014) validated their models in terms of femoral strength and reported a SEE of 543 N, a lower value than the SEE reported in the present study (SEE = 1215 N, table 3). However, the present samples were tested in a configuration resembling single leg stance. They were fractured at an average load of 10620 N. Thevenot et al. tested their samples in an experimental configuration resembling a fall to the side, with a much lower fracture load (average 3188 N, as extrapolated by digitalisation of data from figure 4 in (Thevenot et al. 2014)). The present higher SEE is therefore consistent with the fracture load being three times higher than that found by Thevenot et al. In terms of relative error, the maximum absolute relative error in the prediction of femoral strength was 24% in our study, whereas it was 54% in Thevenot et al. (as extrapolated by digitalisation of data from figure 4 in (Thevenot et al. 2014)).

Other studies have also proposed to use PCA-based models to predict fracture risk (Gregory et al. 2004; Schuler et al. 2010; Whitmarsh et al. 2012). However, those studies used the reconstructed shape and BMD distribution either to obtain three-dimensional anatomical and densitometry measurements that complemented the standard estimation of fracture risk, or to employ the model parameters as features for the classification. The present study, instead, used SSAM-based models to predict femoral strength using a purely mechanistic approach, analogously to how it is done with gold standard CT-based FE models.

The present study is limited by its small sample size, with three proximal human femora tested. However, the accuracy of the adopted SSAM-based method in reconstructing shape and BMD was previously validated using a higher number of samples (Väänänen et al. 2015). As the present focus was on the ability of the reconstructed models to predict strain and femoral strength, only the samples for which full-field strain data from *ex vivo* mechanical tests were available (Grassi et al. 2014b) were used.

The combination of the current epidemiological-based estimation of individual fracture risk could be greatly improved by the addition of a mechanistic prediction of the load that a bone can bear without fracturing (Viceconti et al. 2015). When aiming to manage effectively the future challenges related to known increase of musculoskeletal diseases, such as osteoporosis and bone fractures, we are much limited with the existing medical technology. DXA is the current clinical standard to diagnose osteoporosis and ultimately estimate fracture risk. Adoption of CT for this screening is not realistic in a short-term scenario. Therefore, the current study aimed to improve the understanding of how useful the 3D FE models, as reconstructed from a single 2D DXA image, are to predict femoral strength. Based on the present findings, SSAM-based FE models provided a highly accurate representation of the subject-specific bone mechanics in terms of bone strains ($R^2 > 0.87$, NRMSE < 12%). However, the accuracy in the prediction of femoral strength was inferior to those obtained with the state-of-the-art CT-based models (SEE = 1215 N, against SEE = 155 N for the CT-based models). The greater error in femoral strength estimation was mostly due to the presence of a few outliers in the data (table 3). The present results support the future translation of SSAM-based FE models into the clinics as a tool to complement the current methods for prediction of fracture risk by providing a mechanistic

information of the bone mechanical behaviour. Further, these results could help to tailor future development of SSAM-based reconstructions with the aim to further improve their accuracy towards that of CT-based models.

ACKNOWLEDGEMENTS

The study was supported by the Swedish Research Council (2011-5064, 2015-4795), Swedish Foundation for Strategic Research, Finnish Cultural Foundation. CSC – IT center for science and Lunarc – Center for scientific and technical computing at Lund University are acknowledged for their computational resources.

CONFLICT OF INTEREST

The authors declare that they have no conflict of interest.

REFERENCES

- Bayraktar HH, Morgan EF, Niebur GL, et al (2004) Comparison of the elastic and yield properties of human femoral trabecular and cortical bone tissue. *J Biomech* 37:27–35. doi: 10.1016/S0021-9290(03)00257-4
- Bonaretti S, Seiler C, Boichon C, et al (2014) Image-based vs. mesh-based statistical appearance models of the human femur: Implications for finite element simulations. *Med Eng Phys* 36:1626–1635. doi: 10.1016/j.medengphy.2014.09.006
- Bryan R, Nair PB, Taylor M (2009) Use of a statistical model of the whole femur in a large scale, multi-model study of femoral neck fracture risk. *J Biomech* 42:2171–6. doi: 10.1016/j.jbiomech.2009.05.038
- Burge R, Dawson-Hughes B, Solomon DH, et al (2007) Incidence and economic burden of osteoporosis-related fractures in the United States, 2005–2025. *J Bone Miner Res* 22:465–75. doi: 10.1359/jbmr.061113
- Castro-Mateos I, Pozo JM, Cootes TF, et al (2014) Statistical shape and appearance models in osteoporosis. *Curr Osteoporos Rep* 12:163–173. doi: 10.1007/s11914-014-0206-3
- Cody DD, Gross GJ, Hou FJ, et al (1999) Femoral strength is better predicted by finite element models than QCT and DXA. *J Biomech* 32:1013–1020.
- Cummings SR, Cawthon PM, Ensrud KE, et al (2006) BMD and risk of hip and nonvertebral fractures in older men: a prospective study and comparison with older women. *J Bone Miner Res* 21:1550–6. doi: 10.1359/jbmr.060708
- Dall'Ara E, Eastell R, Viceconti M, et al (2016) Experimental Validation of DXA-based Finite Element models for prediction of femoral strength. *J Mech Behav Biomed Mater* 63:17–25. doi: 10.1016/j.jmbbm.2016.06.004
- Grassi L, Schileo E, Boichon C, et al (2014a) Comprehensive evaluation of PCA-based finite element modelling of the human femur. *Med Eng Phys* 36:1246–1252. doi: 10.1016/j.medengphy.2014.06.021
- Grassi L, Väänänen SP, Amin Yavari S, et al (2014b) Full-field Strain Measurement During Mechanical Testing of the Human Femur at Physiologically Relevant Strain Rates. *J Biomech Eng*. doi: 10.1115/1.4028415
- Grassi L, Väänänen SP, Ristinmaa M, et al (2016) How accurately can subject-specific finite element models predict strains and strength of human femora? Investigation using full-field measurements. *J Biomech* 49:802–806. doi: 10.1016/j.jbiomech.2016.02.032

- Gregory JS, Testi D, Stewart A, et al (2004) A method for assessment of the shape of the proximal femur and its relationship to osteoporotic hip fracture. *Osteoporos Int a J Establ as result Coop between Eur Found Osteoporos Natl Osteoporos Found USA* 15:5–11.
- Järvinen TLN, Jokihäärä J, Guy P, et al (2014) Commentary Conflicts at the heart of the FRAX tool. *CMAJ* 186:165–167.
- Järvinen TLN, Sievänen H, Jokihäärä J, Einhorn TA (2005) Revival of Bone Strength: The Bottom Line. *J Bone Miner Res* 20:717–720.
- Johnell O, Kanis JA (2006) An estimate of the worldwide prevalence and disability associated with osteoporotic fractures. *Osteoporos Int* 17:1726–33. doi: 10.1007/s00198-006-0172-4
- Kanis JA (2002) Diagnosis of osteoporosis and assessment of fracture risk. *Lancet* 359:1929–1936. doi: 10.1016/S0140-6736(02)08761-5
- Kanis JA, Borgstrom F, De Laet C, et al (2005) Assessment of fracture risk. *Osteoporos Int* 16:581–9. doi: 10.1007/s00198-004-1780-5
- Kanis JA, McCloskey E V, Johansson H, et al (2013) European guidance for the diagnosis and management of osteoporosis in postmenopausal women. *Osteoporos Int* 24:23–57. doi: 10.1007/s00198-012-2074-y
- Langton CM, Pisharody S, Keyak JH (2009) Generation of a 3D proximal femur shape from a single projection 2D radiographic image. *Osteoporos Int* 20:455–61. doi: 10.1007/s00198-008-0665-4
- Lekamwasam S (2010) Application of FRAX model to Sri Lankan postmenopausal women. *J Clin Densitom* 13:51–5. doi: 10.1016/j.jocd.2009.09.001
- Liu A, Joe B (1994) Relationship between tetrahedron shape measures. *BIT* 34:268–287. doi: 10.1007/BF01955874
- MacNeil JAM, Adachi JD, Goltzman D, et al (2012) Predicting fracture using 2D finite element modelling. *Med Eng Phys* 34:478–84. doi: 10.1016/j.medengphy.2011.08.008
- Op Den Buijs J, Dragomir-Daescu D (2010) Validated finite element models of the proximal femur using two-dimensional projected geometry and bone density. *Comput Methods Programs Biomed* 104:1–7. doi: 10.1016/j.cmpb.2010.11.008
- Rho JY, Ashman RB, Turner CH (1993) Young's modulus of trabecular and cortical bone material: Ultrasonic and microtensile measurements. *J Biomech* 26:111–119. doi: 10.1016/0021-9290(93)90042-D
- Sarkalkan N, Waarsing JH, Bos PK, et al (2014a) Statistical shape and appearance models for fast and automated estimation of proximal femur fracture load using 2D finite element models. *J Biomech* 47:3107–3114. doi: 10.1016/j.jbiomech.2014.06.027
- Sarkalkan N, Weinans H, Zadpoor AA (2014b) Statistical shape and appearance models of bones. *Bone* 60:129–140.
- Schileo E, Dall'ara E, Taddei F, et al (2008) An accurate estimation of bone density improves the accuracy of subject-specific finite element models. *J Biomech* 41:2483–2491.
- Schuler B, Fritscher KD, Kuhn V, et al (2010) Assessment of the individual fracture risk of the proximal femur by using statistical appearance models. *Med Phys* 37:2560–71.
- Silverman SL, Calderon AD (2010) The utility and limitations of FRAX: A US perspective. *Curr Osteoporos Rep* 8:192–7. doi: 10.1007/s11914-010-0032-1
- Taddei F, Schileo E, Helgason B, et al (2007) The material mapping strategy influences the accuracy of CT-based finite element models of bones: an evaluation against experimental measurements. *Med Eng Phys* 29:973–9. doi:

10.1016/j.medengphy.2006.10.014

- Thevenot J, Koivumäki J, Kuhn V, et al (2014) A novel methodology for generating 3D finite element models of the hip from 2D radiographs. *J Biomech* 47:438–444. doi: 10.1016/j.jbiomech.2013.11.004
- Väänänen SP, Grassi L, Flivik G, et al (2015) Generation of 3D shape, density, cortical thickness and finite element mesh of proximal femur from a DXA image. *Med Image Anal* 24:125–134. doi: 10.1016/j.media.2015.06.001
- Venäläinen MS, Mononen ME, Väänänen SP, et al (2016) Effect of bone inhomogeneity on tibiofemoral contact mechanics during physiological loading. *J Biomech* 49:1111–1120. doi: 10.1016/j.jbiomech.2016.02.033
- Viceconti M, Hunter P, Hose D (2015) Big data, big knowledge: big data for personalised healthcare. *IEEE J Biomed Heal Informatics* 2194:1–1. doi: 10.1109/JBHI.2015.2406883
- Watts NB, Ettinger B, LeBoff MS (2009) FRAX facts. *J Bone Miner Res* 24:975–9. doi: 10.1359/jbmr.090402
- Whitmarsh T, Fritscher KD, Humbert L, et al (2012) Hip fracture discrimination from dual-energy X-ray absorptiometry by statistical model registration. *Bone* 51:896–901. doi: 10.1016/j.bone.2012.08.114
- Whitmarsh T, Humbert L, De Craene M, et al (2011) Reconstructing the 3D Shape and Bone Mineral Density Distribution of the Proximal Femur from Dual-energy X-ray Absorptiometry. *IEEE Trans Med Imaging*. doi: 10.1109/TMI.2011.2163074
- Yang L, Palermo L, Black DM, Eastell R (2014) Prediction of incident hip fracture with the estimated femoral strength by finite element analysis of DXA Scans in the study of osteoporotic fractures. *J Bone Miner Res* 29:2594–600. doi: 10.1002/jbmr.2291